Cryogenic Nonlinear Optics in Titanium In-Diffused Lithium Niobate Waveguides for Quantum Photonics

Der Naturwissenschaftlichen Fakultät
der Universität Paderborn zur
Erlangung des Doktorgrades

Dr. rer. nat.

vorgelegt von

Nina Amelie Lange

Paderborn, April 17, 2026

Summary

Integrated quantum photonic circuits increasingly require cryogenic operation, as key components such as superconducting single-photon detectors and many deterministic quantum light sources only function at low temperatures. This thesis investigates nonlinear frequency conversion in titanium in-diffused periodically poled lithium niobate (Ti:PPLN) waveguides under cryogenic conditions and evaluates their suitability for quantum photonics.

A free-space coupled cryogenic setup was developed, enabling broadband characterization from room temperature to below 10 K. Cryogenic spontaneous parametric down-conversion was demonstrated for the first time and tailored for degenerate telecom photon-pair generation. The measurements reveal both predictable and random temperature-dependent effects. Refractive index changes and thermal contraction can be modeled accurately. In contrast, the strong reduction in charge-carrier mobility leads to persistent pyroelectric and photorefractive fields, which alter mode confinement, increase losses, and limit reproducibility over repeated thermal cycles. Interactions involving TE-modes and pulsed light showed more robust performance, whereas TM-modes and visible-wavelength processes were particularly susceptible. The pyroelectric effect was found to be the main factor governing the cryogenic performance.

Overall, the results show that Ti:PPLN remains a promising platform for cryogenic quantum photonics, provided that internal electric fields are carefully controlled.

Zusammenfassung

Integrierte quantenphotonische Schaltungen erfordern zunehmend kryogenen Betrieb, da supraleitende Einzelphotonen-Detektoren und viele deterministische Quantenlichtquellen nur bei tiefen Temperaturen funktionieren. Diese Arbeit untersucht die nichtlineare Frequenzkonversion in Titan-eindiffundierten Wellenleitern in periodisch gepoltem Lithiumniobat (Ti:PPLN) bei kryogenen Temperaturen und bewertet deren Eignung für die Quantenphotonik.

Es wurde ein freistrahlgekoppelter kryogener Aufbau entwickelt, der breitbandige Charakterisierung von Raumtemperatur bis unter 10 K ermöglicht. Kryogene parametrische Fluoreszenz wurde zum ersten Mal demonstriert und für entartete Photonenpaare im Telekom-Bereich optimiert. Die Messungen zeigen vorhersagbare und zufällige Effekte. Änderungen des Brechungsindex und thermische Kontraktion lassen sich genau modellieren. Dagegen führt die stark verringerte Ladungsträgermobilität zu anhaltenden pyroelektrischen und photorefraktiven Feldern, die räumliche Moden verändern, Verluste erhöhen und die Reproduzierbarkeit limitieren. Prozesse mit TE-Moden und gepulstem Licht erwiesen sich als robuster, während Prozesse mit TM-Moden und sichtbaren Wellenlängen besonders anfällig waren. Der pyroelektrische Effekt erwies sich als der Hauptfaktor, der die kryogene Leistung bestimmt.

Insgesamt zeigen die Ergebnisse, dass Ti:PPLN eine vielversprechende Plattform für die kryogene Quantenphotonik bleibt, sofern die internen elektrischen Felder sorgfältig kontrolliert werden.

Contents

List of Abbreviations **IX**

1 Introduction **1**

2 How to get to know your (cryogenic) waveguide **11**
- 2.1 Theoretical basics - What to know before you start 11
  - 2.1.1 Introduction to nonlinear optics 12
  - 2.1.2 Titanium in-diffused waveguides in lithium niobate 19
  - 2.1.3 Intrinsic material changes at cryogenic temperatures 20
- 2.2 Experimental methods 28
  - 2.2.1 Cryostat configuration for waveguide characterization 28
  - 2.2.2 Waveguide mounting and coupling procedure 32
  - 2.2.3 Nonlinear characterization methods 37

3 Cryogenic SPDC in the telecom range **47**
- 3.1 Experimental methods 48
  - 3.1.1 Waveguide design 50
- 3.2 How it began - Proof-of-principle cryogenic SPDC 51
  - 3.2.1 SPDC performance metrics 51
  - 3.2.2 Spectral properties of signal and idler 52
  - 3.2.3 Evaluation of the proof-of-principle measurement series 56
- 3.3 Tailoring the process - Cryogenic SPDC for degenerate photon pairs . . . 58
  - 3.3.1 Classical characterization of the phase-matching 58
  - 3.3.2 Measuring cryogenic SPDC photons 60
  - 3.3.3 Evaluation of the degenerate measurement series 64
- 3.4 Chapter conclusion 65

4 Widely non-degenerate frequency conversion at cryogenic temperatures **67**
- 4.1 Experimental methods 69
  - 4.1.1 Pump light generation 69
  - 4.1.2 Cryogenic waveguide characterization 71
  - 4.1.3 Cryogenic SPDC 71
  - 4.1.4 Waveguide design 72
- 4.2 Sum-frequency generation for pump light generation 75
- 4.3 Cryogenic waveguiding and phase-matching characterization 78
  - 4.3.1 Linear waveguide performance 78
  - 4.3.2 Variations in the nonlinear phase-matching 85

4.4 Non-degenerate photons from cryogenic SPDC 86
4.4.1 Pump-power dependent performance 87
4.4.2 Joint spectral intensity measurement 89
4.5 Chapter conclusion 92

5 Cryogenic nonlinear optics: what does it teach us? 95
5.1 Deeper insights into the cryogenic performance of lithium niobate 97
5.1.1 Pyroelectric charge accumulation during the cooldown process . 97
5.1.2 Photorefractive damage induced at cryogenic temperatures . . . 100
5.1.3 Experimental refractive index determination using type-0 SFG . 106
5.2 Studies on the reproducibility of cryogenic performance 113
5.2.1 Research questions 113
5.2.2 Experimental setup 115
5.2.3 Measurement series 116
5.2.4 Evaluation of the waveguide performance 117
5.2.5 Key factors affecting the cryogenic waveguides 124
5.3 Chapter conclusion 126

6 Conclusion and Outlook 131
6.1 Key findings in response to the research questions 131
6.2 Perspectives for cryogenic integrated optics 133

7 Bibliography 137

A Appendix 153
A.1 Publications 153
A.2 Statement on the Use of Artificial Intelligence 155
A.3 Supplemental material to Chapter 3 156
A.4 Supplemental material to Chapter 4 156
A.4.1 Further details for the keen experimental scientist 156
A.4.2 Additional measurement data 157
A.5 Supplemental material to Chapter 5 160
A.5.1 Measurements on the individual waveguide groups 160
A.6 A narrative about the cryogenic traffic jam 168

List of Abbreviations

AR Coating	Anti-Reflection Coating
BPF	Band-Pass Filter
BS	Beam Splitter
CAR	Coincidences-to-Accidentals Ratio
CT	Cryogenic Temperature
CW	Continuous-Wave
DM	Dichroic Mirror
FSR	Free Spectral Range
FWHM	Full Width at Half Maximum
HOM	Hong-Ou-Mandel
HWP	Half-Wave Plate
IR	Infrared
JSA	Joint Spectral Amplitude
JSI	Joint Spectral Intensity
L	Lens
LPF	Long-Pass Filter
MgO:PPLN	MgO-doped Periodically Poled Lithium Niobate crystal
NIR	Near-Infrared
NLO	Nonlinear Optic
PBS	Polarizing Beam Splitter
PM Fiber	Polarization-Maintaining Fiber
QPM	Quasi-Phase-Matching
QWP	Quarter-Wave Plate
RT	Room Temperature
SFG	Sum Frequency Generation
SHG	Second Harmonic Generation
SNR	Signal-to-Noise Ratio
SNSPD	Superconducting Nanowire Single-Photon Detector
SPDC	Spontaneous Parametric Down-Conversion
SPF	Short-Pass Filter
TE	Transverse Electric
Ti:PPLN	Titanium in-diffused Periodically Poled waveguide in Lithium Niobate
TM	Transverse Magnetic

Introduction

1

Imagine yourself riding a bicycle through a busy city during rush hour. Most people will agree that traffic has its own personality. You might find yourself in a typical traffic jam - the cars move slowly, but the flow does not stop at all. In this scenario, every car represents a minor obstacle along your route. On a good day, when the conditions are right, even a seemingly endless number of cars somehow organizes into a predicable flow, allowing everyone to eventually find their way home. Now, imagine the same situation on a winter day as a severe snowstorm is approaching. Suddenly, the story gets much more complex. The cars slow down significantly, and as the temperature drops, they may even freeze in place. You want to continue your journey, but the system's mobility has vanished. This change in temperature, which is perhaps only a few tens of degrees, is enough to change the performance of the entire system.

Let's now imagine we change the operation temperature of a device, known for its high performance at room temperature, not only by a few degrees; no, we cool it down by nearly three hundred degrees. Over the past years, I found myself exploring exactly this: what happens to waveguides in lithium niobate when the laboratory goes from its normal "cozy" temperatures down to the realm of liquid helium. This thesis is a story about investigating the performance of the beloved lithium niobate platform under these "uncomfortable", cryogenic conditions. As we will see, if the conditions are right, these waveguides can indeed retain their guiding properties we rely on at room temperature. However, we will also discover that slight changes in the system can define whether we find a clear path or are hindered by a "cryogenic traffic jam".

At this point, you might ask yourself, why take something that works great already and take the effort to test it under cryogenic conditions? Nowadays, we do not only rely on integrated optical components that prove their performance under ambient conditions. We also increasingly ask them to perform under conditions far outside their comfort zone. This becomes more and more important for developing scalable, fully-integrated quantum photonics. The key components for an integrated quantum circuit are quantum light sources, components for routing and manipulating the quantum states, and single-photon detectors [1–3]. While lots of these integrated components are optimized for room temperature operation, individual devices fundamentally require cryogenic operation to be functional. These include in particular highly-efficient, state-of-the-art superconducting detectors, or deterministic quantum light sources that are based on solid-state quantum emitters [4, 5]. Interfacing a large number of optical components demands in general that all combined devices are compatible, which means in this case, all devices must be cryogenically compatible. For this reason, it is crucial to expand the toolbox of cryogenically compatible integrated photonic technologies.

Tremendous effort in this research area is especially taken in the field of photonic quantum computing [6–8]. Gaussian boson sampling (GBS) represents one photonic quantum computing model that has demonstrated evidence of quantum computational advantage [9–12]. The scheme provides an example of a classically hard-to-solve problem that becomes experimentally feasible when utilizing squeezed states. GBS was successfully experimentally demonstrated on large scale, which required hundreds of free-space components to realize the optical network besides the integrated interferometer [11]. True scalability requires significant reduction of free-space optics and ideally fully-integrated technologies. The field of GBS has led to substantial advances in the development of universal photonic quantum computing. However, evolving from these specific realizations toward universal and scalable quantum computing remains an ongoing challenge. While the integrated photonic chip (i.e., the quantum processing unit (QPU)) is typically operated near room temperature, cryogenically operated superconducting detectors are employed for the single-photon detection [11, 12]. For this reason, fundamental challenges for scalability include the massive number of coaxial cables that are required to control and readout the cryogenic detectors and optical loss of the system. The coaxial cables introduce significant passive and active heat load that can easily overload the limited cooling power of the cryostats. This thermal constraint represents a substantial obstacle for leading technology companies such as PsiQuantum [8], Xanadu [12, 13], QuiX Quantum [14, 15], or Quandela [16]. One viable strategy for reducing the heat load involves utilizing all-optical control and readout for the superconducting detectors [17–20]. Moreover, every component interface constitutes a potential loss factor which is especially critical for single-photon applications. In particular, connection points such as waveguide-to-fiber coupling introduce optical loss. Companies working on highly scalable architectures, are thus greatly interested in integrated solutions. For example, PsiQuantum demonstrated a fully-integrated cryogenic technology based on the silicon material platform, including on-chip generation, manipulation, and detection of photonic qubits [8]. Expanding the toolbox of cryogenic integrated photonics represents a huge step toward addressing the bottlenecks for achieving true processor scalability.

Within this research field of cryogenic integrated optics, this work concentrates on cryogenic quantum state generation and manipulating the photon's energy, via nonlinear frequency conversion. Quantum light sources are fundamental resources, enabling the generation of single photons, entangled photon-pairs, squeezed states, or other non-classical states [3, 21]. Integrated single-photon sources can be categorized into two types, each providing specific advantages: parametric photon-pair sources, and solid-state, atom-like single-photon emitters. The first type is realized by pumping a nonlinear waveguide, enabling probabilistic generation of photon pairs, via spontaneous parametric down-conversion (SPDC), or spontaneous four-wave mixing (SFWM) [2]. In the non-classical process of SPDC, one photon from a strong pump beam decays into a photon pair, which properties are dictated by energy and momentum conservation [22–27]. SFWM describes the conversion of two photons into a new pair of photons with different individual energies [28–34]. Fundamentally, the photons are always created in pairs, which is commonly exploited to herald the presence of one photon by detecting its counterpart. In comparison to bulk crystals, the waveguide-based (i.e., integrated) SPDC process benefits from increased conversion efficiencies and the propagation of photon pairs into well-defined waveguide modes [35–37]. Accurate customization of the spectral properties is realized by modifying the waveguide material and dimensions. For example, the waveguide can be tailored to the specific parameters of the pump beam to enable high modal purity of the generated photons, corresponding to a Schmidt number close to unity [38–40]. However, the overall conversion efficiency for SPDC is fundamentally low due to the probabilistic nature of the process. Typically one photon pair is created per 10^5 to 10^{12} pump photons [37, 41, 42]. Moreover, there is a non-zero chance to create two, or more photon pairs. For this reason, increasing the pump power degrades the single-photon purity since the power increase results in larger multi-photon-pair components. Depending on the material platform, established waveguide fabrication technologies allow for the production of highly identical SPDC sources. These can be arranged in large arrays, which is key for scalability. In combination with multiplexing techniques, or photon-number resolved detection, bright and pure single-photon sources can be realized [2, 43–47].

One of the most promising types of solid-state quantum emitters are quantum dot (QD) sources that allow for deterministic single-photon generation [48–51]. These sources can be operated on-demand since every excitation pulse results in the creation of a well-defined quantum state. Depending on the material this can be a single photon, or an entangled photon pair, if a bi-exciton is excited [50, 52, 53]. Resonant excitation can provide near-optimal single-photon purity and high indistinguishability from a single QD [54, 55]. In comparison to SPDC, QDs provide a much narrower spectral bandwidth, typically about 1 GHz compared to 100 GHz for SPDC [56, 57]. This narrow bandwidth represents a key challenge for the uniform fabrication of multiple, identical sources. In particular, the reproducibility is limited due to inhomogeneous broadening causing a spread of the emission wavelength and the random nature of the QD position [2]. Furthermore, QDs often require cryogenic operation to preserve the sub-Poissonian statistics and indistinguishability [5]. Additionally, developing high performance QDs in the telecom range remains an ongoing challenge. However, exceptional progress has been made in this field to enable QD implementation in long-distance fiber networks [58].

Connecting diverse components which operate in different wavelength ranges, requires frequency conversion, for example in the form of entangled-pair sources, connecting the visible and the telecom range [59]. These devices enable entanglement swapping and teleportation to transfer the information of one quantum state to another photon of different energy [56, 57, 60–62]. Nonlinear frequency conversion can be performed both in a bulk crystal, or in an integrated waveguide. However, the confined waveguide modes result in much stronger mode overlap and longer interaction lengths compared to a bulk crystal. Frequency conversion in a waveguide thus allows for significantly higher brightness [63]. Based on well-established fabrication techniques, SPDC in a waveguide is often used as a stand-alone device, but its integration into advanced quantum circuits allows for the direct combination with other components to manipulate and detect the photons on a single chip [2, 64].

The gold standard for single-photon detection are superconducting nanowire single-photon detectors (SNSPDs) [65–67]. These provide near-unity detection efficiency [68, 69], low dark-count rates [70], high timing resolution [71], high count rates [72], and are shown to feature intrinsic photon-number resolution [73–77]. For realizing a fully integrated circuit that profits from efficient SNSPDs, two major challenges need to be overcome. First, integrated pump suppression together with integrated detection remains challenging [78–80]. Since only a small fraction of the pump light is converted to single photons, the remaining pump must be suppressed by at least 100 dB [79, 81], which corresponds to one photon-pair generation per 10^{10} pump photons. Second, full integration requires that all components are cryogenically compatible [2]. This thesis addresses the second issue by adapting integrated SPDC, and its classical counterpart of two photons converted to one photon, to the challenging operation conditions of SNSPDs. Prior to this work, no systematic investigation of integrated SPDC under cryogenic conditions had been reported.

To establish the necessary background for the discussion of cryogenic integration, it is essential to first review well-established material platforms for room-temperature integrated photonic circuits. The research field of integrated photonics builds on diverse material platforms, as it is challenging for one single platform to meet the demands of advanced quantum applications. The individual platforms differ in several key properties. This includes their nonlinearity type, the material bandgap, the waveguide properties, electro-optic capabilities, and fabrication maturity [3]:

- The materials can be distinguished by whether they possess second-order ($\chi^{(2)}$) or third-order ($\chi^{(3)}$) nonlinearity, and the magnitude of their coefficient. High intrinsic nonlinearity is required to realize efficient frequency conversion processes. The nonlinearity determines which type of quantum light source can be implemented. $\chi^{(2)}$ materials enable spontaneous parametric down-conversion and $\chi^{(3)}$ platforms allow for spontaneous four-wave mixing [82].

- The bandgap of the material defines the transparency window. A large bandgap is desired since it allows for broadband operation across the visible, near-infrared, and telecom wavelengths and prevents the presence of additional absorption effects. Broadband operation is critical for widely non-degenerate frequency conversion for which the interacting wavelengths are far apart [3, 59].

- The waveguide properties are primarily given by the refractive index contrast between the core and cladding materials, their dimensions, and surface roughness. High refractive index contrasts enable strong mode confinement and thus high optical intensities which can further enhance the nonlinear interactions. Moreover, strong confinement enables manipulating the effective refractive indices by tailoring the waveguide geometry (i.e., dispersion engineering) [83–85]. Uniform surface quality enhances low optical loss which is particularly critical for preserving fragile quantum states over long interaction lengths [3].

- The electro-optic capabilities of a material define its ability for fast modulation and switching of the quantum states with low power consumption. This is a characteristic feature of $\chi^{(2)}$ materials due to their intrinsic Pockels effect [3, 86].
- Finally, the requirement for repeatable high-quality waveguide fabrication necessitates established manufacturing processes. Crucially, the potential for wafer-scale fabrication and a small integrated device footprint are key for realizing high scalability [59, 82].

The leading material platforms each offer a certain trade-off between the presented, desired properties. Silicon (Si), especially silicon on insulator (SOI), can be considered the most mature platform which benefits significantly from CMOS compatibility. The well-established electronic semiconductor fabrication industry is exploited for fabricating silicon photonic devices with high yield and low cost. The refractive index of silicon is especially high ($n \approx 3.5$), enabling the fabrication of compact devices. However, the performance of pure silicon in the near-infrared and telecom range is often limited by nonlinear losses, such as two-photon absorption [82]. In contrast, Silicon Nitride (SiN) provides a wide bandgap and thus broad transparency window, which expands the possibilities of silicon into the telecom range. It further enables ultra-low propagation losses (0.1 dB/m) [2, 87], making it optimal for single-photon applications. Despite the advanced technologies, the nonlinear functionality of silicon photonics is restricted due to a comparatively weak $\chi^{(3)}$ nonlinearity and its lack of second-order nonlinearity [3]. Lithium niobate ($LiNbO_3$, or LN) stands out as another proven and leading platform for the development of low-loss integrated quantum circuits. It provides a large nonlinear and electro-optic coefficient, a broadband transparency window, and ferroelectric properties [36, 63, 88, 89]. Especially the strong second-order nonlinearity enables efficient frequency conversion [35, 90–93], and the large electro-optic effect allows for ultra-fast modulation [82, 89]. Waveguide fabrication in $LiNbO_3$ employs established techniques such as titanium in-diffusion and ridge waveguides [63]. Recently, lithium niobate on insulator (LNOI), also known as thin-film lithium niobate (TFLN), has gained attraction due to its promising technical advantages [84, 86, 94–105]. These include strong mode confinement with inherently high nonlinearity and the capability to achieve small bending radii, which facilitates scalability [3]. Materials based on III – V compound semiconductors (e.g., InGaP, InP, GaP, or GaAs) stand out due to a very high refractive index. This enables the fabrication of lasers and amplifiers on the same platform as photonic devices. Furthermore, they provide especially high second-order nonlinearities and the bandgap can be tuned by varying the material composition [82]. However, due to their direct bandgap, most commonly used III – V compounds exhibit significantly higher absorption as for example silicon, which is an indirect bandgap material [106]. Compositions such as AlGaAs and InGaP are further limited in fabrication accuracy, as their performance is very sensitive to slight variations in the waveguide dimensions [59].

The work presented in this thesis specifically utilizes lithium niobate for nonlinear frequency conversion due to its excellent material properties and established fabrication. While LNOI offers specific advantages, titanium in-diffusion in z-cut lithium niobate (Ti:$LiNbO_3$) remains a mature and accessible fabrication technology for realizing various integrated devices [63, 107–109]. This technology has been fundamental to the development and fabrication of integrated components including photon-pair sources [81, 110–118], passive and active manipulation of quantum states [119–124], and single-photon detectors [125, 126]. Crucially, the in-diffused waveguides provide weakly confined modes whose mode size is closely matched to the core of standard commercial optical fibers [81, 125, 127]. This facilitates highly efficient coupling between the waveguide and fiber, and also simplifies their integration into free-space optical setups. The combination of high coupling efficiency and established fabrication makes titanium in-diffused waveguides an excellent and robust platform for prototyping experiments.

In order to realize an efficient frequency conversion process, the interacting fields must not only overlap spatially, but also temporally. This implies that the fields must travel with the same speed. The inherent material dispersion causes the beams which differ in frequency to have different propagation velocities. However, the ferroelectric properties of lithium niobate allow to account for this intrinsic phase-mismatch of the individual modes. The applied process is called quasi-phase-matching. This is based on periodic poling, a well-established method to inverse the crystal axis every time the fields are running apart [128–130]. Consequently, through careful selection and accurate fabrication of the poling period, high conversion efficiency for a desired wavelength interaction can be achieved. In the scope of this work, periodic poling is the method that is used to achieve phase-matching for diverse frequency conversion processes in lithium niobate. The fabrication technology for periodically poled titanium in-diffused waveguides in lithium niobate (Ti:PPLN) is well-established by the Integrated Quantum Optics group (IQO) at Paderborn University. All waveguide samples investigated in this thesis are thus fabricated in-house.

Research in recent years has shown an increasing demand for developing cryogenic components integrated on various material platforms [123, 125, 126, 131–138]. Among others, the research at Paderborn University concentrated on the development and characterization of cryogenic devices in the Ti:LiNbO$_3$ platform. Thiele et al. realized electro-optic modulators (EOMs) for phase modulation, directional coupling, and polarization conversion [123, 132]. Höpker et al. showed evanescently coupled superconducting single-photon detectors [125, 126]. Finally, Bartnick et al. demonstrated the first cryogenic integration of nonlinear frequency conversion, namely second harmonic generation (SHG) pumped in the telecom C-band [131]. This is where my work ties in with the research area. Demonstrating the proof-of-principle for cryogenic SHG presented the foundation for the subsequent SPDC characterization, since both processes require the same phase-matching condition. This thesis expands the cryogenic research in Ti:PPLN by SPDC processes, specifically non-degenerate, and degenerate SPDC in the telecom C-band [139, 140], and widely non-degenerate SPDC pumped in the visible range [141].

Besides the studies at Paderborn University, TFLN has shown great performance for cryogenic operation, including nonlinear processes such as SHG and SPDC in the telecom C-band [133], a spectral optical filter [134], and even combined integration of EOMs and SNSPDs on a single LNOI chip [135]. Erbium-doped lithium niobate waveguides fabricated through titanium in-diffusion were shown to enable the storage and reemission of single photons in the telecom band, through the realization of a cryogenic quantum memory [142]. Cryogenic bulk lithium niobate was further employed for terahertz generation [143–145]. Moreover, it has been demonstrated that silicon waveguides exhibit cryogenic compatibility, including single-photon generation via spontaneous four-wave mixing [8, 136, 137], on-chip filtering [146, 147], and integrated superconducting detectors [8, 148]. Another promising platform is barium titanate that was shown to enable the cryogenic integration of optical modulators [8, 149], while graphene allows for efficient EOM performance due to an intrinsic carrier mobility increase at low temperatures [138]. Finally, effort is taken to develop cryogenic packaging methods for integrated devices, including a silicon ring resonator [137], and TFLN [150].

This work in particular focuses on discovering the cryogenic properties of nonlinear frequency conversion in Ti:PPLN. To that end, thorough characterization of the linear and nonlinear waveguide properties under cryogenic conditions was necessary to gain insights into the temperature-dependent material changes. Within the last years, I have been studying the fascinating behavior of cryogenic lithium niobate. This journey comprised various stages, from verifying the proof-of-principle for cryogenic SPDC, to adjusting the cryogenic phase-matching and exploring the physical limits of the material platform. This task can be broken down to three major, interconnected aspects, each defined by a core research question and a corresponding objective:

1. **How can we reliably measure the linear and nonlinear effects of the cryogenic Ti:PPLN waveguides?**
   Designing the cryogenic experiments requires careful consideration since we need to adapt for clearly more challenging operation conditions as for room temperature applications. This raises the question of whether it is feasible to apply the same characterization methods and techniques that work in experiments at room temperature under cryogenic conditions. Waveguides at ambient temperature can be efficiently free-space coupled using two aspheric lenses. In order to implement a comparable coupling method at cryogenic temperatures, a special cryostat with free-space access to the vacuum chamber is required. Moreover, the waveguide coupling cannot be maintained throughout the cooldown, since all components experience thermal contraction. Consequently, the waveguide mount must allow for in situ realignment at cryogenic conditions. Furthermore, spectrally broadband components are necessary to adopt for large changes in the phase-matched wavelengths when varying the temperature by three orders of magnitude. To enable comparative waveguide characterization from room temperature to cryogenic conditions, the experimental setup must feature widely tunable laser sources, broadband free-space optics, and detection tools which cover the wavelength range. I would like to emphasize that these experimental hurdles are not unique to Ti:PPLN waveguides. Consequently, the developed techniques and protocols are transferable to other material platforms. Therefore, our waveguide platform serves as a prototyping system to validate cryogenic characterization methods on a material with established room-temperature properties. The first aim of this thesis can be thus formulated in the following way: **To develop and optimize functional experimental methods for low-temperature integrated optics.**

2. **How does cryogenic operation affect the material platform?**
   The second research question focuses on the intrinsic material changes of lithium niobate. Some temperature-dependent effects can be considered as well-known as they are also prominent during waveguide heating experiments. This includes the temperature dependence of the refractive indices, which results in a shift of the phase-matched wavelength, and the thermal expansion of the material, altering the effective poling period. However, no verified data is available for lithium niobate at cryogenic temperatures. The impact of these effects can be transferred to cryogenic conditions by extrapolating the existing equations for the low temperature range, which provides a first estimation. While these temperature dependencies are readily apparent, cryogenic operation further causes a severe decrease in the mobility of free charge carriers. The consequences of this reduced mobility are much more complex, as they indirectly affect the cryogenic performance through the photorefractive and pyroelectric effect. Both effects can cause an inhomogeneous accumulation of electric charges, resulting in refractive index changes, thus altering the waveguiding or the phase-matching [131, 151–154]. The reduced mobility results in extended lifetimes for these charge effects, causing them to dominate the system performance at cryogenic temperatures. Understanding the extent of these aspects is crucial for realizing tailored cryogenic nonlinear processes. For this reason, the second goal of this work is the following: **To determine and understand the critical temperature-dependent effects that alter the waveguide performance under extremely cold operation conditions.**

3. **What do our observations teach us about the viability of cryogenic lithium niobate?**
   The final research question logically builds on question two. Here, the focus is shifted from understanding the material to exploring implications for future applications. Two steps are necessary to address this issue. First, it is essential to gain detailed insights into the observed cryogenic material performance. Second, and crucially, it requires evaluating these observations to decide if Ti:PPLN waveguides are truly suitable for cryogenic applications. This includes examining the question, under what circumstances is it justified to perform cryogenic (non)linear optics in this platform? Answering this question defines performance boundaries and clearly states which effects must be accounted for when designing future NLO systems. This leads to the final goal: **To assess the fundamental potential of cryogenic Ti:PPLN and define the conditions under which this platform can be beneficial for cryogenic integrated optics.**

The structure of this thesis is designed to guide you through this research journey, with each subsequent chapter providing deeper insights into the cryogenic material properties. Following this introduction, the thesis proceeds in Chapter 2 with a discussion of the theoretical and experimental foundations required to plan and interpret the cryogenic experiments. This chapter presents the theoretical basics of nonlinear optics, details on the Ti:PPLN waveguide platform, and the material changes associated with altering the operation temperature. The experimental part comprises the practical requirements on the cryogenic setup. This includes the cryostat design, the cryogenic waveguide mounting and coupling procedure, and the experimental methods used to characterize the waveguides. Chapter 3 presents the initial experiments of generating single photons in the telecom range from cryogenic SPDC. The first out of two experiments in this series concentrates on characterizing the cryogenic performance of a waveguide which enabled the desired process at room temperature. This experiment represents the proof-of-principle for cryogenic SPDC in the Ti:PPLN platform [139]. In the second experiment, the initial insights into the waveguide behavior are actively applied to tailor the performance of cryogenic SPDC to enable degenerate photon pairs in the telecom C-band [140]. Chapter 4 analyzes the properties of a completely different wavelength combination. Instead of considering the generation of two identical photons, widely non-degenerate frequency conversion is characterized [141]. This measurement series examines the question of which additional challenges must be adapted for when the wavelengths are far apart. Moreover, a different phase-matching type is chosen for this process to gain additional information about the waveguide properties for each polarization. Chapter 5 expands upon the previous results by conducting a detailed investigation of the observed cryogenic effects. This includes an in-depth analysis of the pyroelectric and photorefractive material changes and the reproducibility of the cryogenic waveguide performance. Finally, Chapter 6 summarizes the key outcomes of this thesis, assesses the cryogenic viability of the Ti:PPLN platform, and outlines recommendations for future cryogenic NLO device design.

How to get to know your (cryogenic) waveguide

2

Before we can explore the physics of a cryogenic waveguide in lithium niobate, we need to understand nonlinear optics in this material platform under ambient conditions. This chapter will first provide you with the theoretical basics you need to know about nonlinear optics, titanium in-diffused waveguides in lithium niobate, and the intrinsic material changes that become relevant at cryogenic temperatures (Section 2.1). The second part of this chapter concentrates on the experimental methods to investigate a waveguide not only at room temperature, but also within a cryostat (Section 2.2). This section addresses the first research question of this thesis: *How can we reliably measure the linear and nonlinear effects of the cryogenic Ti:PPLN waveguides?* I will discuss what type of cryostat is suited best, how to mount the waveguide and couple to it, and which nonlinear measurements can be performed. Moreover, you will find some experimental tips and tricks, which can help when setting up your own (cryogenic) waveguide characterization setup.

2.1 Theoretical basics - What to know before you start

Lithium niobate is a nonlinear material, which allows for efficient frequency conversion processes. For this reason, the first section introduces nonlinear optics and three-wave mixing processes, including spontaneous parametric down-conversion (SPDC). The discussion is thereby limited to the fundamental concepts necessary for the context of this thesis. A comprehensive description of the theoretical background of nonlinear optics can be found in chapters 1 - 2 in Ref. [91]. For a detailed theoretical treatment of SPDC, the reader is referred to chapter 11.2 in Ref. [155]. Following the introduction to nonlinear optics, the properties of the employed titanium in-diffused lithium niobate platform are discussed. This includes the design of the waveguides and their refractive index distribution. Furthermore, the principle of periodic poling for quasi-phase-matching is detailed. The final theoretical section concentrates on the temperature-dependent material properties of lithium niobate. In particular, understanding the variations in the refractive indices and the origin of the pyroelectric and photorefractive effect is crucial for the cryogenic operation.

2.1.1 Introduction to nonlinear optics

When an electro-magnetic wave travels through an optical material, it interacts with its dipole moments and induces a polarization. In linear optics, the material response to the electric field strength $\boldsymbol{E}$ is linear. The induced polarization $\boldsymbol{P}$ at the time t can thus be described by [91, p. 2]

$$\boldsymbol{P}(t) = \epsilon_0 \chi^{(1)} \boldsymbol{E}(t) \,. \tag{2.1}$$

The proportionality is given by the vacuum permittivity ϵ_0 and the linear susceptibility $\chi^{(1)}$. For clarity and conciseness, this representation neglects the tensor nature of the susceptibilities. Furthermore, this introductory section assumes an instantaneous polarization response to the electric field, which implies a dispersionless material with zero loss. Nonetheless, the presented equations are well-suited to convey the fundamental principles required for understanding the nonlinear optical processes.

A dielectric material with a large nonlinear coefficient represents a powerful tool to manipulate the spectral properties of a laser beam. In nonlinear optics, Eq. (2.1) must be generalized. This is mostly realized by describing the polarization as a power series of the field strength, expressed by [91, p. 2]

$$\boldsymbol{P}(t) = \epsilon_0 \left(\chi^{(1)} \boldsymbol{E}(t) + \chi^{(2)} \boldsymbol{E}(t)^2 + \chi^{(3)} \boldsymbol{E}(t)^3 + \dots \right) \tag{2.2}$$

$$\equiv \boldsymbol{P}^{(1)}(t) + \boldsymbol{P}^{(2)}(t) + \boldsymbol{P}^{(3)}(t) + \dots \,. \tag{2.3}$$

This expansion introduces the higher-order susceptibilities, in particular, the second- and third-order nonlinear optical susceptibilities $\chi^{(2)}$ and $\chi^{(3)}$. We can define the individual polarization components as the linear polarization $\boldsymbol{P}^{(1)}(t)$, which was already introduced in Eq. (2.1), and the nonlinear polarization terms, given by the second-order nonlinear polarization

$$\boldsymbol{P}^{(2)}(t) = \epsilon_0 \chi^{(2)} \boldsymbol{E}(t)^2 \tag{2.4}$$

and the third-order nonlinear polarization

$$\boldsymbol{P}^{(3)}(t) = \epsilon_0 \chi^{(3)} \boldsymbol{E}(t)^3 \,. \tag{2.5}$$

The number of relevant higher-order components depends on the specific material platform. For lithium niobate, components of even higher order ($\boldsymbol{P}^{(o)}(t)$, with $o \geq 4$) can often be neglected due to their insignificant amplitude. So far, we have seen that an incident electric field induces a polarization, which has the same rapid temporal variation as the field itself. Consequently, the accelerated material charges can emit electro-magnetic radiation. In this case, the time-varying polarization acts as a source of new electro-magnetic field components. This can be seen from the wave equation for a nonlinear optical material, which is often written as [91, p. 4]

$$\nabla^2 \boldsymbol{E} - \frac{n^2}{c^2} \frac{\partial^2 \boldsymbol{E}}{\partial t^2} = \frac{1}{\epsilon_0 c^2} \frac{\partial^2 \boldsymbol{P}_{\mathrm{NL}}}{\partial t^2} \tag{2.6}$$

where n is the refractive index, c the speed of light in vacuum and $\boldsymbol{P}_{\mathbf{NL}}$ combines the nonlinear polarization components. From this equation, it is evident that the nonlinear polarization response drives the electric field. Within this process energy is transferred from the incident field (inducing the polarization) to the newly generated field. Given the conservation of energy, the nonlinear response allows for the generation of classical or even non-classical light at new frequencies. This process of frequency conversion will be explored in more detail in the next section.

Frequency conversion processes

This thesis focuses on frequency conversion processes that are driven by the second-order nonlinear polarization. According to Eq. (2.4), two electrical fields interact in order to induce a third field. These processes are thus referred to as three-wave mixing. Analogously, frequency conversion processes which result from the third-order polarization are called four-wave mixing.

Second-order nonlinear interactions are limited to noncentrosymmetric crystals since $\chi^{(2)}$ vanishes identically for any crystals which display inversion symmetry [91, p. 44].[1] This applies to a wide range of materials. Among others, liquids, gases, and amorphous solids, such as glass, demonstrate inversion symmetry. These materials are inherently unable to produce new frequency components via three-wave mixing. Therefore, lithium niobate is used in this work to realize diverse second-order nonlinear processes. The third-order nonlinear optical susceptibility, however, can exist independent of the inversion symmetry. Consequently, both centrosymmetric and noncentrosymmetric materials with a large $\chi^{(3)}$ can be exploited for four-wave mixing.

We will now explore the different frequency components that can be generated via three-wave mixing. Eq. (2.4) depends on the square of the electric field. This opens the possibility that the two required fields are derived from a single source or from two separate incident fields. To account for the two options, we can describe the optical pump field either using a single frequency ω_1, or including two individual frequency components ω_1 and ω_2. This results in the following two expressions,

$$\boldsymbol{E}(t) = \boldsymbol{E_1}\varepsilon^{-i\omega_1 t} + \text{c.c.} \tag{2.7}$$

and

$$\boldsymbol{E}(t) = \boldsymbol{E_1}\varepsilon^{-i\omega_1 t} + \boldsymbol{E_2}\varepsilon^{-i\omega_2 t} + \text{c.c.}\,, \tag{2.8}$$

with the amplitudes $\boldsymbol{E_1}$ and $\boldsymbol{E_2}$. Substituting these two formulas into Eq. (2.4) yields distinct contributions to the nonlinear polarization at multiple frequencies. The various frequency contributions are presented below.

---

[1] Inversion symmetry demands that a change in the sign of the electric field $\boldsymbol{E}(t)$ causes a change in the sign of the polarization $\boldsymbol{P}^{(o)}(t)$. For every even harmonic term ($o = 2, 4, 6, \ldots$) this results in $\boldsymbol{P}^{(o)}(t) = -\boldsymbol{P}^{(o)}(t)$, which can only be fulfilled if $\chi^{(o)}$ vanishes [91, p. 44].

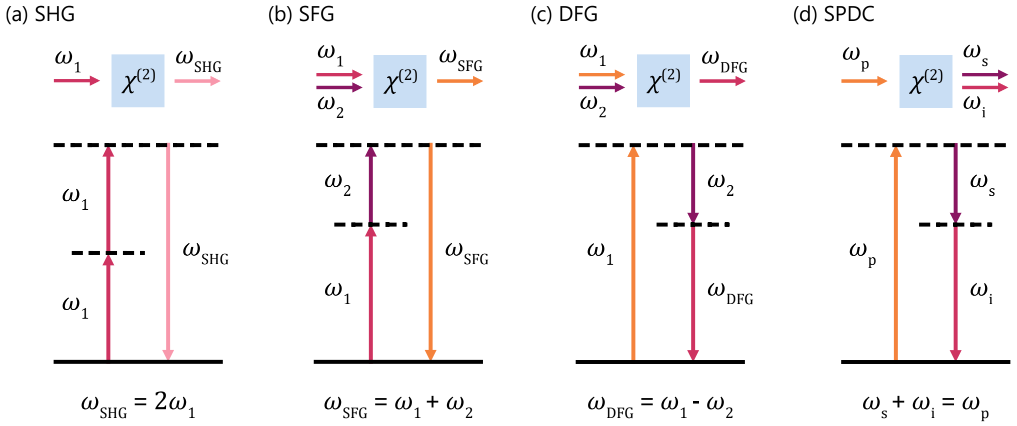

Figure 2.1: Illustration of the different three-wave mixing interactions. The incident and generated fields are displayed together with their energy level diagrams for (a) SHG, (b) SFG, (c) DFG, and (d) SPDC.

Second-harmonic generation (SHG)

The first and most accessible example of nonlinear three-wave mixing is SHG. We consider a single pump beam of frequency ω_1, as described by Eq. (2.7). According to Eq. (2.4), this results in only one nonzero frequency component that can be excited, which is $2\omega_1$. Consequently, this contribution can induce radiation at the second-harmonic frequency. Two photons from the pump beam are destroyed while one photon is generated. This can be illustrated by considering an energy level diagram, in which the two photons excite the system via two virtual energy levels (compare Fig. 2.1 (a)). The system instantaneously relaxes again and thereby emits the second-harmonic photon. This new photon has twice the energy of the pump photons, which is described by $\omega_{\text{SHG}} = 2\omega_1$.

Sum-frequency generation (SFG)

In comparison to SHG, the SFG process represents a more generalized case. While the two interacting photons for SHG often originate from the same pump beam, for SFG, the $\chi^{(2)}$ material is pumped with two individual beams. As defined in Eq. (2.8), these pump beams have different frequencies ω_1 and ω_2. In this scenario, one photon from each beam can contribute in order to create new frequency components. In total, substituting Eq. (2.8) into Eq. (2.4) leads to four distinct nonzero frequency contributions. Two of those are the second-harmonic frequencies of the individual pump fields. One of the other two components is defined by the sum of the two incident energies. This process is thus very similar to the SHG with the difference that the two exciting photons have distinct energies (compare Fig. 2.1 (b)). The SFG frequency is given by $\omega_{\text{SFG}} = \omega_1 + \omega_2$.

Difference-frequency generation (DFG)

Like SFG, the DFG process arises from two different incident frequencies. The fourth nonzero frequency component for a pump field described by Eq. (2.8) is given by the difference of the two pump frequencies. The higher energy photon excites the system to a virtual level and the lower energy photon triggers relaxation over another predefined virtual level (compare Fig. 2.1 (c)). Energy conservation demands that while a new photon at the difference frequency is created, the higher frequency pump photon is destroyed and an additional photon at the lower pump frequency is generated. Therefore, the lower-energy input field is amplified and a new field arises, which is described by $\omega_{\mathrm{DFG}} = \omega_1 - \omega_2$, where $\omega_1 > \omega_2$.

Spontaneous parametric down-conversion (SPDC)

The final three-wave mixing process is SPDC. This interaction is different from the previously discussed processes as a single input field is converted into two output fields. This is very much comparable with the DFG process. However, in this case, the two-photon emission following the absorption of a pump photon is not stimulated, but happens spontaneously. One photon from a pump field with frequency ω_{p} decays into two individual photons (compare Fig. 2.1 (d)). Historically, the two created fields are called the *signal* and *idler* field, which is why we refer to their frequencies as ω_{s} and ω_{i}. Energy conservation for this process is fulfilled by $\omega_{\mathrm{s}} + \omega_{\mathrm{i}} = \omega_{\mathrm{p}}$. The two photons can either have equal energy, or distinct energies, which is fundamentally the reverse interaction of SHG and SFG. Depending on the energy distribution, the process is classified as *degenerate* SPDC ($\omega_{\mathrm{s}} = \omega_{\mathrm{i}}$), or *non-degenerate* SPDC ($\omega_{\mathrm{s}} \neq \omega_{\mathrm{i}}$).

Phase-matching

While the SHG, SFG, and DFG interactions can be described classically, this does not apply to SPDC. The description of single-photon decay necessitates a quantum mechanical formalism. However, the analogy to the SFG process allows some conclusions from the classical approach to be transferred to SPDC. Both processes require the same conditions for energy and momentum conservation. For the three interacting fields, these are given by $\omega_3 = \omega_1 + \omega_2$ and $k_3 = k_1 + k_2$, with the propagation constant k. In general, dispersion of the material causes the fields with distinct frequencies to propagate at different velocities. Consequently, the waves rapidly loose their phase relation, which significantly lowers the effective interaction length. Therefore, the phase mismatch, defined by [155, p. 356]

$$\Delta k = k_3 - k_1 - k_2 = \frac{n_3\omega_3}{c} - \frac{n_1\omega_1}{c} - \frac{n_2\omega_2}{c}, \tag{2.9}$$

must disappear for efficient frequency conversion. This section discusses the principle of periodic poling for quasi-phase-matching (QPM) which prevents dephasing of the interacting waves [129].

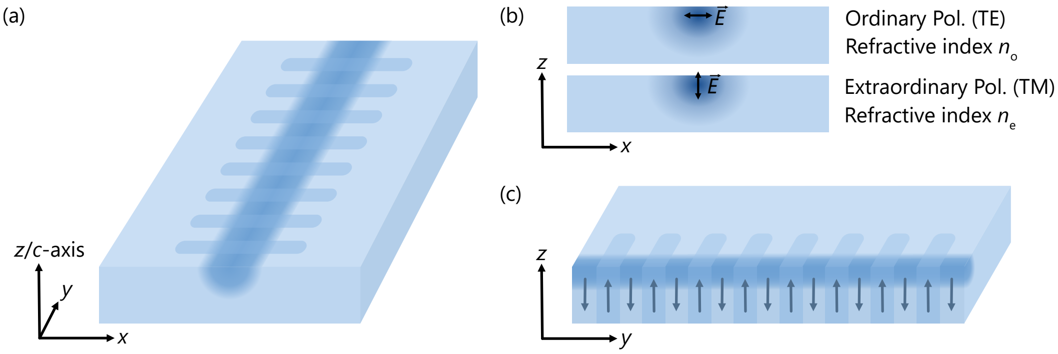

Figure 2.2: Schematic illustration of the z-cut lithium niobate waveguide. (a) The blue area along the y-direction represents the gradual refractive index increase which creates the waveguide. The periodic pattern illustrates the periodic poling. (b) Front view of the waveguide end facet. The dark blue area represents the fundamental mode which is guided through the waveguide. The ordinary-polarized beam (TE) experiences the effective refractive index n_o, the extraordinary-polarized beam (TM) experiences the index n_e, respectively. (c) Cross-section along the periodically poled waveguide. The arrows depict the periodic inversion of the crystal axis.

Periodic poling describes the periodic inversion of the crystal orientation. Since lithium niobate is a ferroelectric material, it always exhibits a spontaneous polarization. This polarization is aligned with the crystalline c-axis, which defines the z-direction of our coordinate system (compare Fig. 2.2). The spontaneous polarization can be permanently reversed by applying a strong external electric field [156]. As a result of the poling process, the traveling waves experience a periodic variation of the sign of the nonlinear susceptibility. The poling period Λ is chosen based on the coherence length $L_\mathrm{c} = \pi/\Delta k$. After this length, the phase mismatch has added up to π, causing destructive interference. By exchanging the crystal orientation at this distance ($\Lambda = 2L_\mathrm{c}$), the generated intensity permanently increases over the crystal length. The QPM results in a modification of the phase mismatch, which is now given by

$$\Delta k_\mathrm{QPM} = k_3 - k_1 - k_2 \pm \frac{2\pi}{\Lambda} \, . \tag{2.10}$$

This additional term provides full tunability with the fabricated poling period. However, the selection of the period requires accurate knowledge of the refractive indices, which can represent a challenge for cryogenic operation (see Section 2.1.3).

Let us now explore the dependence of the generated sum-frequency intensity I_3 on the phase-mismatch Δk (or Δk_QPM) and the effective length L [91, p. 78][2]

$$I_3 = \frac{8 d_\mathrm{eff}^2 \omega_3^2 I_1 I_2}{n_1 n_2 n_3 \epsilon_0 c^2} L^2 \,\mathrm{sinc}^2\left(\frac{\Delta k L}{2}\right) . \tag{2.11}$$

---

[2] This expression can be derived by substituting two input fields, described by plane waves, into the wave equation in Eq. (2.6) (for further details, see Ref. [91, Ch. 2.2]).

Here, d_{eff} represents a simplified notation of the second-order nonlinear susceptibility. While $\chi^{(2)}_{ijk}$ is described by a third-rank tensor (where the indices i, j, k refer to the Cartesian coordinates x, y, z), we can often employ a contracted notation using the two-dimensional matrix

$$d_{il} \equiv d_{\text{eff}} = \frac{1}{2}\chi^{(2)}_{ijk} = \frac{1}{2}\chi^{(2)}_{ikj}\,, \tag{2.12}$$

where $l \in \{1, 2, 3, 4, 5, 6\}$. This simplification is valid if the frequencies of the interacting waves are much smaller than the lowest resonance frequency of the material [91, p. 38]. In this case, the nonlinear susceptibility can be considered as independent of frequency, which allows permutation of the indices j and k.

For lithium niobate, the matrix d_{eff} can be further simplified due to its crystal structure [88]. As a consequence, only three independent coefficients are required to describe the nonlinear susceptibility, given by

$$d_{\text{eff}} = \begin{bmatrix} 0 & 0 & 0 & 0 & d_{31} & -d_{22} \\ -d_{22} & d_{22} & 0 & d_{31} & 0 & 0 \\ d_{31} & d_{31} & d_{33} & 0 & 0 & 0 \end{bmatrix}. \tag{2.13}$$

Frequency conversion is classified into three types, depending on the polarizations of the interacting fields. Type-0 specifies that the pump, signal, and idler wave have the same polarization. Type-I phase-matching is given if signal and idler are polarized orthogonal to the pump, and type-II describes the case that signal and idler have orthogonal polarizations. In this work, type-0 (TM polarization only) and type-II (TE and TM polarization) phase-matching are investigated. The type-0 interaction is given by $P_z \propto d_{33}E_z^2$, while the type-II process is described by $P_x \propto d_{31}E_xE_z$. The strength of the interactions hence depends on the coefficients d_{33} and d_{31}. For lithium niobate, d_{33} is approximately 40 times larger than d_{31}, which can lead to significantly higher conversion efficiencies for type-0 phase-matching compared to type-II [108].

It can be seen from Eq. (2.11), that the sum-frequency intensity strongly depends on the phase mismatch in the form of a sinc^2 function. We will see in the next section, that the same dependence remains valid for the phase-matching of the SPDC process. This is one reason, why it is experimentally advantageous to first perform classical SHG or SFG for the phase-matching characterization before initializing the SPDC measurements. The measurement procedure will be discussed in Section 2.2.3.

Spontaneous parametric down-conversion for single-photon generation

We now discuss the properties of the created SPDC state, as this interaction constitutes the main process investigated within the scope of this work. In the quantum mechanical approach, the interaction of the incident pump field with vacuum fluctuations introduces noise fields. These noise fields with frequencies ω_s and ω_i can be amplified if they satisfy the conditions of energy conservation and minimal phase mismatch. When the nonlinear interaction is sufficiently strong, this amplification results in the generation of signal and idler photon pairs [155, p. 356].

Mathematically, the generated SPDC state can be expressed by [155, p. 359]

$$|\psi\rangle_\mathrm{SPDC} = |0\rangle + B \iint d\omega_\mathrm{s} d\omega_\mathrm{i} f(\omega_\mathrm{s}, \omega_\mathrm{i}) \hat{a}_\mathrm{s}^\dagger(\omega_\mathrm{s}) \hat{a}_\mathrm{i}^\dagger(\omega_\mathrm{i}) |0\rangle \ . \tag{2.14}$$

Here, $B \propto E_\mathrm{p} L$ combines all constants and scales linearly with the amplitude of the pump field E_p and the effective length L. The term $f(\omega_\mathrm{s}, \omega_\mathrm{i})$ is the joint spectral amplitude (JSA), which completely describes the spectral properties and phase information of signal and idler. Furthermore, $\hat{a}_\mathrm{s,i}^\dagger(\omega_\mathrm{s,i})$ are the photon creation operators. We see that the two operators are applied together on the vacuum state, which demonstrates that the photons are always created in pairs. Deterministic separation of the photon pair, for example through different wavelengths or polarizations, enables heralding of single photons.

The JSA combines the conditions of energy and momentum conservation as a function of the signal and idler frequencies. This term is composed of the pump distribution α and the phase-matching function Φ, and is defined by [155, p. 359]

$$f(\omega_\mathrm{s}, \omega_\mathrm{i}) = \alpha(\omega_\mathrm{s} + \omega_\mathrm{i}) \Phi(\omega_\mathrm{s}, \omega_\mathrm{i}) \ . \tag{2.15}$$

The pump distribution describes the spectral properties of the pump beam and can often be approximated by a Gaussian function. It represents all combinations of signal and idler frequencies which fulfill energy conservation. The phase-matching function depends on the length and the dispersion of the crystal. We are already familiar with this function from the sum-frequency intensity (see Eq. (2.11)); it is given by $\Phi = \mathrm{sinc}(\Delta k L/2)$. Therefore, the phase-matching function represents the momentum conservation of the process.

Experimentally, it is convenient to record the square of the absolute value of the JSA. This function is known as the joint spectral intensity (JSI) and is thus defined by $\mathrm{JSI} = |\mathrm{JSA}|^2$. The JSI measurement does not provide any phase information. However, directly recording the JSA remains an experimentally demanding task [157, 158]. Therefore, this thesis focuses on the spectral properties of the SPDC source inferred from the JSI measurement, which provide the primary insights required for the characterization. The practical investigation of the relevant performance metrics of an SPDC source is further detailed in Section 2.2.3.

2.1.2 Titanium in-diffused waveguides in lithium niobate

All waveguide samples which are characterized in this work are fabricated in-house by the IQO group, the Mesoscopic Quantum Optics group (MQO), and the Institute for Photonic Quantum Systems (PhoQS). The waveguides were fabricated by titanium in-diffusion in z-cut lithium niobate (compare Fig. 2.2 for the orientation of the coordinate system). The samples have a height of 0.5 mm and a width of 12 mm. The length is tailored, depending on the waveguide length required for the experiment. For the cryogenic characterization, the total length is polished to about 25 mm to fit the dimensions of the cryostat. Across the width of 12 mm, 75 parallel waveguides are fabricated, which are arranged in groups of three waveguides each. To facilitate alignment of a preselected waveguide, the distance between the waveguides within one group is set to 100 µm and the distance between the groups is 200 µm. Furthermore, lithographically patterned labels mark the group number, which allows to verify the index of the coupled waveguide with a microscope from the top.

For the fabrication, in the first step, mask lithography is used to pattern the titanium strips on the lithium niobate substrate. Next, these strips are in-diffused in an oven, which results in a gradual refractive index increase, forming the waveguide. The periodic poling is afterwards performed either by mask lithography, or by using laser lithography, which enables flexible customization of the periods. Liquid electrodes with the designed periodicity are applied to the top and bottom surface of the sample. Due to the ferroelectric properties of lithium niobate, the application of strong electric fields then leads to periodic inversion of the crystal orientation. After the periodic poling is completed, the electrodes are removed and the waveguide end facets are polished.

Prior to the in-diffusion process, the titanium strips have a width of 5 µm to 7 µm and a thickness of 80 nm. The fabrication is optimized for waveguiding at the telecom range. Especially around 1550 nm, low-loss waveguiding with propagation losses down to 0.03 dB/cm can be achieved [63]. The design yields single-mode waveguides for wavelengths above approximately 1000 nm. The employed frequency conversion processes each involve at least one shorter wavelength, which means that this wave encounters a multi-mode waveguide.

Refractive index distribution

The in-diffusion of titanium results in a gradual increase of the refractive index. This leads to weakly confined waveguide modes which are guided directly below the substrate surface. Due to this inhomogeneous refractive index distribution, the propagation of the electromagnetic fields cannot be described by the bulk refractive index of lithium niobate. Instead, one must account for the effective refractive indices experienced by the guided waves. Since each spatial mode experiences a distinct effective refractive index, each possesses a unique phase-matching condition. If a waveguide supports multiple modes for any of the interacting wavelengths, it imposes a fundamental constraint on the achievable conversion

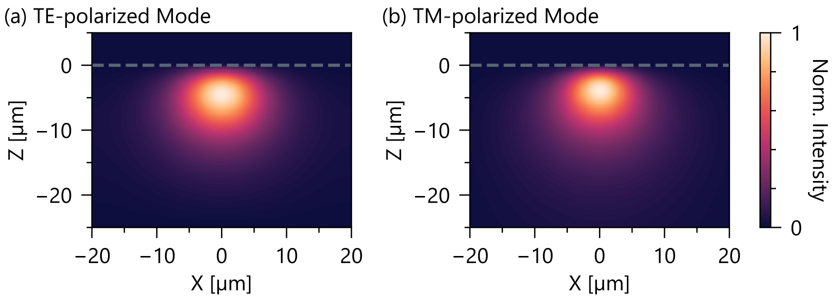

Figure 2.3: Simulation of the spatial mode profile of the (a) TE-polarized and (b) TM-polarized fundamental mode at 1556 nm. The simulation is performed for a titanium strip width of 5 µm and room temperature conditions of 21 °C. The dashed line marks the surface of the waveguide sample.

efficiency; any power coupled to higher-order modes will fail to satisfy the designed phase-matching condition. Consequently, calculating the precise poling period via Eq. (2.10) requires an accurate determination of the effective refractive indices. These can be derived from the refractive index cross sections that arise from the titanium in-diffusion process.

In order to simulate the refractive index distribution, a commercial mode solving software based on the finite-element method (RSoft FemSIM) is used. The simulation takes into account, among others, the refractive index of bulk lithium niobate [159, 160], together with the dimensions of the titanium strip and its diffusion parameters. The simulated fundamental spatial modes of a TE- and TM-polarized beam at 1556 nm are shown in Fig. 2.3 as an example.[3]. While both polarizations are guided, the refractive index profile causes TM-polarized modes (polarized along the crystalline *c*-axis) to travel more closer to the waveguide surface than TE-polarized modes [125]. This mode is thus known to experience higher optical losses due to tiny scratches or particles on the surface. The simulation with the RSoft software was found to accurately describe the spatial mode profiles of the guided modes under ambient conditions. However, simulation of the cryogenic performance poses diverse challenges, which we will examine in the next section.

2.1.3 Intrinsic material changes at cryogenic temperatures

Cryogenic operation of Ti:PPLN waveguides requires consideration of thermal effects which influence the nonlinear interaction. So far, we have explored the principle of frequency conversion, the process of quasi-phase-matching, and the properties of the in-diffused waveguide platform. Up to now, we have neglected all temperature dependencies but these become crucial for understanding the changes at cryogenic temperatures. Let us consider the condition for quasi-phase-matching $\Delta k_{\mathrm{QPM}} = 0$ (compare Eq. (2.10)). The propagation constant for a field of wavelength λ, which experiences the effective refractive

---

[3] This wavelength is relevant for the NLO process discussed in Chapter 4

index n when traveling through the waveguide, can be expressed by

$$k(\lambda) = \frac{2\pi n(\lambda)}{\lambda} . \tag{2.16}$$

However, to precisely describe the phase-matching, we must take into account the temperature dependence of the effective refractive indices $n(\lambda) \longrightarrow n(\lambda, T)$ and the crystal length, i.e., the poling period $\Lambda \longrightarrow \Lambda(T)$. With that, we can modify Eq. (2.10) to find the required poling period at operation temperature T to fulfill the phase-matching condition

$$\frac{1}{\Lambda(T)} = \frac{n_\mathrm{p}(\lambda_\mathrm{p}, T)}{\lambda_\mathrm{p}} - \frac{n_\mathrm{s}(\lambda_\mathrm{s}, T)}{\lambda_\mathrm{s}} - \frac{n_\mathrm{i}(\lambda_\mathrm{i}, T)}{\lambda_\mathrm{i}} . \tag{2.17}$$

This temperature dependence of the poling period is often exploited to tune the phase-matching point of a titanium in-diffused waveguide by varying the crystal temperature. This method enables compensation for fabrication imperfections and operating the frequency converter at the planned wavelength combination. However, this technique is certainly incompatible with cryogenic operation, as the temperature is fixed through the cryostat. Moreover, the tunability becomes negligible in the low Kelvin range, because changes in the refractive indices and the crystal length disappear at 0 K. Consequently, the poling period that is present at cryogenic temperatures is already fixed during fabrication. This means, we rely on precise knowledge of the temperature dependencies to determine the poling period, that must be fabricated at room temperature, which results in cryogenic phase-matching for a designed process.

The empirical refractive index data for bulk lithium niobate, which goes into the RSoft simulations, is based on measurements for operation temperatures from room temperature upwards [159, 160]. However, the Sellmeier equations for the ordinary and extraordinary indices which were found for these temperatures can be extrapolated for the cryogenic temperature range. This provides a first assessment of the magnitude of the shift. We feed the extrapolated Sellmeier equations into the simulation to obtain the estimated shift in the effective refractive indices during the cooldown. This data is shown exemplary in Fig. 2.4 for the TE- and TM-polarized fundamental modes at 1550 nm. Both refractive indices decrease for decreasing temperature. It can be seen that the extraordinary refractive index exhibits a much stronger temperature dependency than the ordinary one. The description of the type-II phase-matching investigated in this work requires knowledge of both indices. The type-0 process relies on the extraordinary index only.

The temperature-dependent poling period is defined by the thermal contraction of the substrate during a cooldown. The available empirical data for the thermal expansion coefficient of congruent lithium niobate in the direction of our waveguides spans temperatures down to 60 K [161, p. 47]. A polynomial fit is performed on this data to describe the change in the length as the contraction coefficient $\alpha(T)$. While a third-order polynomial is sufficient for narrow temperature intervals [161, p. 45], a fifth-order fit is employed to characterize the behavior across the full range from 60 K and 298 K. The higher-order model minimizes the residual error. This fit function is used in the subsequent chapters to describe the poling

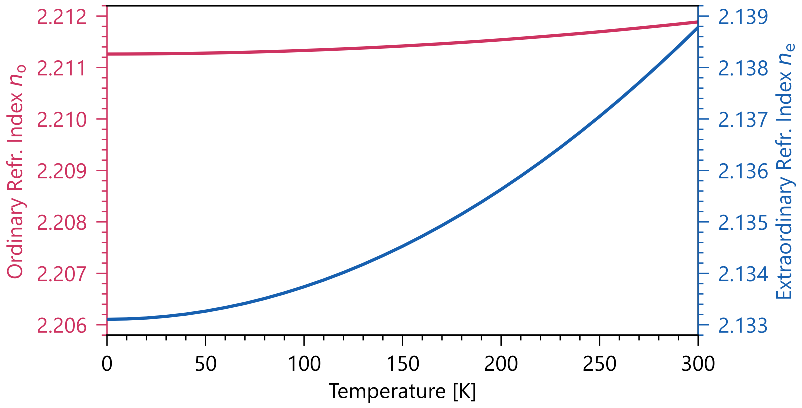

Figure 2.4: Temperature dependence of the effective refractive indices of a titanium in-diffused waveguide. The simulation is performed for the fundamental spatial mode at 1550 nm and a titanium strip width of 7 µm. The TE-polarized mode experiences the ordinary refractive index, the TM-polarized mode experiences the extraordinary refractive index, respectively. For comparison, both y-axes cover an interval of the same size.

period $\Lambda(T)$ for temperatures below room temperature according to $\Lambda(T) = \alpha(T)\Lambda_{\mathrm{RT}}$, with the room temperature poling period $\Lambda_{\mathrm{RT}} = \Lambda(298\,\mathrm{K})$. The function is given by

$$\alpha(T) = a_0 + a_1 T + a_2 T^2 + a_3 T^3 + a_4 T^4 + a_5 T^5\,, \tag{2.18}$$

with the coefficients $a_0 = 0.99801$, $a_1 = 2.93374 \cdot 10^{-7}$, $a_2 = -2.7847 \cdot 10^{-8}$, $a_3 = 4.49085 \cdot 10^{-10}$, $a_4 = -1.36872 \cdot 10^{-12}$, and $a_5 = 1.39948 \cdot 10^{-15}$. Fig. 2.5 shows Eq. (2.18) for the temperature range from 60 K to 300 K. It can be seen that the changes in the length become negligible as the temperature decreases toward 60 K. This is consistent with the trend of the thermal expansion coefficient, which must disappear at 0 K. For this reason, the crystal length and thus the poling period are approximated to remain constant in the cryogenic temperature range from 0 K to 60 K. For this range, $\alpha(60\,\mathrm{K})$ is assumed, which is illustrated in Fig. 2.5 as a dashed line.

It is important to note that the total geometric contraction of the Ti:PPLN waveguide is quite small, approximately 0.2 % over the temperature range of interest. Because of the minor contraction, the shift in the phase-matching conditions is driven predominantly by the temperature-dependent refractive indices of lithium niobate. Nevertheless, Eq. (2.18) is employed to quantify the length contraction, ensuring that the phase-matching model accounts for the total cryogenic changes of the platform.

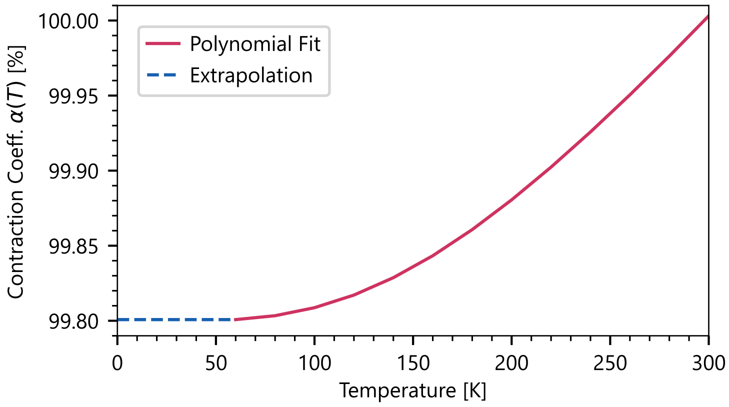

Figure 2.5: Percentage change in the waveguide length and poling period, respectively. The temperature-dependent change is described by the contraction coefficient $\alpha(T)$. For cryogenic temperatures below 60 K, the length is considered to be constant.

Revised temperature dependence of Sellmeier equations

As stated above, direct extrapolation of the Sellmeier equations leads to an initially non-quantified uncertainty for the simulations of the cryogenic modes. Preliminary work for this PhD project concentrated on evaluating the accuracy of this extrapolation for type-II phase-matched SHG. An empirical correction for the effective refractive index data was established by monitoring the temperature-dependent shift of the phase-matched second-harmonic wavelength during a cooldown or warmup procedure. While the extrapolated data predicted a wavelength shift of about 19 nm from room temperature to cryogenic temperatures, the observed experimental shift was approximately 40 % larger. Therefore, the empirical correction provides a much more accurate description of the cryogenic second-harmonic wavelength in our waveguide platform. This correction method and corresponding measurement series were initialized by Bartnick et al. [131], and continued in the scope of my Master's project.

For the case of type-II SHG, Eq. (2.17) can be simplified as both incident fields have the same wavelength $\lambda_\mathrm{s} = \lambda_\mathrm{i} = \lambda$, corresponding exactly to twice the generated wavelength $\lambda_\mathrm{p} = \lambda/2$,

$$\Lambda_\mathrm{SHG}(T) = \frac{\lambda}{2n_\mathrm{TE}(\frac{\lambda}{2}, T) - n_\mathrm{TE}(\lambda, T) - n_\mathrm{TM}(\lambda, T)} = \frac{\lambda}{\Delta n(\lambda, T)}\,. \tag{2.19}$$

The temperature-dependent effective refractive indices are combined to form the single expression $\Delta n(\lambda, T)$. This linear combination is then modified with $\Delta n(\lambda, T) \longrightarrow \Delta n(\lambda, T) + \delta n(T)$, where $\delta n(T)$ is a temperature-dependent fifth-order polynomial function. This correction accounts for any experimental deviations in the shift of the phase-matched second-harmonic wavelength. The fit function was chosen by Bartnick et al. [131], as their initial correction term demonstrated apparent nonlinear behavior in the investigated temperature range from 0 K to 300 K.

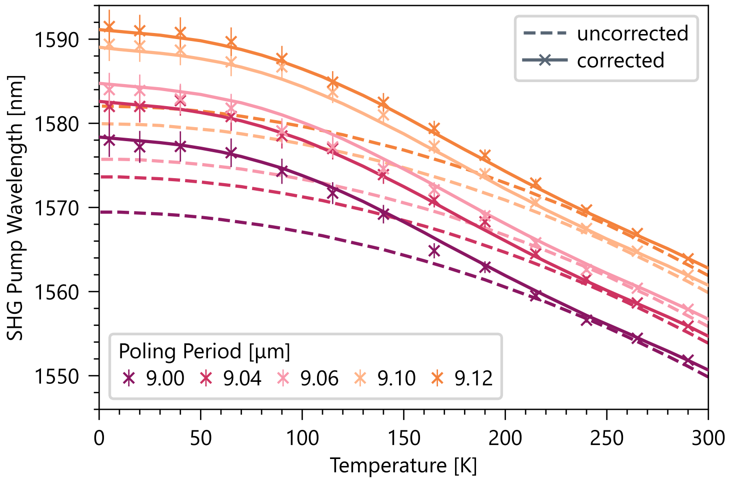

Figure 2.6: Temperature-dependent shift in the measured SHG pump wavelength for five waveguides with different poling periods. The uncorrected simulation is shown as dashed lines and the solid lines represent the corrected simulation using the correction term defined in Eq. (2.21).

In the first experiments by Bartnick et al. [131], one waveguide with a poling period of 9.12 µm was fiber-coupled and characterized in a closed cryostat. The chosen poling period was known to enable phase-matching at room temperature in the telecom C-band. The second-harmonic wavelength was monitored throughout two cooldown and warmup cycles. During my Master's project, I repeated these measurements with a separate waveguide sample using a free-space coupled cryostat. I conducted a step-by-step cooldown while observing five waveguides with different poling periods. These experiments were performed within the same cryostat which is also employed in the scope of this work. A detailed description of the cryostat design can be found in Section 2.2.1.

The measurement of five individual waveguides allowed for finer modifications of the correction term which was defined by Bartnick et al. [131]. Fig. 2.6 shows the measured wavelength shifts for the five waveguides, together with the uncorrected and corrected simulations. The uncorrected curves demonstrate the raw simulation relying on the extrapolated data, while the corrected curves result from applying the following fit to the experimental data

$$\lambda(T) = \Lambda_{\mathrm{SHG}}(T)(\Delta n(\lambda, T) + \delta n(T)) \, . \tag{2.20}$$

While both theoretical models describe the wavelengths well around room temperature, the empirical correction is clearly required to accurately describe the cryogenic second-harmonic wavelengths. Therefore, the determined correction term represents a crucial tool to define the cryogenic poling period for type-II phase-matching. To be precise, this correction can be applied for cryogenic SHG and thus SPDC in the telecom range. All phase-matching calculations in Chapter 3 thus rely on the correction term, which is given by

$$\delta n(T) = b_0 + b_1 T + b_2 T^2 + b_3 T^3 + b_4 T^4 + b_5 T^5 \,, \tag{2.21}$$

with $b_0 = 1.64328 \cdot 10^{-3}$, $b_1 = -4.77961 \cdot 10^{-6}$, $b_2 = 1.06429 \cdot 10^{-7}$, $b_3 = -1.56532 \cdot 10^{-9}$, $b_4 = 6.62398 \cdot 10^{-12}$, and $b_5 = -8.64840 \cdot 10^{-15}$.

Photorefraction and pyroelectricity in lithium niobate

In addition to the need for accurate refractive index data, photorefractive and pyroelectric effects represent further challenges for cryogenic operation. Both effects cause a localized accumulation of electric charges within the lithium niobate substrate [88]. Although caused by different underlying material properties, in both cases, the arising electric fields result in a modification of the refractive index profile of the waveguide. This is caused by the electro-optic effect, which describes the alteration of the refractive index as a function of an applied electric field [88]. As a result, these effects can cause beam distortions during propagation or alter the phase-matching.

The effect of photorefraction is mainly driven by crystal defects which get trapped within the crystal structure during its fabrication [153]. These crystal defects weakly absorb the coupled light intensity, which results in a separation and redistribution of their charge carriers. For instance, the electrons within the bright waveguide area are excited into the conduction band and diffuse into darker regions of the substrate [153]. The induced dislocation of the charge carriers is equivalent to internal electric fields which arise within the crystal.

Lithium niobate has a bandgap of approximately 4 eV [162]. Consequently, a high energy photon from the UV range is required to cause a direct excitation of an electron from the valence band to the conduction band. Intrinsic and extrinsic crystal defects, such as point defects or impurity centers, enhance the absorption of visible light. This process is associated with the formation of stable charge distributions in the form of polarons [163–165]. These polarons are created through the relaxation of excited electrons from the conduction band, or holes from the valence band, into a quasi-particle state, called the electron or hole polaron [162].

It is known that for all variants of lithium niobate, intrinsic defects appear due to slight deviations of the Li:Nb ratio from 1:1. Specifically, for congruently-grown lithium niobate, as it is used in this study, this ratio is typically Li:Nb = 0.94 [166, p. 10]. Consequently, this lithium deficit results in the presence of lithium vacancies; about 6 % of the lithium sites in the crystal lattice are empty. Some of these vacancies get occupied by a niobium ions. These niobium ions placed on original lithium sites are then called lithium anti-sites and denoted as $\mathrm{Nb}_{\mathrm{Li}}$. These crystal defects and impurity centers form additional energy levels within the bandgap, which can act as donor or acceptor centers. Furthermore, small iron impurities are generally present in every lithium niobate crystal. Since iron in the form of Fe^{2+} and Fe^{3+} is known to provoke photorefractive damage [162], these impurities are included here for completeness.

Several kinds of polaron states are known to exist for lithium niobate, which correspond to various energy levels within the bandgap. For a detailed discussion of the generation and dissociation of polarons, as well as the transition energies, the reader is referred to Ref. [162, 167]. Here, a short overview of the different polaron types is given [162]:

1. **Free polarons** are formed by electrons localized at Nb ions that are placed on Nb sites $\mathrm{Nb}_{\mathrm{Nb}}^{4+}$. These free electron polarons can move through the crystal by hopping between neighboring niobium ions. A relatively low photon energy of 1.1 eV ≈ 1130 nm is required to excite an electron from a free polaron into the conduction band.
2. **Bound polarons** are given by electrons localized at Nb ions which are placed on Li sites $\mathrm{Nb}_{\mathrm{Li}}^{4+}$. These bound polarons are trapped at those defects at an energy below the energy of the free polaron. Consequently, higher photon energy of 1.6 eV ≈ 775 nm is necessary to break up a bound polaron.
3. **Bipolarons** correspond to a pair of a bound and a free polaron $\mathrm{Nb}_{\mathrm{Nb}}^{4+} + \mathrm{Nb}_{\mathrm{Li}}^{4+}$. To excite a bipolaron, even higher photon energy of 2.5 eV ≈ 495 nm is required.
4. **Hole polarons** are localized at O^- ions. So far, little is known about the energy level and properties of free hole polarons. However, the bound hole polarons are localized at O^- ions adjacent to lithium vacancies, which have a comparably high absorption energy of 2.5 eV.
5. **Iron impurities** such as Fe^{2+} and Fe^{3+} provide additional inter-band states. Fe^{2+} can change into Fe^{3+} by donating an electron, which forms an electron polaron in the neighborhood. Likewise, an electron can be captured by a Fe^{3+} ion, which forms a deep filled electron trap Fe^{2+}. To excite an electron from this trap, an energy of 2.6 eV ≈ 475 nm is necessary.

The excitation of an electron (hole) into the conduction (valence) band is followed by the spatial transport of this charge carrier through the crystal. The charge carriers can move by the processes of drift, diffusion, and the bulk photovoltaic effect [166, p. 52]. Specifically, photo-excited charge carriers mainly move due to the photovoltaic effect, which results for lithium niobate in a preferred movement along the z-axis [168]. These electrons are then predominantly captured by deep electron traps. This light-induced charge carrier arrangement is different from the initial distribution and thus results in electric fields which disturb the refractive index. Consequently, the linear and nonlinear device performance is subject to dynamic and often non-deterministic fluctuations. Especially for high optical power in the visible or near-infrared range, photorefraction can induce strong beam distortions, such as defocusing, which significantly reduces the overall device performance [151]. Photorefraction in lithium niobate is observed for both, TM- and TE-polarized fields. However, the change in the extraordinary refractive index (influencing TM-polarized modes parallel to the z-axis) is much stronger compared to the ordinary one (influencing TE-polarized modes) [169].

Furthermore, it is shown that photorefraction can be typically characterized by an intensity threshold. If the coupled optical power exceeds this limit, serious damage to the waveguide is observed. This threshold can be increased by operating the waveguide at higher temperature as this results in an increased electron mobility [151, 170]. Consequently, operating lithium niobate waveguides at increased temperatures between approximately 100 °C and 200 °C represents a common strategy to suppress photorefraction [151, 165, 171]. However, this means that decreased operation temperatures are associated with lower tolerated optical power levels.

Especially at cryogenic conditions, photorefraction can have a significant effect on the waveguide performance, which becomes particularly relevant for the cryogenic studies in this work. The extremely low mobility of the photo-excited electrons leads to a strong trapping effect. The charges are likely to experience a “freeze in”, which inhibits their return to the waveguide region, after they got excited into the conduction band and moved into the darker substrate. We will see in Chapter 4 that photorefraction in particular affects the cryogenic performance if the NLO process is pumped with visible light. Moreover, a detailed investigation of the cryogenic photorefractive effect is included in Chapter 5, to determine practical power thresholds.

Pyroelectricity

We have already discussed that lithium niobate is a ferroelectric crystal whose properties are exploited for the periodic poling process. Accordingly, lithium niobate is also classified as a pyroelectric material. The strength of its spontaneous polarization is temperature dependent. A change in the operation temperature ΔT induces a change in the spontaneous polarization $\Delta \boldsymbol{P}_\mathrm{s}$ [156, 172]. The proportionality is defined by the pyroelectric tensor $\boldsymbol{p}$, via $\Delta \boldsymbol{P}_\mathrm{s} = \boldsymbol{p} \Delta T$ [88]. The only nonzero component of the pyroelectric tensor is the z-component which has a negative value. This indicates that the spontaneous polarization is aligned with the z-direction (i.e., parallel to the c-axis) and its strength increases for decreasing temperature.

For z-cut lithium niobate, the cooldown thus causes an accumulation of charge carriers on the top and bottom surface of the crystal. This results in emerging electric fields within the material. In general, under ambient conditions, atmospheric charge carriers from the surroundings can neutralize the accumulating charges on the sample surfaces. However, cryogenic operation demands an evacuated sample space. The vacuum within the cryostat prevents compensation and instead causes continued growth of the field strength. The sum of a multitude of microscopic charge movements results in a non-uniform surface charge accumulation. Spatially inhomogeneous electric fields are generated. Individual fields can result in a sudden discharge if the local field strength becomes too high. The electric fields degrade the device performance, as the waveguides are located directly below the crystal surface. Consequently, the charge fields induced by pyroelectricity and photorefraction can perturb the waveguiding quality and, moreover, also alter the phase-matching along the waveguide.

Specifically, localized perturbations in the refractive index are analogous to a nonuniform poling period. This can be understood as follows; although a consistent poling period over the complete waveguide length is fabricated for the processes characterized in this work, spatial modifications in the refractive index along the waveguide result in varying phase shifts. These local perturbations prevent the phase-matching condition from being consistently satisfied across the entire length of the waveguide. Consequently, the guided modes experience an inconsistent poling period, which reduces the effective length. This can be experimentally deduced from two observations: first, a reduced conversion efficiency, and second, perturbations in the phase-matching spectrum, which manifest themselves in the form of deviations from the ideal sinc^2 function (e.g., asymmetric side peaks).

Previous work has shown that the cooling procedure to cryogenic temperatures leads to unpredictable changes in the electrical and optical crystal properties [131, 132, 154, 173]. These events exhibit the signatures of spontaneous discharges of unbound carriers, which occur stochastically across different time scales throughout the thermal transition. Bartnick et al. [131] observed the shift in the phase-matched SHG wavelength of a Ti:PPLN waveguide throughout the cooldown from 292 K to 4.4 K. Their results demonstrate sudden jumps in the wavelength, as well as slow transitions in which two phase-matched wavelengths are present at the same time. These signatures are a strong indicator that the waveguide properties experience local perturbations, which are related to the accumulation and discharge of pyroelectric fields [131]. Similar to the photorefractive effect, any charges which do not discharge during the cooldown, become localized in form of a “freeze in”, affecting the cryogenic device characteristics.

Consequently, two primary mechanisms are expected to influence the linear waveguiding and nonlinear phase-matching properties at cryogenic temperatures. First, the thermal transition itself may induce localized variations in the refractive index, due to the pyroelectric effect. Second, due to photorefraction, the incident light intensity can cause further damage to the waveguide (by inducing perturbations in the refractive index profile) while the frequency converter operates at a stable cryogenic temperature.

2.2 Experimental methods

This section concentrates on the first research question of how to reliably measure the cryogenic waveguide performance metrics. Considerations for the design of the experimental setup include the cryostat design, waveguide mounting and coupling methods, and finally the measurement procedures. These insights form a foundation for understanding the cryogenic experiments discussed in the subsequent chapters.

2.2.1 Cryostat configuration for waveguide characterization

In order to reach the realm of liquid helium for cryogenic waveguide operation, two primary approaches may be pursued. The first involves fiber-coupling the waveguide to mount it within an enclosed cryostat, whose vacuum chamber is completely isolated from ambient light. Alternatively, advances in cryogenic technologies allow for highly customized cryostat designs. This flexibility enables, among other features, free-space optical access to the vacuum chamber.

The first approach represents a valuable option for Ti:PPLN waveguides due to the high spatial overlap of the waveguide and fiber modes. In this process of fiber-to-waveguide coupling (known as pigtailing), a cleaved glass fiber embedded in a ferrule is attached to the waveguide end facet using UV glue. However, this method is limited in multiple aspects. The fiber coupling requires accurate alignment of the fiber and waveguide core before both components are permanently glued together. This alignment is performed at room temperature and restricts the cryogenic characterization exclusively to the previously fiber-coupled waveguide(s). While this restriction is negligible for waveguides already validated at cryogenic temperatures, it represents a significant obstacle for prototyping experiments that necessitate the initial characterization of multiple waveguides. Furthermore, the glued connection can become brittle at cryogenic temperatures and slight movements due to thermal stress can result in losing the waveguide coupling. Restoring the coupling requires considerable effort, including warming up the system, relieving and cleaning the end facets, and repeating the pigtailing process. Finally, this method does not allow to separate the effects of changes in the coupling efficiency from variations in the waveguide itself. For example, alterations in the spatial mode profile cannot be observed.

In contrast, the free-space coupled cryostat design meets all the specified challenges. Fig. 2.7 provides an overview of the vacuum chamber in opened and closed configurations. The cryostat cover is equipped with transparent windows to couple light to the cryogenic sample. Moreover, the vacuum chamber is integrated into an optical table. This enables direct implementation of the cryogenically operated waveguide into a free-space optical setup. The laser beam is coupled to the waveguide end facets using two aspheric lenses positioned outside the cryostat. Therefore, this design allows to apply the same waveguide coupling method, that is validated for room temperature operation, for the cryogenic measurements. The only difference lies in the windows that separate the cryogenic chamber from the free-space setup at room temperature. For this reason, the cryogenic investigation is not limited to preselected waveguides. Integrated piezo positioners allow for in-situ repositioning at cryogenic temperatures, so that variations in the alignment can be compensated at any time. Furthermore, original changes in the waveguide performance can be detected, including imaging of the guided modes.

The measurements in this work were conducted using a customized closed-cycle helium cryostat (attoDRY800, Attocube). The waveguide sample is mounted on a component stack, which features two piezo positioners (see Fig. 2.7 (a)). These allow for precise movement with a repeatability of less than 2 µm in the x-direction (perpendicular to the waveguide orientation) and z-direction (height). The z-positioner has a travel range of 5 mm and the x-positioner can travel over 15 mm. This distance in x-direction is large enough to scan through all waveguides on a single chip, which has by default a width of 12 mm. The positioners thus provide maximum flexibility for prototyping experiments in which every waveguide should be tested. Furthermore, the positioning in the z-direction is crucial since

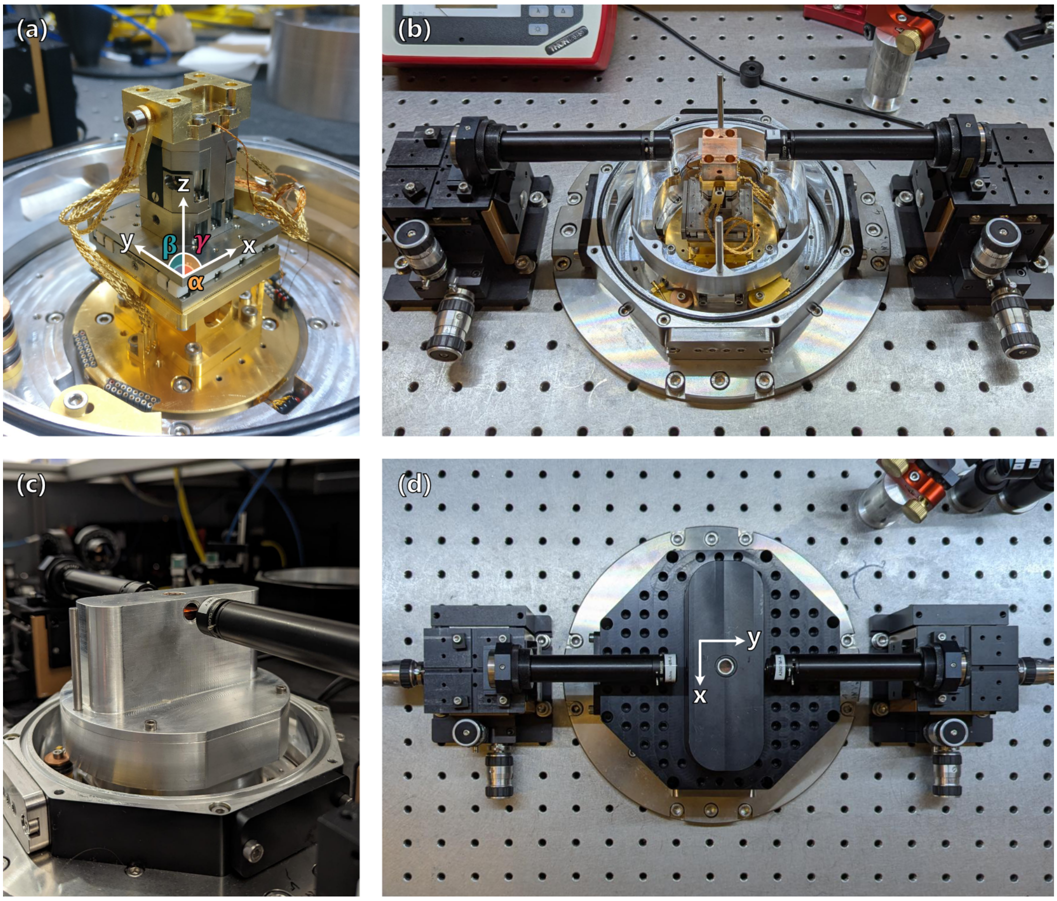

Figure 2.7: Photographs of the free-space coupled cryostat. (a) Waveguide mounting stack, including two piezo positioners, a temperature sensor and a heating unit. (b) Waveguide coupling at room temperature in the opened cryostat, using two aspheric lenses, each mounted on a three-axes stage. (c) Inner shroud, which serves as a cold shield. (d) Fully closed cryostat with the installed vacuum shroud.

the cooldown process causes the complete mounting stack to contract and thus shifts the waveguide height.[4]

No positioner is installed for the y-direction, as the dimensions of the inner cryostat shroud are designed to position the waveguide end facets close to the cryostat windows. This proximity is crucial for coupling light into the cryogenic waveguide using the lenses mounted outside the shroud. For a standard waveguide length of 25 mm, the gap between

---

[4] The initial cryostat configuration did only include the x-positioner, the z-positioner was updated about three years later. The first waveguide coupling approach was to counteract for changes in the waveguide height by readjusting the free-space beam height, which required huge alignment effort. The additional z-positioner thus improved the alignment procedure significantly. All cryogenic measurements presented in Chapter 3 were conducted with the x-positioner only, while the measurements in Chapter 4 and most measurements in Chapter 5 were conducted using both positioners.

end facet and the shroud is only 1.5 mm, ensuring a short working distance. The minimum working distance for our system is about 13 mm. Since the weakly confined modes of Ti:PPLN waveguides have relatively large mode sizes, coupling does not require exceptionally high numerical apertures. This allows for the use of standard aspheric lenses, which can be adjusted to compensate for the thermal contraction of the waveguide during the cooldown.

The brass adapter, which is mounted on top of the stack shown in Fig. 2.7 (a), includes a temperature sensor, that detects the temperature close to the sample, and a heating unit. The heater is controlled via a PID loop. The cold plate can either cool down the system, or be turned off; initially there is no option to adjust the cooling rate. If the cryostat is cooled down with the heater turned off, the cooldown is completed in less than 5 hours. However, for the characterization of lithium niobate, we rely on a slow cooldown so that accumulating pyroelectric charges can partially discharge again before their mobility is reduced significantly. For this reason, our cryostat is equipped with the additional heating unit to ensure a slow cooling rate which does not exceed 1 K/min at any point. This extends the cooldown time to about 8 hours. This cooling rate is ensured at the sample stage only, while the cold plate cools down continuously. Consequently, large temperature gradients can exist in the cryostat when the heater is running with high power. However, the brass adapter is connected to the cold plate via three braided thermal links to enable the lowest possible sample temperature after the cooldown is completed. The base temperature at the sample stage, which was achieved for the following cryogenic measurements, varied between 4.7 K to 6.6 K, depending on the cryostat's condition and maintenance history.

Fig. 2.7 (b) shows the mounting of a waveguide chip on the positioner stack while the cryostat is completely opened. A copper height spacer is screwed to the brass adapter. The lithium niobate chip is placed on top of it using a small amount of thermal grease in between. The grease is sticky enough to keep the sample in place without clamping it, which would introduce additional strain and could alter the optical properties. In order to couple the waveguide, two aspheric lenses are mounted on a three-axes stage each. The height of the waveguide is matched to the optical axis of these stages. The cryostat dimensions require that the lenses stick out to get close to the waveguide end facets. For this reason, each lens is attached with a lens tube to the stages, bridging a distance of approximately 10 cm. This extension makes the lenses sensitive to any vibrations which is why the stages require careful alignment. The lens tubes are further equipped with an iris that is mounted directly behind the lenses. This facilitates the alignment process.

The sample chamber of the cryostat is enclosed by two different covers. Fig. 2.7 (c) and (d) show the inner and outer cover, respectively. In order to close the chamber, the lens tubes must be temporally dismounted, which typically results in slight misalignment after they are reinstalled. The inner shield is connected to the 40 K stage and acts as a cold shield. Attention should be paid that no components or cables are touching the cover to ensure best thermal isolation. From the original three windows of the inner shield, the two side windows were taken out at an early stage, since they introduced additional reflections of the laser beams, which complicated the coupling procedure. As a result, the sample temperature increased by only 0.5 K, which is expected to have a negligible effect on the waveguide performance. The vacuum is maintained by the outer cover, which features three windows to enable optical access to the waveguide end facets and top surface.

2.2.2 Waveguide mounting and coupling procedure

As stated in the previous section, the waveguide sample is fixed to the copper adapter using a small amount of thermal grease. This leaves a degree of freedom for the angle alignment, which is crucial for optimized coupling and cannot be corrected at a later stage. For this reason, it is important to have the beam aligned perfectly straight and to place the waveguide chip parallel to the beam. The following instructions serve as a guide for the keen experimental scientist, to achieve coupling of the waveguide in the introduced cryostat. Fig. 2.8 provides a graphical guide, while the details are discussed in the main text.

1. **Waveguide placement and straight beam alignment.** In the first step, tweezers are used to carefully place the waveguide sample on top of some thermal grease on the mounting stack. Its height is reduced at first to not block the visible alignment laser, which is turned on next. This beam is aligned straight at the optical height of the lens stages. For the beam alignment, the lens tubes are being excluded from the setup for now to allow undisturbed beam alignment. The alignment is performed using one iris in front of the in-coupling stage and another one behind the out-coupling stage. Using a dichroic mirror, the alignment laser is overlapped with the IR pump laser for the later experiments. After the beams are straight, I recommend to add an additional iris in front of the in-coupling stage. This provides two checkpoints for the alignment of the input beam as soon as the waveguide is in place. While this might not be necessary in a stable experimental setup, the waveguide stack moves during the cooldown which can require movement of the input beam. The two pinholes function as a reliable reference point, enabling quick restoration of the original coupling alignment - a feature that has efficiently decreased the alignment time during my experiments.

2. **Central alignment of lens stages.** The input and output lens tubes are placed in the beam path. At this point, only the tubes are attached with no lenses. Each tube possesses an integrated iris to facilitate its alignment. The x- and z-direction of both stages are adjusted so that the transmitted intensity through the integrated irises is maximized.

3. **Angle alignment of the waveguide sample.** For now, the lens tubes are unscrewed again without changing the position of their stages. The sample is moved upwards so that the VIS beam is incident roughly in the center of the waveguide input facet. The back reflection of this facet is observed on one of the pinholes. Gentle pressure is applied on the sample corners using plastic tweezers to modify the angle alignment until the back reflection is overlapped with the incoming beam.

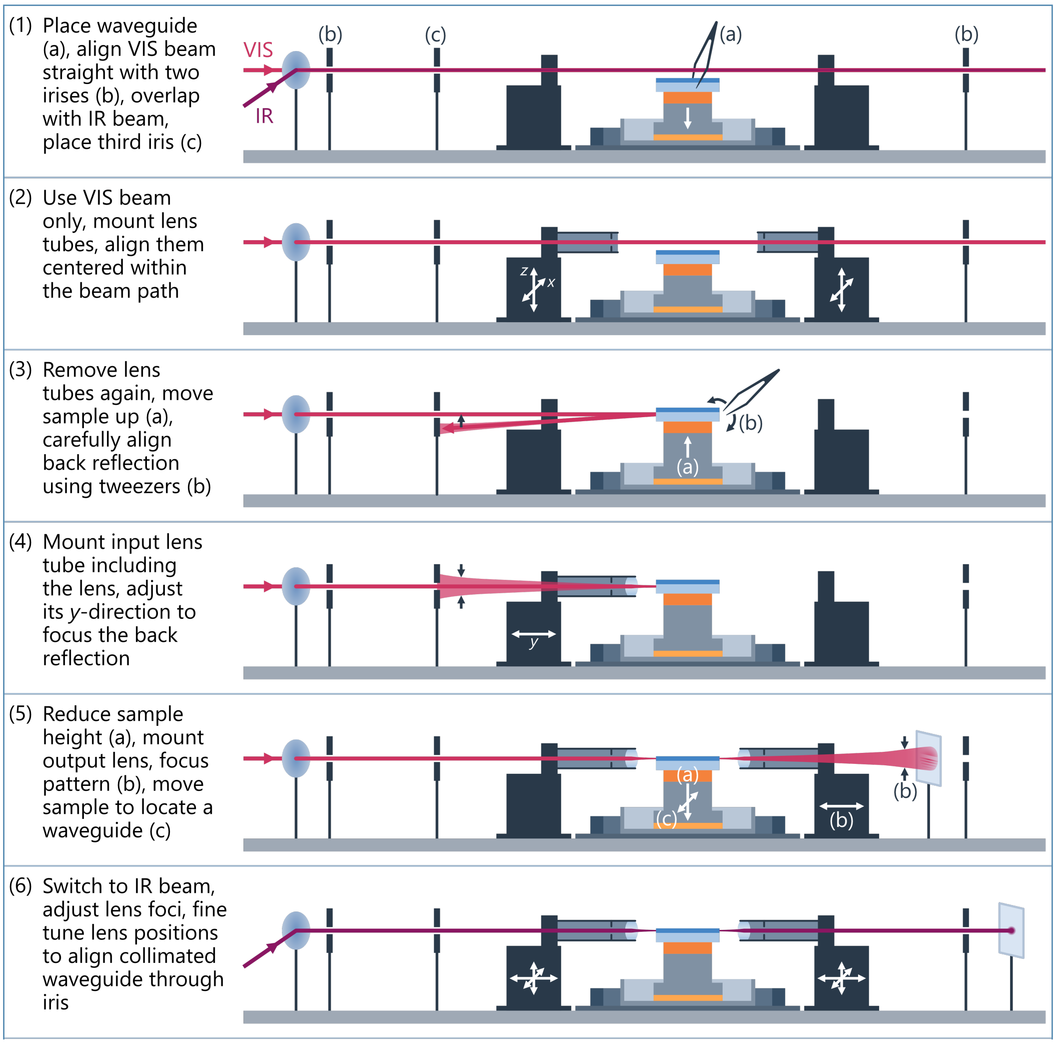

(1) Place waveguide (a), align VIS beam straight with two irises (b), overlap with IR beam, place third iris (c)

(2) Use VIS beam only, mount lens tubes, align them centered within the beam path

(3) Remove lens tubes again, move sample up (a), carefully align back reflection using tweezers (b)

(4) Mount input lens tube including the lens, adjust its y-direction to focus the back reflection

(5) Reduce sample height (a), mount output lens, focus pattern (b), move sample to locate a waveguide (c)

(6) Switch to IR beam, adjust lens foci, fine tune lens positions to align collimated waveguide through iris

Figure 2.8: Graphical guide for waveguide coupling within the free-space coupled cryostat setup. These coupling steps must be performed on the opened cryostat in preparation for the subsequent cooldown.

4. **Alignment of in-coupling focus.** The in-coupling lens is attached together with the lens tube to the stage which was previously aligned in the x- and z-direction. To align the y-direction, again, the back reflection of the input facet is observed on the iris. This reflection approaches a focused spot as soon as the input facet is roughly aligned in the focal plane. The employed translation stages provide 2 mm of travel for precise alignment, while an integrated rail system allows for manual positioning over longer distances. The lens is at first roughly aligned in the y-direction by manually moving the tube mount within the rail. For this, the adjustment screw for the y-direction should be extended approximately halfway to keep enough range of motion for the later optimization. As soon as the back reflection is focused, alignment of the x- and z-axes should be fine tuned to overlap this reflected spot with the input beam.

5. **Alignment of out-coupling focus and waveguide positioning.** The height of the waveguide sample is reduced until the input beam hits the upper edge of the sample, as the waveguides are located just beneath the surface. Next, the out-coupling lens tube is inserted. Its y-direction is set by placing an alignment card at least 30 cm away from the lens and focusing the scattered beam pattern. The scattered pattern must be interpreted correctly in order to precisely adjust the waveguide positioners. If the sample is slightly too high, this results in a uniform light pattern, sharply confined on the top and bottom due to the sample dimensions (see Fig. 2.9 (a)). Moving the sample slightly too low leads to an interference pattern because part of the intensity is reflected from the sample surface (see Fig. 2.9 (b)). The waveguides are located at the transition point between those two patterns. At this height, the x-positioner of the sample stage is moved to find a waveguide, represented by a bright spot on the card (see Fig. 2.9 (c)). Since the waveguides are not optimized for visible light operation, the waveguide spot is surrounded by stray light that is coupled to the substrate.
6. **Fine tuning for the IR laser beam.** After the initial waveguide coupling is completed, the VIS alignment laser is blocked and the IR pump laser is turned on. In my experiments, the pump wavelength was in the range from 775 nm to 1600 nm, which required exchanging the white paper card by a fluorescent card to monitor the transmitted beam. Based on the longer wavelength, the in- and out-coupling focal points are further away than for the visible alignment beam. Fine tuning of the lens stages is thus initialized by adjusting their foci (y-direction). Modification of the focus of each lens often results in basic waveguide coupling which allows for further fine adjustment along all axes. The waveguide spot is collimated and aligned through the rear iris by modifying all axes of the out-coupling lens. It is recommended to use a beam camera, or a power meter, to maximize the transmitted power through the waveguide.

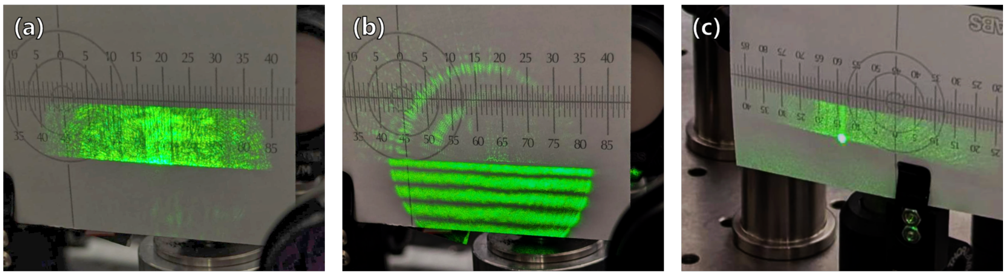

Figure 2.9: Scattered light profile from the waveguide sample, focused on a white card using the out-coupling lens. (a) The sample is moved too high, (b) the sample is slightly too low, and (c) a waveguide is coupled.

Any measurements at room temperature can be performed on the opened cryostat after these alignment steps. Without the cryostat cover, the complete sample surface can be monitored. For this reason, a microscope is placed above the waveguide sample so that the in-coupling facet is observed. The visible alignment laser is used to obtain information about which waveguide is coupled. Scattered light at the input facet can be seen on the microscope, and lithographically patterned waveguide marker reveal the waveguide index. It is especially crucial to determine the index of the coupled waveguide at this stage, before the cryostat is closed. Although the shrouds possess a window on the top, this window is centered and thus does not provide optical top access to the end facets. A future cryostat design should feature top windows that are located as close as technologically possible to the edges.

While the preceding alignment protocol is applicable to room-temperature characterization, the cryogenic operation requires extension of this established procedure. Before closing the cryostat, I recommend to return to the previous step using an alignment laser and optimizing the focal lengths for that visible beam. This often facilitates the verification of the coupling to a waveguide, which is why the cryogenic coupling should be started with a visible beam. Since the cryogenic waveguide is more sensitive to photorefractive damage, it is advisable to chose a low energy visible beam. While a green alignment laser (as shown in Fig. 2.9) is not expected to induce photorefraction at room temperature, the cryogenic alignment should be performed with a low power red laser, e.g., at 635 nm.

After the waveguide index is noted down for the current x-position, the cryogenic investigation is initialized with the following steps. Closing the cryostat requires dismounting the microscope and the lens tubes. The tubes are unscrewed from the stages without touching the alignment screws. Next, the inner and outer shroud are closed and the lens tubes are carefully reattached. In the optimal case, the waveguide is directly coupled again. Otherwise, slight movements of the in-coupling stage should restore the coupling. From now on, it is not possible to see from the top which waveguide is coupled. For this reason, the x-positioner of the waveguide sample should be scanned to determine the distance to the neighboring waveguides. It is possible that the reattachment of the lens tubes results in coupling of a neighboring waveguide. However, coupling to a different group is very unlikely. The distances between the waveguide positions thus reveal which waveguide of a group is coupled and if it is the same one as before. I recommend to couple to the center waveguide of a group before the cooldown is started. The waveguide coupling should be optimized, including collimating the out-coupled beam and aligning it through the iris.

Now, the system is ready to perform the cooldown. The most reliable approach to maintain coupling is to monitor the waveguide movement during the cooldown in intervals and realign the waveguide stage every time. However, this method is not very convenient and for efficient use of time, the cooldown might be performed over night. After the cooldown is completed, the waveguide is initially located outside the beam. Moreover, the positioners display a different location than before. The new values should be noted down. Most alignment changes appear in the waveguide height due to the dimensions of the mounting stack. Nonetheless, experience has shown that the other axes and the angle alignment are not excluded from thermal warp. However, the starting point for restoring the coupling is to move the sample upwards and monitor the changes in the interference pattern from the visible beam. If the transition point of the sample surface can be recognized, slight changes of the waveguide x-position reveal a coupled waveguide.

The targeted waveguide should be close to the initial x-position that was displayed directly after the cooldown. As soon as a waveguide is found, its position is noted down and the distance to the neighboring waveguides is identified. If a central waveguide from a group was coupled at room temperature, the cryogenic waveguide that is found closest to the original position is expected to be from the same group. Should verification of this assumption be desired, one can move the sample along the x-axis until the last waveguide on the sample is located, to compare the distance. In case, multiple different phase-matched processes are fabricated on one chip, the nonlinear characterization (detailed in Section 2.2.3) can also verify the waveguide index. Major changes in the phase-matched wavelength highlight the transition to another phase-matching group. Finally, after the targeted waveguide is identified, the waveguide coupling for the pump wavelength is optimized by fine tuning the lens stages.

Though the described procedure outlines the ideal alignment process, its practical execution often encounters significant difficulties. First of all, the piezo positioners react more stubborn under cryogenic conditions. The same movement in the two opposite directions results in different step sizes. This can cause a slow movement in one direction, while the other direction is scanned too fast so that the waveguides are overlooked. Consequently, it is recommended to always approach the waveguides from the slower direction and to continuously monitor the absolute positioner locations. However, although closed-loop positioners are used, the absolute position of a waveguide can vary by a few micrometers when moving in different directions.

Furthermore, the scattered light profile from the cryogenic chip can look different compared to the room temperature observations. Changing the sample height at room temperature results in an obvious transition point from coupling into the substrate to hitting the surface. However, this transition cannot always be confirmed for the cryogenic sample. This can be caused by slight tilting of the sample along the angles α and β. Variations in these angles can be verified through focusing the input beam on the waveguide facet and detecting the back reflection on an iris. If the back reflection is aligned with the input beam, the waveguide angles remained the same. Unfortunately, deviations cannot be completely compensated with the employed setup. Even though the angle of the input beam can be modified, the lens stages do not allow for angle alignment. Therefore, a tilted input beam would not pass straight through the center of the lens, which causes astigmatism. Any angle movement during the cooldown thus limits the cryogenically achievable coupling efficiency.

The second, and more critical, reason why the transmitted pattern exhibits alterations, lies in the internal material changes. “Frozen in” pyroelectric charges can substantially affect the optical waveguide properties, resulting in significant light scattering from the waveguide mode into the substrate. This reduces the signal-to-noise ratio in the transmitted pattern as the waveguide spot appears less bright compared to the background intensity. Depending on the degree of disturbance, this can seriously impair the coupling process. Circular spots in the noise pattern may be falsely identified as a waveguide mode. For this reason, the periodicity of the suspected waveguide should be reviewed and compared to the fabricated waveguide distances.

In case the visible alignment beam introduces too much scattered light to identify the waveguide position, an alternative approach using the final IR pump wavelength can be pursued. For this, the input polarization is set to TE since this polarization experiences less optical loss than TM. As will be detailed in Chapter 4, the TM-polarized beam is more strongly affected by the cryogenic operation than TE-polarized light. The optical input power should further be limited to the low milliwatt range to avoid photorefractive damage. A beam camera is placed at least 30 cm behind the out-coupling lens and the image from the end facet is focused onto the camera plane. The waveguide is slowly moved along both axes and the scattered pattern on the camera is scanned for a periodically recurring, elliptical-shaped intensity maximum. If this approach does not result in basic waveguide coupling, to be optimized in the next step, the currently investigated cooldown did induce too strong pyroelectric distortions to provide acceptable waveguide performance. In this case, thermal cycling - warming up the sample and repeating the cooldown procedure - can generate an altered charge distribution that enables improved waveguide performance.

2.2.3 Nonlinear characterization methods

The experimental investigation of the waveguide properties that is applied in the subsequent chapters is built upon several fundamental characterization techniques. The principles of these methods are detailed in this section. The essential difference for the measurements at ambient conditions and cryogenic temperatures lies in the waveguide performance and not in the applied measurement protocols. Therefore, the following methods remain valid for cryogenic characterization, provided that waveguide coupling is assured beforehand.

Always start the classical way

As stated in Section 2.1.1, nonlinear three-wave mixing can be separated into classical frequency conversion and their non-classical counterpart. Photon-pair generation via SPDC can only be described non-classically and the generated intensity is strictly within the single-photon regime. This clearly complicates direct beam characterization as detection requires the use of fiber-coupled SNSPDs. Achieving efficient single-photon coupling from a free-space cryogenic setup represents a demanding experimental challenge.

The alignment of the optical setup is significantly facilitated by first performing the classical analogue to the targeted SPDC process. The differences between the experimental setups for the initial classical characterization and the subsequent non-classical measurements are

(a) Up-Conversion

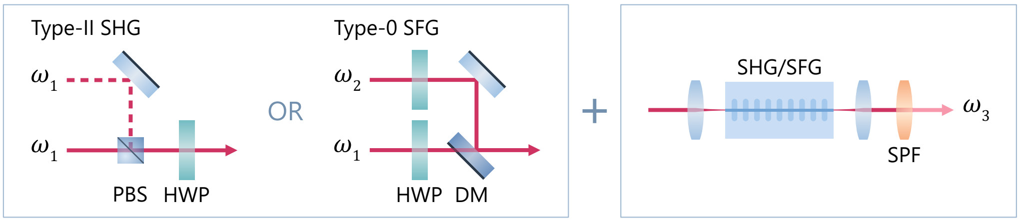

(b) Down-Conversion

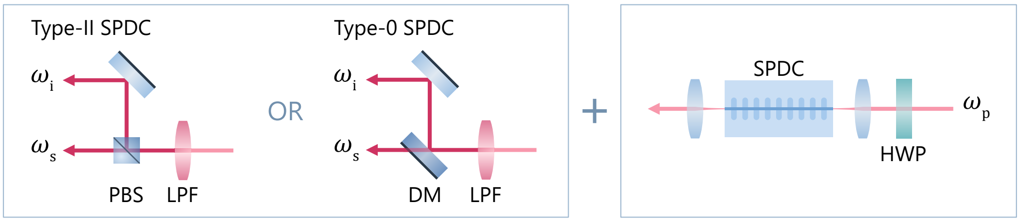

Figure 2.10: Simplified illustration of the basic experimental setup, required for degenerate and non-degenerate SPDC. (a) Classical waveguide characterization, and (b) the non-classical SPDC process. In dependence of the chosen phase-matching, degenerate type-II utilized a polarizing beam splitter (PBS) and non-degenerate type-0 employs a dichroic mirror (DM) for (a) overlapping the pump beams and (b) separating the photon pair, respectively.

schematically illustrated in Fig. 2.10. Depending on whether (almost) degenerate or non-degenerate SPDC is chosen, the classical alignment and characterization is performed via SHG or SFG. Following the optimization of this process, the measurement configuration is inverted by swapping the input and output ports of the experimental setup; the waveguide is pumped through the original out-coupling port, and the resulting SPDC photons are collected from the initial in-coupling port (compare Fig. 2.10 (a) with (b)).

In the scope of this thesis, both degenerate and widely non-degenerate SPDC will be characterized. In the first case, a type-II process is investigated. The two generated photons have approximately the same wavelength, but orthogonal polarizations. This allows for reliable separation of signal and idler with a polarizing beam splitter (PBS). The non-degenerate SPDC is realized via type-0 phase-matching. This means that both photons have the same polarization, but due to their widely separated wavelengths, they can be deterministically isolated using a dichroic mirror (DM). Therefore, the main difference in the two experimental setups is the optical device to separate the signal and idler photons.

Even though the separation could be realized in fiber, higher efficiencies can be achieved for separating the photon pair with a free-space component. The reason for this lies in the spatial mode differences for the two polarizations and unequal wavelengths, respectively. The TM mode travels more closer to the waveguide surface than the TE mode, and widely separated wavelengths strongly differ in their spatial mode size. Hence, the signal and idler photons are first separated in free-space before the fiber coupling of each path is optimized individually. Conversely, this means that the SHG as well as the SFG characterization is set up for two fiber-coupled input beams. While the two input fields that are required for SHG can origin from the same pump beam, two fiber ports are installed to prepare for the subsequent SPDC process. The two ports are overlapped via a PBS (or DM) before being coupled to the waveguide for the SHG (or SFG) characterization.

A few additional details are relevant for the nonlinear waveguide characterization:

1. Polarization control is required for every pump field in order to maximize the conversion efficiency. This is realized by inserting a half-wave plate (HWP) for each pump beam (compare Fig. 2.10). In practice, the type-II SHG measurements are performed using one input port only and adjusting the HWP for diagonal polarization. This way, the waveguide is simultaneously pumped with TE and TM polarization.
2. The intensity of the generated SHG/SFG beam might be low and often the exact phase-matched wavelengths are not known before the initial characterization. In order to align the out-coupling side to a power meter, a visible alignment laser can be beneficial. Its wavelength should be close to the SHG/SFG wavelength. This laser is overlapped with the pump beam and coupled into the waveguide. The in-coupling lens remains optimized for the pump beam, while the out-coupling lens is optimized for the visible alignment beam. When the visible laser is coupled through the waveguide and focused onto the power meter, the generated SHG/SFG signal is also detected. A short-pass filter (SPF) is used to filter the beam from the residual pump intensity.
3. For the classical characterization, the wavelength of the pump laser is scanned in the proximity of the expected phase-matched wavelength, while the generated beam is recorded with the power meter. The measured pump-wavelength dependent SHG/SFG intensity corresponds to the phase-matching spectrum of the waveguide.
4. For aligning the SPDC measurements, the generated classical beam serves as a stationary reference. The pump beam for SPDC is introduced from the opposite direction and aligned to overlap with the existing SHG/SFG beam. This facilitates coupling of the SPDC pump laser to the same waveguide. The photon pairs are filtered with a long-pass filter (LPF).

Besides the filtering, the newly defined out-coupling side (original in-coupling side) remains unchanged since it is already optimized for the SPDC photons. If the fiber coupling stages for the original pump lasers were aligned accurately, the signal and idler photons will be coupled into the fibers.

Non-classical investigation of single photons

Once the classical waveguide characterization is completed, the fiber-coupling stages which were connected to the pump lasers get connected to the SNSPDs for detection. To ensure clarity, the following chapters present a schematically simplified depiction of single-photon detection using SNSPDs. Fig. 2.11 illustrates the SNSPD icon which is employed in the experimental setup schematics. Specifically, the detectors are housed in a separate cryostat, where detection is achieved through flood illumination of the fiber-coupled signal. To account for the polarization-dependent detection efficiency, the input state is optimized for each measurement using an in-line fiber polarization controller. The electrical pulses from the SNSPD are amplified and processed by a time-tagging unit to quantify the detection events.

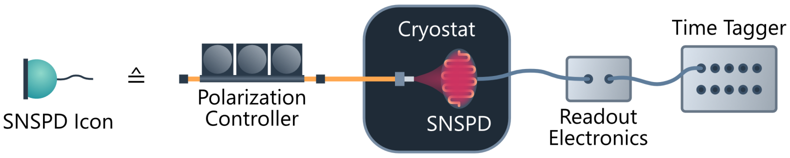

Figure 2.11: Single-photon detection with an SNSPD. The following illustrations of experimental setups use a simplified representation. The individual icon comprises the polarization controller, the actual SNSPD inside a dedicated cryostat, the readout electronics, and the time-tagging unit.

For the non-classical characterization, the signal and idler photons are detected with the SNSPDs. In this work, the SPDC process is always pumped with a pulsed laser. Therefore, a clear temporal correlation between the signal and idler counts can be detected. When optimizing the alignment, it is always advantageous to maximize the coincidence counts in order to avoid accidentally maximizing the coupling to a noise signal. Furthermore, the photon-pair generation can be verified by rotating the polarization of the pump beam. The SPDC efficiency is highly polarization dependent, so that the process can be ideally completely frustrated when the polarization is misaligned by 90°. Residual signal and idler counts for orthogonal polarization typically demonstrate an uncorrelated noise background. The characterization of the SPDC source comprises the measurement of different performance metrics, that are introduced in the following.

The source brightness

The brightness of an SPDC source is defined by the ratio of the coincidence rate $C_{\mathrm{s,i}}$ of signal and idler, divided by the pump power. In this work the pump power within the waveguide is approximated by the transmitted pump power P_{trans} that is measured behind the out-coupling lens. The source brightness is thus given by

$$B = \frac{C_{\mathrm{s,i}}}{P_{\mathrm{trans}}} \,. \tag{2.22}$$

In order to determine the in-waveguide pump power, the coupling efficiency must be known. In most experimental realizations, only the ratio of the transmitted pump power to the input power can be measured. This total transmission is comprised of the in- and out-coupling efficiency and the optical losses within the waveguide. Therefore, estimation of the coupling efficiency requires knowledge of the waveguide losses. Yet, established methods for loss characterization are often ineffective when deployed under cryogenic conditions, due to inconsistencies in the waveguide performance. This will be further elaborated upon in the discussion in Section 4.3.1, which explores the linear waveguide performance under cryogenic conditions.

The Klyshko efficiency

Since the SPDC photons are always created in correlated pairs, one photon is typically utilized to herald the existence of its counterpart. The efficiency of this heralding process strongly depends on the losses in the experimental setup. The photon pair travels through multiple optical components before signal and idler reach their detectors. The Klyshko efficiency represents the total losses in the signal or idler path [174], by taking the ratio of the coincidence rate to the single count rate of the other path. For example, the efficiency for the signal arm is given by [81]

$$\eta_{\mathrm{Klyshko,s}} = \frac{C_{\mathrm{s,i}}}{C_{\mathrm{i}}}\,, \tag{2.23}$$

while we can also define a combined, average Klyshko efficiency for both paths according to

$$\bar{\eta}_{\mathrm{Klyshko}} = \sqrt{\frac{C_{\mathrm{s,i}}^2}{C_{\mathrm{s}}C_{\mathrm{i}}}}\,, \tag{2.24}$$

where C_{s} and C_{i} are the signal and idler count rate, respectively. Consequently, this parameter defines the probability to detect a photon, given the condition that the corresponding herald photon was detected. This makes the Klyshko efficiency a decisive parameter for assessing the performance of the photon-pair source.

The coincidences-to-accidentals ratio

An additional measure for the quality of a photon-pair source is the coincidences-to-accidentals ratio (CAR). It defines the ratio of the true coincidence count rate to the accidental coincidence count rate from a pair source. A high CAR indicates strong temporal correlation and low noise. In the low photon-pair generation probability regime, the accidental rate of a pulsed source can be approximated by the product of the single count rates $C_{\mathrm{s}}C_{\mathrm{i}}$, normalized to the laser repetition rate R_{rep}. The CAR is then given by

$$\mathrm{CAR} = \frac{C_{\mathrm{s,i}}R_{\mathrm{rep}}}{C_{\mathrm{s}}C_{\mathrm{i}}}\,, \tag{2.25}$$

where $C_{\mathrm{s,i}}$ is the raw measured coincidence rate, which includes both the true coincidences and the accidentals.

The spectral purity

The joint spectral amplitude, as introduced in Eq. (2.15), describes the spectral properties of the SPDC source. Therefore, the JSA is directly related to the spectral purity, which represents the number of occupied frequency modes in the spectral distribution. This purity is limited by any spectral correlations of signal and idler. In order to analyze these correlations, a singular-value decomposition, or *Schmidt decomposition*, of the JSA can be performed [175–177]. The two-dimensional, normalized function can be decomposed as the sum of sets of orthonormal functions $\psi_k^*(\omega_\mathrm{s})$ and $\phi_k^*(\omega_\mathrm{i})$ weighted with individual amplitudes r_k [177]

$$f(\omega_\mathrm{s}, \omega_\mathrm{i}) \propto \sum_k r_k \psi_k^*(\omega_\mathrm{s}) \phi_k^*(\omega_\mathrm{i}) \, . \tag{2.26}$$

The effective mode number is then given by $K = 1/\sum(|r_k|^4)$ [176]. These modes are known as the *Schmidt modes*, as they are required to express the JSA. The mode number equals unity if only one mode is occupied, which corresponds to the photons being emitted in a pure state. The higher the effective mode number, the lower the spectral purity.

The second-order correlation function

The second-order correlation function $g^{(2)}$ characterizes the photon-number purity of the SPDC source. Due to the spontaneous character of SPDC, there is a non-zero probability for emitting multi-photon pairs. The correlation function $g^{(2)}(\tau)$ for characterizing a pulsed, single-mode state with zero time delay τ can be expressed in terms of the number operator $\hat{n}$ [155, p. 34]

$$g^{(2)}(0) = \frac{\langle \hat{n}(\hat{n}-1) \rangle}{\langle \hat{n} \rangle^2} \, . \tag{2.27}$$

The number operator measures the number of photons in one pulse. Hence, $g^{(2)}(0)$ represents a direct measure if the generated photons are bunched or anti-bunched [178]. Thereby, $g^{(2)}(0) < 1$ defines non-classical light [178]. To be more precise, $g^{(2)}(0) \leq 0.5$ constitutes the benchmark for single-photon generation, as $g^{(2)}(0) = 0.5$ corresponds to a two-photon Fock state [81]. For a spectrally pure SPDC source, the photon-number statistics follow a thermal distribution, thus the unheralded correlation function is given by $g_\mathrm{u}^{(2)}(0) = 2$. However, if more frequency modes are occupied, the detector measures the convolution of the individual thermal photon statistics. The higher the Schmidt number, the more the convolution approaches a Poissonian photon-number distribution and thus the $g_\mathrm{u}^{(2)}(0)$ approaches unity [179]. This quantity is directly connected to the effective mode number by $g_\mathrm{u}^{(2)}(0) = 1 + 1/K$ [176].

In practice, the unheralded and heralded $g^{(2)}$ functions are measured by inserting a balanced (50:50) beam splitter into the path whose photon statistics are characterized (i.e., the signal or idler path). We refer to the count rates measured for these two output ports of the beam splitter as C_1 and C_2. The count rate of the heralding photons is specified as C_3. We can then describe the unheralded correlation function as

$$g^{(2)}_{\mathrm{u}}(0) = \frac{C_{12} R_{\mathrm{rep}}}{C_1 C_2}\,, \tag{2.28}$$

where C_{12} are the two-fold coincidences and R_{rep} is the laser repetition rate. The heralded $g^{(2)}$ function is given by [81]

$$g^{(2)}_{\mathrm{h}}(0) = \frac{C_{123} C_3}{C_{13} C_{23}}\,, \tag{2.29}$$

with the three-fold coincidences C_{123}. The SPDC process is typically pumped with low optical power, so that the probability P for multi-photon events is much lower than for a single-photon pair, i.e., $P(n \geq 2) \ll P(n = 1)$. Under these conditions, the heralding process enables the realization of high photon-number purity, approximating an ideal single-photon source with $g^{(2)}_{\mathrm{h}}$ approaching zero.

Indistinguishability

The indistinguishability of the photons that are emitted from an SPDC source (e.g., from the signal and idler mode or from subsequent pulses) can be quantified with a Hong-Ou-Mandel (HOM) interference measurement [26]. If two perfectly identical photons are incident simultaneously on two input ports of an ideal 50:50 beam splitter, they interfere so that they always exit the beam splitter through the same output port [155, p. 46]. This principle is employed by combining the photons from different pulses on a beam splitter while tuning their relative time delay τ. The measurement of coincidences between the two output paths in dependence of the time delay results in the typical *HOM dip*. This dip is centered around $\tau = 0$, which represents the point of maximum overlap of the interfering photons. The visibility V_{HOM} of the HOM dip is given by the ratio of coincidences C at zero time delay compared to the coincidences for a temporal delay that is much larger than the bandwidth of the dip $\Delta\tau_{\mathrm{dip}}$

$$V_{\mathrm{HOM}} = 1 - \frac{C(\tau = 0)}{C(\tau \gg \Delta\tau_{\mathrm{dip}})}\,. \tag{2.30}$$

This visibility is directly related to the indistinguishability of the photons. Maximum visibility of 100 % can only be reached if there is never more than one photon in either input port and if those two photons are perfectly indistinguishable and in a pure state [155, p. 47]. If the normalized dip goes below the threshold of 0.5 for classical interference (corresponding to a visibility of $V_{\mathrm{HOM}} \geq 50\,\%$), the measurement verifies a non-classical input state. However, in general, this visibility is limited by any imperfections. This includes, for example, multi-photon events, the spectral overlap, the polarization, or the splitting ratio of the beam splitter.

The joint spectral intensity

The experimental measurement of the JSI is based on a frequency-resolved coincidence measurement. It requires knowledge of the individual signal and idler frequencies of a correlated pair. One common measurement technique is to employ a time-of-flight measurement. The photons travel through a dispersive medium, such as a fiber with large dispersion, and their arrival times at the detectors are correlated to their frequencies. However, this method is often limited in its spectral bandwidth as strong dispersion is usually only given for a few tens of nanometers. This limitation represents a challenge for the cryogenic investigation since the cooldown can result in large shifts of the signal and idler wavelengths in the range of 100 nm. A spectral characterization method that allows direct comparison of the room-temperature and cryogenic performance must provide broadband operation which covers this range. To adapt for this constraint, in this work, the JSI is measured with a home-built single-photon grating spectrometer. The detailed design is illustrated in the next section. The basic principle lies in mapping the photon frequencies to the reflection angle of a blazed grating. SNSPDs are used for detecting the reflected photons to enable single-photon sensitivity. This method is highly versatile, achieving broadband functionality by incorporating suitable broadband optics.

Single-photon grating spectrometer

This section provides an overview of the concept and design of the spectrometer which is employed for the spectral characterization of all SPDC processes that are discussed in the subsequent chapters. The spectrometer's working mechanism is equivalent to that of a tunable band-pass filter. One of these filters is inserted into the fiber-coupled signal and idler arm, respectively. The system transmits only a small section of the incident frequency spectrum at a time. This section can be tuned to collect the transmitted photons for each frequency interval over a chosen integration time.

Declaration

I was responsible for the conception and initial configuration of the spectrometer during my Master's project, achieving basic functionality. This initial methodology, however, suffered from limitations in reproducibility, which required further refinement. During my PhD research, I significantly enhanced the spectrometer's performance by upgrading the original open-loop actuators to closed-loop systems and developing advanced control software. The methodology and concept described in this chapter are presented for the completeness of this dissertation.

The spectrometer design is illustrated in Fig. 2.12. The signal or idler beam is collimated from the fiber and incident on a blazed grating. The grating decomposes the spectral distribution by mapping distinct frequency components to definite reflection angles. It is

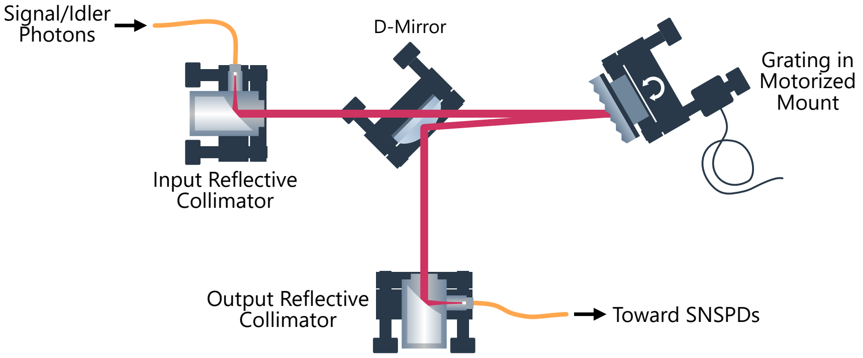

Figure 2.12: Experimental setup of the single-photon grating spectrometer. Reflective collimators ensure broadband and efficient fiber coupling. The horizontal angle of the grating is computer controlled to tune the back-reflected frequency components which are detected by an SNSPD.

aligned in Littrow configuration. This means that the diffraction angle of the first order, which provides highest efficiency, is equal to the angle of the incident beam. The grating is installed in a motorized mirror mount, which enables controlled scanning of the incident angle. Consequently, this results in tuning of the back-reflected frequencies. The grating mount is further slightly tilted downwards, which allows to tap off the back reflected frequency components using a D-shaped mirror and align them to a second collimator. Only the narrowband frequency interval from the spectrum, which is properly coupled into the single-mode output fiber, is transmitted through the complete setup. This fiber is connected to an SNSPD for detecting a spectrum in the single-photon range with extremely low noise.

Broadband functionality is ensured by utilizing reflective fiber collimators instead of collimation optics which are based on an optical lens. Lens-based fiber collimation is limited in its bandwidth since the dispersion of the lens results in different focal points for distinct wavelengths. The reflective collimators (RC04FC-P01, Thorlabs) employ silver-coated off-axis parabolic mirrors. In contrast to a lens, the focal length of a parabolic mirror remains constant over a broad wavelength range. The selected collimator is specified for an operation wavelength from 450 nm up to 2 µm with high reflection of $> 97\,\%$. Moreover, broadband functionality is given by the blazed grating (GR13-0616, Thorlabs). It is optimized for 1600 nm, but it demonstrates high grating efficiency of $> 90\,\%$ over a broadband range of more than 500 nm. Hence, the operation wavelength of the complete spectrometer is mainly defined by the connected fibers. We employ polarization-maintaining fibers (P1-1550PM-FC, Thorlabs), specified for high efficiency in the range from 1440 nm to 1625 nm.

The mirror mount which holds the blazed grating is equipped with a closed-loop piezo actuator (Picomotor actuator model 8311, mks Newport) to control the horizontal alignment. The vertical angle can be adjusted with a manual screw. The spectrometer operation requires a preceding calibration of the device to correlate the grating angles (i.e., the actuator positions) to the transmitted frequency components. For reproducible operation, closed-loop actuators are indispensable. An open-loop system exhibits hysteresis, which leads to an increasing offset that accumulates with each scan. This requires repeated calibrations and (often rather inaccurate) corrections for the accumulated offset.

The calibration is performed by connecting the input port to a tunable continuous-wave laser source and the output to a regular power meter. In order to start the calibration, at first, coupling is optimized for a wavelength which is expected to be part of the signal or idler spectrum, e.g., 1550 nm. The corresponding actuator position is referred to as the zero position of the spectrometer. Next, the calibration range and step size is defined, e.g., from 1520 nm to 1580 nm, in steps of 10 nm. The self-developed software relies on expectation values to estimate the positions for certain wavelength steps away from the zero position. Consequently, the laser wavelength is set to 1520 nm first, and the actuator will perform a scan over a small range around the expected position for this wavelength. The power meter detects a Gaussian intensity profile for the transmitted power in dependence of the scanned positions. The position yielding the maximum power corresponds to the position for the set wavelength. This process is repeated for every wavelength step, which results in a calibration curve that assigns a position value to each tested wavelength. This curve shows a linear trend and is thus fitted by a linear function to enable the subsequent spectral measurement over a continuous wavelength range. Moreover, the maximum transmitted power provides information about the wavelength-dependent spectrometer efficiency. Accurate alignment of the setup can cause each calibration step to provide a similar peak power, which verifies broadband operation with consistent efficiency. In case, the peak power exhibits a non-negligible wavelength dependency, this can be adapted for by correcting the measured single-photon spectrum for the efficiency curve.

For maximum flexibility, the spectrometer is mounted on a breadboard. In general, the performance can slightly vary if the device is moved and reoptimized. The typical fiber-to-fiber throughput of the complete device is (66 ± 2) % and the transmission bandwidth is (1.0 ± 0.1) nm when calibrated around 1550 nm. While this bandwidth defines the overall spectrometer resolution, the calibration reveals that 1 nm can be resolved with 260 individual steps using the piezo actuator. This results in a spectral reproducibility of less than 4 pm to set the central wavelength.

Cryogenic SPDC in the telecom range

3

Nowadays, most of the optical data transport relies on standard fused silica glass fibers, providing broadband transmission, high mechanical strength, and well-established manufacturing [180]. These fibers are optimized for long-distance communication due to their particularly low absorption losses at telecom wavelengths. Two frequency windows are commonly used for data communication since they represent the minima in the absorption band: the O-band (1260 nm – 1360 nm) and the C-band (1530 nm – 1565 nm). The telecom C-band corresponds to the global minimum, which is why most of modern infrastructure and commercially sold optical components are optimized for this range. Consequently, there is a strong demand for quantum light sources operating in this wavelength range. Moreover, superconducting single-photon detectors are available for highly-efficient operation around 1550 nm. The obvious first step on the route toward cryogenic SPDC was to start with the characterization of a waveguide which provides single-photon pairs in the telecom C-band.

At a glance
The process characterized in the following experiments is a type-II SPDC process which is pumped with a TE-polarized pulsed beam at a wavelength of approximately 778 nm. In the degenerate case, we create photons at 1556 nm with orthogonal polarizations:

$$778\text{ nm (TE)} \longrightarrow 1556\text{ nm (TE)} + 1556\text{ nm (TM)}$$

If the phase-matching of the waveguide is not optimized for degeneracy, the signal and idler wavelengths deviate from 1556 nm, while fulfilling energy conservation. If the signal wavelength is larger, the idler wavelength will be shorter than 1556 nm, and vice versa.

By implementing the measurement protocols detailed in Section 2.2, this chapter addresses the second research question: *How does cryogenic operation affect the Ti:PPLN platform?* This measurement series comprises the characterization of two separate Ti:PPLN samples. I cooled down one waveguide which was optimized for degeneracy at room temperature (RT) operation and compared the performance metrics at cryogenic temperature (CT) to the RT results (Section 3.2). This experiment provides valuable proof-of-principle insights into the performance of a cryogenic SPDC source in the Ti:PPLN waveguide platform. The main results include the characterization of the shift in the signal and idler wavelengths, the Klyshko efficiency, and changes in the effective length. This data is published in *Optica* in Ref. [139].

Declaration
These initial measurements are a direct follow-up to my Master's project, titled "Towards Cryogenic Parametric Down-Conversion in Lithium Niobate Waveguides". This study yielded the first observation of temporally correlated photon pairs at cryogenic temperatures, demonstrating proof-of-principle cryogenic SPDC. At this stage, the source efficiency remained severely limited with a Klyshko efficiency of approximately 1 %. As part of my PhD studies presented here, I repeated and expanded upon these earlier measurements.

Following the experiments verifying functionality of cryogenic SPDC, the process was tailored so that the source emits degenerate photons in the telecom C-band under cryogenic conditions (Section 3.3). Careful selection of the required poling period enabled the generation of indistinguishable photons from the source, which was verified by performing a Hong-Ou-Mandel interference measurement. The successful implementation of this experiment demonstrates well understanding of the temperature-dependent wavelength shifts of the signal and idler photons. The key findings of these experiments are published in *Physical Review A* in Ref. [140].

3.1 Experimental methods

The experimental setup is shown in Fig. 3.1 (a). In order to prepare the pump beam for the SPDC process, the signal from a pulsed infrared laser is up-converted via SHG. This is done using a commercial, bulk periodically poled MgO-doped lithium niobate crystal (MgO:PPLN), positioned inside a crystal oven. The oven allows tuning of the second-harmonic wavelength and ensures temperature stability. In this experiment, the temperature is set to 70 °C. The SHG crystal is pumped with an ultrashort pulsed infrared laser (Onefive Origami 15 LP, NKT Photonics). This laser has a central wavelength of (1556.4 ± 0.2) nm, a bandwidth of (11.81 ± 0.02) nm, a repetition rate of 80 MHz, and 191 fs pulse duration.

The generated second-harmonic spectrum exhibits a Gaussian shape with a central wavelength of (778.04 ± 0.01) nm and a bandwidth of (3.22 ± 0.01) nm (see Fig. A.1 in the appendix). For verifying general functionality of cryogenic SPDC, the exact pump wavelength and bandwidth are not relevant. Therefore, in the proof-of-principle measurement series, this beam is directly coupled into the cryogenic waveguide. In the degenerate measurement series, the SHG is additionally spectrally filtered using a $4f$-setup.[1] This is necessary to reduce the spectral bandwidth of the JSI and fine tune the signal and idler

---

[1] The $4f$-setup is implemented in a folded geometry to reduce the number of optical components. The beam is exposed on a blazed grating, positioned in the focal point of a cylindrical lens. A slit with variable width is positioned in the other focal plane, directly followed by a mirror. The mirror is tilted down slightly and a D-shaped mirror is used to separate the input and output beam. The spatial filtering in the Fourier plane results in uniform narrowing, without affecting the spectral and temporal shape. In contrast, a spectral band-pass filter would modify a Gaussian temporal profile to a sinc^2 shape.

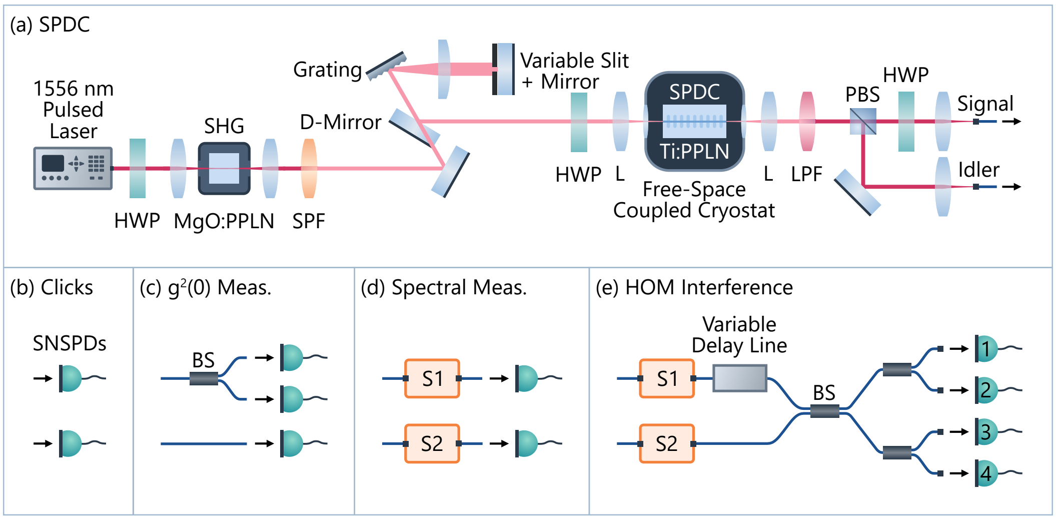

Figure 3.1: Experimental setup to perform the characterization of the cryogenic SPDC source. (a) The waveguide is positioned inside the free-space coupled cryostat and pumped with the SHG from a pulsed laser at 1556 nm. Signal and idler photons are separated by a PBS. (b) - (e) Characterization of the photon pairs using SNSPDs. The measurements include (b) the detector clicks, (c) the second-order correlation function $g^{(2)}(0)$, (d) the spectral properties, and (e) the Hong-Ou-Mandel interference. HWP: half-wave plate, MgO:PPLN: MgO-doped lithium niobate crystal, SPF: short-pass filter, LPF: long-pass filter, D-Mirror: D-shaped mirror, L: lens, (P)BS: (polarizing) beam splitter, S1/S2: grating spectrometer 1/2.

wavelengths for degeneracy, in order to increase the indistinguishability of the photons. The degenerate SPDC source is pumped with the filtered SHG light, featuring a reduced spectral bandwidth of (0.73 ± 0.05) nm at a central wavelength of (779.38 ± 0.01) nm. The (filtered) pump light is coupled to the cryogenic waveguide using two anti-reflection-coated aspheric lenses to optimize the coupling efficiency. Pump suppression is ensured using two long-pass filters (LPF), before the signal and idler photons are separated for subsequent analysis. The characterization of the photon pairs includes separate performance metrics which necessitate individual detector setups.

In order to measure the count rates of the signal and idler photons, two SNSPDs are connected (see Fig. 3.1 (b)). Thereby, each detector is set up as specified previously in Fig. 2.11. The second-order correlation function $g^{(2)}(0)$ is detected by inserting a fiber-coupled 50:50 beam splitter (BS) into one path (see Fig. 3.1 (c)). The spectral distributions of the signal and idler photons are detected by inserting one scanning grating spectrometer, as introduced in Fig. 2.12, into each port (see Fig. 3.1 (d)). As shown in Fig. 3.1 (a), an additional HWP is employed to rotate the signal polarization by 90°. This adjustment is required both to maximize the throughput of the grating spectrometer and to ensure optimal visibility for the subsequent Hong-Ou-Mandel (HOM) interference measurement. For the HOM measurement, again, the two spectrometers are connected to the signal and idler path, respectively (see Fig. 3.1 (e)). Here, the grating angles are set to a fixed value.

The spectrometers act as spectral band-pass filters in order to enhance the spectral purity of the photon-pair source. Furthermore, a variable delay line in one path is used to overlap the signal and idler photons temporally. Both photons then meet at the subsequent 50:50 beam splitter where they interfere. Afterwards, both paths are split again with another 50:50 beam splitter, before each signal is detected with an SNSPD. The additional splitting allows to not only record the decrease in coincidences, but also to verify the bunching of signal and idler into a single port of the interference beam splitter, when utilizing the SNSPDs as click detectors.

3.1.1 Waveguide design

As discussed in Section 2.1.3, the shift in the phase-matched signal (TE-polarized) and idler (TM-polarized) wavelengths can be approximated using the extrapolated refractive index data with the empirical correction term. The signal wavelength decreases and the idler wavelength increases by approximately 90 nm when changing the temperature from room temperature to 4 K. This trend is depicted in Fig. 3.2 for distinct poling periods (8.98 µm - 9.12 µm), which are fabricated on the proof-of-principle waveguide sample. For this sample, degeneracy is realized for an operation temperature in the range from approximately 230 K to 300 K.

The optical components for the single-photon routing and characterization are optimized for the telecom C-band. In order to maximize the efficiency of the experimental setup, the deviation from 1550 nm must be minimized. The smaller the poling period, the further the degeneracy point shifts toward lower temperatures. This results in less separation of the signal and idler wavelength under cryogenic conditions. For this reason, the smallest available poling period of 8.98 µm is chosen for the proof-of-principle measurement series. The same simulation is performed to define the required poling period of 8.81 µm for the degenerate waveguide, when pumping the process at approximately 779 nm. All design parameters of both waveguides under test are summarized in Table 3.1. The experimental operation temperatures were chosen for the wavelength simulations. The degenerate measurement series was performed about one year after the proof-of-principle measurements. The cryostat's minimum attainable temperature has gradually risen over this time, reflecting a degradation in the cooling performance of the system.

Table 3.1: Overview of the design parameters of both waveguide samples, including the poling period Λ, operation temperature T, the theoretical signal and idler wavelengths $\lambda_{s/i}$, and the waveguide length L (which corresponds to the fabricated poling length).

Sample	Λ [µm]	T [K]	λ_s [nm]	λ_i [nm]	L [mm]
Proof-of-principle	8.98	4.7 ± 0.1	1491.82	1626.13	24.4 ± 0.2
Degenerate	8.81	6.4 ± 0.1	1558.1	1558.1	24.3 ± 0.2

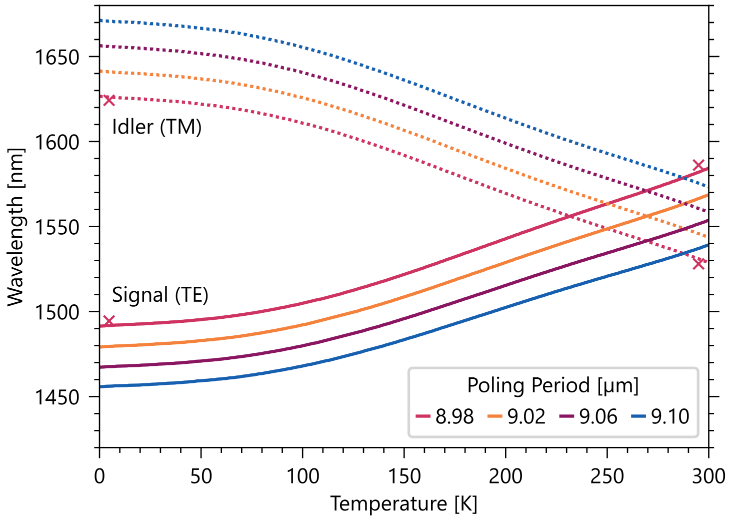

Figure 3.2: Simulated temperature-dependent shift in the signal and idler wavelength of type-II SPDC. The simulation is performed for different poling periods and the pump wavelength of 778.04 nm. The crosses show the spectral measurement results for the poling period of 8.98 µm (which are discussed in Section 3.2).

3.2 How it began - Proof-of-principle cryogenic SPDC

This measurement series comprises the characterization of the waveguide under room temperature and cryogenic temperature conditions. This allows for a direct comparison of the performance metrics at both 295 K and 4.7 K. The experimental results presented in this section were first recorded for the cryogenic waveguide and afterwards repeated at room temperature. This way, I verified that a waveguide was selected which demonstrates cryogenic functionality.

I cooled down the waveguide chip and carried out the classical characterization by performing SHG, as introduced in Section 2.2.3. Only individual waveguides provided a measurable phase-matching spectrum at 4.7 K. One of these waveguides, with the chosen poling period of 8.98 µm, was selected for the SPDC measurements.

3.2.1 SPDC performance metrics

At first, the count rates of the signal and idler detector were recorded. The transmitted pump power was kept at about (17.0 ± 0.6) µW within the measurements, to ensure an average photon-pair generation probability below 0.1. The detection of single and coincidence counts, together with the transmitted pump power, allowed calculation of the brightness (Eq. (2.22)), combined Klyshko efficiency (Eq. (2.24)), and CAR (Eq. (2.25)). Next, a 50:50 beam splitter was inserted into one path to detect the heralded second-order correlation function (Eq. (2.29)). This measurement was conducted for the signal photons and for the

Table 3.2: Correlation metrics of the SPDC source at room temperature and under cryogenic conditions. The table shows the source brightness, the Klyshko efficiency, the coincidences-to-accidentals ratio, and the heralded second-order correlation function.

T [K]	$B\ \left[\frac{\text{pairs}}{\text{smW}}\right]$	$\bar{\eta}_{\text{Klyshko}}$ [%]	CAR	$g_{\text{h}}^{(2)}(0)$
295	$(6.6 \pm 0.3) \cdot 10^5$	8.47 ± 0.03	53.9 ± 0.2	0.033 ± 0.004
4.7	$(3.3 \pm 0.1) \cdot 10^5$	4.77 ± 0.03	32.9 ± 0.2	0.07 ± 0.01

idler photons, respectively. The experimental results for these parameters are summarized in Table 3.2 for RT and CT operation.

The results reveal a consistent reduction under CT which indicates that the device performance is adversely affected by cryogenic operation. Furthermore, the signal and idler count rates exhibited an asymmetry during cryogenic characterization. Specifically, the count rate for the idler photons was $(61\,550 \pm 250)$ counts/s compared to $(217\,700 \pm 500)$ counts/s for the signal photons, while detecting (5520 ± 80) counts/s coincidences. This suggests the presence of polarization-dependent propagation losses within the waveguide. Increased internal losses might be caused by pyroelectricity and photorefraction. This phenomenon is analyzed in more detail in Chapter 4.

The transmitted pump power of (17.0 ± 0.6) µW was measured for an optical input power of (160 ± 5) µW in front of the in-coupling lens. This results in a low overall transmission of the pump beam of (10.6 ± 0.5) %. This value suggests that the cryogenic waveguide experiences strong propagation losses, which can contribute to the limited Klyshko efficiency of (4.77 ± 0.03) %. However, careful consideration is required when interpreting these results, as wavelength-dependent efficiencies can also influence the experimental outcome. The measurement of the JSI in the next section allows to estimate the effective length of the waveguide, which then enables a more comprehensive evaluation of the performance metrics in Section 3.2.3.

3.2.2 Spectral properties of signal and idler

In order to quantify the change in signal and idler wavelength at the different temperatures, the spectral properties were investigated using the grating spectrometers. The marginal spectra were recorded sequentially for the signal and idler paths. For the signal spectrum measurement, the idler path was directly connected to an SNSPD and one spectrometer was inserted into the signal path. I aligned this spectrometer to transmit the expected central signal wavelength. This initial alignment was necessary to set the temporal delays to measure signal and idler counts in coincidence, for maximizing the signal-to-noise ratio (SNR). The marginal spectra were measured with a step size of 0.5 nm. The measured spectra exhibit a Gaussian profile, which was fitted to obtain the central wavelengths

Table 3.3: Spectral metrics of the SPDC source at room temperature and under cryogenic conditions. The table comprises the central signal and idler wavelengths and bandwidths obtained from the marginal spectra and the effective length which is deduced from the JSI measurement.

T [K]	λ_s [nm]	λ_i [nm]	$\Delta\lambda_s$ [nm]	$\Delta\lambda_i$ [nm]	L_{eff} [mm]
295	1586.14 ± 0.12	1528.05 ± 0.04	32.08 ± 0.28	17.27 ± 0.10	7.3 ± 0.3
4.7	1494.45 ± 0.19	1624.24 ± 0.09	27.4 ± 0.5	17.94 ± 0.21	3.65 ± 0.05

and spectral bandwidths. The measurement data and Gaussian fit functions are shown in Fig. 3.3, and the fit parameters can be found in Table 3.3.

The measured central wavelengths are in very good agreement with the simulation, verifying a wavelength shift of about 90 nm. Nevertheless, it can be seen from Fig. 3.2 that the measured separation of the signal and idler wavelength is slightly larger at RT and slightly smaller at CT compared to the simulated values. Consequently, this offset cannot be attributed solely to inaccuracies in the phase-matching model; the observed wavelengths violate energy conservation if the previously measured pump wavelength of (778.04 ± 0.01) nm is taken as a fixed parameter. This points to an offset of the pump wavelength, which was characterized a few days prior to the marginal and JSI measurement. Unfortunately, the pump spectrum was not reviewed again after completion of the spectral SPDC measurements.

The central phase-matched wavelengths are indeed highly sensitive to small variations in the wavelength of the pump beam. The experimental signal and idler wavelengths exhibit a deviation in the range of 2 nm up to 4 nm, compared to the expected values when considering a pump of 778.04 nm. The direct comparison of the experimental and simulated values is given in Table 3.4. In order to evaluate the accuracy of the phase-matching model, the simulation is repeated utilizing the pump wavelength values which are required to fulfill energy conservation for the measured wavelengths. Specifically, energy conservation demands a pump wavelength of 778.28 nm at RT, and a wavelength of 778.32 nm at CT. These slight shifts, deduced from the marginal measurements, can be explained by thermal and mechanical instabilities in the experimental setup and the pump laser wavelength. Notably, the signal and idler wavelengths derived from the second simulation exhibit improved agreement with the experimental data (compare Table 3.4). Especially, the cryogenic values are in very good agreement, which verifies high accuracy of the extrapolated refractive index data in combination with the empirical correction term.

Subsequent to the marginal measurements, both spectrometer setups were connected to detect the JSI. To map the joint spectral distribution, a two-dimensional scan was employed. The idler spectrometer was stepped sequentially. At each wavelength setting, a complete scan of the signal range was recorded. The measured JSIs are visualized in Fig. 3.3. The integration time for every wavelength combination was chosen to be 30 s

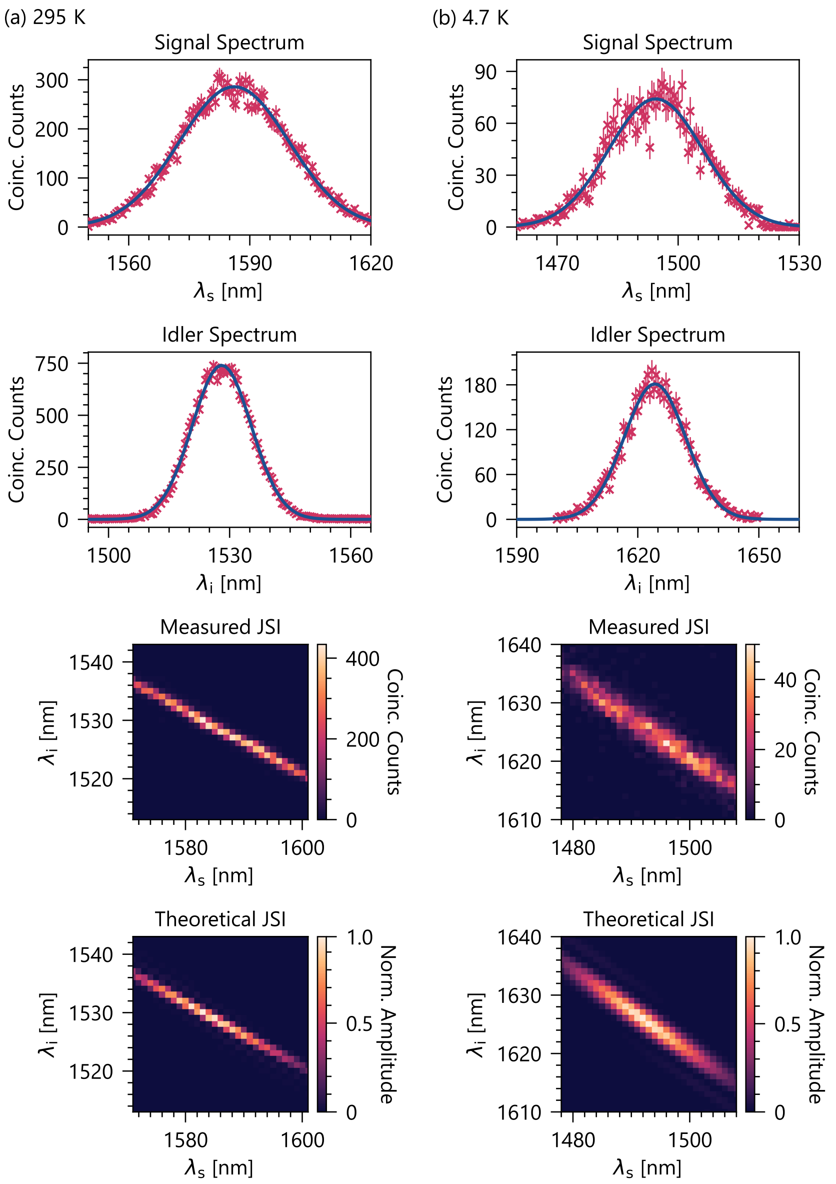

Figure 3.3: Comparison of the spectral measurement results for the signal and idler photons (a) at room temperature (295 K) and (b) at cryogenic temperature (4.7 K). The measured marginal spectra and JSI are shown together with the theoretical JSI. The solid lines in the marginal spectra represent Gaussian fits and the error bars correspond to Poisson errors.

Table 3.4: Comparison of the central wavelengths, which were extracted from the experimental marginal spectra, to the simulation values. The uncertainties of the measured wavelengths can be found in Table 3.3. The simulation was performed first for the pump wavelength of 778.04 nm that was measured several days prior to the marginals. The second simulation considers the pump wavelength which is deduced from the measured signal and idler wavelengths, which must fulfill energy conservation.

a) 295 K

	λ_s [nm]	λ_i [nm]
Measurement	1586.14	1528.05
Sim. $\lambda_p = 778.04$ nm	1581.99	1531.00
Sim. $\lambda_p = 778.28$ nm	1584.36	1529.72

b) 4.7 K

	λ_s [nm]	λ_i [nm]
Measurement	1494.45	1624.24
Sim. $\lambda_p = 778.04$ nm	1491.82	1626.13
Sim. $\lambda_p = 778.32$ nm	1494.05	1624.71

for the CT measurement. At RT, a reduced integration time of 20 s was chosen as the measurement featured significantly higher coincidence count rates. Both JSI measurements were performed with a wavelength step size of 1 nm, which resulted in a measurement time of up to 10 hours. Mechanical or thermal drifts within the free-space setup and fluctuations in phase-matching conditions cannot be entirely excluded over a duration of several hours. For this reason, the central signal and idler wavelengths and bandwidths (listed in Table 3.3) were extracted from the marginal spectra which required a recording time of approximately 20 min, and not from the JSI.

JSI simulation and effective length estimation

At both temperature regimes, the experimental JSIs exhibit an elongated elliptical profile, signifying strong spectral correlations between the signal and idler wavelengths. However, a distinct difference is observed in both the orientation angle and the width of the minor axis of the distribution. These changes are compared to the theoretical changes in the JSI which are expected during the cooldown. In order to simulate the JSI, the measured pump wavelength and spectral width, the poling period, and the extrapolated effective refractive indices are taken into account. As discussed in Section 2.1.3, the effective length of the waveguide incorporates localized perturbations in the refractive indices, that arise from the interplay among the photorefractive and pyroelectric effect. For this reason, the effective length is kept as a variable parameter, to perform an optimization until the simulation fits the measured JSI best. This way, the effective length is estimated from the JSI measurement.

The JSI corresponds to the absolute square of the JSA, which is given by the product of the pump distribution function and the phase-matching function (compare Eq. (2.15)). Since the pump spectrum exhibits a Gaussian shape, the simulation considers the following form of the pump distribution,

$$\alpha(\omega_\mathrm{s}+\omega_\mathrm{i}) = \exp\left[-\frac{((\omega_\mathrm{s}+\omega_\mathrm{i})-\omega_\mathrm{p})^2}{2\sigma^2}\right], \tag{3.1}$$

where σ is the standard deviation, directly related to the spectral bandwidth $\Delta\omega_\mathrm{p}$ of the pump beam, according to $\Delta\omega_\mathrm{p} = 2\sqrt{2\ln(2)}\sigma$. The temperature-dependent phase-matching function is given by

$$\Phi(\omega_\mathrm{s},\omega_\mathrm{i},T) = \mathrm{sinc}\left[\Delta k(\omega_\mathrm{s},\omega_\mathrm{i},T)\frac{L(T)}{2}\right], \tag{3.2}$$

with the effective length $L(T)$ that is treated as the optimization parameter. The simulation of the JSI is performed for a two-dimensional array of frequencies $(\omega_\mathrm{s},\omega_\mathrm{i})$, centered around $\omega_\mathrm{p}/2$. This frequency array is chosen to have the same resolution as the measurement to ensure maximum comparability. For every frequency pair, the pump distribution and phase-matching function are calculated. Next, the two amplitudes are multiplied and the absolute square is taken: JSI = $|\alpha(\omega_\mathrm{s}+\omega_\mathrm{i})\Phi(\omega_\mathrm{s},\omega_\mathrm{i},T)|^2$. This simulation is compared to the normalized two-dimensional measurement array, to determine the effective length, which results in the distribution that has the smallest deviation from the measured JSI.

Based on the simulations which best match the measurement data, the effective length is assumed to decrease from (7.3 ± 0.3) mm at RT to (3.65 ± 0.05) mm at CT. The corresponding theoretical JSIs can be found in Fig. 3.3. It can be seen that the reduction in effective length at cryogenic temperatures is consistent with a broadening of the phase-matching function and, consequently, the JSI. This broadening was clearly observed for the measured JSI. Moreover, the simulations verify the slight change in the measured orientation angle. This change mainly results from a variation in the slope of the pump distribution function when considering a different interval of signal and idler wavelengths. As the JSI is displayed in dependence of wavelength, instead of frequency, its angle depends on the central wavelengths. In contrast to the pump distribution, the phase-matching function exhibits only a marginal shift in orientation, resulting from variations in the group velocities of the interacting modes. These observations were verified by analyzing the two functions $\alpha(\omega_\mathrm{s}+\omega_\mathrm{i})$ and $\Phi(\omega_\mathrm{s},\omega_\mathrm{i},T)$ independently.

3.2.3 Evaluation of the proof-of-principle measurement series

The quantification of the effective length reduction facilitates a more comprehensive evaluation of the performance metrics derived from the correlation measurements (listed in Table 3.2). The brightness of a waveguide source scales linearly with the effective length of the sample [181]. In accordance with the observed 50 % reduction in effective length, the source brightness exhibits a decline by the same factor. The reduced brightness also affects the SNR of the source, which is evident in the Klyshko efficiency. From the equations given in Section 2.2.3, we can derive that these performance metrics are related via the coincidences-to-accidentals ratio, according to

$$\mathrm{CAR} = \frac{R_{\mathrm{rep}}}{P_{\mathrm{trans}}} \frac{\eta^2_{\mathrm{Klyshko}}}{B} \,. \tag{3.3}$$

The measurements were performed for the same repetition rate and transmitted pump power at RT and CT. This allows to rearrange this equation to yield the change in Klyshko efficiency as follows

$$\frac{\eta_{\mathrm{Klyshko,RT}}}{\eta_{\mathrm{Klyshko,CT}}} = \sqrt{\frac{\mathrm{CAR}_{\mathrm{RT}}}{\mathrm{CAR}_{\mathrm{CT}}} \frac{B_{\mathrm{RT}}}{B_{\mathrm{CT}}}} \,. \tag{3.4}$$

The relevant changes in the CAR and brightness, taken from Table 3.2, are (1.64 ± 0.02) and (2.00 ± 0.02), respectively. According to Eq. (3.4), this results in a change in the Klyshko efficiency of 1.81, which is just outside the error margins of the measured variation of (1.78 ± 0.02). The close agreement shows that the decrease in Klyshko efficiency is consistent with the reduced brightness at a constant noise level.

In fact, the measurements of Klyshko efficiency, CAR, and brightness are not independent, they all depend on various functions of coincidences and single counts from the signal and idler modes. These measurements alone are insufficient to conclusively attribute the observed variations to a decrease in effective length. This is because it is difficult to disentangle the interplay of noise, loss, and generation probability. Nevertheless, the changes in the performance metrics are certainly consistent with a reduction in the effective length by a factor of 2, as deduced from the spectral measurements. This was verified by measuring a change by the same factor ((2.00 ± 0.02)) in the brightness, which depends linearly on the effective length. Finally, the measurement of the heralded second-order correlation function quantifies the photon-number purity of the SPDC source. While the $g^{(2)}_{\mathrm{h}}(0)$ slightly increases from (0.033 ± 0.004) to (0.07 ± 0.01) at CT, the value remains well below the threshold of 0.5 for a two-photon Fock state, both at RT and CT. This verifies heralded single-photon generation under cryogenic conditions.

In conclusion, this measurement series demonstrated that Ti:PPLN waveguides for SPDC are compatible with cryogenic operation. Despite changing the operation temperature by almost two orders of magnitude, the source remained fully operational. Notwithstanding its functionality, a comparative analysis reveals that all cryogenic figures of merit are consistent with a twofold reduction in the SNR relative to RT performance.

The spectral analysis verified the expected wavelength shift of about 90 nm for the signal and idler mode. Since all optical components are optimized for the telecom C-band, strong deviations from 1550 nm result in increased optical transmission losses. However, the detected cryogenic wavelengths of approximately 1494 nm and 1624 nm are still covered by the specifications of most components, including the AR-coated lenses, the polarizing beam splitter, and optical fibers. Nevertheless, the substantial spectral separation of 130 nm between the cryogenic signal and idler wavelengths poses a challenge for collimation, as a single aspheric lens cannot optimize the beam profile for both modes simultaneously. This limits the achievable Klyshko efficiency.

The observed broadening of the JSI serves as a distinct signature of a reduced effective length. This decrease is attributable to photorefractive and pyroelectric effects, which become more pronounced at CT. As these effects can also increase the cryogenic propagation losses, they might have also caused the reduced cryogenic Klyshko efficiency. These phenomena are investigated further in the remainder of this work. While the degenerate measurement series, presented in the next section, aims to minimize wavelength dependencies by characterizing a degenerate SPDC source, Chapters 4 and 5 incorporate a more detailed investigation of the temperature-dependent material changes.

3.3 Tailoring the process - Cryogenic SPDC for degenerate photon pairs

This experiment concentrates on the characterization of a Ti:PPLN waveguide offering degenerate photon pairs at a cryogenic temperature of 6.4 K. The cryogenic investigation encompasses a comprehensive characterization of the phase-matching properties through an SHG and JSI measurement. This is followed by an evaluation of SPDC performance metrics. Finally, the indistinguishability of the generated photons is quantified through a HOM interference measurement. The experimental detector setups to carry out these measurements are displayed in Fig. 3.1 (b) - (e).

3.3.1 Classical characterization of the phase-matching

Prior to the cooldown, the propagation losses at 1550 nm of all waveguides were characterized at RT using the Fabry-Pérot-resonator method presented in [182]. The waveguide which exhibited the target poling period and minimal propagation losses was selected for cryogenic characterization. The average loss at RT was found out to be (0.09 ± 0.01) dB/cm for TE-polarized light and (0.07 ± 0.01) dB/cm for the TM-polarized beam.

The cryogenic waveguide was first characterized classically using a tunable CW pump laser, to determine the phase-matched second-harmonic wavelength. This value corresponds to the degenerate signal and idler wavelength, when the interaction is driven by a pump at exactly half the target wavelength. The SHG measurement was thus required to accurately define the pump wavelength for the subsequent SPDC measurements.

The measurement data for the cryogenic phase-matching spectrum is presented in Fig. 3.4. The phase-matching function for an ideal waveguide is expected to show a sinc^2 shape. However, the actual interaction inside the Ti:PPLN waveguide can be altered by fabrication imperfections, pyroelectricity, and photorefraction [88]. The exact shape can be modeled accurately by considering a nonuniform refractive index distribution along the waveguide. This results in a very slight asymmetry of the sinc^2 function, which takes into account small imperfections of the phase-matching. The fitting procedure employed for this analysis is presented in [131]. Fig. 3.4 illustrates that the measured spectrum is well-reproduced

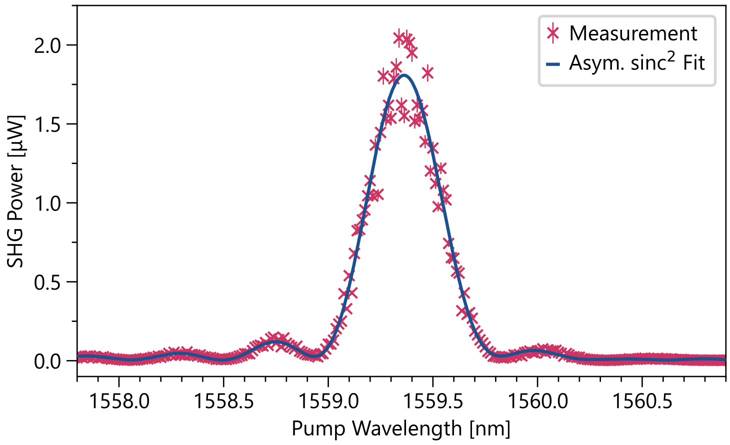

Figure 3.4: Measurement of the cryogenic phase-matching spectrum for the SHG process, pumped with (22.0 ± 0.1) mW. An asymmetric sinc^2 function is fitted to the measurement data. The fit considers a nonuniform refractive index distribution along the waveguide. The error bars correspond to an uncertainty of ± 3 %, which is specified for the employed power meter.

by the fit across the entire range. The fit reveals an effective length of (18.8 ± 0.3) mm, which corresponds to (77.4 ± 1.4) % of the total waveguide length. Consequently, the phase-matching condition is satisfied for this segment of the waveguide, validating high precision of the fabrication and exceptional regularity of the poling period. Moreover, the fitted spectrum is very close to an ideal sinc^2 function; the overlap is 99.9 %.

In comparison to the proof-of-principle measurement series, the cryogenic effective length of this waveguide is significantly longer. This indicates that the waveguide performance within this measurement was only marginally affected by parasitic influences of pyroelectricity and photorefraction. It is important to highlight that a key distinction between the two measurement series, presented in this chapter, lies in the thermal history of the two waveguide samples. While the waveguide from the proof-of-principle series had gone through multiple cryogenic cycles prior to data acquisition, the sample investigated here was freshly fabricated. This pristine waveguide had no prior exposure to thermal cycling or high optical pump powers. Consequently, both the spectral data and SPDC performance metrics represent its initial characterization during the very first cooldown. It cannot be ruled out that repeated thermal cycling may result in permanent modifications of the refractive indices or may induce charge carrier dynamics with exceptionally long relaxation times. Section 5.2 concentrates on evaluating the reproducibility of the cryogenic phase-matching.

In addition to the effective length of the waveguide, the fit function reveals the phase-matched wavelength of $\lambda_{\text{pm,meas}} = (1559.36 \pm 0.02)$ nm. The error is given by the absolute wavelength accuracy of the tunable laser source. In comparison to the expected value $\lambda_{\text{pm,theo}} = 1558.1$ nm, the measured wavelength is slightly higher. This discrepancy can arise from various factors. Since the simulation is based on the empirical refractive index correction, this induces an experimental uncertainty. However, the proof-of-principle measurement series has verified high accuracy of the model. The small deviation can be explained by marginal perturbations in the refractive indices. In fact, the phase-matched wavelength changed to $\lambda_{\mathrm{pm,meas}} = (1558.60 \pm 0.02)\,\mathrm{nm}$ in the second cooldown of this sample, which was performed more than a month later. This strongly indicates that pyroelectric charges gather randomly at different locations inside the crystal which results in slight phase-matching variations for every cycle. Consequently, spontaneous changes in the accumulating charges can be assumed to be the primary cause of the discrepancy between experiment and theory. Nevertheless, the experimental wavelengths are indeed very close to the theoretical result, which clearly demonstrates accurate fabrication and good predictability of the phase-matching under cryogenic conditions.

3.3.2 Measuring cryogenic SPDC photons

Next, the cryogenic SPDC process was pumped with the pulsed SHG from the bulk crystal, using the setup visualized in Fig. 3.1. I conducted the measurements of both the performance metrics and spectral properties following the same procedure used in the proof-of-principle measurement series (Section 3.2).

SPDC source performance

The waveguide was pumped with an optical power of $(66.1 \pm 0.1)\,\mu\mathrm{W}$, which featured a photon-pair generation probability of 0.01. The cryogenic performance metrics are summarized in Table 3.5. For a direct comparison, the data obtained for the proof-of-principle source have been included in this table. The results demonstrate a substantial improvement relative to the cryogenic proof-of-principle waveguide. Specifically, the brightness and Klyshko efficiency of the degenerate source are considerably higher by a factor of 1.8 and 2.9, respectively. The $g_{\mathrm{h}}^{(2)}(0)$ value is a factor of 4.1 smaller. Moreover, the brightness measured for this source is comparable to the result obtained for the proof-of-principle waveguide when it was operated under RT conditions. The Klyshko efficiency and second-order correlation function even surpass the RT performance by a factor of 1.6 and 1.9, respectively.

The spectral shape of the SHG phase-matching spectrum, that was close to the ideal function and yielded a high effective length of $(77.4 \pm 1.4)\,\%$, already indicated that this waveguide seems to be barely affected by photorefraction and pyroelectricity. The clear enhancement of the performance metrics, compared to the cryogenic proof-of-principle SPDC source, further support this conclusion.

Table 3.5: Correlation metrics of the cryogenic degenerate SPDC source, in comparison to the results for the proof-of-principle waveguide. The table shows the source brightness, the Klyshko efficiency, and the heralded second-order correlation function.

Sample	T **[K]**	$B\left[\frac{\text{pairs}}{\text{smW}}\right]$	$\bar{\eta}_{\text{Klyshko}}$ **[%]**	$g_{\text{h}}^{(2)}(0)$
Proof-of-principle	295	$(6.6 \pm 0.3) \cdot 10^5$	8.47 ± 0.03	0.033 ± 0.004
Proof-of-principle	4.7	$(3.3 \pm 0.1) \cdot 10^5$	4.77 ± 0.03	0.07 ± 0.01
Degenerate	6.4	$(6.0 \pm 0.3) \cdot 10^5$	13.62 ± 0.08	0.017 ± 0.002

Joint spectrum of signal and idler

The JSI was detected by scanning the two grating spectrometers and detecting the coincidence counts. To increase the number of coincidence counts when spectrally filtering with the spectrometers, the optical pump power was increased to (133 ± 1) μW. The spectral shape of the JSI is not expected to change significantly by increased multi-photon components. The long effective length yielded 1200 coincidence counts detected over the 4 s integration time at the intensity maximum. Furthermore, based on the narrow pump bandwidth, this JSI exhibited a narrower spectral bandwidth compared to the previous, non-degenerate JSI. Because the distribution was more localized, I could record the complete spectral profile by scanning an interval of roughly 15 nm with a step size of 0.2 nm, on both the signal and idler axes. The recorded JSI is displayed in Fig. 3.5, together with the marginal spectra for signal and idler. The marginals are extracted from the measurement data by taking the projection on the two axes.

The marginals were analyzed by applying a Gaussian fit in order to obtain the central wavelengths and bandwidths. The shape of the signal spectrum deviates from the Gaussian shape. This is caused by a slight asymmetry of the pump spectrum, which was induced by filtering with the $4f$-setup. The signal spectrum has a central wavelength of $\lambda_{\text{s}} = (1559.3 \pm 0.5)$ nm with a bandwidth of $\Delta\lambda_{\text{s}} = (6.33 \pm 0.12)$ nm. The idler spectrum is centered at the same wavelength $\lambda_{\text{i}} = (1559.3 \pm 0.6)$ nm with a smaller bandwidth of $\Delta\lambda_{\text{i}} = (3.26 \pm 0.03)$ nm. The errors of the central wavelengths equal the spectrometer transmission bandwidths and the uncertainties in the marginal bandwidths arise from the error in the spectrometer calibration together with the uncertainty of the Gaussian fit.

The JSI measurement reveals that the signal and idler wavelengths are identical and align closely with the previously measured phase-matched wavelength for SHG ((1559.36 ± 0.02) nm). I recorded the JSI approximately one week after the SHG spectrum during the same cooldown cycle, which means that the waveguide was maintained under cryogenic conditions. The results remained consistent, which verifies that no significant variation in the phase-matching did happen at a constant cryogenic temperature. This indicates that despite the potential buildup of pyroelectric charges during thermal transitions, this SPDC source permits stable operation, provided the operation temperature is held constant.

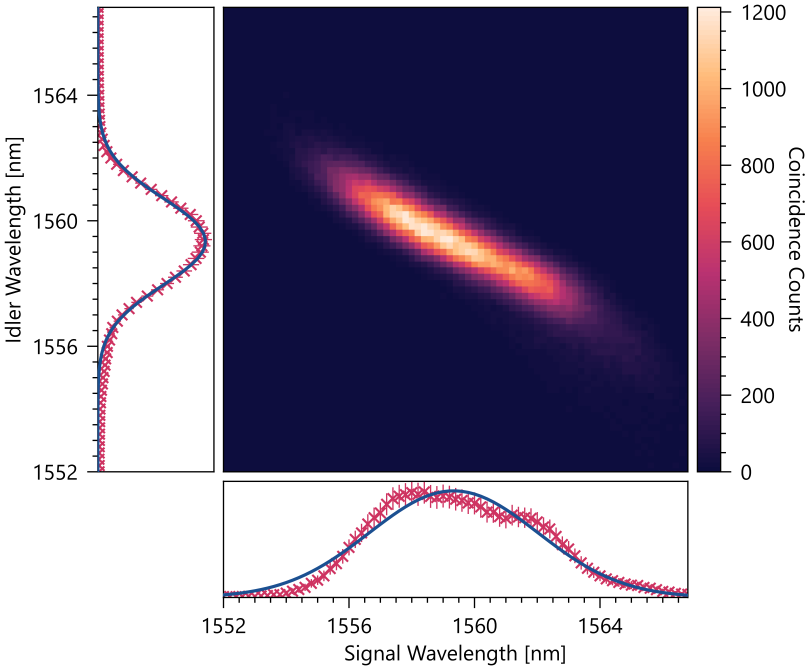

Figure 3.5: Measured JSI of the degenerate cryogenic SPDC source. The JSI is shown together with the marginal signal and idler spectra, corresponding to the projection on the two axes. A Gaussian fit is applied to the marginal data and the error bars correspond to Poisson errors.

Demonstration of indistinguishability

As it was already evident in the proof-of-principle measurement series, the difference in the signal and idler bandwidths results from the angular orientation of the JSI; this alignment is fundamental to the phase-matching properties of lithium niobate. These correlations in the signal and idler wavelengths limit the spectral purity of the SPDC source. In order to quantify the correlations, a Schmidt decomposition was performed for the measured JSI [177], by applying Eq. (2.26). This results in a Schmidt number of 2.72, which corresponds to a spectral purity of 0.37. One approach to increase this purity involves spectral filtering of the signal and idler modes. This was done for the HOM interference measurement.

Having shown that the SPDC source generates single photons under cryogenic operation and the signal and idler spectra overlap at the same central wavelength, the indistinguishability was verified in the other degrees of freedom by performing a HOM interference measurement. This experiment was conducted in the second cooldown of this sample. The repeated cooldown caused a slight change in the phase-matched wavelength ((1558.60 ± 0.02) nm), in comparison to the initial cooldown ((1559.36 ± 0.02) nm). This reduced the overlap of the signal and idler spectra in this experiment.

The spectrometers S1 and S2 were connected to the signal and idler path. They provide transmission bandwidths of $\Delta\lambda_\mathrm{s} = (0.96 \pm 0.03)$ nm and $\Delta\lambda_\mathrm{i} = (1.12 \pm 0.03)$ nm. These filters were aligned by first setting one filter to the central marginal wavelength and then fine-tuning the other grating to maximize the spectral overlap. Slight differences in the grating position and spectral bandwidth limit the visibility of the HOM measurement. The individual transmission spectra of the spectrometers were recorded using a tunable CW laser. The spectral overlap was 76.3 %, which sets an upper limit for the achievable visibility.

The spectrally filtered, polarization-aligned, and temporally overlapped photons interfere at the subsequent 50:50 beam splitter. While monitoring the coincidence counts between the two output paths is, in principle, sufficient to record the HOM dip, each path is split again by an additional beam splitter. This constitutes a convenient method to obtain enhanced information about the photon number. By measuring the twofold coincidence rates between all four detectors, both the HOM dip between the output ports and a simultaneous peak within each individual output port can be recorded. The latter represents the bunching of the photon pair into one output port of the beam splitter.

The single and coincidence counts were recorded while tuning the temporal delay $\Delta\tau$ in steps of 1 ps. In order to maximize total counts while compensating for potential power fluctuations, I performed 30 repeated scans and summed up the results. With an integration time of 30 s, the total data acquisition took approximately 8 h. The measurement data is presented in Fig. 3.6. In order to normalize the two axes, Gaussian fits were applied to all coincidence measurements. For clarity, only the averaged fits for the peak and dip are displayed. For perfect temporal overlap ($\Delta\tau = 0$), Fig. 3.6 shows a clear peak in the coincidences C_{12} and C_{34}, which demonstrates the bunching of the signal and idler photons into one output port. Concurrently, a significant dip appears in the twofold coincidences between the different interference paths. This dip drops below the threshold of 0.5, which further verifies non-classicality of the signal and idler mode. The HOM visibility is calculated from Eq. (2.30), considering the sum of all coincidence counts which were detected between the distinct interference ports $C = C_{13} + C_{14} + C_{23} + C_{24}$. According to Eq. (2.30), these total coincidences at zero time delay are put into relation to the coincidences beyond the dip (corresponding to the baseline of the fit). This results in a HOM visibility of $V_\mathrm{HOM} = (66.3 \pm 0.5)$ %.

The visibility is mainly limited by imperfections in the spectral filtering, as well as discrepancies in the signal and idler spectra. Although the spectrometer alignment was empirically optimized for maximum visibility, their transmission spectra were not perfectly overlapped; their overlap was 76.3 %. The observed reduction in visibility can be further explained by the finite extinction ratio of the PBS and slight deviations in its angular alignment relative to the axes of the waveguide chip. Due to these effects, a small fraction of photons is directed into the incorrect path. This results in both photons from the photon pair entering the interference beam splitter at the same input port, which affects the recorded coincidence statistics. Higher visibility might be achieved in future experiments by using identical band-pass filters and an additional half-wave plate in front of the PBS.

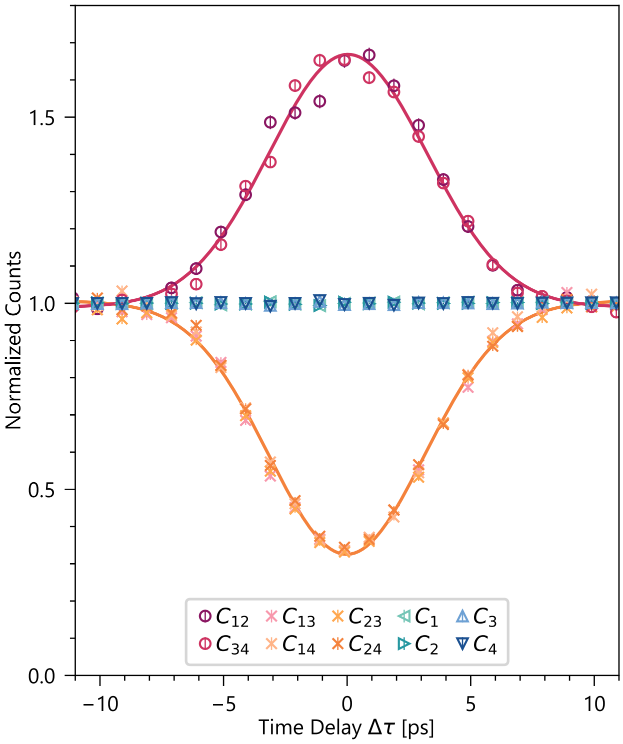

Figure 3.6: Hong-Ou-Mandel interference measurement of the cryogenic SPDC photons. The plot displays the normalized twofold coincidence counts and single counts of the SNSPDs in dependence of the time delay between signal and idler. Coincidences between two detectors within one beam splitter path are shown as circles, coincidences between detectors in opposite paths as crosses, and single counts are plotted as triangles. The error bars correspond to Poisson errors and the solid lines represent a Gaussian fit to the peak and dip, respectively.

3.3.3 Evaluation of the degenerate measurement series

In conclusion, the degenerate waveguide sample proved enhanced cryogenic performance relative to the proof-of-principle waveguide, which can be directly seen from the performance metrics listed in Table 3.5. The degenerate source exhibited significantly improved source brightness, Klyshko efficiency, and photon-number purity verified by a lower $g_{\mathrm{h}}^{(2)}(0)$ value of (0.017 ± 0.002). Furthermore, the results for the HOM interference measurement clearly demonstrated bunching of the signal and idler photons, by recording a visibility of (66.3 ± 0.5) %. This verified that the cryogenic SPDC source is capable of producing degenerate photons. Moreover, the experimental phase-matched wavelengths were in close agreement with the simulation, and the phase-matching function was approaching the ideal sinc^2 shape. This demonstrates accurate and uniform fabrication of the poling period, which is maintained under cryogenic conditions. Therefore, these results validate reliable control of this cryogenic nonlinear interaction.

3.4 Chapter conclusion

In this chapter, I have discussed the experiments that established the foundation for cryogenic nonlinear optics, specifically SPDC, in the Ti:PPLN platform. While the measurements detailed in Section 3.2 represented the proof-of-principle experiment, verifying basic functionality and spectral shifts induced by the thermal transition, the experiments discussed in Section 3.3 demonstrated that the phase-matched wavelength can be tailored to suit a customized wavelength interaction. This was shown by precise prediction of the poling period required to achieve efficient phase-matching for the cryogenic degenerate process. The close agreement of the measured phase-matched wavelengths with the simulation demonstrated the accuracy of the empirical model. This accuracy is indispensable because the poling period is the only parameter that can be used to tune the phase-matching in a cryostat, and, most importantly, it must be defined before the waveguide fabrication. Although no absolute cryogenic effective refractive indices are available and the phase-matching can be locally altered by pyroelectricity and photorefraction, the degenerate SPDC source provided a phase-matched wavelength within 1.5 nm of the design value.

The proof-of-principle measurements comprised a like-to-like comparison of the SPDC source performance at RT and CT. The analysis revealed a reduced performance at cryogenic conditions. Specifically, the source brightness, Klyshko efficiency, and CAR decreased by a factor of two. This results in a twofold reduction in the SNR compared to RT operation. Together with the spectral broadening of the JSI - which indicates a twofold reduction in the effective interaction length - this suggests that the decreased SNR originates from “frozen-in” pyroelectric and photorefractive charges. These perturbations can further increase the internal waveguide losses at CT, which can contribute to the reduced SNR. The substantial shift in signal and idler wavelengths during the cooling process prevents a direct comparison between the different operation temperatures. Consequently, it is more physically meaningful to evaluate the relative performance of various waveguides under identical cryogenic conditions, rather than attempting a direct comparison between their cryogenic and RT behavior.

To this end, I found that the degenerate waveguide outperformed the proof-of-principle one across all figures of merit at CTThe effects of photorefraction and pyroelectricity can cause unpredictable phase-matching alterations which might remain over long time scales. One essential difference between the two characterized waveguide samples can be found in their history. The data presented for the degenerate waveguide was recorded directly after fabrication. However, the proof-of-principle waveguide had a long history of prior exposure to both thermal cycling and high optical pump power. It is reasonable to assume that earlier experiments may have led to permanent changes in the refractive indices. This assumption is further supported by the observation that the proof-of-principle waveguide exhibited a relatively short effective length (approximately 30 % of the total length) during RT operation, which was performed subsequent to the cryogenic measurements.

The observations from these measurement series indicate that the cryogenic waveguide is prone to experience photorefractive and pyroelectric damage, causing inhomogeneous electric field distributions. As the charge carrier mobility decreases at CT, the induced charge fields “freeze in”, making it increasingly difficult to dissolve them. The electric fields result in refractive index modifications, causing unwanted phase shifts and thus phase-matching distortions. Furthermore, these alterations manifest themselves in the observed reduced effective length, or spectral deviations from the expected sinc^2 shape. An additional possible consequence are increased optical waveguide losses, as changes in the refractive index profile affect the capability of the in-diffused waveguides to confine the light. If the refractive index changes are sufficiently strong, they act as scattering centers and waveguiding is no longer ensured. The photons are then diverted into the substrate, resulting in increased transmission losses and distortions in the spatial mode profile. Consequently, the photon propagation is increasingly perturbed by trapped electrical charges, leading to degraded waveguide performance at cryogenic temperatures.

Despite the discussed limitations, one key finding of this chapter is that cryogenic SPDC in Ti:PPLN waveguides is achievable and capable of high performance, provided that the operation parameters are carefully optimized. This optimization might include limiting optical pump power and photon energy, restricting phase-matching to specific polarization, or managing the durability constraints of the waveguide. For this reason, the subsequent chapter provides an extended investigation of the underlying factors influencing the cryogenic performance. This involves examining the roles of wavelength and polarization, identifying asymmetries in the spatial modes of TE- and TM-polarized light, and assessing the total cryogenic waveguide throughput.

Widely non-degenerate frequency conversion at cryogenic temperatures

4

As shown in Chapter 3, titanium in-diffused waveguides in lithium niobate enable type-II SPDC in the telecom range under cryogenic temperatures. The performance, however, is affected by photorefraction and pyroelectricity. The susceptibility of the waveguide to these effects is highly dependent on the specific nonlinear optical process and the waveguide characteristics. Photorefraction, on the one hand side, can be typically described by a definite intensity threshold. Nevertheless, this threshold cannot be generalized. It varies for different waveguide samples, depending on the number and density of impurity centers. On the other hand, pyroelectricity has a spontaneous character. The accumulating charges gather randomly at different locations inside the crystal. Consequently, also the fraction of charges which experience a discharge varies for repeated cooldown cycles, resulting in an arbitrary charge distribution at CT. These effects certainly add an unpredictable ingredient to the overall cryogenic performance of the Ti:PPLN waveguides.

Notwithstanding this spontaneous nature, certain general physical principles are known to influence the degree of the two effects. Photorefraction is generally observed for TM- and TE-polarized light, but the change in the extraordinary refractive index (affecting TM polarization) is much larger compared to the ordinary one (affecting TE polarization) [169]. In addition, the photorefractive intensity threshold decreases with increasing photon energy [169]. Moreover, the pyroelectric effect results in changes in the spontaneous polarization, which is aligned with the crystalline *c*-axis [88]. As a consequence, the arising electric fields are oriented in this direction and also mainly affect the TM-polarized modes.

At a glance
The cryogenic process characterized in this experiment is a non-degenerate type-0 SPDC process, where all fields are TM-polarized. The process is pumped with a pulsed beam of approximately 590 nm which is generated in a separate, heated waveguide using SFG. The phase-matching of the cryogenic waveguide is optimized so that the created signal and idler photons have a central wavelength of around 1556 nm and 950 nm:

$$590\text{ nm (TM)} \longrightarrow 1556\text{ nm (TM)} + 950\text{ nm (TM)}$$

This cryogenic NLO process is particularly susceptible to distortions, which are induced by both effects. We will explore the cryogenic performance of this widely non-degenerate frequency conversion by implementing both type-0 SFG and SPDC. For lithium niobate, type-0 phase-matching - utilizing TM-polarized modes exclusively - accesses the largest element of the second-order nonlinear susceptibility tensor (d_{33}) [108]. This means that the type-0 process is expected to provide stronger conversion efficiencies than the previously characterized type-II interaction. However, while we rely on successful mode guiding for TM polarization, especially this polarization is more strongly affected by both effects, than the TE-polarized modes. Moreover, the NLO process either generates a visible beam at 590 nm (SFG), or is pumped by visible light (SPDC). In order to avoid photorefractive damage, the optical power of this high-energy beam must be kept at a low level.

The specific wavelength combination can be of interest for quantum teleportation experiments, in which the information of a photon from a quantum dot could be transferred to the telecom range [56, 57, 61]. Furthermore, in the scope of this thesis, this nonlinear process was actively chosen due to its enhanced susceptibility to photorefraction and pyroelectricity, in comparison to the previously characterized type-II interactions. The results significantly deepen the understanding of how cryogenic conditions influence the lithium niobate properties and provide insights into the achievable performance limits. The primary findings discussed here are published in *Optics Express* in Ref. [141]. This chapter maintains the structure of this publication, but contains expanded data sets and more detailed methodological and technical explanations.

The experimental setup utilizes two distinct Ti:PPLN waveguides which are designed to phase-match the same wavelength interaction, but at different operation temperatures. To drive the cryogenic SPDC, the visible pump light is first generated via SFG, as no laser source emitting at the target wavelength was available. The pump light generation is implemented in a waveguide housed within a high-temperature crystal oven. This waveguide sample is dedicated exclusively to performing SFG at elevated temperatures, to mitigate photorefractive damage. This process is characterized for both CW and pulsed operation. As both waveguides employ the same phase-matched wavelengths, the observations for the heated SFG serve as a comparative framework and can be adopted for the cryogenic waveguide. The second waveguide sample is the primary device under test which is solely operated within the free-space coupled cryostat. This sample is characterized according to its linear transmission, the nonlinear SFG phase-matching, and finally its SPDC efficiency.

This chapter is organized as follows. First, the complete experimental methods are introduced, including the optical setups and the waveguide design for both samples. Next, the operation of the actively heated waveguide is described, including its characterization and pump light generation for SPDC. These measurements are followed by the investigation of the cryogenic waveguide with regard to its linear and nonlinear properties. Finally, the cryogenic chip is pumped with the SFG from the heated chip and the properties of the SPDC photons are analyzed.

4.1 Experimental methods

The complete experimental setup is depicted in Fig. 4.1 and can be separated into three main parts: (a) the heated pump light generation via SFG, (b) the linear and nonlinear characterization of the cryogenic waveguide, and (c) the cryogenic SPDC process. Fig. 4.1 (d) illustrates the single-photon grating spectrometer which is inserted into the cryogenic SPDC setup for recording the JSI. First, the three individual setup designs are discussed in detail. This is followed by a specification of the waveguide sample designs, completing the description of the experimental methods. Finally, the results obtained from the three core experiments are presented and analyzed in Sections 4.2 to 4.4.

4.1.1 Pump light generation

The pump light generation is shown in Fig. 4.1 (a). The crystal oven is employed to fine-tune the phase-matching to achieve maximum conversion at 590 nm. The operation temperature can be tuned up to 210 °C with a stability of 0.01 °C. The poling periods span from 8.99 µm to 9.11 µm while the central period is optimized for about 175 °C. This allows, on the one hand side, to tune the temperature in both directions and on the other hand side, to chose from multiple poling periods to optimize the result.

For the SFG process, two laser beams are coupled into the waveguide. The first laser is a near-infrared (NIR) CW laser that is tunable from 910 nm to 980 nm with a maximum output power of about 80 mW (CTL 950, TOPTICA Photonics). In a first test, this laser is combined with a second tunable CW laser emitting in the telecom C-band (T500S, EXFO) for characterizing the phase-matching properties. This measurement is performed with two CW lasers since the narrow spectral bandwidth allows to resolve the phase-matching spectrum without significant broadening due to the laser bandwidths. The wavelength of the telecom laser is fixed to 1556 nm, while the wavelength of the NIR laser is scanned. Following this nonlinear characterization, the telecom CW laser is exchanged by the pulsed femtosecond laser, in order to generate the pulsed pump light for SPDC. This pulsed laser was also used to pump the SHG in the earlier measurements described in Chapter 3 (Onefive Origami 15 LP, NKT Photonics). This laser has a central wavelength of (1556.4 ± 0.2) nm, a spectral bandwidth of (11.81 ± 0.02) nm, and a repetition rate of 80 MHz. The pulsed wavelength is not tunable. For this reason, the telecom CW laser in the first experiment is set to the same wavelength as the pulsed laser, in order to obtain comparable results in both measurements.

The pulsed laser is further spectrally filtered with a $4f$-setup to decrease its spectral bandwidth while increasing the pulse duration (see Fig. 4.2). Although the filtering reduces the available pump power, this process increases the generated SFG intensity by creating a better match of the interacting bandwidths and increasing the temporal overlap with the CW laser. This is critical since the temporal overlap is the factor that represents the major constraint on the efficiency.

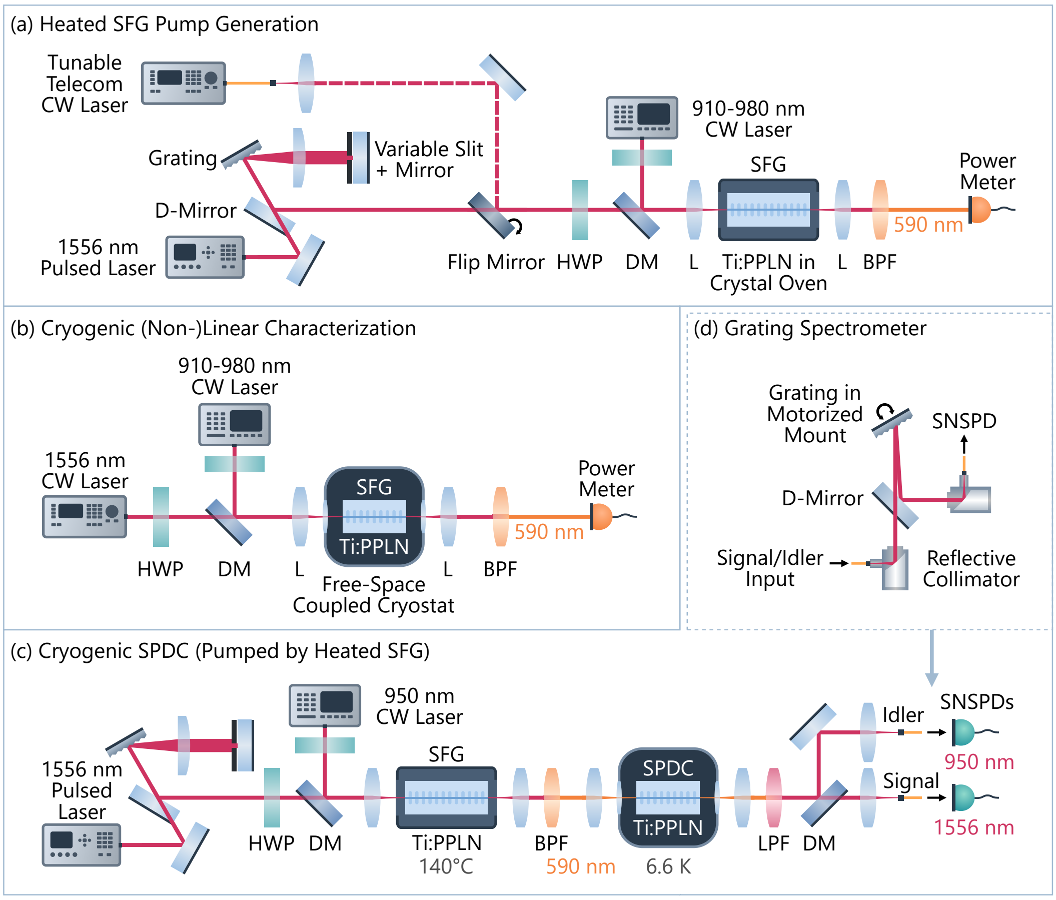

Figure 4.1: Experimental setups to characterize non-degenerate nonlinear frequency conversion. (a) SFG is performed in the heated waveguide to characterize its performance and to generate the pump light for the SPDC experiment. (b) Next, the CW SFG is repeated for the cryogenic waveguide to investigate the waveguide quality. (c) Finally, both setups are combined to couple the SFG from the heated waveguide into the cryogenic chip to pump SPDC. (d) The spectral properties of signal and idler are characterized by using one grating spectrometer setup in each arm. D-Mirror: D-shaped mirror, HWP: half-wave plate, DM: dichroic mirror, L: aspheric lens, Ti:PPLN: periodically poled titanium in-diffused waveguides in lithium niobate, BPF: band-pass filter, SPF: short-pass filter, SNSPD: superconducting nanowire single-photon detector.

The polarization in each path is controlled with a HWP to provide TM polarization, before both the NIR and the telecom laser are overlapped with a long-pass DM. Both beams are coupled together into the heated waveguide with an uncoated aspheric lens with a focal length of 13.9 mm. The aspheric lens on the out-coupling side is AR-coated for the visible range, has a focal length of 8.0 mm, and a high numerical aperture of 0.5 to ensure all generated light is collimated. On the out-coupling side, two SPFs at 850 nm are used to filter out the pump light. In addition, a BPF is set up, consisting of one SPF at 650 nm and one LPF at 550 nm. This filter combination is required to ensure any higher harmonic light from the

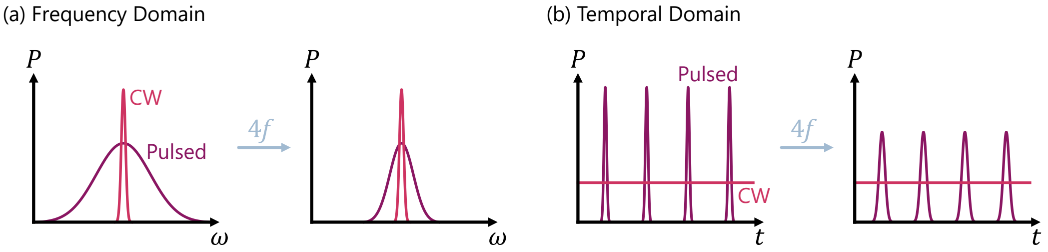

Figure 4.2: Illustration of the spectral and temporal transformation of the pulsed beam within the $4f$-configuration. (a) The spectral bandwidth is decreased, reducing the mismatch with the CW bandwidth. (b) The pulse duration is increased, providing an enhanced, albeit still limited, temporal overlap with the CW laser.

two lasers is filtered out as well. Without these filters, especially the SHG from both lasers around 778 nm and 475 nm will cause additional noise in the setup. Further details for the keen experimental scientist on the pump generation can be found in Appendix A.4.1.

4.1.2 Cryogenic waveguide characterization

The waveguide sample optimized for cryogenic operation is positioned inside the free-space coupled cryostat. During the measurement series presented in this chapter, the base temperature at the sample stage was about (6.6 ± 0.2) K. Before operating the cryogenic chip as an SPDC source, the cryogenic waveguide modes, transmission and phase-matching are evaluated. The experimental setup for this measurement is similar to the setup used for the heated SFG process and is shown in Fig. 4.1 (b). Both CW lasers are coupled into the chip, this time using an achromatic, aspheric lens with longer working distance (focal length of 15 mm). The minimum distance between the waveguide chip and the lens, positioned outside of the cryostat, is defined by the position of the cryostat window. The generated SFG light is out-coupled with another achromatic lens (focal length of 15 mm), AR-coated in the visible range. The same filter combination as in the heated experiment is used.

4.1.3 Cryogenic SPDC

In order to operate the cryogenic waveguide as an SPDC source, both setups are combined to pump this waveguide with the pulsed SFG signal (see Fig. 4.1 (c)). To mitigate optical loss associated with fiber coupling, the two setups are connected via a free-space link spanning approximately 2.5 m. The generated photon pairs are first filtered by LPFs at 850 nm and then split by a DM that cuts at 1180 nm. The signal and idler photons are coupled into PM single-mode fibers each and detected by SNSPDs. Both, detectors and the attached fibers in the cryostat are optimized for an operation wavelength of 1550 nm. This limits the detection performance for the idler photons around 950 nm, so that this path is expected to exhibit higher losses.

In order to characterize the spectral properties of the SPDC photons, the two spectrometers are used, as shown in Fig. 4.1 (d). For these experiments, one spectrometer is kept unchanged since it is already optimized for 1550 nm, but the second one is adjusted to be operated around 950 nm. This includes exchanging the blazed grating and connected PM fibers. The new grating is optimized for 750 nm instead of 1600 nm and specified to feature high efficiency around 950 nm. Moreover, the python code to perform the calibration was expanded in its functionality to be operated with the tunable 950 nm laser. The calibration reveals that the two spectrometers have a Gaussian transmission profile with unequal bandwidths of $\Delta\lambda_\mathrm{s} = (0.92 \pm 0.01)$ nm and $\Delta\lambda_\mathrm{i} = (0.52 \pm 0.03)$ nm. This is because the two gratings have a different number of grooves. The spectrometers are first used to detect the signal and idler marginal spectra and finally to measure the JSI.

4.1.4 Waveguide design

Both waveguide samples used for this measurement series are optimized to phase-match the wavelength interaction 1556 nm + 950 nm → 590 nm when all fields are TM-polarized, but at different operation temperatures. As stated in Section 2.1.3, the simulation of the effective refractive indices using RSoft provides good accuracy for ambient conditions. We can thus directly calculate the poling period for the heated waveguide. The calculations for cryogenic temperatures, however, rely on the low-temperature extrapolation. For the previously investigated type-II process, I could account for the discrepancy between simulation and experiment using the empirical correction term. Since this correction is applied to the linear combination of all three involved refractive indices, it is not possible to use the same term for the type-0 process.

From the previous measurements it was not feasible to extract an individual correction for the ordinary and extraordinary refractive indices. As will be demonstrated in Section 5.1.3, non-degenerate type-0 phase-matching can indeed be utilized to experimentally estimate the Sellmeier equations for our waveguides. This specific method is reserved for that later section. It is important to note here, that the simulated extraordinary refractive indices closely match the ones that can be derived from the cryogenic experiment. For this reason, I decided to go with the unchanged effective refractive indices for the fundamental modes TM_{00}, as I got them from the RSoft simulation. Based on this simulation data, I calculated the required cryogenic poling periods Λ for the upcoming experiments, according to

$$\frac{1}{\Lambda(T)} = \frac{n_{\mathrm{TM00}}(\lambda_\mathrm{p}, T)}{\lambda_\mathrm{p}} - \frac{n_{\mathrm{TM00}}(\lambda_\mathrm{s}, T)}{\lambda_\mathrm{s}} - \frac{n_{\mathrm{TM00}}(\lambda_\mathrm{i}, T)}{\lambda_\mathrm{i}} \,. \tag{4.1}$$

The chip operated in the crystal oven has a total length of 40 mm. The poling periods span from 8.99 µm to 9.11 µm and are chosen so that the central one phase-matches 1556 nm + 950 nm → 590 nm at a temperature of 175 °C. The cryogenic chip has a length of 22.9 mm.[1]

---

[1] One end facet was partly broken during fabrication and the sample was shortened to this length, which is just long enough to be coupled cryogenically using the long working distance lenses.

This sample has four different poling regions. Among others, two waveguide groups are poled to phase-match the type-0 interaction at RT. They have a period of 9.35 µm and 9.40 µm, respectively. Another region, consisting of five waveguide groups is optimized for CT phase-matching at 5 K. These poling periods span from 9.58 µm to 9.70 µm. The end facets of both waveguide samples possess an AR coating, enabling high transmission (> 99 %) for about 950 nm and 1550 nm on the in-coupling side and high transmission around 590 nm on the out-coupling side.

Spatial waveguide modes

All waveguides on both chips are chosen to have a small width, defined by a titanium strip with a width of 5 µm. This limits the number of higher order spatial modes that are supported by the waveguides. As discussed in Section 2.1.2, Ti:PPLN waveguides permit multiple spatial modes for wavelengths shorter than approximately 1000 nm. This means that the waveguide is multi mode for the idler photon around 950 nm. By choosing a small waveguide width of 5 µm, the number of higher order spatial modes can be limited. I simulated the guided spatial modes for all three interacting wavelengths using RSoft for both operation temperatures of 175 °C and 5 K (see Fig. 4.3). Independent on the temperature, the number of modes is the same and these modes are very similar in size and shape. The modes are shown together with their effective refractive indices n. These are reduced at cryogenic temperatures in the second decimal place. This reduction directly results from the strong temperature dependence of the extraordinary refractive index. However, the refractive index contrast between the in-diffused titanium and the surrounding lithium niobate remains mostly unchanged. The simulated modes thus remain similar as well.

Since the chosen wavelengths are widely non-degenerate and the Ti:PPLN waveguides provide low confinement, there is a strong difference in size for the fundamental modes TM_{00} (see (a), (b), (d) in Fig. 4.3). The spatial overlap of three modes E_1, E_2, and E_3 is given by

$$\eta_{\text{overlap}} = \frac{\left(\iint E_1 E_2 E_3 dA\right)^3}{\left(\iint E_1^3 dA\right)\left(\iint E_2^3 dA\right)\left(\iint E_3^3 dA\right)} . \tag{4.2}$$

To calculate the overlap from the simulated modes, the integral is carried out by summing over the matrix elements. This results in the following approximation for the three-mode overlap

$$\eta_{\text{overlap}} \approx \frac{\left(\sum_{x,z} E_{1,x,z} E_{2,x,z} E_{3,x,z}\right)^3}{\left(\sum_{x,z} E_{1,x,z}^3\right)\left(\sum_{x,z} E_{2,x,z}^3\right)\left(\sum_{x,z} E_{3,x,z}^3\right)} . \tag{4.3}$$

When comparing the three fundamental modes that are phase-matched for the chosen interaction, this results in an overlap of 23.0 % at 175 °C and 22.9 % at 5 K. This overlap sets a theoretical upper limit for the overall achievable conversion efficiency of the SFG and SPDC process, when only considering the spatial mode overlap.

(I) Spatial modes of the heated waveguide at 175°C

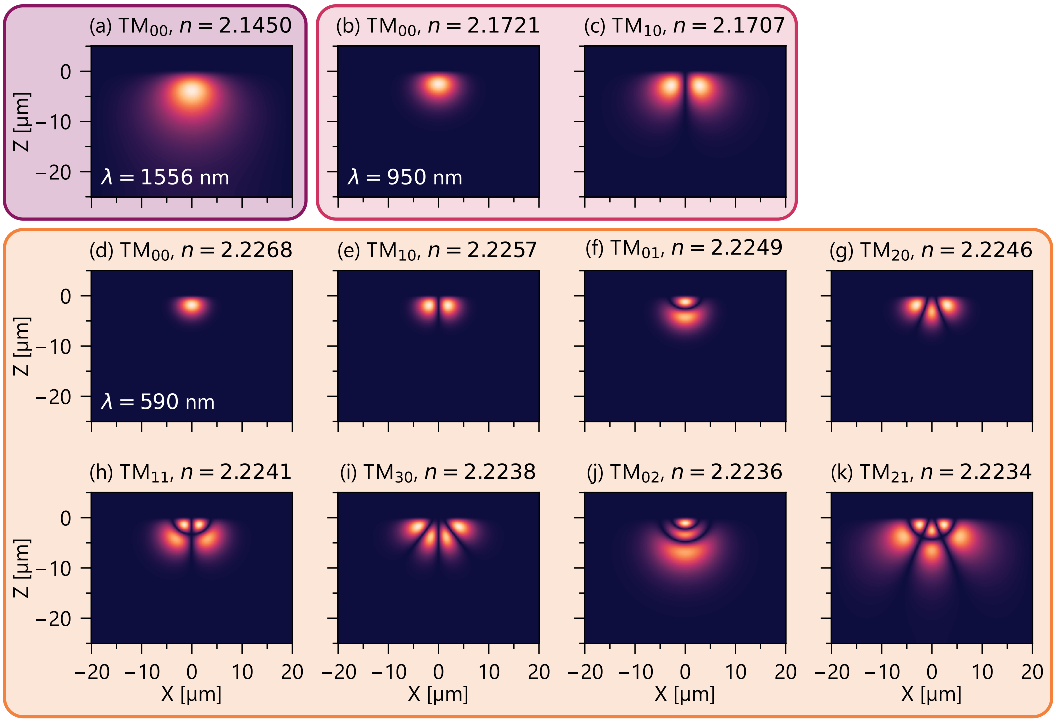

(II) Spatial modes of the cryogenic waveguide at 5 K

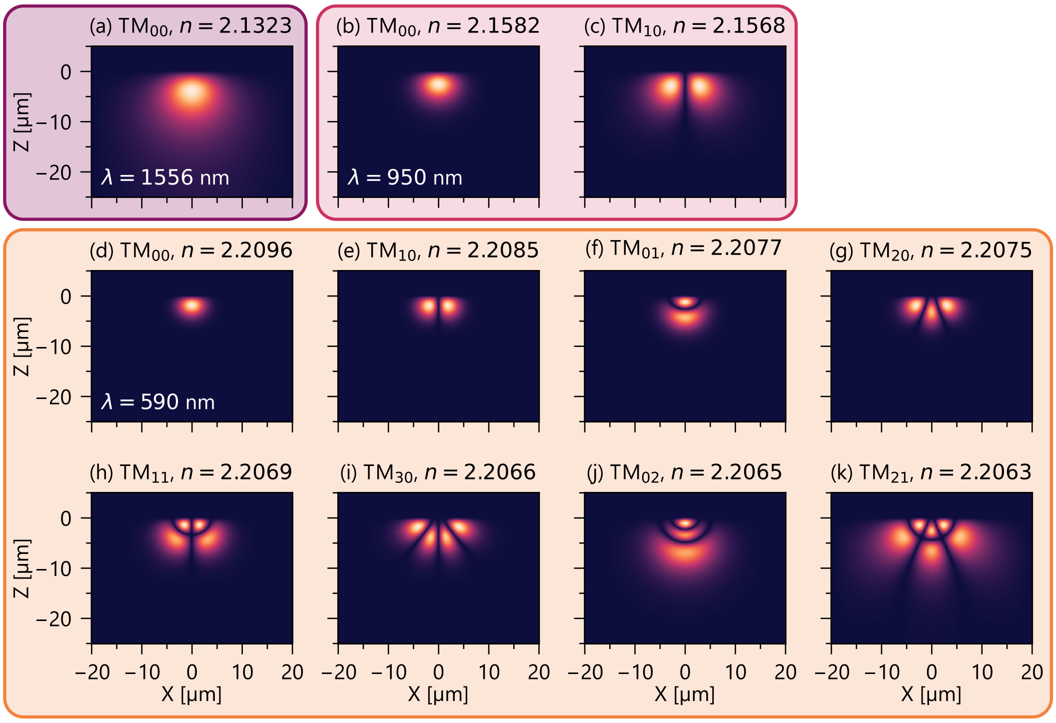

Figure 4.3: Comparison of the simulated spatial modes for 5 µm wide Ti:PPLN waveguides at (I) 175 °C and (II) 5 K. (a) At 1556 nm the waveguide only supports the fundamental mode, (b) - (c) in addition to the fundamental mode, one higher order mode is guided at 950 nm, and (d) - (k) the waveguide becomes highly multi-mode at 590 nm.

At a wavelength of 950 nm, the waveguides support only one higher order spatial mode TM_{10} in addition to the fundamental one (see (c) in Fig. 4.3). The significantly smaller mode size in the visible range results in guiding of seven higher order modes (see (e) - (k) in Fig. 4.3). The multi-mode behavior of the waveguide represents a challenge, as it cannot be guaranteed that the full intensity of the laser beam is coupled to the fundamental mode, which further limits the conversion efficiency. Even though the free-space beam, that is coupled to the waveguide, would have a Gaussian profile with maximum overlap with the fundamental mode, part of the intensity is always coupled into higher order spatial modes. Careful alignment of the in-coupled beam can minimize this proportion. However, this means that part of the idler photons around 950 nm will occupy the TM_{10} mode and are thus not properly coupled to the single-mode fiber that is permanently connected to the SNSPD. In addition to the detector being optimized for 1550 nm, this is another reason to expect that the idler arm exhibits higher losses than the signal path.

4.2 Sum-frequency generation for pump light generation

In the first step, I characterized the phase-matching of the heated SFG chip at 175 °C by pumping with both CW lasers. The optical power measured in front of the in-coupling lens was 27.7 mW for the telecom laser and 48.4 mW for the NIR laser, which was the maximum achievable power reachable over the full scanning range. The transmission for the combination of in-coupling lens, waveguide, and out-coupling lens was measured to be $T_{1556\mathrm{nm}} = 23.1\,\%$ and $T_{950\mathrm{nm}} = 51.4\,\%$. Here, the coupling of the 1556 nm beam was limited because the chosen collimation package was not matched to the focal length of the in-coupling lens. However, since the CW measurements aimed on investigating the phase-matching spectrum only, the limited coupling efficiency was not critical for this experiment.

Over the scanned range, I observed six peaks in the SFG intensity, corresponding to six phase-matched processes involving different spatial modes. Since each spatial mode experiences a slightly different effective refractive index (compare the simulations in Fig. 4.3 (I)), this results in different phase-matching conditions. For each mode, I set the tunable laser to the peak wavelength, re-optimized the in-coupling lens to generate maximum SFG power, and performed a detailed wavelength scan. Furthermore, I took a mode image of the generated SFG beam for the point of maximum intensity. This was done by exchanging the out-coupling lens with a 50x magnifying objective and focusing on the beam camera. The measured phase-matching spectra and the spatial mode profiles of the SFG beam are shown in Fig. 4.4.

The spatial modes can be clearly identified from the taken mode images. Each image shows only one spatial mode; no overlap with additional modes is visible. This shows that the use of two CW lasers enables the generation of a specific spatial mode in the visible range. Moreover, all SFG spectra show a prominent main peak and a spectral shape close to a

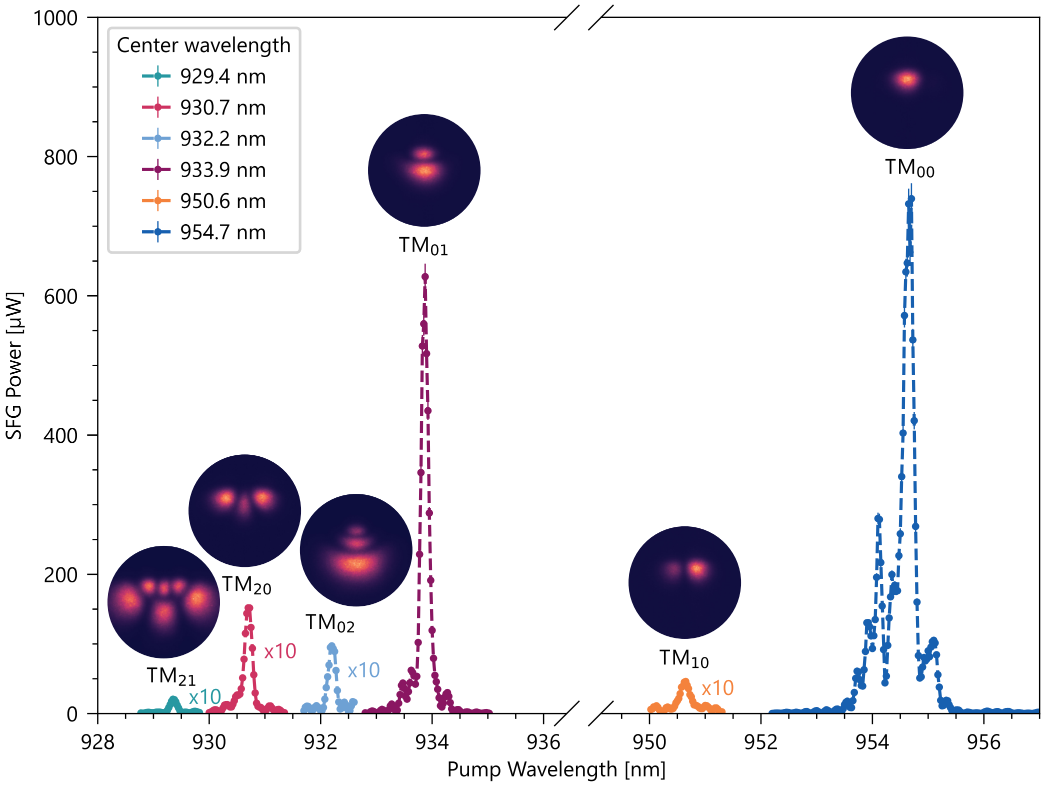

Figure 4.4: Phase-matched SFG processes in the heated waveguide with a poling period of 9.11 µm operated at 175 °C. The wavelength of the telecom laser was kept constant at 1556 nm, while scanning the NIR wavelength. Within the scanning range, six processes can be identified. The insets show images of the generated SFG mode taken with the mode camera. Please note, that the intensity of the four smaller peaks was multiplied by a factor of 10 to make the data more clearly visible.

sinc^2 function, which verifies accurate waveguide fabrication. I detected the transverse magnetic modes TM$_{21}$, TM$_{20}$, TM$_{02}$, TM$_{01}$, TM$_{10}$, and TM$_{00}$.

The generated modes TM$_{01}$ and TM$_{00}$ reach the highest intensities. To properly display the other four modes in Fig. 4.4, these spectra are magnified by a factor of 10. Due to the low intensity, I assume that these interactions can be neglected for the phase-matching considerations of the SPDC process. While I concentrate on the phase-matched process of all three beams being coupled in the fundamental modes (TM$_{00}$), these results show that the generated TM$_{01}$ mode reaches comparable intensity. This is due to the significant spatial overlap of 34.8 % between this specific mode and the fundamental modes of the other beams. Notably, this value exceeds the 23.0 % overlap, which is achieved when exclusively considering the fundamental modes of all three beams. From this measurement, I can conclude that any intensity that gets coupled to the TM$_{01}$ mode at 590 nm may be converted to SPDC photons. Moreover, the conversion efficiency of this secondary interaction is assumed to be similar to that of the designed interaction. The difference, however, lies in the generated signal and idler wavelengths, which will be different from the design. The close agreement between the simulated spatial modes for the heated and cryogenic waveguides (see Fig. 4.3) justifies using the heated phase-matching data to predict performance in the cryogenic system.

I further observed that the coupling of the 950 nm beam is highly sensitive to the position of the in-coupling lens. Tiny movements of the lens from left to right result in an apparent transition from the fundamental mode being excited to the higher order mode TM_{10}. This was verified by performing slight movements of the lens when observing the coupled spatial mode on the camera. This sensitivity of the lens position requires careful alignment of the in-coupling stage throughout all measurements. For this reason, when optimizing the coupling of the NIR beam, I did not only rely on achieving maximum transmitted power, but I also verified that the fundamental mode was coupled by using the mode camera.

Following the CW phase-matching investigations, I focused on the generation of the pulsed pump light, employing the waveguide which showed highest CW SFG intensity. The temperature of the SFG chip was tuned to 140 °C, so that the phase-matching point was adjusted for generating 590 nm. I additionally tuned the slit width in the $4f$-setup. The unfiltered pump spectrum had a spectral bandwidth of 11.81 nm and a pulse duration of 208 fs. The pump bandwidth, which maximized the SFG power, was 0.8 nm and the pulse duration increased to 1.5 ps.

The heated SFG waveguide was pumped with maximum input power of 74.12 mW for the CW 950 nm laser and 2.31 mW for the pulsed 1556.4 nm beam. Under these pumping conditions, an SFG power of 46.8 µW was obtained. The external nonlinear conversion efficiency is given by [81]

$$\eta = \frac{P_{\text{out}}}{P_{\text{in},1} P_{\text{in},2} L^2}, \tag{4.4}$$

where P_{out} is the out-coupled, generated SFG power, $P_{\text{in},1}$ and $P_{\text{in},2}$ are the in-coupled power values for the two input lasers, and L is the poled waveguide length of 40 mm. This results in a conversion efficiency of 1.71 %/Wcm^2 for this process. This efficiency is limited by the finite spatial overlap of the differently sized fundamental waveguide modes and the temporal overlap of the pulsed with the CW laser. The spectrally filtered pulsed laser generates 1.5 ps pulses at an 80 MHz repetition rate. Consequently, the total time per second during which the two lasers can interact can be approximated by 120 µs. This restricts the temporal overlap to about 0.012 %.

The wavelength spectrum of the generated SFG beam was detected with a single-photon sensitive spectrometer (Andor Shamrock SR-500i) equipped with an EMCCD camera (Andor Newton 970P). The measured spectrum can be found in the appendix (see Fig. A.2). The central wavelength of the generated pump beam is (590.016 ± 0.002) nm and the full width at half maximum (FWHM) is (0.150 ± 0.003) nm. Consequently, the target wavelength of 590 nm was reached with high accuracy. The measured parameters are used to simulate the expected cryogenic JSI of the SPDC source in Section 4.4.2.

4.3 Cryogenic waveguiding and phase-matching characterization

Before coupling the SFG pump beam into the cryogenic waveguide, its linear and nonlinear performance under CT must be established. The measurements were performed on the experimental setup illustrated in Fig. 4.1 (b). These experiments specifically aimed to identify differences between the propagation of TE- and TM-polarized modes. The waveguide is evaluated with respect to its linear guiding quality and nonlinear phase-matching properties.

The sample was cooled down eight times over a period of six months. However, a quantitative comparison of each cooldown is beyond the scope of this section. The following discussion focuses only on the individual cooldowns that yielded a measurable cryogenic SFG signal. It should be noted that the stochastic nature of the pyroelectric effect often resulted in cycles with negligible signal, precluding a comprehensive comparison across all eight cooldowns. Instead, this section aims to evaluate the cryogenic transmission, spatial mode profiles, and phase-matching based on the successful iterations. A detailed analysis of the reproducibility and reliability of cryogenic Ti:PPLN can be found in Section 5.2.

4.3.1 Linear waveguide performance

This section is started with a short, primarily observational overview of the experimental results. I observed an inconsistent behavior of the waveguide sample; the performance for separate cooldowns varied from (at this point, I will quote from my lab book)

> *“I have a lot of trouble to couple properly to the waveguides because the transmitted power is super low and there is scattered light around the modes”*,

to

> *“The cryogenic modes were super easy to find and looked very clear”*.

In my opinion, these two quotes give a proper impression of how different the cryogenic performance can be, when repeating the same cooldown procedure. In four cooldowns, I observed that the waveguides supported guiding of the TE-polarized modes, while coupling of the TM-polarized modes was challenging. This applied to both CW lasers (at 1556 nm and 950 nm). The TE mode could be clearly identified by observing the collimated mode profile on a fluorescent card. The TM mode, however, was not visible at all after rotating the polarization. The centers of the mode distributions are at slightly different heights, which explains why polarization rotation does not result in optimized coupling for the orthogonal polarization. However, at RT this is sufficient to achieve basic coupling, so that further alignment can be performed by optimizing the transmitted mode.

At cryogenic temperatures, I relied on inspecting the transmitted intensity with the 50x magnifying objective and a beam camera to optimize coupling. I had to abort four cycles since I could not achieve coupling of the TM mode, instead a noise pattern was observed with the camera. This raises the assumption that most of the in-coupled light got scattered into the substrate instead of being guided through the waveguide. It is noteworthy that this observation was consistent across the entire waveguide sample. However, in the other cooling cycles, TM polarization yielded indeed a collimated mode, although with reduced transmission compared to the TE-polarized modes.

Cryogenic waveguide efficiency

The transmitted optical power was systematically recorded for five waveguides, which demonstrated cryogenic coupling for both polarizations. These measurements were initially conducted at CT and subsequently repeated following the system's return to RT, in order to track changes in the waveguiding. I studied the transmission for both CW lasers (1556 nm and 950 nm) and both polarizations (TE and TM). The input power P_{in} in front of the in-coupling lens, was set to 5 mW for every measurement and I detected the output power P_{out}, which was collimated by the 50x magnifying objective. This objective was employed for out-coupling to facilitate the simultaneous acquisition of mode images together with the transmission measurements. The total transmitted output power is composed of

$$P_{\text{out}} = P_{\text{in}} T_{\text{lens,in}} \eta_{\text{in}} T_{\text{window}}^2 T_{\text{waveguide}} \eta_{\text{out}} T_{\text{lens,out}} \,, \tag{4.5}$$

where $T_{\text{lens,in/out}}$ are the transmission values of the in- and out-coupling lenses, $\eta_{\text{in/out}}$ their coupling efficiencies, T_{window} is the transmission of a single cryostat window of which two are in the beam path, and $T_{\text{waveguide}}$ is the waveguide transmission.

The in-coupling lens is achromatic with an NIR-AR coating, specified with a reflectivity of $R < 0.7\,\%$. Further, the out-coupling end facet is AR-coated and the out-coupling objective has a high numerical aperture of 0.42, so that it collects most of the light. Therefore, I approximate $T_{\text{lens,in}} \approx 1$ and $\eta_{\text{out}} \approx 1$. I measured the transmission through the two cryostat windows and took the square root. This transmission of a single window $T_{\text{window}} \approx 93\,\%$ matches the data sheet well. This value remains constant over the relevant wavelength range. Additionally, the detected objective transmission $T_{\text{lens,out,1556}} = 59.5\,\%$ and $T_{\text{lens,out,950}} = 63.4\,\%$ fit to the specifications. From these measurements and approximations, it is not possible to extract $T_{\text{waveguide}}$ and η_{in}, which is why I show the combined "waveguide efficiency" according to

$$T_{\text{waveguide}} \eta_{\text{in}} = \frac{P_{\text{out}}}{P_{\text{in}} T_{\text{window}}^2 T_{\text{lens,out}}} \,. \tag{4.6}$$

This measurement series was designed to investigate two main phenomena: first, whether "frozen in" pyroelectric or photorefractive charges can recombine during the transition to RT; and second, to what extent the waveguide performance exhibits polarization dependency. An overview of the experimental measurements and the corresponding research questions they aim to address is provided in Table 4.1. At first, the transmission

Table 4.1: Overview of the measurement conditions (operation Temperature T and pressure p) and associated research objectives in order to investigate thermal recombination and polarization effects in the waveguiding.

T [K]	p [mbar]	Research Question
7 (CT)	$1.6 \cdot 10^{-5}$ (Vacuum)	To what extent do the cryogenic waveguides exhibit a polarization-dependent performance?
296 (RT)	16 (Vacuum)	Do “frozen in” charges recombine during a warmup from 7 K to 296 K, based on their increase in thermal energy, or does the low-pressure environment suppress discharges?
296 (RT)	≈1000 (Vented)	Is active venting required following a warmup to enable complete relaxation of pyroelectric charge fields?
296 (RT)	≈1000 (Opened)	Does the process of removing the shroud and subsequently realigning the lenses introduce significant variations in the coupling efficiency?

measurement was performed at CT. Next, I warmed up and repeated the measurement while the sample chamber was still under vacuum. However, the pressure increased from $1.6 \cdot 10^{-5}$ mbar at 7 K to 16 mbar at RT, since the vacuum pump is by default turned off during the warmup. I wanted to investigate if there is a major improvement in the waveguide performance when venting the chamber, which would mean that the vacuum prevents discharges although the thermal energy is increased. Unfortunately, the pressure increase during warmup did not allow to investigate these effects completely independently. In the third measurement, the system was vented and the pressure increased further to ambient conditions. In the final measurement, the shroud was removed. Here, Eq. (4.6) was modified by $T_{\mathrm{window}} = 1$, since no window was in the beam path. The in- and out-coupling lens must be dismounted and realigned afterwards when removing the cryostat cover. The last measurement thus provides information about the reproducibility of the waveguide coupling when restarting the alignment procedure.

Fig. 4.5 shows the changes in the waveguide efficiency $T_{\mathrm{waveguide}}\eta_{\mathrm{in}}$ for both wavelengths and polarizations. All efficiencies are reduced at CT and then demonstrate a significant increase when warming up to RT, even though the system is still under reduced pressure. Furthermore, the efficiency for TE-polarized light consistently exceeds the efficiency of the TM-polarized beam. This observation applies to both wavelengths. When venting the chamber, the efficiencies for TE-polarized light present a very slight trend of being increased while the average efficiency for TM polarization remains mostly unchanged. The final measurement demonstrates similarly small variations compared to having the shroud closed, but no clear trend is recognizable.

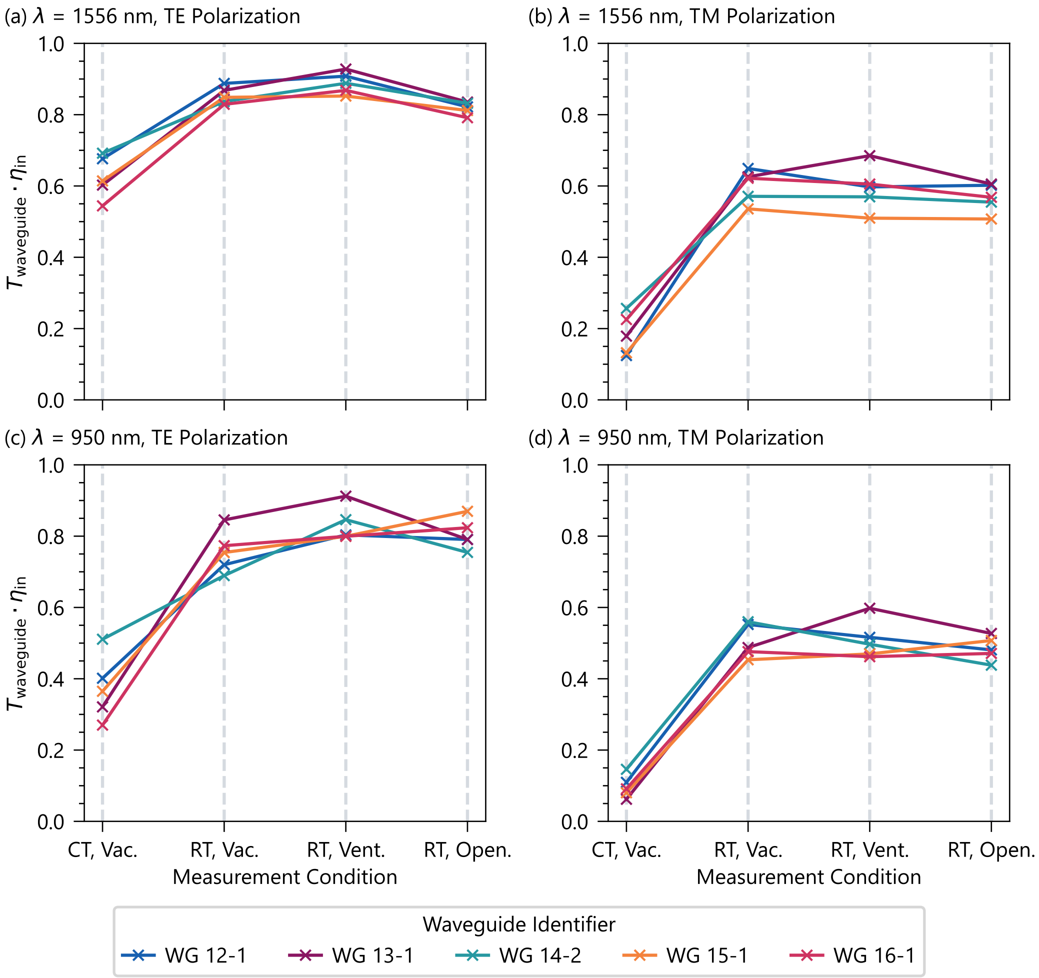

Figure 4.5: Variations in the combined waveguide transmission and in-coupling efficiency for five waveguides during four measurement stages. The measurement was performed at cryogenic temperatures (CT, Vac.), then at room temperature when the chamber was still under vacuum (RT, Vac.), after venting the chamber (RT, Vent.), and after opening the system (RT, Open.). For better comparison, the data points are connected and all data is shown on the same y-axis scale. Individual waveguides are labeled according to their group and index, e.g., "WG 12-1" refers to the first waveguide of group 12.

Overall, the three measurements at RT yield a comparable result and the cryogenic efficiency is strongly reduced. From these observations, four key conclusions can be drawn:

1. The TE-polarized modes demonstrate considerably higher waveguide efficiency in every measurement, compared to the TM-polarized modes. It is well known, that the internal waveguide losses at RT are in general higher for TM polarization, as the center of the mode is located closer to the surface. This makes the traveling field more sensitive to surface imperfections such as tiny scratches or dust particles. The measurement data

shows that this difference clearly persists under cryogenic conditions. The observed gap in efficiency further indicates that the TM-polarized modes are particularly susceptible to “frozen in” charges resulting from the cooldown.

2. In all four combinations of wavelength and polarization, the efficiency is strongly reduced at cryogenic conditions. While variations in the absolute coupling efficiency cannot be ruled out, the five waveguides demonstrate a highly consistent behavior. This consistency suggests that the observed results are caused by intrinsic material changes. This conclusion is supported by the following measurements evaluating the waveguide losses and mode profiles (see Figs. 4.6 and 4.7).
3. Warming up, without venting the chamber to ambient pressure, causes a major improvement in the performance. The RT efficiency did not vary whether the system was still at low pressure, or vented. This means that plenty of the cryogenic distortions to the waveguiding can be resolved during the warmup process already. Unfortunately, the impact of the warmup and the pressure cannot be completely separated since the warmup itself resulted in a pressure increase. However, the measurements show that this default warmup procedure in the attocube system clearly causes material changes, so that the waveguide can recover from the cryogenic charge carrier “freeze in”.
4. As expected, the RT measurements with the vented sample chamber and with the opened shroud do not show a substantial difference in the waveguide efficiency. This demonstrates that the coupling can be reliably restored after remounting the lenses. This observation further supports the assumption that the reduced cryogenic performance is not due to misalignment of the coupling stages.

A closer look on the internal waveguide losses

Under all four measurement conditions, mode images were recorded for the five waveguides and a wavelength scan was performed in order to investigate the internal waveguide losses. These measurements allow more detailed conclusions about the in-coupling efficiency and waveguide transmission, individually.

Two examples for the recorded mode images can be found in the appendix in Fig. A.3 for the waveguides 13-1 and 14-2, respectively. As it can be seen from Fig. 4.5, waveguide 13-1 demonstrated reduced waveguide efficiency at CT, but great results under ambient conditions. Waveguide 14-2, on the other hand, was the best performing waveguide at cryogenic conditions, but not at RT. Fig. A.3 shows that both waveguides exhibit a confined waveguide mode under all measurement conditions. While the TE modes show a clean profile at CT and RT, the cryogenic TM modes always demonstrate a noise pattern together with the fundamental mode. After the warmup, the relative intensity of the noise is reduced. Furthermore, there are no evident differences in the mode sizes when comparing the images. This is a relevant observation since these results indicate that the cryogenic in-coupling efficiency should reach comparable values, as when coupling to the RT waveguide. As a result, the reduced waveguide efficiency appears to be caused by a decreased waveguide transmission rather than a change in the coupling efficiency.

This statement can be verified when inspecting the transmitted intensity during the wavelength scans. Since a waveguide acts as a Fabry-Pérot resonator, the intensity contrast of a wavelength scan is a direct measure for the internal losses [182]. Considering the sample used in this measurement series, one end facet exhibits an AR coating for 950 nm and 1550 nm. This prohibits using the default equation by Regener et al. [182], to identify the absolute waveguide losses. However, the end facet still reflects a small amount of the signal so that the transmitted intensity shows Fabry-Pérot oscillations when scanning the wavelength. A comparison of the contrast at RT and CT thus provides a qualitative comparison of the losses.

Fig. 4.6 presents the measured transmitted intensity for waveguide 14-2 when scanning the telecom laser. The data for waveguide 13-1 has been added to the appendix as another example (see Fig. A.4). The scanning resolution was limited by the laser properties, enabling a smallest step size of 1 pm. To account for the differences in the average transmitted power of the four measurements, the data was normalized according to $P_{\mathrm{norm}}(\lambda) = (P(\lambda) - P_{\mathrm{mean}})/P_{\mathrm{mean}}$, with $P(\lambda)$ the individual data points and P_{mean} the mean of all data points. The measured free spectral range (FSR) of the oscillations matches the expected FSR of about 24 pm for the waveguide length of 22.9 mm. This verifies that the oscillations are indeed created in the waveguide and do not origin from another cavity in the setup. The expected FSR for the NIR laser is 9.1 pm. Although the scan around 950 nm was performed with a small step size of 0.25 pm, no oscillations were visible in the transmitted intensity. The NIR scan did not yield a result for either polarization at CT or RT. This is caused by the AR coating for 590 nm that is applied to one end facet, which also provides low reflection for longer wavelengths up to about 1100 nm. For this reason, both end facets can be considered AR coated for 950 nm. Consequently, only the scans in the telecom range are discussed.

The data shown in Fig. 4.6 clearly demonstrates a decreased contrast at cryogenic temperatures. While the TE-polarized power at cryogenic conditions still exhibits very clean oscillations with a high contrast, the contrast for TM polarization is strongly reduced. As expected, the TM contrast at RT is lower than for TE-polarized light. At cryogenic conditions, this difference between TE and TM becomes even more significant. In general, scanning the TE-polarized wavelength reliably revealed oscillations in the transmitted power. Detecting the oscillations with the TM-polarized beam did not work consistently. It was helpful to place a pinhole in the transmitted beam path to spatially filter out the noise originating from the substrate modes. While this action enhanced the clarity of the oscillations, the results remained less consistent than those observed for TE polarization.

The contrast measurement is independent of the coupling efficiency and solely represents the internal waveguide losses. The reduction in the TM-polarized contrast is thus a clear signature of a decreased waveguide transmission. This is consistent with the observations for the spatial modes, which permanently exhibited background noise for TM polarization. During the repeated thermal cycles, I could observe that the amount of stray light varied

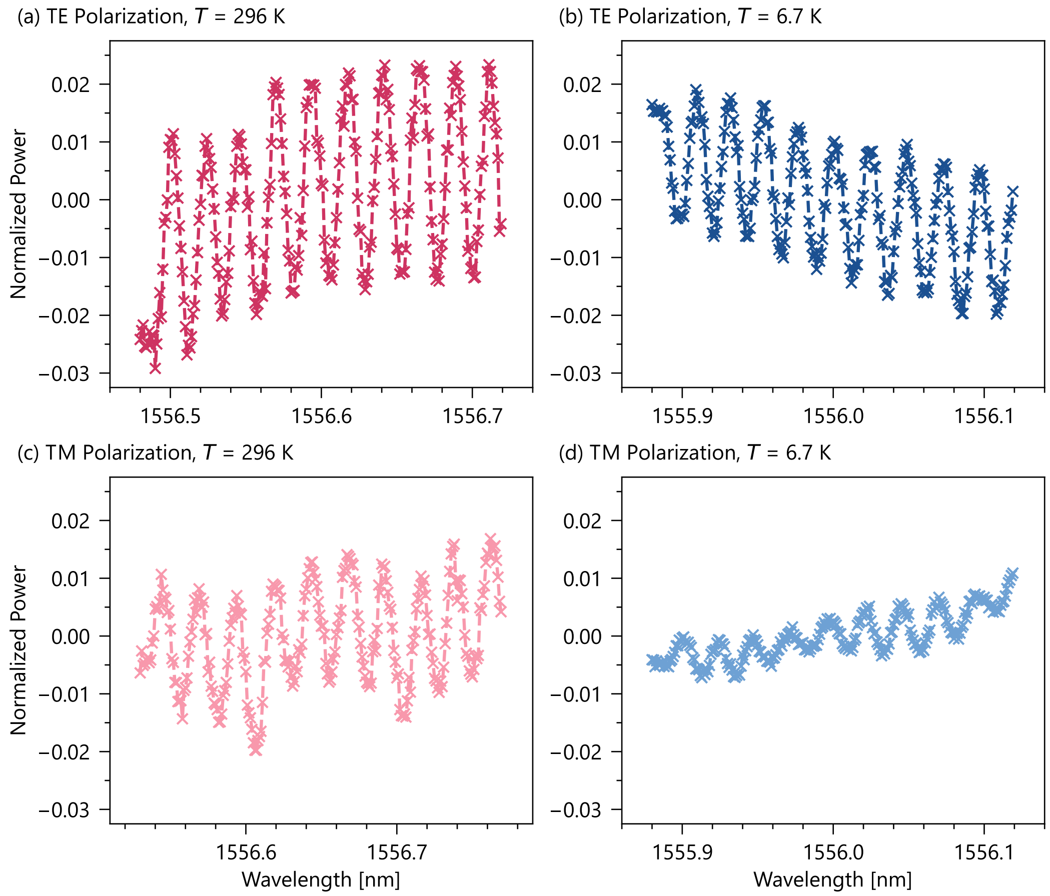

Figure 4.6: Normalized transmitted power through waveguide 14-2, measured while scanning the input wavelength. The scan was performed using TE and TM polarization at room temperature of 296 K and cryogenic temperature of 6.7 K. For better comparison, all data is shown on the same y-axis scale.

from cooldown to cooldown. In the last cycle, I again recorded the spatial mode images for waveguide 14-2 (see Fig. 4.7). The differences between the cryogenic modes for the two polarizations were very distinct. At both wavelengths, the intensity of the guided TM-polarized modes is in the same order of magnitude as surrounding substrate modes. However, the TE-polarized modes are clearly separated from the background.

It is evident that any light intensity that is scattered into the substrate is not confined in the waveguide and manifests itself as higher waveguide loss. This affects the measurements of the waveguide efficiency for TM polarization (see Fig. 4.5), as the power meter detects the fundamental mode, but also the substrate modes. This was evidenced by the introduction of a spatial filter (pinhole) in the detection path. Consequently, the true guided power of the TM mode is even lower as an inspection of the overall transmission would suggest. From these observations, I can conclude that the waveguides demonstrate reduced linear

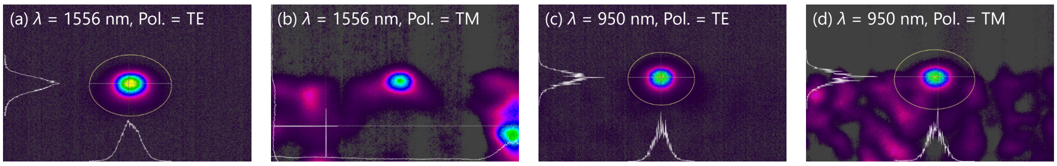

Figure 4.7: Cryogenic spatial mode images of waveguide 14-2 for both CW lasers and both polarizations, recorded during cooldown 8. The intensity of the substrate modes for TM-polarized light is in the same order of magnitude as the guided waveguide mode itself.

waveguiding performance when operated at CT. Especially the TM-polarized mode is strongly affected by the accumulating pyroelectric and photorefractive charges.

4.3.2 Variations in the nonlinear phase-matching

Since waveguide 14-2 showed the best cryogenic performance in the linear measurements, the nonlinear experiments concentrate on this waveguide. The poling period is 9.64 µm. Using the setup shown in Fig. 4.1 (b), I detected the CW phase-matching spectrum for the SFG process involving the fundamental modes. As the linear waveguiding performance demonstrated inconsistencies between repeated cycles, I also observed fluctuations in the cryogenic phase-matching. Waveguide 14-2 was characterized three times under the same conditions, during two cycles. The first measurement was performed in the sixth cooldown, the other two measurements in the seventh cooldown. The changes in the spectrum are shown in Fig. 4.8. The time difference between the measurements one and two was about one month. Measurements two and three were carried out with two days in between.

The cryogenic waveguide consistently experienced significant phase-matching distortions across all measurements. The spectral shape shows deviations from the ideal sinc^2-shape, since the main peak is accompanied by irregular side peaks of varying intensity. The maximum cryogenic conversion efficiency in these measurements was 0.88 %/Wcm^2 when generating (2.4 ± 0.2) µW SFG power, which is about a factor of two smaller than the value measured with the heated waveguide sample at a temperature of 140 °C. It is important to emphasize that a direct comparison between these two values is not feasible due to fundamental differences in the experimental configurations. The SFG process in the heated sample was pumped by overlapping the CW and pulsed laser, representing a significant constraint on the conversion efficiency. In contrast, the cryogenic waveguide discussed here is operated with CW pump light and has a different poling period. Furthermore, potential variations in the coupling efficiency cannot be ruled out. However, even though the cryogenic measurement was not limited by the temporal overlap of both CW lasers, this conversion efficiency is lower than the pulsed, heated efficiency. This indicates that the overall efficiency is reduced under cryogenic conditions. This observation is consistent with the previously discussed results for the waveguide transmission. The increased waveguide losses for TM polarization directly limit the achievable conversion efficiency.

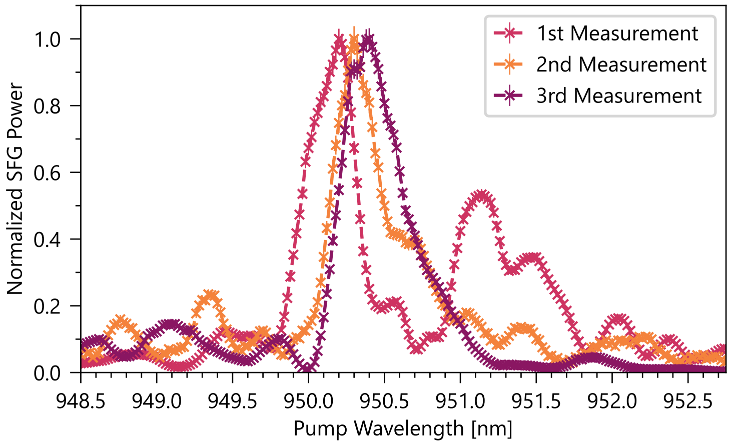

Figure 4.8: Measurements of the cryogenic phase-matching of waveguide 14-2. The SFG peak power was normalized to one to better represent the changes in the spectral shape. Measurements two and three were taken about a month after the first measurement, during a separate cooldown.

From Fig. 4.8, it can also be seen that the general spectral shape varies between all three measurements and the main peak shows a slight wavelength shift. This variation can be traced back to the spontaneous and unpredictable behavior of the accumulating charges. However, as the overall shift is limited to approximately 0.3 nm, the central wavelength remains reproducible within a small window throughout the measurement series. This indicates that while cryogenic operation generally constrains the conversion efficiency, it allows for a consistent phase-matched wavelength across separate cooldown cycles and individual measurement sets.

The low conversion efficiency and the scattered light did not allow to repeat the multimode phase-matching characterization that was performed for the heated SFG process (see Section 4.2). When scanning the NIR wavelength over a longer range, I did not detect additional peaks in the generated SFG intensity. This observation is attributed to the already limited SNR of the phase-matching for the fundamental modes. The discussed phase-matching configuration is subsequently employed to operate the cryogenic waveguide as a non-degenerate SPDC source.

4.4 Non-degenerate photons from cryogenic SPDC

The cryogenic SFG measurements verified that the waveguide supports the designed TM-polarized type-0 phase-matching under cryogenic conditions, albeit with reduced efficiency. The next step was combining the heated SFG pump light generation and the cryogenic waveguide to perform the SPDC experiment. This was done using the experimental setup shown in Fig. 4.1 (c). The pulsed SFG beam at 590 nm was coupled through the cryogenic waveguide and the generated signal and idler photons were detected with SNSPDs. The photons in the telecom range are referred to as signal photons, while the photons around 950 nm are referred to as idler photons.

4.4.1 Pump-power dependent performance

I measured the total clicks of the signal and idler detector and the coincidence counts between both. This was done in dependence of the pump power for an integration time of 60 s. This data is shown in Fig. 4.9 (a). A logarithmic scale is used for the y-axis to display all count rates on the same axis. From this, it can be directly seen that there is a significant difference in the signal and idler count rate. The detected idler counts around 950 nm are about a factor of 10 higher than the signal counts at about 1556 nm. This was unexpected since both SNSPDs are optimized for the signal photon's wavelength in the telecom range. Consequently, the signal path was expected to have lower losses than the idler path. The difference in counts is thus more likely to be caused by additional noise photons reaching the idler detector, than significant loss in the signal path.

The number of counts in the idler arm increased even more when changing the polarization of the pump beam from TM to TE polarization. This resulted in a strong increase of idler counts, while there was a significant drop of the signal and coincidence counts. The polarization dependence points to another nonlinear frequency conversion process which is phase-matched when pumping the cryogenic waveguide with TE-polarized light. I assume that this process yields idler photons which reach the detector. However, the wavelength of the signal photons might be too long to either be properly coupled into the optical fiber connected to the SNSPD, or to trigger a detection event in case the photons reach the detector. Since the observed process yields a high idler count rate, these photons can artificially increase the detected idler counts, even when the polarization is set to TM. Slight imperfections, for example in the employed HWP, can cause a remnant of TE polarization which might excite this process.

The nonlinear coefficient for lithium niobate is the highest for a TM-polarized type-0 process. Therefore, a process pumped with TE polarization has a lower nonlinear coefficient, according to the untreated material parameters [108]. However, the preceding discussion of the cryogenic linear performance demonstrated that the waveguiding itself is strongly degraded for TM-polarized light. Consequently, cryogenic operation could affect the TM-polarized photons so significantly that TE-pumped interactions achieve higher experimental efficiency. For this reason, a cryogenic TE-polarized type-0 interaction can be of great interest.

Apart from the difference in measured counts, Fig. 4.9 (a) shows that all counts increase almost linearly for increasing input power. This shows that the available pulsed input power of about 30 μW does not induce additional photorefractive damage as this would cause a saturation, or even reduction of the counts for high pump power. This could indicate that the cryogenic waveguide demonstrates improved tolerance to a coupled beam

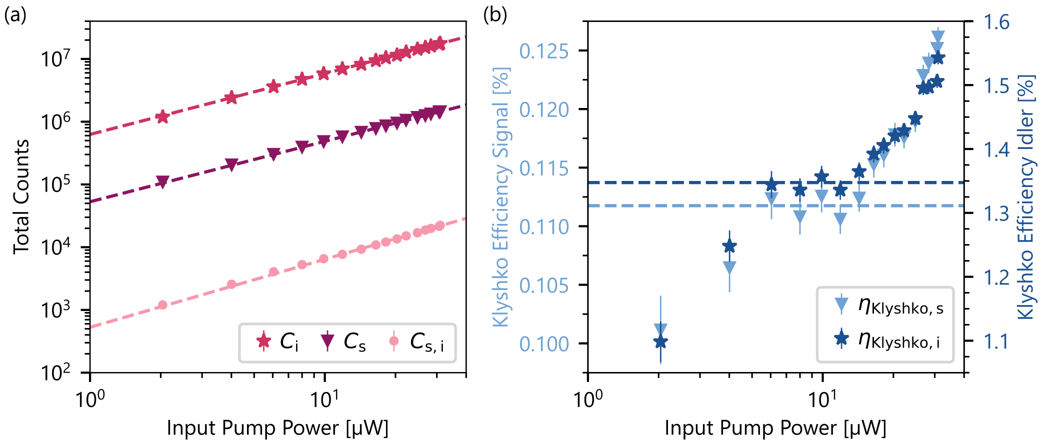

Figure 4.9: Detected total counts from the cryogenic SPDC source for increasing the optical pump power. (a) Total counts of signal, idler, and coincidences for an integration time of 60 s. (b) Klyshko efficiency of signal and idler, calculated from the measured counts. The dashed lines serve as a guide to the eye.

in the visible range when operated in pulsed rather than CW mode. However, the available pump power was limited by the heated SFG conversion efficiency. Therefore, the cryogenic response could not be inspected for higher optical power to examine the performance boundaries.

Furthermore, since an increase in operation temperature could mobilize “frozen-in” charges, it is important to note that temperature effects can be ruled out for these observations. During the nonlinear measurements, a slight increase in the sample temperature was observed, induced by the in-coupled, pulsed light. Nevertheless, this temperature change was small, below 1 K, compared to the waveguide temperature of (6.6 ± 0.2) K when the waveguide was kept dark. For this reason, changes in the phase-matching or waveguiding cannot be solely based on changes in the operation temperature.

The measurement of the single and coincidence counts allows for direct calculation of the Klyshko efficiency using Eq. (2.23), to represent the losses in the signal and idler arm. The input-power-dependent Klyshko efficiencies for both arms are shown in Fig. 4.9 (b). The overall efficiencies are very low, approximately 0.11 % in the signal path and 1.35 % in the idler path. In the absence of noise counts, the Klyshko efficiency directly indicates the losses that are present from the photon-pair generation to the detector. This is because it represents the ratio of detected coincidences to single counts, which is the same, when considering an ideal photon-pair source with no losses. However, in this case, the Klyshko efficiency for the signal arm is particularly low because it is artificially reduced by the noise counts in the idler arm. Any uncorrelated noise increases the measured single counts while the coincidences are unchanged.

In the small pump power regime around 10 µW, a slight plateau can be recognized before the values increase for increasing pump power. This plateau represents the region where the source primarily generates single photon pairs. Within this range, the Klyshko efficiency remains stable because the probability of generating multiple pairs is negligible. As the pump power increases beyond this range, the detected efficiencies begin to rise. This transition indicates an increasing mean photon number, where the contribution of higher-order photon pairs affects the measurement. However, this increased Klyshko efficiency, measured for raised pump power, does not represent the true losses in the experimental setup, which is why the plateau region must be considered for this estimation.

The first two measurement points are below the plateau. I assume this to be a sign of a constant noise background that adds to the power-dependent nonlinear noise counts. In the low pump power regime, a constant noise background is the dominant contribution. Consequently, the reduced SNR results in a decreased Klyshko value at low pump power. In general, the overall small Klyshko efficiencies indicate either high noise, or that a large amount of photons already gets lost inside the waveguide due to the reduced waveguiding.

4.4.2 Joint spectral intensity measurement

In addition to the signal and idler counts, their correlated spectral properties were characterized by measuring the JSI. For this, the SPDC process was pumped with the maximum input power of 33.0 μW. The detected transmitted pump power behind the out-coupling lens was 4.6 μW, which corresponds to 13.9 % transmission. However, this transmission at 590 nm is limited since the out-coupling end facet and the out-coupling lens possess an AR coating for the NIR-IR wavelength range.

In order to detect the JSI, the two spectrometer setups (see Fig. 4.1 (d)) were inserted into the signal and idler path, respectively. The angles of the two gratings were scanned step by step while detecting the number of coincidence counts. The employed spectrometer design requires that every wavelength interval is detected individually. Moreover, for the low conversion efficiency, a long integration time per measurement point was necessary to resolve the spectral distribution. The JSI must be fundamentally limited to the area of the pump distribution, which is given by energy conservation. For this reason, I adjusted the measurement code to restrict the measured array to a linear region which covers the expected JSI distribution, to decrease the measurement time. I performed the same measurement twice, thereby integrating for 80 s at every measurement point. Both measurements were performed within the same cooldown cycle (cooldown 7), with a break of one day in between. The results were very similar, indicating no significant changes due to photorefraction during the measurement time. The total counts of both measurements were summed up and the resulting JSI is shown in Fig. 4.10 (a).

As a comparison for the experimental result, the expected cryogenic JSI is simulated using the theoretical effective refractive index data which was discussed in Section 2.1.3. The simulation further includes the spectral profile of the pump beam, the fabricated poling period, the resolution of the spectrometers, and the effective length over which all three

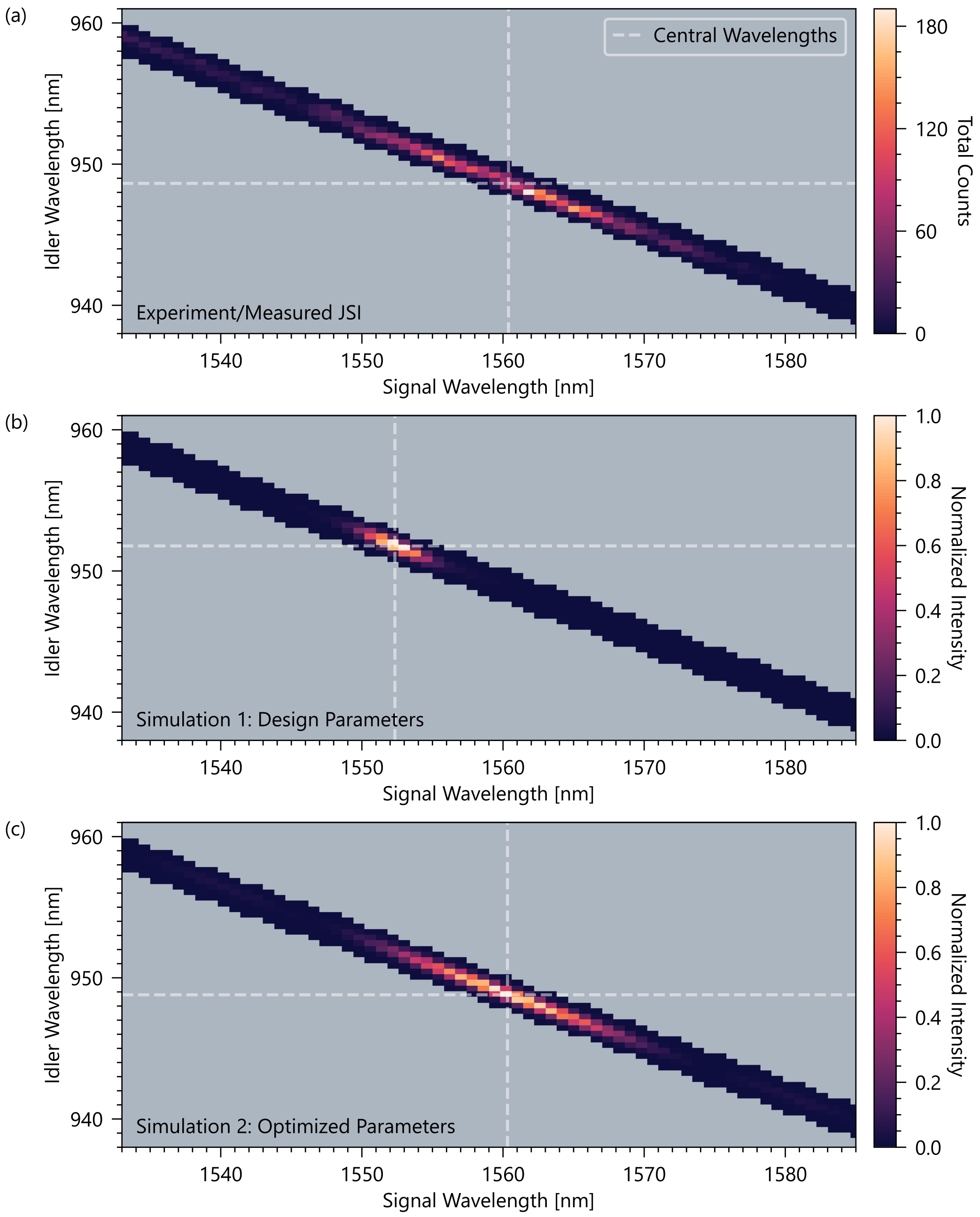

Figure 4.10: Joint spectral intensity of the signal and idler photons from the cryogenic SPDC source. (a) Measured total coincidence counts, summarized for two individual measurements with an integration time of 80 s each. The measurement range was restricted to cover a linear section around the pump distribution function. No data was recorded within the gray area. (b) Simulated JSI for the design parameters (effective length of 22.9 mm, poling period of 9.64 µm). (c) Optimized JSI simulation (effective length of (3.8 ± 0.3) mm, poling period of (9.654 ± 0.002) µm).

Table 4.2: Overview of the central signal and idler wavelengths. The values are obtained from a Gaussian fit that was applied to the projection of the JSI on the x- and y-axis, respectively. The experimental values are taken from the JSI shown in Fig. 4.10 (a). Simulation 1 is performed using the design parameters, presented in Fig. 4.10 (b). Simulation 2 considers optimization of the effective length and the poling period to fit the experiment, as shown in Fig. 4.10 (c).

Parameter	**Experiment**	**Simulation 1**	**Simulation 2**
Signal Wavelength [nm]	1560.4 ± 0.3	1552.31 ± 0.04	1560.44 ± 0.04
Idler Wavelength [nm]	948.6 ± 0.2	951.78 ± 0.02	948.75 ± 0.02

fields interact. To account for the spectrometer resolution, the simulation is first performed with higher resolution than the measurement. This simulated JSI is then convolved with the Gaussian transmission profile of each spectrometer along the two axes, respectively. The spectrometer bandwidths of $\Delta\lambda_\mathrm{s} = (0.92 \pm 0.01)\,\mathrm{nm}$ and $\Delta\lambda_\mathrm{i} = (0.52 \pm 0.03)\,\mathrm{nm}$ are in the same order of magnitude as the measurement step size $\delta\lambda_\mathrm{s} = 0.8\,\mathrm{nm}$ and $\delta\lambda_\mathrm{i} = 0.4\,\mathrm{nm}$. This results in an artificial broadening of the JSI along both axes during the measurement. A comparison of the simulation with the measured data thus requires taking the spectrometer transmission bandwidths into account. After the simulated data is convolved with the spectrometer profile, the JSI is finally down-sampled to display the result with the measurement's resolution.

In the first simulation, all parameters are kept fixed to the design. The poling period is set to 9.64 µm and the effective length is equal to the full waveguide length of 22.9 mm. The first simulation is shown in Fig. 4.10 (b). In comparison to the measurement result, this approach yields a JSI for which the center wavelengths are slightly shifted and the signal and idler bandwidths are more narrow band. The central wavelengths are presented in Table 4.2. The offset can be explained either by a slight variation between the extrapolated refractive indices and the experimental ones, or by small fabrication uncertainties in the waveguide dimensions, or poling period. Nevertheless, since the total shift is only within a few nanometers (approximately 8 nm and 3 nm in the signal and idler wavelength, respectively), this shows that the extrapolated refractive indices describe the process already very well and no significant correction is required for TM polarization.

The difference in spectral signal and idler bandwidth results from deviations in the bandwidth of the phase-matching function. The effective length determines the phase-matching width and thus affects the broadening of the JSI along the axis of the pump distribution function. When assuming an effective conversion process over the full waveguide length, this corresponds to a narrow phase-matching bandwidth, i.e., a more confined JSI. The measurement shows that the experimental JSI is further extended and thus the effective length must be significantly reduced.

To account for this experimental discrepancy, in the next step, a second simulation is performed using an optimization algorithm. This time, variations in the effective length and the poling period are allowed so that the deviation of the simulated JSI and our measured distribution is actively minimized. This optimization provides an estimation for the experimental effective length. Furthermore, the simulation allows a slight deviation of the poling period, to let both JSIs overlap at the same central wavelengths. This is required to get a more accurate result for the effective length. Fig. 4.10 (c) displays the optimized simulation and the central wavelengths are included in Table 4.2.

According to this optimization, the effective length of the waveguide is (3.8 ± 0.3) mm, corresponding to about 16.6 % of the designed waveguide length which was periodically poled during fabrication. The short effective length clearly reflects the limited cryogenic waveguide performance, as it was also evident in the linear waveguide characterization. Nonetheless, the optimized poling period is (9.654 ± 0.002) µm, which deviates by only 0.15 % from the designed period of 9.64 µm. This is therefore within the fabrication imperfections. Consequently, the minimal deviation of the poling period verifies the accuracy of the theoretical model and that it allows to reliably achieve phase-matching for the designed wavelength combination. In consistency with the preceding measurements for the cryogenic SFG, the results for the SPDC experiments verify that the designed NLO process can be experimentally realized. It is evident, however, that the achievable efficiency is limited at cryogenic temperatures. Notwithstanding these difficulties, it was shown that the proposed phase-matching can be realized within small tolerances.

4.5 Chapter conclusion

This chapter addressed the second research question of this thesis: *How does cryogenic operation affect the Ti:PPLN platform?* To evaluate the temperature-dependent effects that alter the waveguide performance at cryogenic conditions, the phase-matching was restricted to TM-polarized modes and visible pump light was employed. The same phase-matched process was first characterized when actively heated and afterwards at 6 K. As expected, the heated waveguides performed well; the transmitted spatial modes showed a clear profile. Coupling to the cryogenic waveguides was more demanding. The conducted experiments demonstrate the necessity of clearly separating the effects of cryogenic operation on the two orthogonal polarizations. While the TE-polarized modes were collimated, the TM-polarized beam could either not be coupled to a waveguide at all, or it was transmitted with low intensity. During one cooldown, in which waveguiding for TM polarization could be verified, the transmitted power was investigated for five waveguides. The cryogenic combined waveguide efficiency at a wavelength of 1556 nm was approximately 63 % for TE-polarized light and only about 18 % for TM-polarized light. The same trend was observed for a wavelength of 950 nm, with an efficiency of approximately 37 % for TE polarization and 10 % for TM polarization. These data indicate significant differences in cryogenic waveguiding for the two polarizations.

The internal waveguide losses were found to increase under cryogenic conditions. While the spatial mode sizes did not differ (indicating consistent coupling efficiency), the contrast of the wavelength scans decreased from RT to CT (indicating higher losses). Unfortunately, the AR coating on one end facet prohibited the quantitative analysis of the waveguide losses. Only qualitative conclusions can be drawn here. At cryogenic temperatures, substrate modes were observed together with the TM-polarized modes. These observations support the assumption of substantially increased losses, as the light was not properly confined anymore within the waveguide region. This scattering into the substrate was much more visible for TM polarization, which matches the expectations since the emerging electric fields are mainly aligned parallel to this polarization.

The SFG spectrum was observed in two consecutive cooldowns, which showed that the spectral shape is subject to change between different cycles, but also within the same cooldown. This demonstrates that the phase-matching is affected by the complex interplay of increased charge carrier density and severely restricted charge mobility, affecting the extent of both pyroelectricity and photorefraction. This combination acts as a performance limit, which, due to the specific orientation of the induced fields, particularly constrains the feasibility of TM-polarized waveguiding. This raises the question, whether pyroelectricity or photorefraction is the dominant effect that limits cryogenic operation of Ti:PPLN. From the presented data, it is not possible to isolate the distinct roles of both effects. Therefore, this question is addressed in Section 5.1.

The SPDC characterization was consistent with the preceding measurements. The Klyshko efficiency was limited to approximately 0.11 % and 1.35 %, which indicates that a large proportion of the generated photons was lost within the waveguide already. The measurement of the JSI allowed to perform an estimation of the effective length, which corresponds to only 16.6 % of the total waveguide length. This supports once more the conclusion that there is a varying effective refractive index along the waveguide. Nevertheless, both nonlinear experiments, the SFG and SPDC, verified that the designed phase-matching point could be realized with good accuracy. Despite the compromised efficiency, the fundamental operation of the intended phase-matched process was verified experimentally.

The central outcome of this chapter is that the TM-polarized phase-matched process demonstrates high susceptibility to the photorefractive and pyroelectric effect. The cryogenic operation strongly affected the TM-polarized light and caused slight, but unpredictable variations in the linear waveguiding and nonlinear response. The extent of the increase in waveguide losses was not consistent during repeated cooldowns. This means that the “freeze in” of pyroelectric charges can be considered a probabilistic process. Not every cooldown cycle produces identical charge distributions, which explains why TM-polarized photons experience variable propagation losses. Furthermore, it cannot be ruled out that pyroelectric charge accumulation is a cumulative process, so that the charges do not fully recover when the sample is warmed up to room temperature. Nevertheless, I did not see a consistent evolution of the coupling getting worse with the repeated cooldowns. Instead, some cooldowns enabled proper coupling while others did not, but no chronological trend was recognizable. To evaluate the reproducibility of cryogenic performance metrics in detail, Section 5.2 comprises a study of 15 waveguides that were subjected to six thermal cycles.

Future investigations could further involve cryogenic phase-matching of a TE-polarized type-0 interaction, applying pulsed cryogenic operation only, and enhanced filtering of the SPDC photons to prevent the detection of photons from additional phase-matching. Unfortunately, the origin of the noise counts in the idler arm could not be identified. If this experiment is repeated in future studies, the signal and idler arm should be spectrally filtered closely around the detected JSI. Additionally, a polarization filter should be placed behind the waveguide to test if all generated photons are TM-polarized. Moreover, a comparison of the cryogenic nonlinear performance to room temperature operation could be of interest. However, for a fixed poling period, the phase-matched wavelengths for this NLO process shift significantly during the cooldown. According to the simulation, the central signal and idler wavelengths for the characterized waveguide shift to approximately 1700 nm and 900 nm at room temperature. Therefore, a like-for-like comparison at room temperature of the same waveguide and the same combination of pump laser and SFG frequency is not directly possible.

Cryogenic nonlinear optics: what does it teach us?

5

The preceding chapters were primarily motivated by the implementation of specific SPDC processes within the Ti:PPLN waveguide platform at cryogenic temperatures. Following initial proof-of-principle experiments, these interactions were tailored to realize both degenerate and widely non-degenerate photon pair generation. Throughout this experimental journey, however, both pyroelectricity and photorefraction were found to have a significant impact on the waveguide performance. A more systematic investigation of these effects is necessary to provide the foundation required to answer the third main research question: *What do our observations teach us about the viability of cryogenic lithium niobate?*

This final chapter addresses these effects through two primary research studies. First, Section 5.1 provides a thorough analysis of the physical properties of the titanium in-diffused lithium niobate platform under cryogenic conditions. By isolating the pyroelectric effects induced during thermal transitions and characterizing the photorefractive response at low temperatures, this section establishes a detailed understanding of the platform's electro-optic behavior. Furthermore, it introduces an experimental technique for the precise determination of cryogenic effective refractive indices, resulting in a modified Sellmeier equation tailored to the specific waveguides.

Building upon this physical foundation, the second study in Section 5.2 evaluates the practical viability of the Ti:PPLN platform for cryogenic integrated optics. This is addressed through a comprehensive measurement series involving 15 waveguides across six cooling cycles. By organizing these waveguides into distinct experimental groups, the study investigates how different conditions influence long-term performance and reliability. Finally, this chapter reviews these observations to define the operational parameters under which cryogenic lithium niobate can be utilized for future quantum optical applications.

The mystery of sample LB42az

As a brief introduction to this final chapter, I wish to share a specific narrative from the laboratory involving the Ti:PPLN sample labeled *LB42az*. In science, we often seek the "Eureka!" moment; however, unexpected results typically provide more insight than the validation of a theory. This thought is famously captured by Isaac Asimov:

> *"The most exciting phrase to hear in science, the one that heralds new discoveries, is not 'Eureka!' but 'That's funny...' "*

The behavior of LB42az serves as a perfect example of these “funny”, unpredictable variations observed when characterizing individual waveguide chips across multiple thermal cycles. These observations served as a primary motivation for the deeper investigation into pyroelectric and photorefractive damage presented in this chapter, as we sought to understand the hidden mechanisms driving such inconsistent performance.[1]

The characterization of LB42az began with high expectations; at room temperature, the sample exhibited clean mode profiles and SHG phase-matching spectra that closely followed the expected sinc^2 shape. However, upon cooling to cryogenic temperatures, the behavior changed significantly. The CT modes displayed dominant, symmetric scattering into the substrate - a phenomenon specifically isolated to the periodically poled waveguides. Although, at this time, early mode images were captured under over-saturated conditions, they clearly demonstrated this persistent scattering. The subsequent CT SHG measurements yielded no measurable signal. This result remained consistent during a second cooldown a month later, with the modes remaining scattered and the cryogenic SHG signal undetected.

The observations shifted during a third cooldown six months later. In this instance, CT SHG was functional, with waveguides near the chip’s edge exhibiting higher brightness and cleaner spectral shapes than those toward the center. This behavior stands in contrast to typical observations at room temperature. Usually, waveguides near the substrate edge are more susceptible to inhomogeneities in the photoresist. In the center, however, the more uniform resist thickness typically results in superior waveguide performance. Despite this, a waveguide in the outermost periodically poled group (WG 5-2) yielded a cryogenic phase-matching spectrum that closely followed the theoretical model. This stability allowed for the measurement of cryogenic SPDC, achieving a Klyshko efficiency of 19 %. Notably, the SHG spectrum remained unchanged following the SPDC measurements, suggesting an absence of photorefractive damage. Moreover, subsequent RT measurements confirmed that the sample had returned to its initial performance level.

However, this state was not maintained in a final cooldown one month later. During this cycle, the Klyshko efficiency reached only 1 %. While the spectral shape of WG 5-2 was only slightly distorted compared to the previous cycle, the waveguides toward the center of the chip again exhibited significant deviations from the sinc^2 profile. This unsteady performance across different cooling cycles highlights the lack of reproducibility in these early trials and underscores the necessity for the systematic studies that follow.

---

[1] A full presentation of the data from these various cooldown cycles is omitted here for brevity, as the primary aim of this narrative is to illustrate the inherent lack of reproducibility in early cryogenic trials.

5.1 Deeper insights into the cryogenic performance of lithium niobate

At a glance
This section presents a systematic investigation into how cryogenic operation influences the performance of the titanium in-diffused lithium niobate platform, including both optical and electrical properties. To begin, Section 5.1.1 examines the independent effects of pyroelectricity induced by thermal transitions during the cooling and warming cycles. Subsequently, the study in Section 5.1.2 focuses on the photorefractive effect under cryogenic conditions. Furthermore, Section 5.1.3 details an experimental method for determining the cryogenic effective refractive indices, which enables the derivation of a modified Sellmeier equation specifically for the investigated waveguides. Collectively, the studies presented here provide a comprehensive understanding of the interplay between the optical and electrical properties of lithium niobate at low temperatures.

5.1.1 Pyroelectric charge accumulation during the cooldown process

To provide context for the subsequent discussion, it is useful to briefly review the underlying pyroelectric mechanisms in lithium niobate. The material's pyroelectric properties cause a temperature-dependent shift in spontaneous polarization [156, 172]. A cooldown to cryogenic temperatures thus results in a change in polarization strength, which manifests itself in the form of unscreened bound charges. For z-cut lithium niobate, the strong polarization causes charge carriers to accumulate on the top and bottom surface of the waveguide chip. This results in localized electric fields which are aligned in the z-direction, i.e., parallel to the crystal axis. Since the in-diffused waveguides are close to the top surface, the electric fields disturb the refractive index profile due to the electro-optic effect.

Declaration
The experimental results discussed in this section were obtained as part of a collaborative study published in *Materials for Quantum Technology* in Ref. [154]. While the primary measurements and analysis were carried out by F. Thiele and T. Hummel, I was actively involved in the scientific interpretation of the data and the preparation of the manuscript. A summary of these findings is included here for the sake of completeness, as these results are essential for evaluating the overall performance of cryogenic lithium niobate in terms of its pyroelectric properties. For the technical details and comprehensive analysis, the reader is referred to the original publication [154].

The pyroelectric influences on the Ti:LN platform were characterized with a simultaneous measurement of alterations in the electrical and optical properties during the thermal transition. The generation of pyroelectric charges was inspected by measuring the electrical

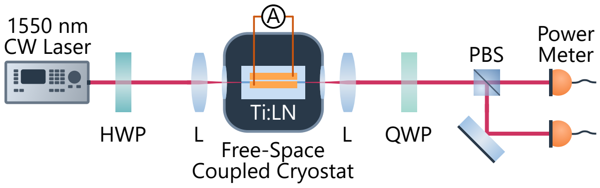

Figure 5.1: Experimental setup to investigate the alterations in the optical and electrical signal from the waveguide during the thermal transition. Changes in the optical signal are deduced from the intensities measured in the output paths of the PBS. In order to measure variations in the electrical signal, the waveguide is equipped with two electrodes. The current is measured with an ampere meter outside the cryostat. HWP/QWP: half-/quarter-wave plate, L: aspheric lens, Ti:LN: titanium in-diffused waveguide in lithium niobate, PBS: polarizing beam splitter.

charge flow through the waveguide. For this, the waveguide under test was fabricated with two electrodes on the top. The electrodes are aligned along the waveguide, whereas one electrode overlaps with the waveguide area while the second one is placed at a distance of 9 µm next to it. This configuration mainly detects the vertical electrical field components within the waveguide. The pyroelectric charges are expected to move primarily along this direction, based on the orientation of the spontaneous polarization. The electrodes on the waveguide surface can collect these charges which results in a macroscopic, measurable current.

Variations in the optical properties were detected using the Sénarmont method, which measures the birefringence between the TE- and TM-polarized waveguide modes [152]. Based on their different effective refractive indices, both polarizations collect an unequal phase when propagating through the waveguide. This phase difference continuously changes during a thermal transition from RT to CT as the refractive indices possess a temperature dependence. Moreover, localized refractive index alterations induced by pyroelectric charges lead to additional phase shifts that overlap with the steady trend. The relative phase between the orthogonally polarized modes can be deduced from the transmitted light by interfering both polarizations [154].

Fig. 5.1 shows the employed experimental setup. The waveguide is mounted in the free-space coupled cryostat and pumped by a CW laser beam at a wavelength of 1550 nm and optical power of 2.2 mW. The input polarization is set to 45° using a HWP. Consequently, the beam is coupled to both the TE- and TM-polarized waveguide modes. The electrodes are wire bonded and connected to a break-out board, which enables measurement of the current with a RT ampere meter, providing sub-picoampere sensitivity. The transmitted polarizations are interfered using a quarter-wave plate and a PBS. The intensities of the output ports of the PBS are directly related to the phase difference between the TE- and TM-polarized modes [154]. The optical phase shifts in the transmitted beam are thus analyzed by detecting the optical power in both output ports using two power meters. The measured intensities are normalized, by the sum of both outputs, which ensures that the measurement result is independent of the coupling efficiency. This is crucial, as thermal drifts within the experimental setup during temperature cycles necessitate frequent realignment, which is incompatible with maintaining a stable coupling efficiency.

The waveguide was cooled down from RT to 25 K (due to heat load constraints of the cryostat) and warmed up again, while continuously recording the temperature, optical output, and generated pyroelectric current. Analysis of the data identified "discontinuities" in both signals: abrupt changes in the otherwise slowly varying optical phase and spikes in the electrical current. These discontinuities were classified as either purely optical, purely electrical, or correlated if they occurred within a 6 s time window. Across the entire temperature range, clear correlations between pyroelectric current spikes and sudden changes in the birefringence were observed. This confirmed that temperature-induced pyroelectric effects strongly disturb both the electrical and optical behavior of the waveguide. Since the pyroelectric fields modulate the refractive indices via the electro-optic effect, the guided modes are subject to abrupt phase jumps.

To compare the frequency of each discontinuity type across different temperature ranges, separate histograms were generated for the cooldown and warmup, representing the number of events within temperature intervals of 30 K (see Fig. 5 in Ref. [154]). During the cooldown, the majority of pyroelectric discharges and associated optical discontinuities appeared within the central temperature range of 195 K down to 115 K, with electrical events dominating in this interval. Below approximately 100 K, the frequency of both electrical and optical perturbations dropped significantly, indicating a vanishing influence of pyroelectricity in the low temperature regime. A similar behavior was observed for the warmup: as the waveguide is heated, the charge mobility and the pyroelectric coefficient increase again [183, 184], leading to renewed discharges and correlated optical perturbations above approximately 100 K. For higher temperatures, the number of discontinuities steadily increased during the complete warmup procedure. In order to separate the implications of the pyroelectric effect from photorefractive impacts, the cooldown and warmup were repeated without coupling any light through the waveguide, while recording the electrical current from the sample. A comparable number of discontinuities in the electrical signal was observed. This indicates that the low optical pump power of 2.2 mW did not induce significant photorefractive material alterations in the prior measurement.

From the data sets, it can be concluded that a substantial amount of pyroelectric charges is generated by the thermal transition during the cooldown. These charges accumulate within the substrate until the charge density reaches a critical threshold and the charges recombine in an abrupt discharge. The reduced pyroelectric coefficient and low charge carrier mobility at cryogenic temperatures are expected to result in a decreased generation probability of pyroelectric charges and an increased threshold required for their recombination. This is consistent with the observation that the frequency of discontinuities decreases considerably for temperatures below approximately 100 K.

These results may lead to the practical conclusion that the Ti:LN platform offers reliable cryogenic operation at stable temperatures, provided that only pyroelectric influences are considered. However, the reduced frequency of detected discharges in the cryogenic regime does not necessarily imply a decrease in the magnitude of the pyroelectric fields.

Instead, a lower discharge rate suggests that accumulated charges are likely “frozen in”, resulting in a persistent and potentially inhomogeneous charge distribution following the completion of the cooldown cycle.

5.1.2 Photorefractive damage induced at cryogenic temperatures

In practice, the cryogenic efficiency of waveguiding and frequency conversion is governed by a complex interplay between the pyroelectric effects and photorefraction. This section focuses on the independent influence of photorefraction, which is achieved by performing all measurements at a stable temperature of approximately 7 K. As the reduced charge carrier mobility makes discharges unlikely below 100 K [154], operation at 7 K minimizes the contribution of pyroelectric charge generation. The cooling rate of the cryostat was strictly limited to 1 K/min to give the accumulated charges more time to discharge before their mobility vanishes. Even with controlled cooling, residual charges remain once the sample is thermally stabilized at CT. This means that the cryogenic waveguides are initially affected by pyroelectricity. However, here, a measurement technique is introduced which aims to mobilize all types of “frozen-in” charges, whether they originated from thermal transitions or optical exposure. Because the fundamental material changes induced by both pyroelectricity and photorefraction are traced back to non-uniform charge distributions, the specific source of these charges does not impact the significance of the applied method.

While photorefractive damage is commonly mitigated by operating waveguides at elevated temperatures (typically between 100 °C and 200 °C), this approach is obviously not viable in cryogenic environments. Given that the threshold for acceptable optical power increases substantially with temperature, this threshold is significantly lowered under cryogenic conditions.Because of the diminished charge carrier mobility, the “frozen-in” distribution of de-localized charges is expected to remain static unless external energy is supplied to re-mobilize the charges. Rather than relying on thermal energy, this energy can also be supplied optically by introducing an auxiliary laser beam into the system.

Declaration
The results discussed in this section are published in collaboration with the IQO group in the *Journal of Applied Physics* in Ref. [185]. The underlying study examines the influence of photorefractive effects on the spectral profile of an SFG phase-matching function. Within this work, two separate waveguides were characterized: one operated at elevated temperatures and the other one operated cryogenically. The measurements at elevated temperatures were conducted by R. Pollmann. These verified that thermal stabilization at temperatures up to 200 °C can mitigate power-induced spectral alterations [185]. I performed the cryogenic measurements discussed herein, including the experimental design, data acquisition, and analysis. This low-temperature investigation focuses on assessing the potential of an auxiliary green laser beam for enhancing the charge carrier mobility.

The experimental approach explored in this section adapts the “optical cleaning” method that was first introduced by Kösters et al. [186, 187]. They exposed the surface of a lithium niobate waveguide with a moving, green light beam while heating the sample to moderate temperatures. This beam enabled pushing photoexcitable electrons, along the crystalline *c*-axis, out of the illuminated region. While the energy of green photons is significantly less than the band gap energy, recent experiments on conductive domain walls also indicate that green light can result in increased charge carrier density or mobility [188]. The green wavelength fits well to the known energy level of the bi-polaron in lithium niobate, which can be excited with the green laser light and broken into the more mobile free and bound polaron states [162, 189].

To mitigate photorefractive effects in lithium niobate waveguides, Kirsch et al. [190] adapted this technique by co-coupling an auxiliary green laser beam alongside the primary NLO pump light. This approach enabled Kirsch et al. to demonstrate both in-situ photorefractive curing at room temperature and post-exposure recovery after photorefractive damage had occurred. Notably, their experimental approach successfully mobilized de-localized charges without the need for additional heating. Here, I implemented this optical mitigation strategy within a cryogenic environment to evaluate its influence on the “freeze-in” effect.

To systematically evaluate cryogenic photorefraction and validate the proposed method for active carrier mobilization, I employed the widely non-degenerate NLO process that was previously described in Chapter 4. This phase-matched process is highly sensitive to pyroelectric and photorefractive perturbations since all fields are TM-polarized and one of the interacting wavelengths is in the visible range. In this section, CW-driven SFG is performed in the cryogenic waveguide, while the spectral shape and peak power of the phase-matching spectrum are evaluated. The phase-matching point differs only slightly from the process characterized in Chapter 4. Here, two CW lasers at a wavelength of approximately 1570 nm and 960 nm are combined to generate an SFG beam centered around 595 nm.

Fig. 5.2 illustrates the experimental setup to characterize the influence of photorefraction. This setup remains nearly identical to the configuration previously depicted in Fig. 4.1 (b), with two key modifications. The heated crystal oven is substituted by the free-space coupled cryostat, and a green auxiliary laser is integrated into the setup to examine the charge carrier re-mobilization. The green laser beam originates from a laser diode with an optical power of 1 mW and a wavelength of 532 nm. The tunable CW telecom laser is set to a fixed wavelength of 1570 nm and combined with the tunable CW NIR laser that is scanned around 960 nm.

The characterization of the cryogenic waveguide was carried out in four distinct stages:

1. Initially, the cryogenic phase-matching spectrum was measured, presenting a perturbed shape due to “frozen-in” charges. To evaluate the long-term stability of the existing charge distribution, the waveguide was kept at constant temperature of 7 K without illumination for one week, before the spectrum was measured again.

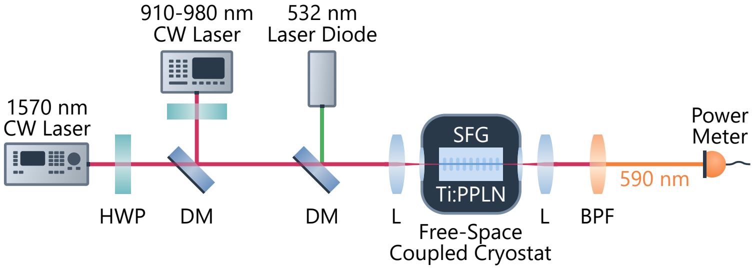

Figure 5.2: Experimental setup to study the photorefractive effect in the cryogenic waveguide. The SFG process is pumped with two CW lasers, while an auxiliary green laser beam is introduced to evaluate its influence on “frozen-in” charge carriers. HWP: half-wave plate, DM: dichroic mirror, L: aspheric lens, BPF: band-pass filter.

2. Next, the green laser was activated while continuously monitoring the phase-matching spectrum. This procedure was performed to determine whether the green illumination can mobilize the charges and induce detectable changes in the phase-matching profile.
3. Subsequently, the green laser was deactivated, and the SFG pump power was increased incrementally. At each power level, I recorded the phase-matching spectrum and the generated peak power to isolate the variations induced solely by high pump power. This series of measurements was designed to identify the onset of photorefractive damage to the waveguide’s nonlinear properties.
4. Finally, the green laser was re-introduced to assess its ability to mitigate the photorefractive perturbations induced by the high-power pump. While maintaining constant green illumination, I recorded the phase-matching spectrum at regular intervals to track its development over time and identify any recovery processes.

All SFG experiments were performed in the same waveguide at 7 K. In the first experiment, the input power of the telecom laser was set to (24.4 ± 0.8) mW, measured in front of the in-coupling lens. The pump power of the second laser was set to a similar level of (23.6 ± 0.8) mW. The cryogenically measured phase-matching spectrum is shown in Fig. 5.3 (a). The spectral shape exhibits initial distortions, as it deviates significantly from a sinc^2 profile. This distortion is attributed to the combined effects of pyroelectric charge build-up during the cooldown and photorefractive damage due to excessive optical pump power.

To test the temporal stability of the disturbed spectrum, the waveguide was subsequently kept at constant temperature with no in-coupled light for one week. Afterwards, I repeated the measurement, but this time using lower input power values. The photorefractive damage is expected to be primarily induced by the higher energy pump laser in the NIR and the generated SFG signal in the visible range. Therefore, from now on, the power of the NIR laser was reduced strongly to (1.80 ± 0.06) mW to avoid additional photorefractive damage, induced by the measurement itself. The power of the telecom laser was kept constant at (20.0 ± 0.6) mW. The spectrum measured with these input power values exhibits

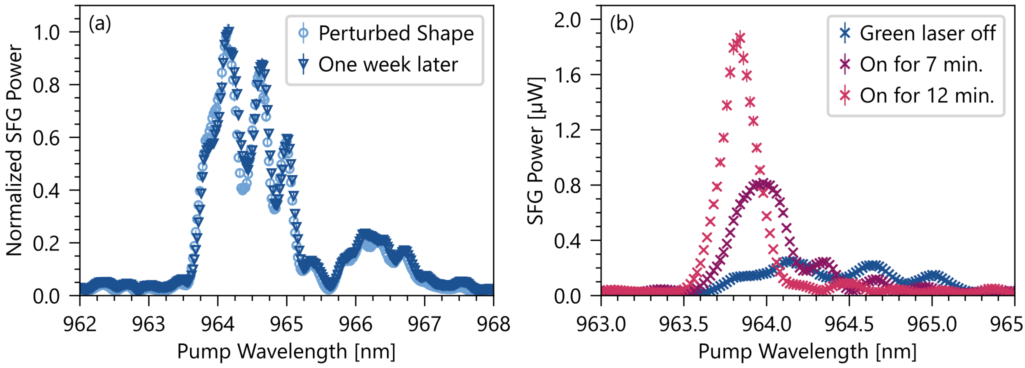

Figure 5.3: Normalized SFG spectra of the cryogenic waveguide. (a) The waveguide shows an initially perturbed spectrum. This spectral shape does not change after one week, indicating that the charges are not moving under cryogenic conditions. (b) When the light from a green laser diode is coupled to the waveguide, the spectrum changes. The dark blue data points correspond to the same measurement as shown in (a), when the green light is still turned off.

no significant changes compared to the measurement one week prior (see Fig. 5.3 (a)). This suggests that, in the absence of sufficient thermal or optical energy, the dislocated charges remain immobilized under cryogenic conditions for at least one week.

Optical cleaning approach

To explore the possibility of actively mobilizing the “frozen-in” charges, in the second experiment, the pump power values were kept at the low level, while additionally activating the green laser. I measured the phase-matching spectrum repeatedly at regular intervals. Fig. 5.3 (b) shows the induced changes after waiting for 7 min and 12 min. Remarkably, the spectral shape began to evolve within a few minutes, after it remained unchanged for one week when no light was coupled. After only 7 min of auxiliary laser exposure, the spectrum approached the expected sinc^2 shape with less pronounced side lobes. Additionally, the wavelength that yields maximum SFG power experienced a blue shift.

Following 12 min of illumination, the maximum generated power increased significantly from (0.25 ± 0.01) µW to (1.87 ± 0.06) µW and the shape of the phase-matching spectrum was close to the ideal shape. These findings indicate that sufficient optical energy can mobilize trapped charge carriers even at cryogenic temperatures. This enables the carriers to recombine or migrate to new lattice positions, thereby allowing for modification of the phase-matching characteristics.

In the third measurement series, the green laser was switched off and I investigated the impact of incrementally increasing the pump power on the phase-matching. Fig. 5.4 (a) displays the dependence of the SFG peak power on the NIR pump power. At first, the SFG peak power increases linearly, as expected for the low pump power regime without

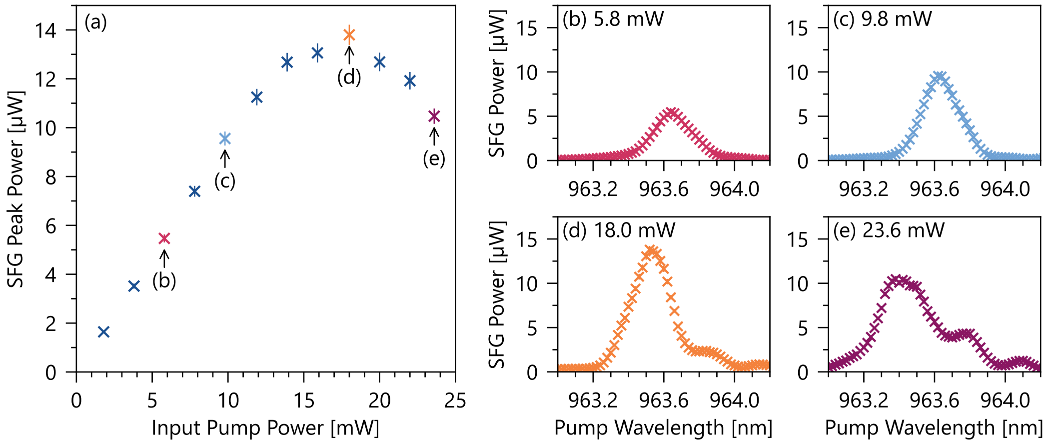

Figure 5.4: An increase in the NIR pump power leads to photorefractive disturbances in the nonlinear waveguide response. Any initial damage was compensated before employing the green illumination (see Fig. 5.3). (a) The pump power is gradually increased. The SFG peak power first increases and then drops again. (b) - (e) Individual spectra measured for different pump powers. Increased power results in broadening of the spectrum and the evolution of side peaks.

inducing photorefractive damage. However, when the pump power exceeds approximately 15 mW, the slope reaches a maximum before the generated power begins to decrease. This effect can be explained by photorefraction rather than pump-depletion or saturation, because the generated power (12 µW) is much lower than the provided power at either the telecom (20 mW) or NIR pump wavelength (15 mW). This assumption is supported by the observation of increasing distortions in the phase-matching spectrum. The individual spectra at lower pump power (see Fig. 5.4 (b), (c)) exhibit a single and well-defined peak at a consistent central wavelength. Spectra recorded at higher pump power (see Fig. 5.4 (d), (e)) show a shift toward shorter wavelengths and the emergence of side peaks. The amount of distortion clearly grows as the pump power is increased. These results indicate that the cryogenic waveguide exhibits an evident threshold for optical power. Specifically, this threshold was observed for the combination of an input pump power of 18 mW at approximately 964 nm and a generated SFG power of about 14 µW around 595 nm.

After photorefractive damage was induced using excessive pump power levels, this damage was partly mitigated again by repeating the simultaneous coupling of the green laser. Here, the input power of the NIR laser was reduced again to 1.8 mW, before the green laser was re-activated and the phase-matching spectrum was monitored over time. The temporal changes in SFG peak power are shown in Fig. 5.5 (a). The data demonstrates an increase in SFG peak power. Simultaneously, the individual spectra in Fig. 5.5 (b) - (e) verify the disappearance of the previously formed side peaks. These variations seem to slowly saturate after about 19 min. After this time, a notable improvement of the nonlinear response is visible. However, in comparison to the first application of green light, the phase-matching spectrum did not fully recover. The SFG peak power did not reach the

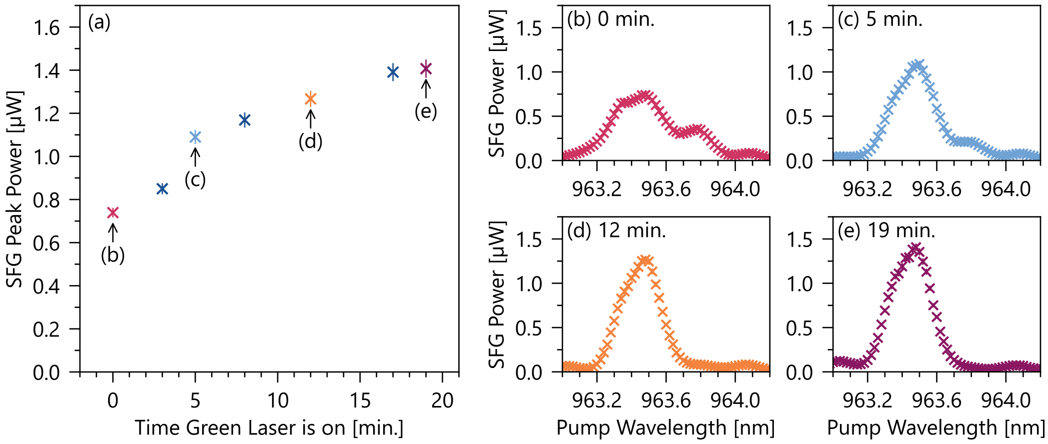

Figure 5.5: Repeating the simultaneous coupling of the green laser partially mitigates the photorefractive damage previously caused by high optical power (see Fig. 5.4). (a) Keeping the green light activated for about 19 min results in an increase of the SFG peak power. (b) SFG spectrum measured before the green light was turned on. (c) - (e) Individual spectra measured over time after activating the green laser, demonstrating an improvement in spectral shape.

same level as before and this time, the central peak shifts to even shorter wavelengths. This partial recovery suggests that while green illumination can relax a significant portion of the photorefractive damage, some residual effects persist after repeated cycles of damage and healing.

Moreover, a consistent blue shift was observed throughout the measurements. It has been shown before that photorefractive damage can result in a blue shift of the phase-matched wavelength [153]. However, the observed blue shift did not only occur for the experiment, where the pump power was increased (which was meant to induce photorefraction), but also for the first green light application (which was meant to relax the damage). Specifically, the maximum SFG power initially occurred for a pump wavelength of (964.16 ± 0.02) nm. The wavelength then shifted to (963.84 ± 0.02) nm during the first green light exposure, changed to (963.38 ± 0.02) nm when increasing the power, and finally remained almost unchanged at (963.48 ± 0.02) nm during the repeated green light coupling. These observations imply that the photorefractive perturbations in the cryogenic waveguide are only partially reversible. Although the coupling of the green laser increased the generated SFG power and enhanced the spectral shape, the blue shift indicates that the charge carrier distribution and refractive index changes did not fully recover to their initial states.

Assessment of photorefractive mitigation

The dislocated charges at cryogenic temperatures remain immobilized for at least one week if no thermal or optical energy is supplied. However, sufficient optical energy can mobilize these charges even under cryogenic conditions. The cryogenic investigation confirmed that auxiliary green illumination actively interacts with the “frozen-in” charge distribution. This was evidenced by the clear modifications observed in the phase-matching spectra. However, while the green laser succeeded in mobilizing charge carriers and thus partially relaxing the photorefractive damage, some residual effects remain. The observed blue shift suggests that the currently used green laser diode does not allow to fully reverse the photorefractive damage at cryogenic temperatures. The phase-matching spectrum did not fully recover to its prior state after repeating the green illumination.

Building on these results, future work should focus on optimizing the presented mitigation protocol. Potential refinements include modification of the auxiliary laser beam parameters - such as implementing pulsed operation, exploring alternative wavelengths, or precisely calibrating the required optical power and exposure duration. Furthermore, a comprehensive theoretical study of the cryogenic material parameters and the exact energy levels of the polarons can support optimization of the auxiliary light properties.

Beyond optical methods, the relaxation of trapped charge carriers could be further enhanced through the controlled application of external electric fields or the integration of conductive coatings on the waveguide surface. Combining different approaches could lead to a routine, in-situ “healing procedure” capable of maintaining the device performance over extended operational periods. Successfully managing photorefraction in cryogenic lithium niobate waveguides would clearly expand the potential of this versatile platform for advanced quantum photonic applications.

5.1.3 Experimental refractive index determination using type-0 SFG

Accurate description of the cryogenic Ti:PPLN waveguides demands knowledge about the effective refractive indices, as the transition from RT to cryogenic conditions induces a strong shift. As described in Section 2.1.3, the empirical refractive index data for bulk lithium niobate can be found in Refs. [159] and [160], for the ordinary and extraordinary refractive indices, respectively. This data was obtained from measurements performed at RT and above. The cryogenic extrapolation of these curves builds the foundation for RSoft simulations, which provide an approximation for the effective refractive indices for a specific waveguide geometry. This extrapolation inherently introduces an uncertainty. This could be seen clearly from a deviation in the cryogenically phase-matched SHG wavelength of a type-II process (see Section 2.1.3). The characterization of type-II phase-matching enables the derivation of an empirical correction term. However, this correction is applicable only to a specific linear combination of the interacting refractive indices, which encompasses both TE- and TM-polarized modes. For this reason, type-II phase-matching cannot be employed to determine the separate effective refractive indices for the individual polarizations.

In contrast, a type-0 phase-matched NLO process, which is fundamentally limited to a single polarization, represents a valuable tool to experimentally identify the refractive index data for this polarization. In this section, an empirical technique is presented, which allows to characterize the dispersion of the cryogenic waveguides. This approach is based on the methods presented in Refs. [191] and [192], where experimentally measured phase-matched wavelength combinations were fitted with a Sellmeier equation to improve the accuracy of the Sellmeier coefficients. Both works characterize a type-0 quasi-phase-matched process; first, in an optical parametric oscillator in an MgO-doped lithium niobate crystal [191], and second, for an SPDC process in a KTP crystal [192]. Here, integrated type-0 widely non-degenerate SFG is employed in the Ti:PPLN platform, which was detailed before in Chapter 4.

The refractive index determination takes into account that the three interacting fields of pump, signal, and idler obey energy and momentum conservation. Accordingly, the underlying Sellmeier equation $n(\lambda)$ must fulfill the quasi-phase-matching condition

$$\Delta k_{\mathrm{QPM}} = \frac{n(\lambda_{\mathrm{p}})}{\lambda_{\mathrm{p}}} - \frac{n(\lambda_{\mathrm{s}})}{\lambda_{\mathrm{s}}} - \frac{n(\lambda_{\mathrm{i}})}{\lambda_{\mathrm{i}}} \pm \frac{2\pi}{\Lambda} \overset{!}{=} 0\,, \tag{5.1}$$

for the corresponding wavelengths λ and the poling period Λ. Based on energy conservation, the measurement of two phase-matched wavelengths (λ_{s} and λ_{i}) allows to calculate the third one

$$\lambda_{\mathrm{p}} = \left(\frac{1}{\lambda_{\mathrm{s}}} + \frac{1}{\lambda_{\mathrm{i}}}\right)^{-1} . \tag{5.2}$$

The general shape of both Sellmeier equations for TE and TM polarization is highly similar, with the extraordinary equation (TM) featuring one additional term. The equation for the ordinary refractive index (TE) has the form [159]

$$n_{\mathrm{o}}(\lambda, T)^2 = a_1 + \frac{a_2 + b_1 f(T)}{\lambda^2 - (a_3 + b_2 f(T))^2} + b_3 f(T) - a_4\lambda^2\,, \tag{5.3}$$

with the wavelength in microns and $f(T)$ containing the temperature dependence, which is given by

$$\begin{align} f(T) &= (T - T_0)(T + T_0 + 546) \tag{5.4}\\ &= (T - 24.5\,^\circ\mathrm{C})(T + 570.82)\,, \tag{5.5}\end{align}$$

with the temperature T in °C. The Sellmeier equation for the extraordinary refractive index is described by [160]

$$n_{\mathrm{eo}}(\lambda, T)^2 = a_1 + \frac{a_2 + b_1 f(T)}{\lambda^2 - (a_3 + b_2 f(T))^2} + b_3 f(T) - a_4\lambda^2 + \frac{a_5 + b_4 f(T)}{\lambda^2 - a_6^2}\,. \tag{5.6}$$

The supplementary term corresponds to an additional resonance term, which only becomes relevant if the wavelength approaches the resonance wavelength $a_6 \approx 11.35\,\mu\mathrm{m}$ [160]. The experimental refractive index determination in this section concentrates on the wavelength range from 400 nm to 1800 nm. As this considered range is far away from the resonance wavelength a_6, I approximate the term $(a_5 + b_4 f(T))/(\lambda^2 - a_6^2)$ as a constant, with $\lambda = 1.5\,\mu\mathrm{m}$.

The empirical method presented here aims to deduce the Sellmeier equation for a specific waveguide geometry at a fixed temperature. Therefore, the term $f(T)$ is constant and can be combined with the coefficients a_i and b_i. This allows to reduce both Sellmeier equations (Eqs. (5.3) and (5.6)) to a compact, temperature-independent form, given by [159]

$$n_{\mathrm{o/eo}}(\lambda)^2 = A_1 + \frac{A_2}{\lambda^2 - A_3^2} - A_4\lambda^2 \,. \tag{5.7}$$

The newly defined coefficients are derived from the literature Sellmeier coefficients [159, 160], assuming a cryogenic temperature of $T = -268\,^\circ\mathrm{C} \approx 5\,\mathrm{K}$.[2] These literature values for bulk lithium niobate act as initial Sellmeier coefficients, which will be optimized in a two step process to find tailored Sellmeier equations for the cryogenic Ti:PPLN waveguides.

This optimization technique necessitates a data set of experimentally characterized phase-matched wavelength combinations $\{\lambda_\mathrm{s}, \lambda_\mathrm{i}\}$ for distinct poling periods. The characterization is performed on the same experimental setup, as in the preceding photorefraction measurements (see Fig. 5.2). Here, the only difference is that no green laser diode is employed. The wavelength of the telecom laser (λ_s) is fixed and the wavelength of the NIR laser (λ_i) is scanned. The idler wavelength which results in maximum SFG power is recorded and the corresponding wavelength λ_p is calculated from Eq. (5.2).

Two distinct waveguide samples are characterized, which provide multiple waveguide groups, phase-matching cryogenic type-0 SFG. The first sample possesses 7 µm wide waveguides with poling periods for TM polarization and the waveguides of the second sample have a width of 5 µm and poling periods for TE polarization. The different waveguide widths are attributable to the fact that the first sample was not custom made for this experiment. However, this section mainly aims to present the technique, which can be applied in future work to additional waveguide geometries. The two distinct samples enable the derivation of one Sellmeier equation which describes the fundamental TM-polarized modes and one for the fundamental TE-polarized modes at cryogenic conditions.

The measured phase-matched idler wavelengths in dependence of the fabricated poling periods are shown in Fig. 5.6. The data for TM polarization was taken at a temperature of 6.7 K for the signal wavelength fixed to $\lambda_\mathrm{s} = 1570\,\mathrm{nm}$; the data for TE polarization was measured at 6.8 K with $\lambda_\mathrm{s} = 1556.4\,\mathrm{nm}$. In these measurement series each investigated

---

[2] For the ordinary refractive index, A_1 is given by $A_1 = a_1 + b_3 f(T)$, while the extraordinary Sellmeier equation defines this parameter as $A_1 = a_1 + b_3 f(T) + (a_5 + b_4 f(T))/(\lambda^2 - a_6^2)$, with the approximation $\lambda = 1.5\,\mu\mathrm{m}$. The other coefficients remain the same for both polarizations and are described by $A_2 = a_2 + b_1 f(T)$, $A_3 = a_3 + b_2 f(T)$, and $A_4 = a_4$.

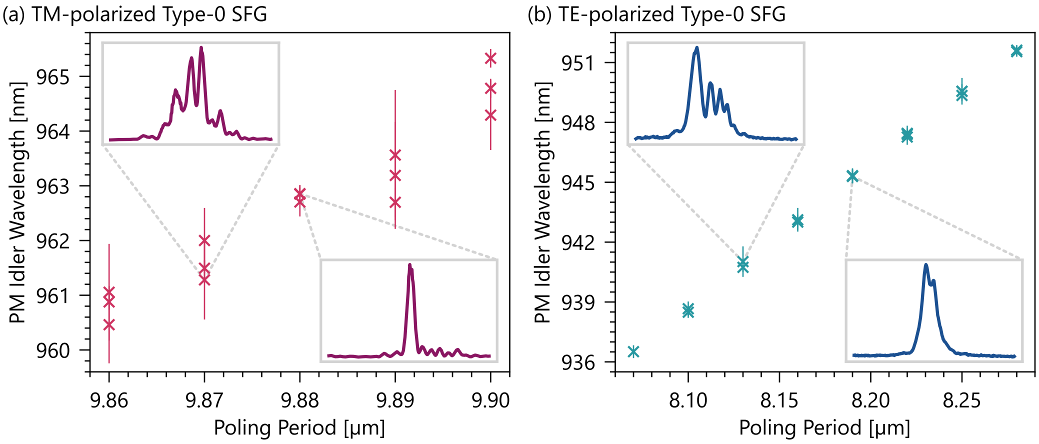

Figure 5.6: Phase-matched (PM) idler wavelengths for distinct poling periods, measured for (a) TM-polarized and (b) TE-polarized SFG. The wavelengths were obtained from the phase-matching spectra by fitting a Gaussian function. The error bars correspond to the FWHM. Two examples of the phase-matching spectra are shown as inset plots in (a) and (b) to visualize strong differences in the spectral shapes.

waveguide exhibited phase-matched SFG under cryogenic conditions. However, the measured phase-matching spectra vary in their spectral shape and width. In order to determine the central idler wavelengths, a Gaussian function was fitted to each spectrum. This fit does not need to describe the spectral shape accurately, as the only required parameter for the optimization is the phase-matched idler wavelength. The full widths at half maximum (FWHM) were chosen as the uncertainties in the central wavelengths, which are displayed as the errorbars. Note that the y-axes scale differently for Fig. 5.6 (a) and (b), due to the variety of available poling periods for the TE-polarized process. The average FWHM is similar for both polarizations, 0.96 nm for TM and 0.77 nm for TE. Two phase-matching spectra are presented for each polarization as insets in Fig. 5.6 to provide examples for the observed differences in the spectral shapes.

These data sets build the foundation for the optimization algorithm. Both polarizations are analyzed separately, but the evaluation follows the same principle. The individual steps of the procedure are discussed below:

1. The simulation tool RSoft is used to calculate the effective refractive indices at a temperature of 5 K for the given waveguide geometries (n_{eo} for 7 µm wide waveguides and n_{o} for a width of 5 µm). The indices are simulated for a list of wavelength values ranging from 400 nm to 1800 nm. These simulated effective refractive indices are plotted over the wavelength in Fig. 5.7 (a) and (b). This broad wavelength range not only provides coverage of the wavelengths relevant to the SFG process (approx. 590 nm to 1570 nm), it is also chosen to improve the accuracy of the Sellmeier fit performed in the next step. This fit yields a Sellmeier equation that can be applied to design diverse frequency conversion processes at other wavelengths.

2. The simulated data points are fitted with the Sellmeier equation in Eq. (5.7) to obtain the set of coefficients $\{A_1, A_2, A_3, A_4\}$ which describe the simulated data best. The initial guess for this fit takes into account the coefficients for bulk lithium niobate [159, 160]. Both the Sellmeier equation for the initial guess and the fitted curve to the simulation data are shown in Fig. 5.7 (a) and (b). The simulated effective refractive indices are slightly larger than those for the bulk crystal, which is associated with the titanium in-diffusion that results in a refractive index increase. The determination of this "simulated Sellmeier equation" completes the first optimization step.

3. The second step utilizes the experimental data. For every waveguide that was characterized, the following parameters are compiled: $\{\Lambda_{\mathrm{RT}}, T, \lambda_{\mathrm{s}}, \lambda_{\mathrm{i}}, \lambda_{\mathrm{p}}\}$. This set comprises the fabricated room-temperature poling period Λ_{RT}, the operation temperature T, and all three phase-matched wavelengths. Here, an increased number of characterized waveguides improves the accuracy of the optimization results.

4. The wanted Sellmeier equation $n(\lambda)$ must fulfill

$$\alpha(T)\Lambda_{\mathrm{RT}} = \left[\frac{n(\lambda_{\mathrm{p}})}{\lambda_{\mathrm{p}}} - \frac{n(\lambda_{\mathrm{s}})}{\lambda_{\mathrm{s}}} - \frac{n(\lambda_{\mathrm{i}})}{\lambda_{\mathrm{i}}}\right]^{-1} \tag{5.8}$$

   for each parameter set $\{\Lambda_{\mathrm{RT}}, T, \lambda_{\mathrm{s}}, \lambda_{\mathrm{i}}, \lambda_{\mathrm{p}}\}$. Here, it is employed that the poling period at temperature T is given by $\Lambda(T) = \alpha(T)\Lambda_{\mathrm{RT}}$, using the contraction coefficient $\alpha(T)$ defined in Eq. (2.18). To determine the refractive index function $n(\lambda)$, an optimization algorithm is employed to identify the set of coefficients $\{A_1, A_2, A_3, A_4\}$ for Eq. (5.7). This is achieved by utilizing a minimization function that reduces the discrepancy between the fabricated poling period Λ_{RT} and the theoretical poling period derived from the experimental data. The initial guess for the Sellmeier coefficients is the fit of the RSoft simulation data, as this model is expected to provide a robust starting estimation. For every iteration, the algorithm calculates the residual for each parameter set $\{\Lambda_{\mathrm{RT}}, T, \lambda_{\mathrm{s}}, \lambda_{\mathrm{i}}, \lambda_{\mathrm{p}}\}$, ultimately minimizing the sum of these deviations to identify the Sellmeier equation that best describes the experimental results.

Consequently, the optimized coefficients $\{A_1, A_2, A_3, A_4\}$ allow to calculate the fabricated poling period Λ_{RT} from the measurement results with high accuracy. Conversely, this means that a Sellmeier equation was deduced, which describes the effective refractive indices for the characterized waveguide at the given operation temperature more accurately as the former model, which relied exclusively on the RSoft simulations. Both the simulated curves and the optimized Sellmeier equations for TM and TE polarization are shown in Fig. 5.7 (c) and (d), respectively. The absolute deviation between both Sellmeier equations is small, as the refractive indices differ in the order of 10^{-4}. The total deviation $\Delta n_{\mathrm{o/eo}}(\lambda)$ is presented separately in an inset plot for each polarization. The absolute coefficients for the simulated and optimized curves are listed in Table 5.1.

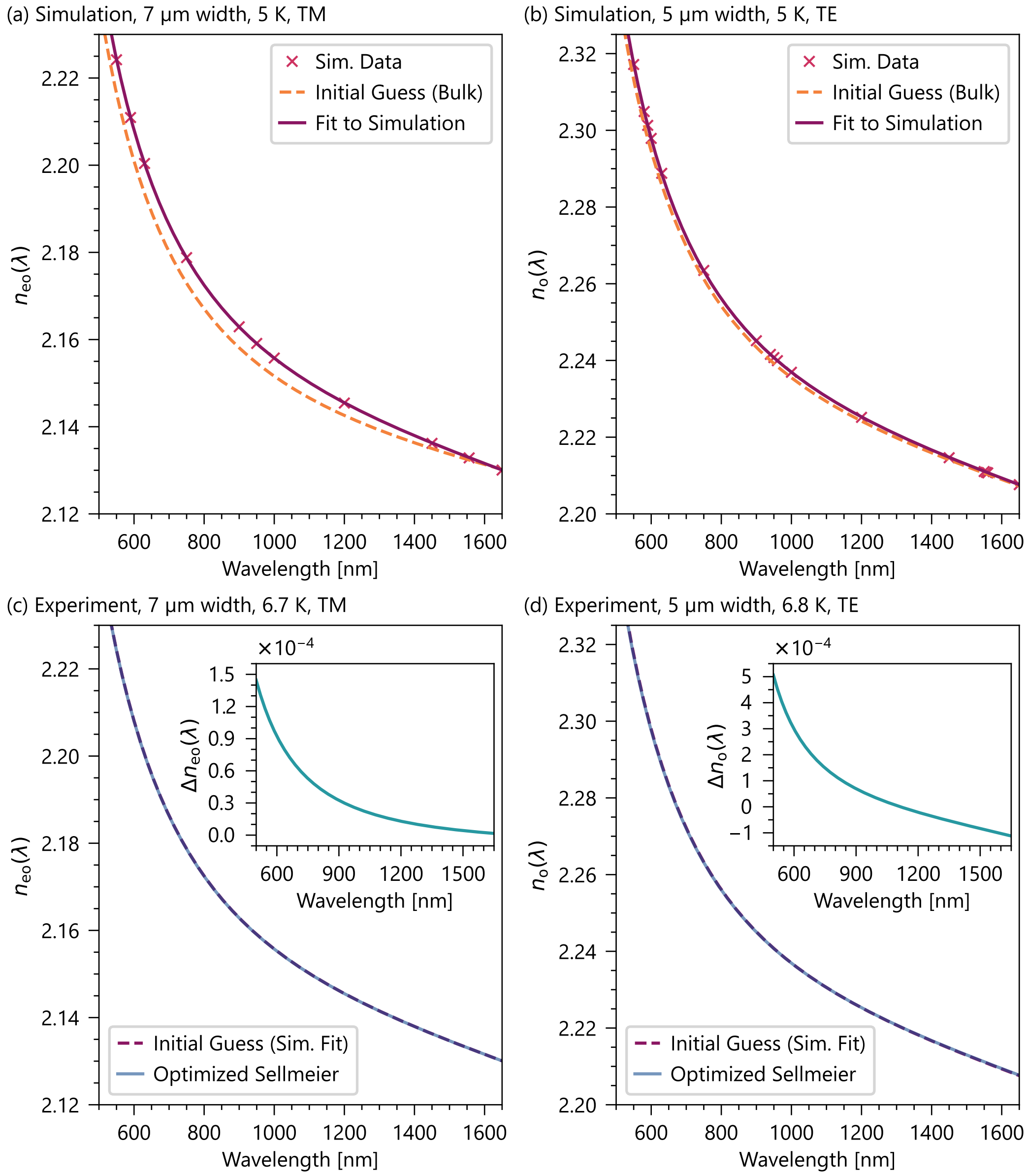

Figure 5.7: Wavelength-dependent refractive index data of lithium niobate for TM-polarized (left side) and TE-polarized (right side) light. In the first optimization step ((a), (b)), the Sellmeier equation in Eq. (5.7) is fitted to the simulation data obtained from RSoft simulations. The initial guess for this fit is the literature data for bulk lithium niobate. In the second step ((c), (d)), the algorithm identifies the optimal Sellmeier coefficients by minimizing the residuals between the fabricated poling period and the period calculated from the experimental data. The initial guess for this optimization is the fit to the simulation data performed in (a) and (b). The inset plots show the absolute deviation between the simulated and optimized Sellmeier equations.

Table 5.1: Coefficients for the temperature-independent Sellmeier equation (Eq. (5.7)). The table lists the coefficients for the simulated curves (fitted to RSoft simulation data) and the empirically optimized curves (deduced from experimental data) for TM and TE polarization. The data was analyzed for a waveguide width of 7 µm and 5 µm, respectively, which was defined by the experimental conditions.

Coefficient	**Sim. TM (7 µm, 5 K)**	**Opt. TM (7 µm, 6.7 K)**	**Sim. TE (5 µm, 5 K)**	**Opt. TE (5 µm, 6.8 K)**
A_1	4.565 92	4.565 97	4.911 40	4.911 57
A_2	0.101 278	0.101 133	0.115 569	0.115 103
A_3	0.205 042	0.205 042	0.235 483	0.235 347
A_4	0.024 431 1	0.024 431 8	0.029 841 9	0.029 657 8

The introduced optimization algorithm is built on two necessary key assumptions. First, high accuracy of the fabricated poling period is presumed, as the optimization treats this value as the target parameter toward which it must converge. The periodical poling of the characterized waveguide samples was fabricated with laser lithography, ensuring high precision in the poling period. However, this accuracy could be further improved by employing electron beam lithography. Second, precise knowledge of the temperature dependence of these poling periods is required. As discussed in Section 2.1.3, published data for the thermal expansion coefficient span temperatures down to 60 K [161, p. 47], which allows an accurate description of the thermal contraction down to this temperature. Although the exact contraction for lower temperatures is not known, further changes in the length can be assumed minimal since the thermal expansion coefficient must disappear at 0 K.

Despite the barely noticeable deviation in the simulated and optimized Sellmeier equations, the optimized functions result in an apparent shift of several nanometers in the wavelengths when calculating the phase-matching point for an NLO process. As an example, we consider a fully TM-polarized SPDC process, with the same parameters that were used for the SFG characterization (7 µm wide waveguides at a temperature of 6.7 K). For a pump wavelength of 590 nm and a poling period of 9.56 µm, a calculation based on the simulation data results in a signal wavelength of $\lambda_\mathrm{s} = (1554.20 \pm 0.02)$ nm and an idler wavelength of $\lambda_\mathrm{i} = (951.02 \pm 0.01)$ nm. When using the experimentally optimized Sellmeier equation, a signal wavelength of $\lambda_\mathrm{s} = (1547.15 \pm 0.02)$ nm and an idler wavelength of $\lambda_\mathrm{i} = (953.68 \pm 0.01)$ nm are predicted. The widely non-degenerate SPDC process detailed in Chapter 4 was implemented in a waveguide with a 5 µm width. Consequently, the accuracy of the refined Sellmeier equation cannot be directly validated against these specific SPDC results due to the difference in waveguide geometries.

As the optimization strongly relies on the measured phase-matched wavelengths, a shift in these experimental wavelengths results in a varying Sellmeier equation. Indeed, the overall waveguide performance and the exact phase-matching point can differ in repeated cooling cycles due to the interplay of pyroelectricity and photorefraction. Specifically, this observation is discussed next in Section 5.2. The presented model thus serves as a useful tool to determine the effective refractive indices, but the accuracy of the determined Sellmeier equations should be increased in future studies. This includes repeating the procedure for several thermal cycles and also multiple waveguide samples of the same fabrication parameters.

5.2 Studies on the reproducibility of cryogenic performance

At a glance
The measurement series addresses the third main research question: *What do our observations teach us about the viability of cryogenic lithium niobate?* To define the conditions under which the investigated Ti:PPLN platform can be beneficial for cryogenic integrated optics, I evaluated the performance of 15 waveguides across a series of six cooling cycles. These waveguides are organized into five groups, each subjected to distinct experimental conditions. These measurements were developed to address specific research considerations detailed in the preceding chapters.

The measurements are performed with the same waveguide sample that was employed for the cryogenic degenerate SPDC process, discussed in Section 3.3. During these experiments, this sample demonstrated notable cryogenic performance, specifically, an SHG phase-matching spectrum close to the ideal shape (see Fig. 3.4). The widely non-degenerate, exclusively TM-polarized phase-matching is highly sensitive to “frozen-in” charges. Therefore, the degenerate type-II process was selected for the reproducibility studies, as it demonstrated higher potential for enabling reliable phase-matching throughout repeated cooling cycles.

5.2.1 Research questions

The chosen Ti:PPLN sample contains five waveguide groups (WGGs) featuring poling periods that are optimized for cryogenic degeneracy in the telecom wavelength range. All groups are characterized by their linear waveguiding properties and the nonlinear SHG response when pumped with approximately 1550 nm. However, the specific experimental conditions for each group vary in terms of either the temporal pump profile (CW or pulsed) or the incident optical power. Each group is therefore dedicated to a distinct measurement; an overview is provided in Table 5.2. These measurements were developed to explore specific research questions that emerged as candidates for further investigation, following the findings of the prior chapters. Five core objectives were formulated to guide this investigation. The corresponding research questions and experimental protocols are detailed below.

Table 5.2: Overview of the experimental SHG measurements designed for each individual waveguide group (WGG). The table summarizes the poling period Λ, the theoretical phase-matched SHG wavelength λ_{SHG} at cryogenic temperature (6 K), the temperature of the experiment (RT: room temperature, CT: cryogenic temperature), and the associated measurements.

WGG	Λ [µm]	λ_{SHG} [nm]	Temp.	Measurement Conditions
8	8.77	1553.9	CT	Pulsed - Increasing power
9	8.78	1554.9	CT	Pulsed - Low power
10	8.79	1556.0	RT, CT	CW - Low power
11	8.80	1557.0	CT	CW - Increasing power
12	8.81	1558.1	CT	CW - High power & green laser coupling

1. **To what extent does the cryogenic cooling process itself influence the waveguiding properties?**
   Objective: Evaluate the influence of the pyroelectric effect on charge carrier distribution and its subsequent impact on the (non)linear properties of the cryogenic waveguides.
   Experiments: Two groups of waveguides are characterized exclusively at low optical power levels to isolate thermal effects from power-induced damage. Any distortions in the waveguiding can be attributed to underlying pyroelectric fields. WGG 9 is analyzed using pulsed excitation, while WGG 10 is monitored under CW operation.

2. **How sensitive is the cryogenic performance of the waveguides to high incident optical power?**
   Objective: Identify the critical power thresholds that trigger the onset of detectable photorefractive damage in the cryogenic regime.
   Experiments: The SHG response of two WGGs is analyzed during an incremental increase in pump power. Power-dependent changes in the conversion efficiency or phase-matching spectrum indicate photorefractive damage. WGG 8 is characterized using pulsed light, while WGG 11 is characterized exclusively with CW light.

3. **Are the observed photorefractive effects limited to CW operation, or do they remain significant under pulsed excitation?**
   Objective: Assess whether cryogenic waveguides exhibit greater resilience to pulsed excitation than to CW operation.
   Experiments: A comparative study is conducted using two WGGs (8, 9) dedicated to pulsed operation and three separate WGGs (10, 11, 12) utilized exclusively with CW light.

4. **What strategies can be employed to re-mobilize trapped charges in order to restore or enhance waveguide performance?**
   Objective: Investigate the practical viability of elevating the charge carrier mobility through both thermal preparation (pre-cooldown) and optical mitigation (in-situ at cryogenic temperatures).

Experiments: Two distinct approaches are tested. First, during the measurement series, the waveguide sample is removed from the cryostat three times and actively heated to 175 °C, where it is held for 30 min, before the phase-matching is analyzed again. Second, WGG 12 is characterized under high CW pump power while simultaneously coupling the auxiliary green laser beam.

5. **To what extent is the cryogenic (non)linear waveguide performance reproducible across multiple thermal cycles?**
   Objective: Identify variations in the cryogenic performance and determine whether passive warming to room temperature and ambient venting are sufficient, to reset the material's internal charge state and ensure reproducible nonlinear performance.
   Experiments: The same waveguide sample undergoes six consecutive cryogenic cycles. Between cycles, the sample is returned to room temperature and the vacuum chamber is vented for several hours to simulate standard laboratory handling. Room-temperature characterization is restricted to low-power CW operation to prevent additional photorefractive damage. Notably, an active high-temperature heat-up is performed prior to the first and fifth cycles to serve as a baseline. This aims to dissipate persistent charge carrier distributions, ensuring a well-defined, "pristine" initial state for the cooldown.

5.2.2 Experimental setup

The experimental setup around the free-space coupled cryostat was optimized to enable efficient transitioning between the diverse measurement protocols for each waveguide group. Optimization involved providing access to all required laser sources, without the need to exchange optical fibers, and to set up fixed detection stages for both the transmitted infrared beam and the generated visible SHG light. This ensured a high degree of reproducibility in data acquisition for the individual thermal cycles. The optimized experimental setup is visualized in Fig. 5.8.

The tunable telecom CW laser (T500S, EXFO) and the pulsed IR laser (Onefive Origami 15 LP, NKT Photonics) are overlapped using a flip mirror. In addition, a visible light source is set up, originating either from a red laser, or from the green laser diode. The red laser is used for general alignment, whereby its optical pump power is limited to 1 mW. The green laser is exclusively employed to test the photorefraction mitigation technique for WGG 12. This group was actively selected for the green illumination as it is on the edge of the tested area. This way, scattered green light is expected to remain low for most of the other waveguides.

The out-coupled beam is spectrally separated with a DM and one power meter (PM) is set up for each path. The distance from the waveguide end facet to the sensors was empirically optimized, so that both the IR beam and the SHG signal are simultaneously focused on their associated power meters. A beam camera is mounted together with the IR PM on a common rail carrier. Calibrated mechanical stops ensure a highly reproducible alignment. The fixed position of the beam camera serves as a spatial reference, ensuring that each waveguide

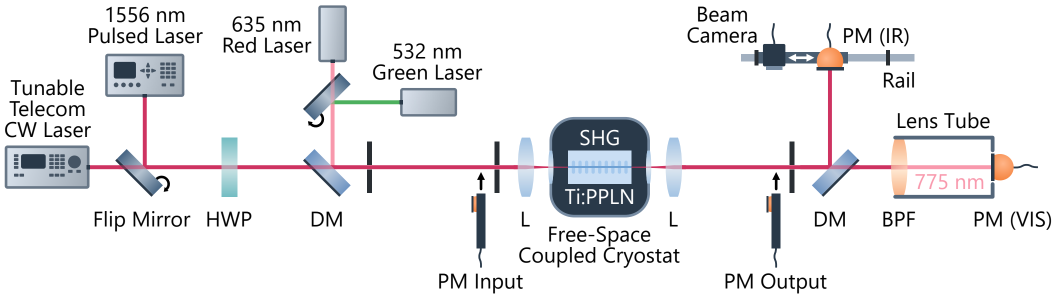

Figure 5.8: Experimental setup to characterize the distinct WGGs according to their IR waveguiding and SHG response. Both signals are detected simultaneously. Two flip mirrors are installed to chose from CW or pulsed excitation, as well as to select a visible laser source (for alignment or photorefraction mitigation). A movable power meter (PM) is used to detect the IR input and output power at any time at predefined positions. HWP: half-wave plate, DM: dichroic mirror, L: aspheric lens, BPF: band-pass filter.

is aligned to the same position when switching between neighboring channels. This is a critical feature to facilitate the cryogenic alignment. The VIS PM is shielded from ambient light using a lens tube. The BPF (550 nm - 850 nm) suppresses potential third-harmonic light from the pump lasers and the green light when characterizing WGG 12.

5.2.3 Measurement series

The experimental setup in Fig. 5.8 was utilized to perform a systematic series of six cooldown (CD) cycles, combined with room-temperature (RT) phase-matching measurements of WGG 10 and the application of the previously introduced heat-up (HU) method. The chronological sequence of these stages is visualized in Fig. 5.9. Initially, RT phase-matching spectra for WGG 10 were recorded to establish a baseline for the sample, which remained untouched for approximately nine months. This was followed by the first HU and a subsequent RT measurement to track any induced shifts in the phase-matching properties. After two initial cooldown cycles, the RT measurement was repeated to serve as an indicator of whether cryogenic operation has a long-term influence on the room-temperature phase-matching. Following two additional CDs, a second HU was executed to facilitate a “reset” of potentially persistent charge carrier distributions. The final two CDs were followed by a concluding sequence of RT, HU, and RT characterizations to evaluate the stability of any induced charge distributions and the effectiveness of the thermal reset once more.

This complete measurement series was carried out over a time span of approximately 1.5 months. The cooldown and warmup procedures were performed with a slow temperature change limited to 0.8 K/min. As the vacuum might pretend compensation of accumulated charge fields, each warmup was followed by venting the vacuum chamber for several hours before another cooldown was initialized. The majority of the individual measurements were performed with a maximum rest period of two days. However, CD 5

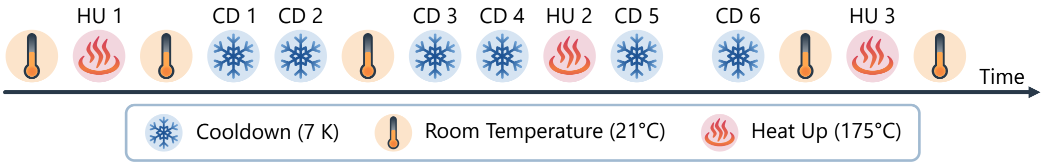

Figure 5.9: Schematic timeline of the experimental sequence. The characterization comprised six consecutive cooldown (CD) cycles, five room-temperature phase-matching measurements of WGG 10, and three controlled heat-up (HU) processes. While the majority of the stages followed a continuous chronological order, an extended ten-day interval occurred between CD 5 and CD 6.

and CD 6 were suspended for a period of ten days. This is noted here as significant changes were observed in the cryogenic performance of these two cooling cycles.

The phase-matching shifts by approximately 26 nm between RT and CT operation. While the cryogenically phase-matched wavelengths are within the bandwidth of the pulsed pump laser, this laser is not tunable and does not match the RT wavelengths. Therefore, the RT characterization is limited to CW pump light and a comparison of the pulsed performance at both experimental temperatures is not feasible. The CW phase-matching spectra are recorded by scanning the pump wavelength, while measuring the SHG power and the transmitted pump power. In contrast, the pulsed SHG measurements at CT exclusively record three power values: the input and transmitted pump power, together with the SHG power. A wavelength-dependent measurement is not possible, as the SHG is generated by the complete, broadband pump spectrum.

5.2.4 Evaluation of the waveguide performance

A full, detailed description of the measurements and experimental results for each waveguide group are included in Appendix A.5.1. Here, I concentrate on the salient features of the results which answer the research questions. First, a brief overview of the general performance across the thermal cycles is provided to contextualize the findings. In the initial cooldown (CD 1), the linear waveguiding of TM-polarized light was severely limited, despite the sample having remained unexposed to cryogenic temperatures or high optical power for nine months prior. While coupling of the TE-polarized beam yielded a well-defined, collimated waveguide mode, the TM-polarized mode exhibited significant propagation losses and scattering, preventing the detection of a measurable CW SHG signal.

This poor TM-waveguiding quality persisted throughout CD 2. In CD 3, measurements on WGG 12 confirmed that no improvement had occurred; consequently, this cycle was ended early to focus the characterization on the impact of the upcoming second heat-up (HU 2). The subsequent CD 4 confirmed that the performance remained consistently poor and unchanged in comparison to CD 2. All waveguides from the five inspected groups demonstrated a very uniform response for TM-polarized pump light within the distinct thermal cycles. However, following HU 2, the cryogenic waveguides finally exhibited proper TM-mode confinement, which was achieved by simply rotating the input polarization from TE to TM. Consequently, CD 1 and CD 5, which were both performed subsequent to a heat-up, resulted in completely different waveguiding qualities. This enabled the detection of SHG signals across all groups in CD 5. In the final cooldown (CD 6), the waveguiding quality enhanced even more, which consistently yielded the highest performance levels recorded throughout the entire measurement series.

In summary, the pulsed operation did provide a measurable SHG signal in each thermal cycle, while CW pumped SHG was only successful in the last two cooldowns. The pulsed efficiencies varied in the individual cycles and maximizing the SHG power required adjusting the pump polarization almost completely to TM, in order to compensate for high propagation losses of this polarization. To allow for a direct comparison between the diverse experimental protocols, the key observations at each chronological stage are summarized in Table 5.3. This overview examines the performance of all WGGs across the six thermal cycles, where each group is graded based on its linear waveguiding quality and nonlinear SHG stability. The grading scale is classified as follows: (++) Optimal (peak performance recorded in this series), (+) Stable (a clear, detectable SHG response), (~) Compromised (significant reduction in conversion efficiency), (−) No signal (absence of detectable SHG), and (x) Not evaluated (measurement omitted).

Before revisiting the research questions defined in Section 5.2.1, I would like to detail two specific experiments. The step-wise pulsed power increase for WGG 8 caused a sudden drop in the transmitted and SHG power when exceeding a certain threshold. I conducted a more detailed measurement of this drop, to investigate the waveguides' susceptibility to high incident power, thereby addressing research question 2. Following this discussion, the reproducibility of the RT measurements is evaluated, which were performed at different stages throughout the measurement series: before any cooldown, following a poorly performing cooldown, and subsequent to the best performing cooldown. These measurements address research questions 4 and 5, by evaluating the implications of the heat-up procedure and discussing whether the return to RT is sufficient to dissolve persistent charge fields present at CT.

Table 5.3: Overview of the key observations made at the individual measurement stages. The performance of each waveguide group 8 - 12 is assessed according to the following grading scale: (++) Optimal, (+) Stable, (~) Compromised, (−) No signal, and (x) Not evaluated.

Stage	8	9	10	11	12	Observations
🌡 ♨ 🌡			++			2.5 year old sample showed very uniform phase-matching spectra for WGG 10 at RT. The HU induced a spectral shift of −1.5 nm. Peak power and spectral shape remained almost unchanged.
❄	++	+	−	−	−	All cryogenic waveguides demonstrated guiding for TE-polarized modes, while TM polarization yielded a scattered mode profile. No SHG signal could be measured for CW operation; generated SHG power was recorded for the pulsed WGGs only. Here, the waveguiding collapsed abruptly when exceeding a certain power threshold.
❄	~	~	−	−	−	Again, CW operation did not yield an SHG signal. Pulsed operation allowed to detect the generated SHG power. However, the conversion efficiency and the acceptable power threshold decreased compared to CD 1.
🌡			++			SHG spectra and peak power were consistent with prior RT tests. After two cooling cycles, the spectra shifted by approx. + 1 nm, but no long-term distortions were observed.
❄	x	x	x	x	−	Only WGG 12 was characterized, which did not provide waveguiding for TM-polarized light and no SHG signal could be measured. This cooldown was aborted as no improvement was observed, in order to allow for more repeated cooldown cycles within the given time frame.
❄	~	~	−	−	−	Again, no SHG signal could be recorded for CW operation. Pulsed performance, in particular the conversion efficiency, was very consistent with the observations for CD 2.
♨ ❄	+	+	+	+	+	Following the second HU, the pulsed conversion efficiency was increased again and the CW operation yielded measurable phase-matching spectra for the first time.
❄	++	++	++	++	++	Both the pulsed and CW performances improved even more in the final cooldown. The CW peak power increased by roughly one order of magnitude and all spectra shifted by approx. + 2 nm.
🌡 ♨ 🌡			++			Spectral shape and intensity were very consistent with preceding measurements. The final HU resulted in a relatively minor wavelength shift.

Photorefraction induced by excessive pulsed pump power

While increasing the power for waveguide 8-1 in the final cooldown, I started a continuous measurement over a time of 10 min. This data is shown in Fig. 5.10. The measurement covers two distinct time intervals spanning each about 5 min: first, the time when I increased the transmitted pump power from 5 mW to approximately 15 mW, at which the waveguiding collapsed, and second, the subsequent period in which the experimental setup was left untouched. The second interval thus represents the time in which the waveguide adapts to the high power, clearly demonstrating strong dynamics on short time scales.

The first interval exhibits a multitude of plateau regions, where the pump power was kept constant for a few seconds. The transitions between the plateaus result from the manual adjustment of the next power step using a HWP. Within the first approximately 200 s, the plateaus are flat, demonstrating that the waveguides can maintain stable power levels. A closer look on the following plateau regions reveals that both power values started to decrease for constant pump power. This indicates that the waveguide already demonstrated unstable operation at these points, but the quick readjustment of the power allowed to record a few more measurement points before the waveguiding collapsed completely. Both signals dropped significantly within about 20 s. As soon as the detected power values dropped, the input pump power was kept constant (at 97.8 mW). The power drop was followed by an oscillating trend which did not saturate within the recorded measurement time.

This temporal decay was analyzed more closely employing WGG 9, after completing the designed experiments for this group in the final cooldown. Until that time, this WGG did only experience low optical pulsed power of 4 mW. These waveguides were analyzed

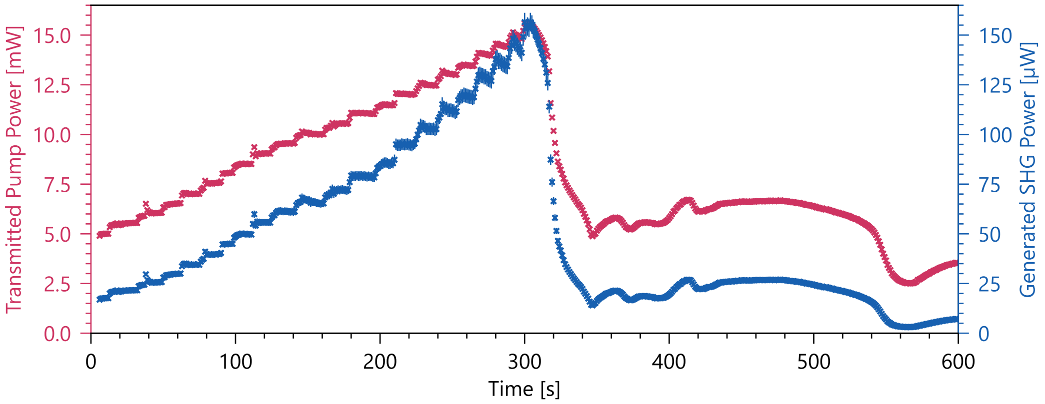

Figure 5.10: Temporal measurement of the transmitted pump power and generated SHG power for WG 8-1 while incrementally increasing the pump power within the first approximately 300 s. The data was recorded within cooldown 6. After both power values dropped rapidly, the setup was not touched anymore to analyze if the power stabilizes after several minutes.

regarding whether they respond with a similarly fast power drop as WGG 8 when suddenly exposed to high power values. The waveguides were coupled with low power first, then the beam was blocked to increase its power to the maximum value, and unblocked again. This way, the waveguides were abruptly coupled with a high input power of 124 mW. The temporal behavior of the detected power values is visualized in Fig. 5.11.

All three waveguides demonstrated similar behavior: both the transmitted pump and the SHG power declined strongly within approximately 40 s. The measurement data on a linear scale (Fig. 5.11 left side) shows that the power settled at a significantly decreased level compared to the initial power measured directly in the second when the waveguide was exposed to the pump beam. When comparing the average power measured in the last 100 s to the first detected power value, the transmitted pump power dropped by 82.1 %, 90.5 %, and 94.3 % for the waveguides 9-1, 9-2, and 9-3, respectively. The data representation on a logarithmic scale (Fig. 5.11 right side) visualizes that this power drop corresponds to a two-step process. The power decreases exponentially at first and then experiences a second, even faster decay. The inflection points are marked in Fig. 5.11 using vertical lines. These times were corrected by the first 6 s in which the beam was blocked, leading to an initial exponential decay time of approximately 15 s to 30 s.

These results clearly demonstrate that the cryogenic waveguides are not resistant to high peak powers under pulsed excitation. The waveguiding performance deteriorates drastically due to the induced photorefractive damage. The flat plateau regions observed for transmitted pump powers up to approximately 10 mW (see Fig. 5.10) suggest a potential regime of stability, provided the optical power remains below a threshold. However, as the SHG source was only operated at constant power for several seconds, these plateaus may not represent the long-term behavior. To draw definite conclusions, future investigations should focus on the long-term stability of pulsed operation at fixed power levels. In addition, more data is necessary to evaluate the recovery dynamics of the waveguides under cryogenic conditions, specifically, whether waveguiding properties are partially restored after extended rest periods.

For the pulsed measurement, I want to note that the detected SHG signal was accompanied by the third-harmonic generation (THG) of the pulsed pump beam. Although this beam was filtered out and did not contribute to the detected SHG power, its wavelength (≈ 520 nm) is close to the wavelength of the green laser diode (532 nm) used to affect the charge carrier mobility. Consequently, the THG could affect the SHG response of the waveguide. Depending on the optical power, this green light might either reduce the photorefractive power thresholds by inducing photorefractive damage itself, or might enhance the waveguide's susceptibility to high optical power. However, as the excitement of the THG was unavoidable in these measurements, it is not possible to isolate the individual contributions of the pump light, SHG, and THG on the breakdown of the waveguiding.

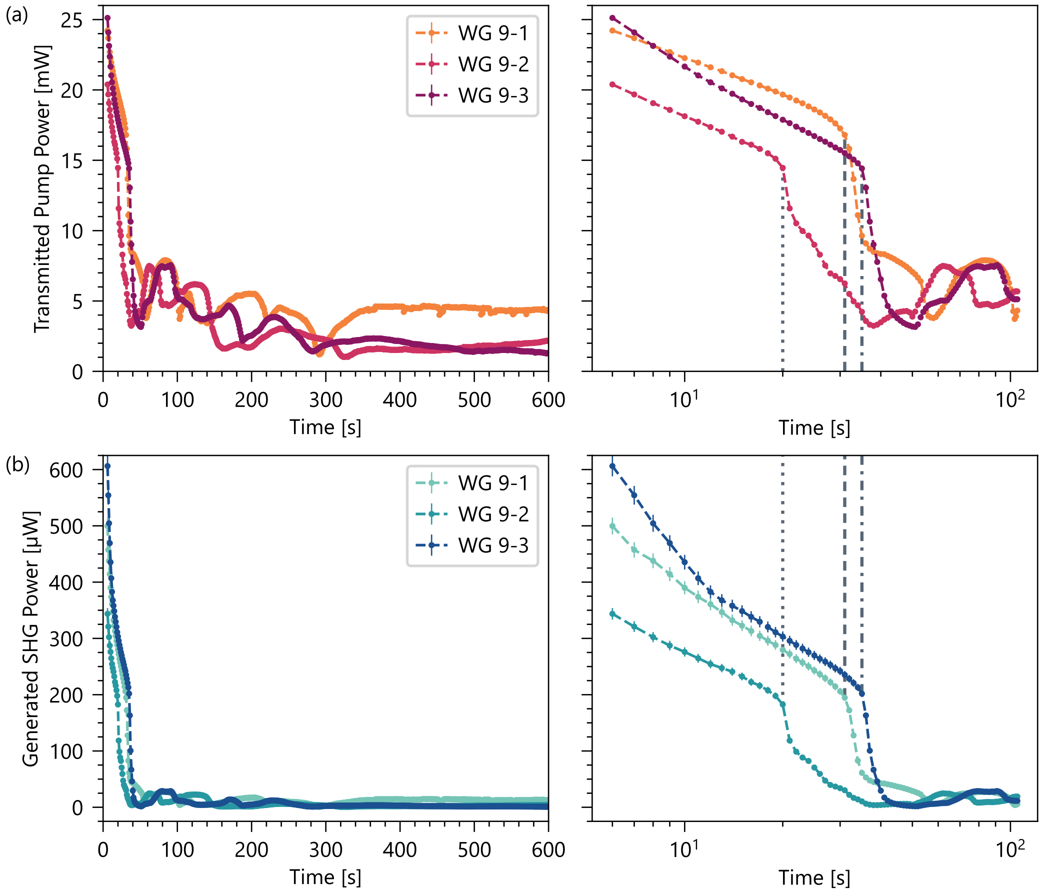

Figure 5.11: Temporal progression of (a) the transmitted pump power and (b) the generated SHG power for WGG 9 after an immediate increase of the pulsed input power. The same data is presented twice, on a linear scale (left side) and additionally on a logarithmic scale (right side) to visualize the power drop within the first seconds. The vertical lines represent the times where the power values experience an even stronger decrease compared to the initial exponential decay.

Decoupling of room-temperature and cryogenic performance

The RT nonlinear response of WGG 10 was characterized at different stages throughout the measurement series. The transmitted pump power was kept constant at (3.4 ± 0.2) mW. The data is shown in Fig. 5.12. All waveguides show a similar spectral shift between the measurements. Despite this total shift, the spectral shape reveals no significant changes and the generated power is similar. Consequently, this indicates that the waveguides are likely altered by a diverse but homogeneous charge carrier distribution, rather than strongly localized fields. Much like a constant noise floor whose intensity may vary, there appears to be a regular electric field whose strength determines the exact position of the spectrum.

The first heat-up induced obvious variations in the material itself; in contrast to the initial measurement, the spectra shifted by approximately −1.5 nm. Although the short-term exposure to increased temperatures was expected to elevate the charge carrier mobility, which can result in a compensation of built-up electric fields, the spectral shape was slightly more asymmetric following the first heat-up. After conducting two cooling cycles, the RT spectra shifted by about +1 nm. After completing the final cooldown, the spectra shifted only slightly by approximately −0.2 nm, with no significant changes in the spectral shape. This means that despite four cooling cycles and another heat-up, the RT spectra were almost identical. The last heat-up again resulted in a slight blue shift.

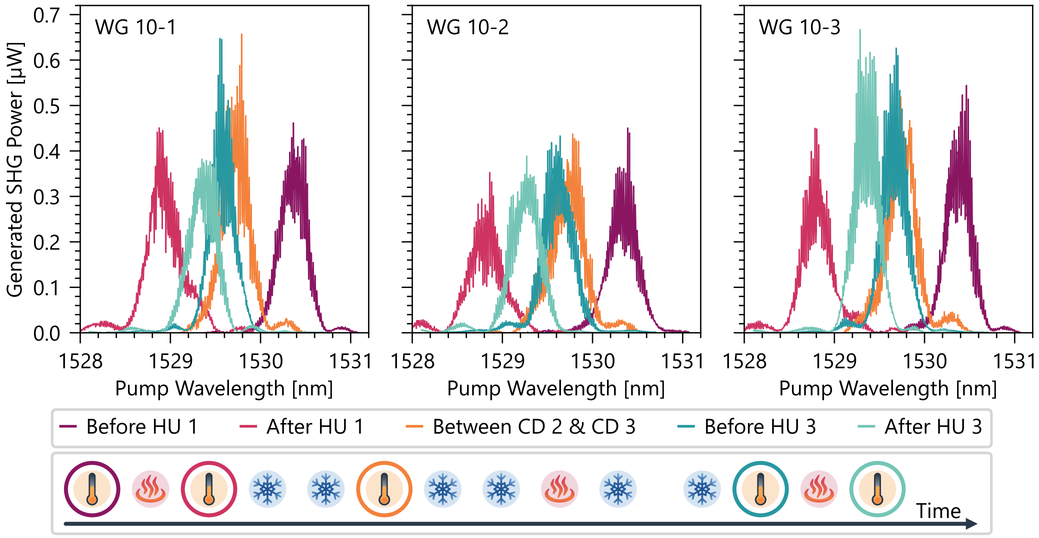

Figure 5.12: Measurement of the alterations in the phase-matching spectra of WGG 10 at RT. The color-coded measurement timeline is included here to depict the chronological order of the individual experiments. The theoretical phase-matched SHG wavelength for this group is 1529.6 nm at a temperature of 294 K.

Moreover, the phase-matched wavelengths measured following HU 1 and HU 3 were not the same, which demonstrates that the heating procedure does not serve as a reliable "reset" to an equilibrium state. Further research is required to evaluate the exact outcomes of repeated heat-ups and to optimize the procedure, including testing higher temperatures and longer periods during which the chip is kept at that temperature.

The measurements performed on WGG 10 demonstrate that the waveguides exhibit a certain hysteresis; the temperature history of the sample affects the exact phase-matching point at RT. However, the spectra differ only slightly in their wavelengths, and the spectral shape and intensity remains almost unchanged. Consequently, even exceptionally poor waveguiding quality during a cooldown does not induce long-term degradation of the RT phase-matching properties. Conversely, a uniform and intense SHG spectrum at RT provides no guarantee of successful waveguiding in a subsequent cooldown. Instead, the RT performance appears to be largely uncorrelated with the cryogenic waveguide behavior.

5.2.5 Key factors affecting the cryogenic waveguides

The discussed observations provide the empirical foundation necessary to revisit and address the initial research questions, focusing on the platform's cryogenic behavior:

1. **To what extent does the cryogenic cooling process itself influence the waveguiding properties?**
   Results: All waveguides exhibited comparable behavior for TM-polarized light, regardless of their exposure to high optical power. This suggests that the cooldown itself is the primary factor influencing the cryogenic waveguiding, not photorefraction. A highly similar general shape of the phase-matching spectra was observed for all CW-operated WGGs; the spectra exhibited an asymmetrical shape with side peaks only on the shorter wavelength side. Moreover, a consistent spectral shift of +2 nm in the phase-matching points from CD 5 to CD 6 was observed for these groups. This indicates that the same modifications to the "frozen-in" charges happened to all three groups. This points to a broad pyroelectric charge carrier distribution that spreads across multiple waveguide groups, thereby inducing a highly uniform deformation of the refractive index across the entire region. These perturbations barely affect the TE-polarized modes, as this polarization consistently resulted in a collimated mode. Ultimately, these findings indicate that the success of a cooling cycle can be assessed early: a poorly confined TM mode profile serves as an indicator of a significant underlying pyroelectric field, which can fundamentally limit the linear waveguiding quality before nonlinear experiments even begin.

2. **How sensitive is the cryogenic performance of the waveguides to high incident optical power?**
   Results: Under CW operation at a wavelength of 1555 nm, the phase-matching spectra remained stable up to the maximum available input pump power of 25 mW (corresponding to about 7.5 mW transmitted power, compare Fig. A.8). Consequently, the type-II process in this sample is robust in the CW regime within this power range. While the pyroelectric distortions altered the general spectral shape already directly after completing the cooldown, this shape was not additionally affected by the available pump power. This indicates that CW input power up to 25 mW does not induce photorefraction if the general cryogenic waveguiding is sufficient to enable SHG. In contrast, pulsed excitation revealed a clear operational threshold, as higher maximum power was available. While the SHG power initially scaled quadratically, the waveguiding changed into a rapid collapse at higher powers. Depending on the thermal cycle, stable operation was maintained up to approximately 98 mW of average input pump power (corresponding to about 15 mW transmitted power, compare Fig. 5.10), before the onset of photorefraction. This might define a practical limit for pulsed nonlinear processes in this configuration, which verifies strong robustness to photorefraction when using pulsed pump light.

3. **Are the observed photorefractive effects limited to CW operation, or do they remain significant under pulsed excitation?**
   Results: Since no photorefractive onset was observed within the available CW power range, a direct comparison of CW and pulsed thresholds requires further investigation at higher CW intensities. However, the results suggest that for this specific sample, classical photorefraction plays a secondary role compared to the dominant distortions induced by the pyroelectric effect. While pulsed excitation eventually triggers a collapse for average transmitted pump power in the low milliwatt range, the primary bottleneck for cryogenic performance remains the electrostatic environment created during the cooling process.

4. **What strategies can be employed to re-mobilize trapped charges in order to restore or enhance waveguide performance?**
   Results: The measurement series indicates that neither active heating nor green-light illumination, in their current implementations, provide a consistently reliable method for performance recovery. While both techniques were evaluated across two cycles, the outcomes remained inconsistent. CD 1 and CD 5 yielded entirely different waveguiding performance regarding the scattered TM-polarized modes, although both cycles were directly following a heat-up. However, both cycles revealed a similar conversion efficiency for WGG 8, which on the other hand points to a partly relaxing effect of the heat-up on the charge carrier distribution. In the final cooldown, the green laser induced a homogeneous shift of $-1\,\mathrm{nm}$ in the phase-matching spectra, but both the generated peak power and the spectral shape were not improved. These strategies remain promising but require systematic optimization; specifically, complete charge relaxation may necessitate higher temperatures, extended annealing duration, or a more precise calibration of the green illumination intensity and exposure intervals.

5. **To what extent is the cryogenic (non)linear waveguide performance reproducible across multiple thermal cycles?**
   Results: The performance was found to be highly non-reproducible across repeated thermal cycles. While the first four cooldowns (CD 1–4) exhibited poor TM waveguiding and no detectable CW SHG signal, performance improved significantly in CD 5 and reached its peak in CD 6. Although the pulsed measurements were successful throughout all cooldowns, optimizing the SHG power necessitated changing the input polarization almost completely to TM. Therefore, also the pulsed-operated WGGs experienced tremendous transmission losses for the TM-polarized modes. The variance in cryogenic performance strongly indicates that the build-up of pyroelectric fields is a stochastic process, where the magnitude and distribution of induced charges differ with every cooling cycle, regardless of identical external parameters. However, the phase-matching spectra recorded at RT exhibited an almost unperturbed shape in every measurement, which suggests that most pyroelectric charges do relax when the system returns to RT.

These findings lead to a primary conclusion regarding the cryogenic performance: the dominant limiting factor for the characterized process is the influence of "frozen-in" pyroelectric charges, rather than photorefraction. The collective trends in the CW phase-matching spectra indicate that these pyroelectric charges, induced directly by the cooling process, fundamentally alter both phase-matching and waveguiding before high-power thresholds are even reached. These results suggest that the pyroelectric charge distributions are not localized to the micrometer scale, but instead extend across multiple waveguide groups, remaining largely uniform over several millimeters transverse to the waveguide orientation. Consequently, the consistency of the TM-mode response serves as a reliable diagnostic tool for the early-stage assessment of a cooling cycle. If the TM-polarized light fails to produce a well-confined transmitted mode, it indicates a significant underlying pyroelectric field that will likely limit the linear waveguiding quality. In such instances, repeated thermal cycling can be employed as a strategy to redistribute these charges, potentially enabling enhanced performance in subsequent cooldowns.

5.3 Chapter conclusion

Building upon the cryogenic SPDC implementations in Chapters 3 and 4, this chapter addressed the final research question of this work: *What do our observations teach us about the viability of cryogenic lithium niobate?* As the previous results had highlighted significant pyroelectric and photorefractive constraints, the studies presented here transitioned toward a more systematic investigation of the platform's underlying physical properties. These measurements revealed a complex relationship between thermal transitions, electrostatic charge distributions, and nonlinear optical performance. By systematically decoupling the effects of pyroelectricity and photorefraction, this chapter determined the primary mechanisms influencing cryogenic waveguide performance and established the conditions under which stable operation was achievable.[3]

The measurements discussed in Section 5.1.1 demonstrated a clear correlation between pyroelectric current spikes and sudden changes in the waveguide's birefringence during thermal cycling. This verified that thermally induced modifications in the charge distributions generate apparent, measurable shifts in the optical waveguide properties. As the frequency of discharges is significantly reduced at cryogenic temperatures, a persistent and inhomogeneous charge distribution remains "frozen in" as the cooldown process is completed.

This pyroelectric effect, rather than optical photorefraction, constitutes the dominant bottleneck for cryogenic performance. The electrostatic environment present at cryogenic temperatures, can fundamentally alter both linear waveguiding and phase-matching conditions. Crucially, during the reproducibility studies in Section 5.2, this process was found to be highly stochastic; identical cooling parameters resulted in vastly different outcomes across repeated cycles. This is consistent with the observations I made for the sample used for the widely non-degenerate nonlinear process, detailed in Section 4.3.1. The detectable modifications in the macroscopic waveguide performance metrics have their origin in myriad microscopic charge carrier displacements. Inherently, a significant change in the operation temperature by nearly three hundred degrees results in a varying charge configuration for repeated thermal cycles.

The pyroelectric investigations were followed by a study of the independent influence of photorefraction in Section 5.1.2. In preparation to this study, the phase-matching spectrum of a waveguide was measured twice: immediately after the cooling process was completed and after one week during which the waveguide had been kept in the dark at a constant temperature. The spectral shape was completely stable, indicating a long lifetime of induced charge distributions at CT. However, these "frozen-in" charges were actively mobilized by activating the auxiliary green laser beam. Consequently, an apparent interaction of this beam with the charges was visible. Although the result was not fully repeatable in a second attempt, this mitigation protocol represents a promising approach to relax persistent charge distributions.

During the reproducibility studies, the green auxiliary laser was examined again, by introducing this beam into the cryogenic SHG process. Here, it induced a shift in the phase-matched wavelength by approximately 2 nm while the spectral shape remained unchanged. This behavior was only observed for one of two cooling cycles. This showed again that the green light possesses the potential to enhance the cryogenic charge carrier mobility, but this protocol demands further optimization. In addition to this optical mitigation technique, a thermal annealing approach was evaluated to reset charge profiles prior to a cooling cycle. While the cryogenic waveguides demonstrated enhanced performance for TM polarization in one out of two cycles following a heat-up, this data set is not sufficient

---

[3] In case I have caught your attention with the "cryogenic traffic jam" metaphor at the beginning of this thesis, I have added an illustrative description of the results in Appendix A.6.

to draw definite conclusions. Therefore, while the presented mitigation strategies such as auxiliary green-light illumination and thermal annealing show promise for mobilizing the charges, they currently lack the consistency required for a reliable “healing” protocol.

The photorefractive measurements in Section 5.1.2 further revealed a clear onset of damage during the type-0 SFG process; this occurred when pumping with approximately 15 mW at 960 nm and 20 mW at 1570 nm. In contrast, the type-II SHG process detailed in Section 5.2 remained stable up to the maximum available CW pump power of 25 mW (at 1555 nm). This suggests a higher resilience for the type-II telecom process compared to the visible-light-driven type-0 configuration. This trend is consistent with the broader performance disparities observed in Chapters 3 and 4. Since the type-0 interaction relies exclusively on the TM-polarized mode, it is inherently more susceptible to induced charge distributions. This fundamental sensitivity explains the higher robustness of the type-II configuration implemented in this work.

In contrast to the CW operation in Section 5.1.2, pulsed excitation of type-II SHG revealed a distinct operational threshold; once exceeded, the waveguide experienced an abrupt collapse of the guided mode. However, the available average pump power for the pulsed beam was considerably higher (124 mW) than the accessible CW power (25 mW). The measurement shown in Fig. 5.10 demonstrates that the pump power could be raised to more than 90 mW before the waveguiding collapsed. Note, that this value represents the average power, while the peak power is significantly higher (approximately 5.2 kW). Overall, the cryogenic waveguides exhibited more stable performance for pulsed operation compared to CW pump light. Specifically, the pulsed excitation yielded a measurable SHG signal in every cooling cycle, although the TM-polarized mode was not well confined. Strong optical losses in this mode could be compensated by rotating the polarization of the pump beam so that it exhibited a major TM-polarized component and only a low proportion of TE-polarized light.

Finally, the type-0 SFG measurements detailed in Section 5.1.3 served as a basis for deriving an experimental Sellmeier equation, providing a more accurate model for the specific waveguide geometry than previous simulations. This empirical model can be applied to various waveguide designs and operation temperatures. As the absolute phase-matching point of the characterized Ti:PPLN waveguides is affected by the internal charge fields, the accuracy of a specific Sellmeier equation should be increased by repeatedly recording the phase-matching spectra in multiple cooldowns.

In conclusion, the discussed results indicate that stable cryogenic operation is feasible, provided the preceded cooling cycle induced only weak pyroelectric fields and the optical power is maintained below a calibrated threshold. This conclusion holds in particular for pulsed excitation. In line with observations at room temperature [163, 193], pulsed excitation proved more robust against cryogenic photorefraction than CW pumping. This consistency suggests that the advantages of pulsed operation for nonlinear stability are maintained across a wide thermal range.

The TM-mode response was found out to provide a reliable early-stage indicator of cooling success, where failures in the mode confinement signalize the degree of underlying pyroelectric distortions. This makes repeated thermal cycling a necessary strategy for redistributing stochastic charge patterns and enhancing performance in subsequent cooldowns, as the observations indicate that pyroelectric accumulation is not a cumulative process. To transition the titanium in-diffused platform from a series of "lucky" experimental cycles to a predictable quantum photonic tool, future efforts must prioritize the stabilization of the pyroelectric environment. Managing these internal field distributions remains the definitive next step in harnessing the full potential of lithium niobate for cryogenic quantum technologies.

Conclusion and Outlook 6

This work has systematically characterized the cryogenic optical properties of titanium in-diffused lithium niobate waveguides and established the experimental and theoretical framework required to evaluate their viability for nonlinear quantum photonics at low temperatures. The objectives of this project were structured around three central research questions, which were defined in the introduction.

6.1 Key findings in response to the research questions

How can we reliably measure the linear and nonlinear effects of the cryogenic Ti:PPLN waveguides? *Aim: Develop and optimize functional experimental methods for low-temperature integrated optics.*

To address this first research question, the work began with the development of an experimental framework dedicated to re-configurable, free-space access to Ti:PPLN waveguides at cryogenic temperatures. A custom free-space coupled cryostat was employed throughout all measurement series. It provided mechanical stability for in-situ alignment below 10 K and integrated piezo controllers to compensate thermal contraction and maintain optimal mode overlap. Based on this system, a protocol for waveguide mounting and cryogenic alignment was established (Section 2.2.2). Furthermore, the developed experimental setup enabled broadband characterization across a wide wavelength range for SPDC, SHG, and SFG measurements from room temperature down to approximately 4 K. Using this setup, SPDC at cryogenic temperatures was demonstrated to be feasible in Ti:PPLN waveguides, with clearly measurable phase-matching and photon correlations (Section 3.2). The combination of theoretical simulations and empirically corrected temperature-dependent material parameters allowed the cryogenic phase-matching to be predicted with an accuracy of about $1-2$ nm, which enabled implementation of a cryogenic degenerate SPDC process (Section 3.3). The resulting experimental framework proved to be robust and readily adaptable to a variety of nonlinear optical processes and measurement configurations, as detailed in Chapters 3 to 5. Overall, this work establishes a validated and transferable experimental methodology for the linear and nonlinear optical characterization of integrated waveguides under cryogenic conditions.

How does cryogenic operation affect the material platform? *Aim: Determine and understand the critical temperature-dependent effects that alter the waveguide performance under extremely cold operation conditions.*

Building upon the established measurement framework, the second research question focused on identifying how cryogenic operation alters the intrinsic material and waveguide properties of Ti:PPLN. The temperature-dependent changes can be grouped into a predictable and a stochastic component. The predictable effects include the reduction in refractive indices and the thermal contraction of the material, which cause well-defined shifts in the phase-matching. The stochastic effects arise from the strong decrease in charge-carrier mobility, giving rise to persistent and spatially diverse pyroelectric and photorefractive fields. The pyroelectric charge accumulation during the thermal transition to cryogenic temperatures results in "frozen-in" inhomogeneous internal fields that modify both the phase-matching conditions and mode confinement. Following the cooldown, photorefraction can introduce additional instability and loss, whose onset was observed at different optical power levels.

These internal electric fields manifest in observable performance degradation. Measurements with differently polarized light revealed a pronounced asymmetry between the orthogonally polarized TE- and TM-modes (Section 4.3.1). While the TE-polarized modes remained mostly stable in a series of repeated cooldowns, the TM-polarized modes degraded due to their stronger sensitivity to the induced electric fields. Moreover, variable optical losses and probabilistic effective lengths indicate a strong cycle-to-cycle and sample-to-sample variability of the overall cryogenic performance.

Together, these pyroelectric and photorefractive contributions define the performance boundary for cryogenic operation, demonstrating that the intrinsic electro-optic properties of lithium niobate become limiting factors once the charge-carrier mobility is suppressed. However, photorefraction was found to be less critical than the pyroelectric effect, as the waveguides often showed degraded performance immediately after the cooldown, before exposure to high optical power (Section 5.2). Consequently, the cryogenic behavior of Ti:PPLN waveguides is primarily limited by static electric fields that accumulate from the pyroelectric effect, whereas photorefraction plays a secondary role. Detailed knowledge of both effects is essential for any low-temperature design strategy.

What do our observations teach us about the viability of cryogenic lithium niobate? *Aim: Assess the fundamental potential of cryogenic Ti:PPLN and define the conditions under which this platform can be beneficial for cryogenic integrated optics.*

With the key cryogenic effects characterized, the final research question turned toward evaluating the overall viability of Ti:PPLN for nonlinear and quantum photonic applications at low temperatures. Two separate mitigation strategies were explored, aimed at increasing charge-carrier mobility and modifying the "frozen-in" charge distribution (Chapter 5). Optical activation of trapped charges was investigated using an auxiliary green laser beam, which temporarily mobilized charge carriers and produced measurable shifts of the phase-matching condition. Thermal annealing between cooldowns was also evaluated; the heat-up protocols induced a spectral shift of the room-temperature phase-matching, indicating a modification in the underlying charge configuration. However, no consistent improvement was observed in subsequent cooldowns. While both methods show potential for charge control, they currently lack reproducibility.

Beyond these mitigation attempts, process-specific insights were obtained that define the operational boundaries of Ti:PPLN. The type-II (TE-TM) processes in the telecom range (Chapter 3) were more stable than the type-0 (TM) interactions driven at visible wavelengths (Chapter 4), consistent with the lower electric-field coupling of TE-polarized modes. Moreover, pulsed operation yielded more robust performance than CW excitation, with measurable SHG signals obtained in every cooldown during the reproducibility studies (Section 5.2).

The experimental datasets further enabled refinement of the effective refractive index model. An empirical Sellmeier equation, derived from the type-0 SFG measurements (Section 5.1.3), provides improved accuracy for predicting cryogenic phase-matching in this waveguide geometry. However, the system's intrinsic stochastic behavior implies that precise dispersion models require repeated measurements and iterative optimization of the Sellmeier coefficients.

Overall, stable operation of the titanium in-diffused platform is feasible when the field buildup is moderate and optical powers are carefully optimized. The success of a cryogenic measurement ultimately hinges on effective pyroelectric field control. Reproducibility therefore demands well-defined stabilization or compensation protocols. If these internal fields can be managed or dynamically neutralized, cryogenic z-cut lithium niobate remains a promising platform for nonlinear and quantum photonic applications.

6.2 Perspectives for cryogenic integrated optics

The insights gained through this work highlight several opportunities to extend and refine cryogenic integrated optics in the future. The following section outlines potential experimental improvements, design strategies to further stabilize lithium niobate under cryogenic conditions, and an alternative research direction by considering thin-film lithium niobate (TFLN) for cryogenic photonic applications.

The cryogenic performance of the Ti:PPLN platform could be improved by further investigating and refining the presented mitigation protocols. Specifically, the auxiliary green laser beam offers numerous possibilities for optimization. For example, the exact optical power and exposure duration should be carefully calibrated throughout repeated measurements. Moreover, the influence of a pulsed auxiliary beam can be characterized in future studies. The heat-up protocol can be also be adapted by extending the time interval at elevated temperatures or by testing higher operation temperatures to achieve a more complete reset of persistent charge-carrier distributions. If a well-calibrated pre-heating step prior to cooldown proves beneficial, a dedicated heating stage could be integrated into the cryostat design. This would allow regular heating to be carried out immediately before each cooling cycle, with the sample already mounted inside the cryostat.

One promising approach for mitigating pyroelectric field accumulation lies in optimizing the waveguide design. This involves introducing conductive surface layers that can dissipate the charges at low temperatures. This concept has recently been explored to prevent pyroelectric damage in integrated superconducting single-photon detectors on z-cut lithium niobate [194]. Ideally, the coating material should be transparent and remain sufficiently conductive during cooldown to flush away the pyroelectric charges. For this application, the material should further become insulating once the detectors reach their operational critical temperature (typically around 3 K). A thin carbon layer represents one potential candidate, as carbon loses its conductivity at cryogenic temperatures. In initial tests, such carbon coatings successfully protected unbonded detectors from pyroelectric discharge [194]. However, the protection failed when wire-bonded detectors were examined. The bond wires are expected to introduce additional charge currents, leading to potential differences that could no longer be compensated. All bonded devices showed clear signs of electrical arcing visible under the microscope [194].

Since the carbon layer reduced pyroelectric damage for unbonded detectors, similar coatings might also help to mitigate charge-induced waveguide degradation of Ti:PPLN structures. Nevertheless, carbon coatings were found to noticeably increase the optical propagation losses of titanium in-diffused lithium niobate [194]. One possible approach could be to pre-select individual waveguides for cryogenic measurements by first characterizing the sample at room temperature before applying a coating. Subsequently, the sample surface could be coated with carbon, while the specific waveguide areas are left blank. The coated sections might be interconnected by narrow carbon stripes that cover the waveguide region only over very short distances to maintain the optical performance. As the measurements in this work have shown that the pyroelectric fields tend to be homogeneous across several waveguide groups (Section 5.2.4), even a conductive coating applied alongside the actual waveguide region could contribute to the charge compensation and thus enhance cryogenic nonlinear optical processes.

Alternatively, transparent conductive oxides such as indium tin oxide (ITO) represent promising candidates for charge-compensation layers. Owing to their combination of electrical conductivity and optical transparency [195], these coatings can maintain charge dissipation without significantly disturbing guided optical modes. In an initial test, ITO was deposited on a Ti:LN waveguide sample and its resistivity was measured during a cooldown [194]. The layer remained fully conductive over the complete temperature range, showing only a minor increase in resistivity at cryogenic conditions. In addition, this coating introduced much lower propagation losses compared to the carbon layer. However, the optical performance of cryogenic ITO-coated waveguides has not yet been characterized. While the integration of superconducting detectors would require an additional insulation layer between the conductive ITO and the detector material [194], this isolation is unnecessary for cryogenic frequency-conversion experiments. Consequently, a continuous ITO layer covering the full sample surface could provide an effective method to suppress pyroelectric charging in lithium niobate waveguides. Exploring this approach represents a highly promising direction for future work.

Furthermore, conductive surface layers could also enable the application of controlled external electric fields, allowing an active stabilization of the internal fields under cryogenic conditions. Applying a uniform bias across the entire sample could help to neutralize accumulated pyroelectric charges and implement a stable, homogeneous internal field that influences the waveguides only minimally. Following the compensation of pyroelectric charge fields, the operation parameters for cryogenic nonlinear processes can be further optimized. This includes, for example, operation with pulsed excitation at reduced optical power levels and the preference for type-II phase-matching configurations that involve both polarizations. These limitations keep the induced photorefractive damage at a minimum and reduce the dependence of the nonlinear process on effective waveguiding of TM-polarized modes. Finally, to enable the combined integration of (coated) Ti:PPLN waveguides in z-cut lithium niobate with superconducting detectors, hybrid material approaches could be explored, in which the detectors are fabricated on a substrate exhibiting lower intrinsic pyroelectricity.

Ultimately, a particularly promising direction for future research lies in extending the present work from Ti:PPLN to TFLN, offering much stronger optical mode confinement and thus significantly higher nonlinear conversion efficiencies [94, 96, 101]. The cryogenic suitability of TFLN has already been demonstrated for various applications, including nonlinear frequency conversion [133], spectral filtering [134], and the integration of EOMs with SNSPDs [135]. Although recent publications confirm that TFLN maintains excellent performance at cryogenic temperatures, the role of pyroelectric and photorefractive effects in cryogenic TFLN remains largely unexplored. A systematic investigation of these effects would therefore be an important step toward understanding the fundamental limitations of this platform.

Based on its strong confinement, efficient optical coupling to TFLN waveguides, both using free-space alignment and fiber coupling, remains technically challenging. Considering the specific setup used in this work, substantial redesign of the employed cryostat would be required to enable cryogenic TFLN characterization. Specifically, the working distance of approximately 13 mm between the end facets and the external lenses prevents the use of high-numerical-aperture objectives needed for efficient free-space coupling. Cryogenic coupling could therefore require placing both the waveguide sample and the objectives inside the cryostat chamber, on independently adjustable translation stages. However, to realize this configuration, the repeatability of the movement steps at cryogenic temperatures must be enhanced compared to the piezo positioners used in the current system. In particular, the smaller mode sizes of the TFLN waveguides require highly precise positioning. Alternatively, the cryogenic TFLN chip can be mounted together with a fiber (or fiber array), which is either positioned close to the end facet, or permanently attached to the chip. Photonic packaging concepts employing on-chip grating couplers that are permanently glued to optical fibers represent a particularly promising approach for realizing stable cryogenic TFLN operation [150, 196].

The combination of distinct approaches for active or passive control of the pyroelectric fields - through optimizing the mitigation protocols, applying conductive coatings, or modifying the waveguide design - represents a promising concept for future cryogenic quantum photonics in lithium niobate.

Bibliography 7

[1] J. L. O'brien, A. Furusawa, and J. Vučković, Photonic quantum technologies, Nature Photonics **3**, 687–695 (2009).

[2] J. Wang, F. Sciarrino, A. Laing, and M. G. Thompson, Integrated photonic quantum technologies, Nature Photonics **14**, 273–284 (2020).

[3] G. Moody, V. J. Sorger, D. J. Blumenthal, P. W. Juodawlkis, W. Loh, C. Sorace-Agaskar, A. E. Jones, K. C. Balram, J. C. F. Matthews, A. Laing, et al., 2022 Roadmap on integrated quantum photonics, Journal of Physics: Photonics **4**, 012501 (2022).

[4] M. D. Eisaman, J. Fan, A. Migdall, and S. V. Polyakov, Invited review article: single-photon sources and detectors, Review of Scientific Instruments **82**, 071101 (2011).

[5] A. W. Elshaari, W. Pernice, K. Srinivasan, O. Benson, and V. Zwiller, Hybrid integrated quantum photonic circuits, Nature Photonics **14**, 285–298 (2020).

[6] S. Slussarenko and G. J. Pryde, Photonic quantum information processing: a concise review, Applied Physics Reviews **6**, 041303 (2019).

[7] M. AbuGhanem, Information processing at the speed of light, Frontiers of Optoelectronics **17**, 33 (2024).

[8] PsiQuantum team, A manufacturable platform for photonic quantum computing, Nature **641**, 876–883 (2025).

[9] C. S. Hamilton, R. Kruse, L. Sansoni, S. Barkhofen, C. Silberhorn, and I. Jex, Gaussian boson sampling, Physical Review Letters **119**, 170501 (2017).

[10] N. Quesada, J. M. Arrazola, and N. Killoran, Gaussian boson sampling using threshold detectors, Physical Review A **98**, 062322 (2018).

[11] H.-S. Zhong, H. Wang, Y.-H. Deng, M.-C. Chen, L.-C. Peng, Y.-H. Luo, J. Qin, D. Wu, X. Ding, Y. Hu, et al., Quantum computational advantage using photons, Science **370**, 1460–1463 (2020).

[12] L. S. Madsen, F. Laudenbach, M. F. Askarani, F. Rortais, T. Vincent, J. F. Bulmer, F. M. Miatto, L. Neuhaus, L. G. Helt, M. J. Collins, et al., Quantum computational advantage with a programmable photonic processor, Nature **606**, 75–81 (2022).

[13] H. Aghaee Rad, T. Ainsworth, R. Alexander, B. Altieri, M. Askarani, R. Baby, L. Banchi, B. Baragiola, J. Bourassa, R. Chadwick, et al., Scaling and networking a modular photonic quantum computer, Nature **638**, 912–919 (2025).

[14] C. Taballione, R. van der Meer, H. J. Snijders, P. Hooijschuur, J. P. Epping, M. de Goede, B. Kassenberg, P. Venderbosch, C. Toebes, H. van den Vlekkert, et al., A universal fully reconfigurable 12-mode quantum photonic processor, Materials for Quantum Technology **1**, 035002 (2021).

[15] C. Taballione, M. C. Anguita, M. de Goede, P. Venderbosch, B. Kassenberg, H. Snijders, N. Kannan, W. L. Vleeshouwers, D. Smith, J. P. Epping, et al., 20-mode universal quantum photonic processor, Quantum **7**, 1071 (2023).

[16] N. Maring, A. Fyrillas, M. Pont, E. Ivanov, P. Stepanov, N. Margaria, W. Hease, A. Pishchagin, A. Lemaître, I. Sagnes, et al., A versatile single-photon-based quantum computing platform, Nature Photonics **18**, 603–609 (2024).

[17] M. de Cea, E. E. Wollman, A. H. Atabaki, D. J. Gray, M. D. Shaw, and R. J. Ram, Photonic readout of superconducting nanowire single photon counting detectors, Scientific Reports **10**, 9470 (2020).

[18] A. Youssefi, I. Shomroni, Y. J. Joshi, N. R. Bernier, A. Lukashchuk, P. Uhrich, L. Qiu, and T. J. Kippenberg, A cryogenic electro-optic interconnect for superconducting devices, Nature Electronics **4**, 326–332 (2021).

[19] F. Thiele, T. Hummel, A. N. McCaughan, J. Brockmeier, M. Protte, V. Quiring, S. Lengeling, C. Eigner, C. Silberhorn, and T. J. Bartley, All optical operation of a superconducting photonic interface, Optics Express **31**, 32717–32726 (2023).

[20] F. Thiele, N. Lamberty, T. Hummel, and T. Bartley, Optical bias and cryogenic laser readout of a multipixel superconducting nanowire single photon detector, APL Photonics **9**, 076118 (2024).

[21] L. Caspani, C. Xiong, B. J. Eggleton, D. Bajoni, M. Liscidini, M. Galli, R. Morandotti, and D. J. Moss, Integrated sources of photon quantum states based on nonlinear optics, Light: Science & Applications **6**, e17100 (2017).

[22] W. Louisell, A. Yariv, and A. Siegman, Quantum fluctuations and noise in parametric processes. I. Physical Review **124**, 1646 (1961).

[23] D. C. Burnham and D. L. Weinberg, Observation of simultaneity in parametric production of optical photon pairs, Physical Review Letters **25**, 84 (1970).

[24] C. Hong and L. Mandel, Experimental realization of a localized one-photon state, Physical Review Letters **56**, 58 (1986).

[25] L.-A. Wu, H. Kimble, J. Hall, and H. Wu, Generation of squeezed states by parametric down conversion, Physical Review Letters **57**, 2520 (1986).

[26] C.-K. Hong, Z.-Y. Ou, and L. Mandel, Measurement of subpicosecond time intervals between two photons by interference, Physical Review Letters **59**, 2044 (1987).

[27] P. G. Kwiat, K. Mattle, H. Weinfurter, A. Zeilinger, A. V. Sergienko, and Y. Shih, New high-intensity source of polarization-entangled photon pairs, Physical Review Letters **75**, 4337 (1995).

[28] R. L. Abrams and R. C. Lind, Degenerate four-wave mixing in absorbing media, Optics Letters **2**, 94–96 (1978).

[29] R. K. Jain and R. C. Lind, Degenerate four-wave mixing in semiconductor-doped glasses, Journal of the Optical Society of America **73**, 647–653 (1983).

[30] P. Kumar and J. H. Shapiro, Squeezed-state generation via forward degenerate four-wave mixing, Physical Review A **30**, 1568–1571 (1984).

[31] R. E. Slusher, L. W. Hollberg, B. Yurke, J. C. Mertz, and J. F. Valley, Observation of squeezed states generated by four-wave mixing in an optical cavity, Physical Review Letters **55**, 2409 (1985).

[32] M. Reid and D. Walls, Generation of squeezed states via degenerate four-wave mixing, Physical Review A **31**, 1622 (1985).

[33] B. Yurke, Squeezed-coherent-state generation via four-wave mixers and detection via homodyne detectors, Physical Review A **32**, 300 (1985).

[34] M. D. Levenson, R. M. Shelby, and S. H. Perlmutter, Squeezing of classical noise by nondegenerate four-wave mixing in an optical fiber, Optics Letters **10**, 514–516 (1985).

[35] G. Fujii, N. Namekata, M. Motoya, S. Kurimura, and S. Inoue, Bright narrowband source of photon pairs at optical telecommunication wavelengths using a type-II periodically poled lithium niobate waveguide, Optics Express **15**, 12769–12776 (2007).

[36] O. Alibart, V. D'Auria, M. De Micheli, F. Doutre, F. Kaiser, L. Labonté, T. Lunghi, É. Picholle, and S. Tanzilli, Quantum photonics at telecom wavelengths based on lithium niobate waveguides, Journal of Optics **18**, 104001 (2016).

[37] C. Couteau, Spontaneous parametric down-conversion, Contemporary Physics **59**, 291–304 (2018).

[38] P. J. Mosley, J. S. Lundeen, B. J. Smith, P. Wasylczyk, A. B. U'Ren, C. Silberhorn, and I. A. Walmsley, Heralded generation of ultrafast single photons in pure quantum states, Physical Review Letters **100**, 133601 (2008).

[39] R.-B. Jin, R. Shimizu, K. Wakui, H. Benichi, and M. Sasaki, Widely tunable single photon source with high purity at telecom wavelength, Optics Express **21**, 10659–10666 (2013).

[40] N. Bruno, A. Martin, T. Guerreiro, B. Sanguinetti, and R. T. Thew, Pulsed source of spectrally uncorrelated and indistinguishable photons at telecom wavelengths, Optics Express **22**, 17246–17253 (2014).

[41] S. Tanzilli, H. De Riedmatten, H. Tittel, H. Zbinden, P. Baldi, M. De Micheli, D. B. Ostrowsky, and N. Gisin, Highly efficient photon-pair source using periodically poled lithium niobate waveguide, Electronics Letters **37**, 26–28 (2001).

[42] C. Zhang, Y.-F. Huang, B.-H. Liu, C.-F. Li, and G.-C. Guo, Spontaneous parametric down-conversion sources for multiphoton experiments, Advanced Quantum Technologies **4**, 2000132 (2021).

[43] X.-s. Ma, S. Zotter, J. Kofler, T. Jennewein, and A. Zeilinger, Experimental generation of single photons via active multiplexing, Physical Review A **83**, 043814 (2011).

[44] F. Kaneda, B. G. Christensen, J. J. Wong, H. S. Park, K. T. McCusker, and P. G. Kwiat, Time-multiplexed heralded single-photon source, Optica **2**, 1010–1013 (2015).

[45] G. J. Mendoza, R. Santagati, J. Munns, E. Hemsley, M. Piekarek, E. Martín-López, G. D. Marshall, D. Bonneau, M. G. Thompson, and J. L. O'Brien, Active temporal and spatial multiplexing of photons, Optica **3**, 127–132 (2016).

[46] M. Grimau Puigibert, G. H. Aguilar, Q. Zhou, F. Marsili, M. D. Shaw, V. B. Verma, S. W. Nam, D. Oblak, and W. Tittel, Heralded single photons based on spectral multiplexing and feed-forward control, Physical Review Letters **119**, 083601 (2017).

[47] S. I. Davis, A. Mueller, R. Valivarthi, N. Lauk, L. Narvaez, B. Korzh, A. D. Beyer, O. Cerri, M. Colangelo, K. K. Berggren, et al., Improved heralded single-photon source with a photon-number-resolving superconducting nanowire detector, Physical Review Applied **18**, 064007 (2022).

[48] J. Cibert, P. M. Petroff, G. J. Dolan, S. J. Pearton, A. C. Gossard, and J. H. English, Optically detected carrier confinement to one and zero dimension in GaAs quantum well wires and boxes, Applied Physics Letters **49**, 1275–1277 (1986).

[49] R. Ashoori, Electrons in artificial atoms, Nature **379**, 413–419 (1996).

[50] I. Aharonovich, D. Englund, and M. Toth, Solid-state single-photon emitters, Nature Photonics **10**, 631–641 (2016).

[51] Y. Arakawa and M. J. Holmes, Progress in quantum-dot single photon sources for quantum information technologies: a broad spectrum overview, Applied Physics Reviews **7**, 021309 (2020).

[52] O. Benson, C. Santori, M. Pelton, and Y. Yamamoto, Regulated and entangled photons from a single quantum dot, Physical Review Letters **84**, 2513–2516 (2000).

[53] P. Michler, "Quantum Dot Single-Photon Sources", in *Single Semiconductor Quantum Dots* (Springer Berlin Heidelberg, 2009), pp. 185–225.

[54] N. Somaschi, V. Giesz, L. De Santis, J. Loredo, M. P. Almeida, G. Hornecker, S. L. Portalupi, T. Grange, C. Anton, J. Demory, et al., Near-optimal single-photon sources in the solid state, Nature Photonics **10**, 340–345 (2016).

[55] X. Ding, Y. He, Z.-C. Duan, N. Gregersen, M.-C. Chen, S. Unsleber, S. Maier, C. Schneider, M. Kamp, S. Höfling, et al., On-demand single photons with high extraction efficiency and near-unity indistinguishability from a resonantly driven quantum dot in a micropillar, Physical Review Letters **116**, 020401 (2016).

[56] S. V. Polyakov, A. Muller, E. B. Flagg, A. Ling, N. Borjemscaia, E. Van Keuren, A. Migdall, and G. S. Solomon, Coalescence of single photons emitted by disparate single-photon sources: the example of InAs quantum dots and parametric down-conversion sources, Physical Review Letters **107**, 157402 (2011).

[57] T. Huber, M. Prilmüller, M. Sehner, G. S. Solomon, A. Predojević, and G. Weihs, Interfacing a quantum dot with a spontaneous parametric down-conversion source, Quantum Science and Technology **2**, 034016 (2017).

[58] Y. Yu, S. Liu, C.-M. Lee, P. Michler, S. Reitzenstein, K. Srinivasan, E. Waks, and J. Liu, Telecom-band quantum dot technologies for long-distance quantum networks, Nature Nanotechnology **18**, 1389–1400 (2023).

[59] L. Duan, T. J. Steiner, P. Pintus, L. Thiel, J. E. Castro, J. E. Bowers, and G. Moody, Visible-telecom entangled-photon pair generation with integrated photonics: guidelines and a materials comparison, ACS Photonics **12**, 118–127 (2025).

[60] C. H. Bennett, G. Brassard, C. Crépeau, R. Jozsa, A. Peres, and W. K. Wootters, Teleporting an unknown quantum state via dual classical and Einstein-Podolsky-Rosen channels, Physical Review Letters **70**, 1895 (1993).

[61] D. Bouwmeester, J.-W. Pan, K. Mattle, M. Eibl, H. Weinfurter, and A. Zeilinger, Experimental quantum teleportation, Nature **390**, 575–579 (1997).

[62] F. Bussières, C. Clausen, A. Tiranov, B. Korzh, V. B. Verma, S. W. Nam, F. Marsili, A. Ferrier, P. Goldner, H. Herrmann, et al., Quantum teleportation from a telecom-wavelength photon to a solid-state quantum memory, Nature Photonics **8**, 775–778 (2014).

[63] W. Sohler, H. Hu, R. Ricken, V. Quiring, C. Vannahme, H. Herrmann, D. Büchter, S. Reza, W. Grundkötter, S. Orlov, et al., Integrated optical devices in lithium niobate, Optics & Photonics News **19**, 24–31 (2008).

[64] J.-H. Kim, S. Aghaeimeibodi, J. Carolan, D. Englund, and E. Waks, Hybrid integration methods for on-chip quantum photonics, Optica **7**, 291–308 (2020).

[65] G. N. Gol'tsman, O. Okunev, G. Chulkova, A. Lipatov, A. Semenov, K. Smirnov, B. Voronov, A. Dzardanov, C. Williams, and R. Sobolewski, Picosecond superconducting single-photon optical detector, Applied Physics Letters **79**, 705–707 (2001).

[66] L. You, Superconducting nanowire single-photon detectors for quantum information, Nanophotonics **9**, 2673–2692 (2020).

[67] F. P. Venza and M. Colangelo, Research trends in single-photon detectors based on superconducting wires, APL Photonics **10**, 040901 (2025).

[68] D. V. Reddy, R. R. Nerem, S. W. Nam, R. P. Mirin, and V. B. Verma, Superconducting nanowire single-photon detectors with 98 % system detection efficiency at 1550 nm, Optica **7**, 1649–1653 (2020).

[69] J. Chang, J. Los, J. Tenorio-Pearl, N. Noordzij, R. Gourgues, A. Guardiani, J. Zichi, S. Pereira, H. Urbach, V. Zwiller, et al., Detecting telecom single photons with $(99.5^{+0.5}_{-2.07})\%$ system detection efficiency and high time resolution, APL Photonics **6**, 036114 (2021).

[70] J. Chiles, I. Charaev, R. Lasenby, M. Baryakhtar, J. Huang, A. Roshko, G. Burton, M. Colangelo, K. Van Tilburg, A. Arvanitaki, et al., New constraints on dark photon dark matter with superconducting nanowire detectors in an optical haloscope, Physical Review Letters **128**, 231802 (2022).

[71] B. Korzh, Q.-Y. Zhao, J. P. Allmaras, S. Frasca, T. M. Autry, E. A. Bersin, A. D. Beyer, R. M. Briggs, B. Bumble, M. Colangelo, et al., Demonstration of sub-3 ps temporal resolution with a superconducting nanowire single-photon detector, Nature Photonics **14**, 250–255 (2020).

[72] G. V. Resta, L. Stasi, M. Perrenoud, S. El-Khoury, T. Brydges, R. Thew, H. Zbinden, and F. Bussières, Gigahertz detection rates and dynamic photon-number resolution with superconducting nanowire arrays, Nano Letters **23**, 6018–6026 (2023).

[73] C. Cahall, K. L. Nicolich, N. T. Islam, G. P. Lafyatis, A. J. Miller, D. J. Gauthier, and J. Kim, Multi-photon detection using a conventional superconducting nanowire single-photon detector, Optica **4**, 1534–1535 (2017).

[74] T. Schapeler, F. Schlue, M. Stefszky, B. Brecht, C. Silberhorn, and T. J. Bartley, “Optimizing photon-number resolution with superconducting nanowire multi-photon detectors”, in Proc. SPIE 13448, Advanced Photon Counting Techniques XIX (2025), 134480C.

[75] T. Schapeler, N. Lamberty, T. Hummel, F. Schlue, M. Stefszky, B. Brecht, C. Silberhorn, and T. J. Bartley, Electrical trace analysis of superconducting nanowire photon-number-resolving detectors, Physical Review Applied **22**, 014024 (2024).

[76] M. Sidorova, T. Schapeler, A. D. Semenov, F. Schlue, M. Stefszky, B. Brecht, C. Silberhorn, and T. J. Bartley, Jitter in photon-number-resolved detection by superconducting nanowires, APL Photonics **10**, 086113 (2025).

[77] T. Schapeler, I. Mischke, F. Schlue, M. Stefszky, B. Brecht, C. Silberhorn, and T. J. Bartley, Practical considerations for assignment of photon numbers with SNSPDs, APL Quantum **3**, 016102 (2026).

[78] N. C. Harris, D. Grassani, A. Simbula, M. Pant, M. Galli, T. Baehr-Jones, M. Hochberg, D. Englund, D. Bajoni, and C. Galland, Integrated source of spectrally filtered correlated photons for large-scale quantum photonic systems, Physical Review X **4**, 041047 (2014).

[79] C. M. Gentry, O. S. Magaña-Loaiza, M. T. Wade, F. Pavanello, T. Gerrits, S. Lin, J. M. Shainline, S. D. Dyer, S. W. Nam, R. P. Mirin, et al., "Monolithic source of entangled photons with integrated pump rejection", in Conference on Lasers and Electro-Optics, Optica Publishing Group (2018), JTh4C.3.

[80] J. Brockmeier, T. Schapeler, N. Amelie Lange, J. Philipp Höpker, H. Herrmann, C. Silberhorn, and T. J. Bartley, Harnessing temporal dispersion for integrated pump filtering in spontaneous heralded single-photon generation processes, New Journal of Physics **27**, 074101 (2025).

[81] N. Montaut, L. Sansoni, E. Meyer-Scott, R. Ricken, V. Quiring, H. Herrmann, and C. Silberhorn, High-efficiency plug-and-play source of heralded single photons, Physical Review Applied **8**, 24021 (2017).

[82] A. Dutt, A. Mohanty, A. L. Gaeta, and M. Lipson, Nonlinear and quantum photonics using integrated optical materials, Nature Reviews Materials **9**, 321–346 (2024).

[83] M. Jankowski, J. Mishra, and M. M. Fejer, Dispersion-engineered $\chi^{(2)}$ nanophotonics: a flexible tool for nonclassical light, Journal of Physics: Photonics **3**, 042005 (2021).

[84] C. J. Xin, J. Mishra, C. Chen, D. Zhu, A. Shams-Ansari, C. Langrock, N. Sinclair, F. N. C. Wong, M. M. Fejer, and M. Lončar, Spectrally separable photon-pair generation in dispersion engineered thin-film lithium niobate, Optics Letters **47**, 2830–2833 (2022).

[85] J. Mishra, M. Jankowski, A. Y. Hwang, H. S. Stokowski, T. P. McKenna, C. Langrock, E. Ng, D. Heydari, H. Mabuchi, A. H. Safavi-Naeini, et al., Ultra-broadband mid-infrared generation in dispersion-engineered thin-film lithium niobate, Optics Express **30**, 32752–32760 (2022).

[86] Y. Hu, D. Zhu, S. Lu, X. Zhu, Y. Song, D. Renaud, D. Assumpcao, R. Cheng, C. Xin, M. Yeh, et al., Integrated electro-optics on thin-film lithium niobate, Nature Reviews Physics **7**, 237–254 (2025).

[87] J. F. Bauters, M. J. R. Heck, D. D. John, J. S. Barton, C. M. Bruinink, A. Leinse, R. G. Heideman, D. J. Blumenthal, and J. E. Bowers, Planar waveguides with less than 0.1 dB/m propagation loss fabricated with wafer bonding, Optics Express **19**, 24090–24101 (2011).

[88] R. S. Weis and T. K. Gaylord, Lithium niobate: summary of physical properties and crystal structure, Applied Physics A **37**, 191–203 (1985).

[89] G. Chen, N. Li, J. D. Ng, H.-L. Lin, Y. Zhou, Y. H. Fu, L. Y. T. Lee, Y. Yu, A.-Q. Liu, and A. J. Danner, Advances in lithium niobate photonics: development status and perspectives, Advanced Photonics **4**, 034003–034003 (2022).

[90] R. Regener and W. Sohler, Efficient second-harmonic generation in Ti:$LiNbO_3$ channel waveguide resonators, Journal of the Optical Society of America B **5**, 267–277 (1988).

[91] R. W. Boyd, *Nonlinear Optics*, Third Edition (Academic Press, 2008).

[92] C. Wang, C. Langrock, A. Marandi, M. Jankowski, M. Zhang, B. Desiatov, M. M. Fejer, and M. Lončar, Ultrahigh-efficiency wavelength conversion in nanophotonic periodically poled lithium niobate waveguides, Optica **5**, 1438–1441 (2018).

[93] M. Stefszky, R. Ricken, C. Eigner, V. Quiring, H. Herrmann, and C. Silberhorn, High-power waveguide resonator second harmonic device with external conversion efficiency up to 75%, Journal of Optics **20**, 065501 (2018).

[94] G. Poberaj, H. Hu, W. Sohler, and P. Günter, Lithium niobate on insulator (LNOI) for micro-photonic devices, Laser & Photonics Reviews **6**, 488–503 (2012).

[95] A. Boes, B. Corcoran, L. Chang, J. Bowers, and A. Mitchell, Status and potential of lithium niobate on insulator (LNOI) for photonic integrated circuits, Laser & Photonics Reviews **12**, 1700256 (2018).

[96] J. Lin, F. Bo, Y. Cheng, and J. Xu, Advances in on-chip photonic devices based on lithium niobate on insulator, Photonics Research **8**, 1910–1936 (2020).

[97] K. Luke, P. Kharel, C. Reimer, L. He, M. Loncar, and M. Zhang, Wafer-scale low-loss lithium niobate photonic integrated circuits, Optics Express **28**, 24452–24458 (2020).

[98] S. Saravi, T. Pertsch, and F. Setzpfandt, Lithium niobate on insulator: an emerging platform for integrated quantum photonics, Advanced Optical Materials **9**, 2100789 (2021).

[99] D. Zhu, L. Shao, M. Yu, R. Cheng, B. Desiatov, C. Xin, Y. Hu, J. Holzgrafe, S. Ghosh, A. Shams-Ansari, et al., Integrated photonics on thin-film lithium niobate, Advances in Optics and Photonics **13**, 242–352 (2021).

[100] U. A. Javid, J. Ling, J. Staffa, M. Li, Y. He, and Q. Lin, Ultrabroadband entangled photons on a nanophotonic chip, Physical Review Letters **127**, 183601 (2021).

[101] X. Wang, X. Jiao, B. Wang, Y. Liu, X.-P. Xie, M.-Y. Zheng, Q. Zhang, and J.-W. Pan, Quantum frequency conversion and single-photon detection with lithium niobate nanophotonic chips, npj Quantum Information **9**, 38 (2023).

[102] S. Babel, L. Bollmers, M. Massaro, K. H. Luo, M. Stefszky, F. Pegoraro, P. Held, H. Herrmann, C. Eigner, B. Brecht, et al., Demonstration of Hong-Ou-Mandel interference in an LNOI directional coupler, Optics Express **31**, 23140–23148 (2023).

[103] X. Shi, S. S. Mohanraj, V. Dhyani, A. A. Baiju, S. Wang, J. Sun, L. Zhou, A. Paterova, V. Leong, and D. Zhu, Efficient photon-pair generation in layer-poled lithium niobate nanophotonic waveguides, Light: Science & Applications **13**, 282 (2024).

[104] Q.-T. Zhu, X.-X. Fang, and H. Lu, Wavelength-tunable and high-heralding-efficiency quantum photon source in a birefringent phase-matched lithium niobate waveguide, Optics Letters **50**, 1853–1856 (2025).

[105] S. Babel, L. Bollmers, F. Roeder, W. Ridder, C. Golla, R. Köthemann, B. Reineke, H. Herrmann, B. Brecht, C. Eigner, et al., Ultrabright, two-color photon pair source

based on thin-film lithium niobate for bridging visible and telecom wavelengths, Optics Express **33**, 52729–52743 (2025).

[106] W. Qarony, A. S. Mayet, E. Ponizovskaya-Devine, S. Ghandiparsi, C. Bartolo-Perez, A. Ahamed, A. Rawat, H. H. Mamtaz, T. Yamada, S.-Y. Wang, et al., Achieving higher photoabsorption than group III-V semiconductors in ultrafast thin silicon photodetectors with integrated photon-trapping surface structures, Advanced Photonics Nexus **2**, 056001 (2023).

[107] R. Alferness, "Titanium-Diffused Lithium Niobate Waveguide Devices", in *Guided-Wave Optoelectronics* (Springer Berlin Heidelberg, 1988), pp. 145–210.

[108] P. R. Sharapova, K. H. Luo, H. Herrmann, M. Reichelt, T. Meier, and C. Silberhorn, Toolbox for the design of $LiNbO_3$-based passive and active integrated quantum circuits, New Journal of Physics **19**, 123009 (2017).

[109] M. Santandrea, M. Stefszky, G. Roeland, and C. Silberhorn, Characterisation of fabrication inhomogeneities in Ti:$LiNbO_3$ waveguides, New Journal of Physics **21**, 123005 (2019).

[110] A. Martin, A. Issautier, H. Herrmann, W. Sohler, D. B. Ostrowsky, O. Alibart, and S. Tanzilli, A polarization entangled photon-pair source based on a type-II PPLN waveguide emitting at a telecom wavelength, New Journal of Physics **12**, 103005 (2010).

[111] H. Herrmann, X. Yang, A. Thomas, A. Poppe, W. Sohler, and C. Silberhorn, Post-selection free, integrated optical source of non-degenerate, polarization entangled photon pairs, Optics Express **21**, 27981–27991 (2013).

[112] S. Krapick, H. Herrmann, V. Quiring, B. Brecht, H. Suche, and C. Silberhorn, An efficient integrated two-color source for heralded single photons, New Journal of Physics **15**, 33010 (2013).

[113] L. Sansoni, K. H. Luo, C. Eigner, R. Ricken, V. Quiring, H. Herrmann, and C. Silberhorn, A two-channel, spectrally degenerate polarization entangled source on chip, npj Quantum Information **3**, 1–5 (2017).

[114] K.-H. Luo, V. Ansari, M. Massaro, M. Santandrea, C. Eigner, R. Ricken, H. Herrmann, and C. Silberhorn, Counter-propagating photon pair generation in a nonlinear waveguide, Optics Express **28**, 3215–3225 (2020).

[115] A. Warke and K. Thyagarajan, Direct generation of two-pair frequency entanglement via dual periodic poling in lithium niobate waveguides, The European Physical Journal Plus **137**, 1–9 (2022).

[116] C. Kießler, H. Conradi, M. Kleinert, V. Quiring, H. Herrmann, and C. Silberhorn, Fiber-coupled plug-and-play heralded single photon source based on Ti:$LiNbO_3$ and polymer technology, Optics Express **31**, 22685–22697 (2023).

[117] R. Pollmann, F. Roeder, V. Quiring, R. Ricken, C. Eigner, B. Brecht, and C. Silberhorn, Integrated, bright broadband, two-colour parametric down-conversion source, Optics Express **32**, 23945–23955 (2024).

[118] F. Roeder, A. Gnanavel, R. Pollmann, O. Brecht, M. Stefszky, L. Padberg, C. Eigner, C. Silberhorn, and B. Brecht, Ultra-broadband non-degenerate guided-wave bi-photon source in the near and mid-infrared, New Journal of Physics **26**, 123025 (2024).

[119] R. Alferness, R. Schmidt, and E. Turner, Characteristics of Ti-diffused lithium niobate optical directional couplers, Applied Optics **18**, 4012–4016 (1979).

[120] C. Huang, C. Lin, Y. Chen, and Y. Huang, Electro-optic Ti:PPLN waveguide as efficient optical wavelength filter and polarization mode converter, Optics Express **15**, 2548–2554 (2007).

[121] M. Allgaier, V. Ansari, L. Sansoni, C. Eigner, V. Quiring, R. Ricken, G. Harder, B. Brecht, and C. Silberhorn, Highly efficient frequency conversion with bandwidth compression of quantum light, Nature Communications **8**, 1–6 (2017).

[122] K.-H. Luo, S. Brauner, C. Eigner, P. R. Sharapova, R. Ricken, T. Meier, H. Herrmann, and C. Silberhorn, Nonlinear integrated quantum electro-optic circuits, Science Advances **5**, eaat1451 (2019).

[123] F. Thiele, F. vom Bruch, J. Brockmeier, M. Protte, T. Hummel, R. Ricken, V. Quiring, S. Lengeling, H. Herrmann, C. Eigner, et al., Cryogenic electro-optic modulation in titanium in-diffused lithium niobate waveguides, Journal of Physics: Photonics **4**, 034004 (2022).

[124] Y. Li, Z. Yang, H. Chen, R. Liu, J. Peng, F. Fu, T. Yang, H. Guan, X. Yang, H. Di, et al., TE/TM mode electro-optic conversion based on a titanium diffusion lithium niobate waveguide with a polarization-maintained fiber structure, Applied Optics **62**, 8661–8669 (2023).

[125] J. P. Höpker, T. Gerrits, A. Lita, S. Krapick, H. Herrmann, R. Ricken, V. Quiring, R. Mirin, S. W. Nam, C. Silberhorn, et al., Integrated transition edge sensors on titanium in-diffused lithium niobate waveguides, APL Photonics **4**, 56103 (2019).

[126] J. P. Höpker, V. B. Verma, M. Protte, R. Ricken, V. Quiring, C. Eigner, L. Ebers, M. Hammer, J. Förstner, C. Silberhorn, et al., Integrated superconducting nanowire single-photon detectors on titanium in-diffused lithium niobate waveguides, Journal of Physics: Photonics **3**, 034022 (2021).

[127] R. Alferness, V. Ramaswamy, S. Korotky, M. Divino, and L. Buhl, Efficient single-mode fiber to titanium diffused lithium niobate waveguide coupling for $\lambda = 1.32$ µm, IEEE Journal of Quantum Electronics **18**, 1807–1813 (1982).

[128] M. Yamada, N. Nada, M. Saitoh, and K. Watanabe, First-order quasi-phase matched $LiNbO_3$ waveguide periodically poled by applying an external field for efficient blue second-harmonic generation, Applied Physics Letters **62**, 435–436 (1993).

[129] S. Tanzilli, W. Tittel, H. De Riedmatten, H. Zbinden, P. Baldi, M. DeMicheli, D. B. Ostrowsky, and N. Gisin, PPLN waveguide for quantum communication, European Physical Journal D **18**, 155–160 (2002).

[130] Y. Niu, X. Yan, J. Chen, Y. Ma, Y. Zhou, H. Chen, Y. Wu, and Z. Bai, Research progress on periodically poled lithium niobate for nonlinear frequency conversion, Infrared Physics & Technology **125**, 104243 (2022).

[131] M. Bartnick, M. Santandrea, J. P. Höpker, F. Thiele, R. Ricken, V. Quiring, C. Eigner, H. Herrmann, C. Silberhorn, and T. J. Bartley, Cryogenic second-harmonic generation in periodically poled lithium niobate waveguides, Physical Review Applied **15**, 024028 (2021).

[132] F. Thiele, F. vom Bruch, V. Quiring, R. Ricken, H. Herrmann, C. Eigner, C. Silberhorn, and T. J. Bartley, Cryogenic electro-optic polarisation conversion in titanium in-diffused lithium niobate waveguides, Optics Express **28**, 28961–28968 (2020).

[133] Y. Cheng, X. Li, L. Feng, H. Li, W. Sun, X. Song, Y. Ding, G. Guo, C. Wang, and X. Ren, Efficient cryogenic nonlinear conversion processes in periodically-poled thin-film lithium niobate waveguides, Laser & Photonics Reviews **19**, 2401491 (2025).

[134] Y. Cheng, L. Feng, J. He, X. Song, X. Han, Y. Ding, C. Wang, G. Guo, M. Zhang, D. Dai, et al., Cryogenic lithium-niobate-on-insulator optical filter, Optics Letters **49**, 1969–1972 (2024).

[135] E. Lomonte, M. A. Wolff, F. Beutel, S. Ferrari, C. Schuck, W. H. Pernice, and F. Lenzini, Single-photon detection and cryogenic reconfigurability in lithium niobate nanophotonic circuits, Nature Communications **12**, 6847 (2021).

[136] L.-T. Feng, Y.-J. Cheng, X.-Z. Qi, Z.-Y. Zhou, M. Zhang, D.-X. Dai, G.-C. Guo, and X.-F. Ren, Entanglement generation using cryogenic integrated four-wave mixing, Optica **10**, 702–707 (2023).

[137] D. Witt, L. Chrostowski, and J. Young, Packaged cryogenic photon pair source using an effective packaging methodology for cryogenic integrated optics, Applied Physics Letters **127**, 021105 (2025).

[138] B. S. Lee, B. Kim, A. P. Freitas, A. Mohanty, Y. Zhu, G. R. Bhatt, J. Hone, and M. Lipson, High-performance integrated graphene electro-optic modulator at cryogenic temperature, Nanophotonics **10**, 99–104 (2021).

[139] N. A. Lange, J. P. Höpker, R. Ricken, V. Quiring, C. Eigner, C. Silberhorn, and T. J. Bartley, Cryogenic integrated spontaneous parametric down-conversion, Optica **9**, 108–111 (2022).

[140] N. A. Lange, T. Schapeler, J. P. Höpker, M. Protte, and T. J. Bartley, Degenerate photons from a cryogenic spontaneous parametric down-conversion source, Physical Review A **108**, 023701 (2023).

[141] N. A. Lange, S. Lengeling, P. Mues, V. Quiring, W. Ridder, C. Eigner, H. Herrmann, C. Silberhorn, and T. J. Bartley, Widely non-degenerate nonlinear frequency conversion in cryogenic titanium in-diffused lithium niobate waveguides, Optics Express **33**, 50451–50469 (2025).

[142] M. F. Askarani, M. L. G. Puigibert, T. Lutz, V. B. Verma, M. D. Shaw, S. W. Nam, N. Sinclair, D. Oblak, and W. Tittel, Storage and reemission of heralded telecommunication-wavelength photons using a crystal waveguide, Physical Review Applied **11**, 054056 (2019).

[143] S.-W. Huang, E. Granados, W. R. Huang, K.-H. Hong, L. E. Zapata, and F. X. Kärtner, High conversion efficiency, high energy terahertz pulses by optical rectification in cryogenically cooled lithium niobate, Optics Letters **38**, 796–798 (2013).

[144] S. Carbajo, J. Schulte, X. Wu, K. Ravi, D. N. Schimpf, and F. X. Kärtner, Efficient narrowband terahertz generation in cryogenically cooled periodically poled lithium niobate, Optics Letters **40**, 5762–5765 (2015).

[145] G. K. Kitaeva, V. Kornienko, K. Kuznetsov, I. Pentin, K. Smirnov, and Y. B. Vakhtomin, Direct detection of the idler THz radiation generated by spontaneous parametric down-conversion, Optics Letters **44**, 1198–1201 (2019).

[146] Z. Shu, Y. Li, X. Liu, H. Han, Y. Xiao, J. Huang, H. Xu, W. Zhang, L. You, Z. Wang, et al., On-chip superconducting nanowire single-photon detectors integrated with pump rejection for entanglement characterization, Photonics Research **13**, 1067–1073 (2025).

[147] Y. Li, Z. Shu, X. Liu, Y. Xiao, J. Huang, H. Xu, C. Ding, L. You, Z. Wang, and H. Li, Cryogenic-compatible ultrahigh rejection and narrowband sinusoidal bragg filter for integrated quantum photonics, Optics Express **33**, 52541–52550 (2025).

[148] C. Schuck, X. Guo, L. Fan, X. Ma, M. Poot, and H. X. Tang, Quantum interference in heterogeneous superconducting-photonic circuits on a silicon chip, Nature Communications **7**, 10352 (2016).

[149] F. Eltes, G. E. Villarreal-Garcia, D. Caimi, H. Siegwart, A. A. Gentile, A. Hart, P. Stark, G. D. Marshall, M. G. Thompson, J. Barreto, et al., An integrated optical modulator operating at cryogenic temperatures, Nature Materials **19**, 1164–1168 (2020).

[150] Y. Wang, Y. Ma, X. Wang, Z. Zhao, Y. Li, and T. Yang, Temperature-insensitive cryogenic packaging for thin-film lithium niobate photonic chips, Photonics **12**, 545 (2025).

[151] J. Rams, A. Alcázar-de-Velasco, M. Carrascosa, J. Cabrera, and F. Agulló-López, Optical damage inhibition and thresholding effects in lithium niobate above room temperature, Optics Communications **178**, 211–216 (2000).

[152] J. Parravicini, J. Safioui, V. Degiorgio, P. Minzioni, and M. Chauvet, All-optical technique to measure the pyroelectric coefficient in electro-optic crystals, Journal of Applied Physics **109**, 033106 (2011).

[153] S. Pal, B. K. Das, and W. Sohler, Photorefractive damage resistance in Ti:PPLN waveguides with ridge geometry, Applied Physics B **120**, 737–749 (2015).

[154] F. Thiele, T. Hummel, N. A. Lange, F. Dreher, M. Protte, F. v. Bruch, S. Lengeling, H. Herrmann, C. Eigner, C. Silberhorn, et al., Pyroelectric influence on lithium niobate during the thermal transition for cryogenic integrated photonics, Materials for Quantum Technology **4**, 015402 (2024).

[155] A. Migdall, S. V. Polyakov, J. Fan, and J. C. Bienfang, *Single-Photon Generation and Detection: Physics and Applications* (Academic Press, 2013).

[156] S. Jachalke, E. Mehner, H. Stöcker, J. Hanzig, M. Sonntag, T. Weigel, T. Leisegang, and D. C. Meyer, How to measure the pyroelectric coefficient?, Applied Physics Reviews **4**, 21303 (2017).

[157] G. S. Thekkadath, B. A. Bell, R. B. Patel, M. S. Kim, and I. A. Walmsley, Measuring the joint spectral mode of photon pairs using intensity interferometry, Physical Review Letters **128**, 023601 (2022).

[158] I. Hurvitz, A. Shukhin, L. Vidro, H. Eisenberg, and A. Arie, Phase analysis of biphoton joint spectra by interference between different SPDC sources, Optica Quantum **2**, 358–364 (2024).

[159] G. J. Edwards and M. Lawrence, A temperature-dependent dispersion equation for congruently grown lithium niobate, Optical and Quantum Electronics **16**, 373–375 (1984).

[160] D. H. Jundt, Temperature-dependent Sellmeier equation for the index of refraction, $\mathrm{n_e}$, in congruent lithium niobate, Optics Letters **22**, 1553–1555 (1997).

[161] K. Wong, *Properties of Lithium Niobate* (INSPEC, 2002).

[162] P. Reichenbach, T. Kämpfe, A. Haußmann, A. Thiessen, T. Woike, R. Steudtner, L. Kocsor, Z. Szaller, L. Kovács, and L. M. Eng, Polaron-mediated luminescence in lithium niobate and lithium tantalate and its domain contrast, Crystals **8**, 214 (2018).

[163] F. Jermann, M. Simon, and E. Krätzig, Photorefractive properties of congruent and stoichiometric lithium niobate at high light intensities, Journal of the Optical Society of America B **12**, 2066–2070 (1995).

[164] J. Villarroel, J. Carnicero, F. Luedtke, M. Carrascosa, A. García-Cabañes, J. M. Cabrera, A. Alcazar, and B. Ramiro, Analysis of photorefractive optical damage in lithium niobate: application to planar waveguides, Optics Express **18**, 20852–20861 (2010).

[165] M. Imlau, H. Badorreck, and C. Merschjann, Optical nonlinearities of small polarons in lithium niobate, Applied Physics Reviews **2**, 040606 (2015).

[166] T. Volk and M. Wöhlecke, *Lithium Niobate: Defects, Photorefraction and Ferroelectric Switching* (Springer Berlin Heidelberg, 2008).

[167] O. F. Schirmer, M. Imlau, C. Merschjann, and B. Schoke, Electron small polarons and bipolarons in $LiNbO_3$, Journal of Physics: Condensed Matter **21**, 123201 (2009).

[168] V. Fradkin and R. Magomadov, Anomalous photovoltaic effect in $LiNbO_3$:Fe in polarized light, JETP Letters **30**, 686–688 (1979).

[169] F. Chen, Optically induced change of refractive indices in $LiNbO_3$ and $LiTaO_3$, Journal of Applied Physics **40**, 3389–3396 (1969).

[170] M. Carrascosa, J. Villarroel, J. Carnicero, A. García-Cabañes, and J. Cabrera, Understanding light intensity thresholds for catastrophic optical damage in $LiNbO_3$, Optics Express **16**, 115–120 (2008).

[171] S. M. Kostritskii, O. G. Sevostyanov, M. Aillerie, and P. Bourson, Suppression of photorefractive damage with aid of steady-state temperature gradient in nominally pure $LiNbO_3$ crystals, Journal of Applied Physics **104**, 114104 (2008).

[172] S. B. Lang, Pyroelectricity: from ancient curiosity to modern imaging tool, Physics Today **58**, 31–36 (2005).

[173] S. L. Bravina, A. N. Morozovska, N. V. Morozovsky, and Y. A. Skryshevsky, Low-temperature pyroelectric phenomena in lithium niobate single crystals, Ferroelectrics **298**, 31–42 (2004).

[174] D. N. Klyshko, Use of two-photon light for absolute calibration of photoelectric detectors, Soviet Journal of Quantum Electronics **10**, 1112 (1980).

[175] A. Ekert and P. L. Knight, Entangled quantum systems and the schmidt decomposition, American Journal of Physics **63**, 415–423 (1995).

[176] A. Eckstein, A. Christ, P. J. Mosley, and C. Silberhorn, Highly efficient single-pass source of pulsed single-mode twin beams of light, Physical Review Letters **106**, 013603 (2011).

[177] A. Christ, C. Lupo, M. Reichelt, T. Meier, and C. Silberhorn, Theory of filtered type-II parametric down-conversion in the continuous-variable domain: quantifying the impacts of filtering, Physical Review A **90**, 23823 (2014).

[178] A. Christ, K. Laiho, A. Eckstein, K. N. Cassemiro, and C. Silberhorn, Probing multimode squeezing with correlation functions, New Journal of Physics **13**, 33027 (2011).

[179] W. Mauerer, M. Avenhaus, W. Helwig, and C. Silberhorn, How colors influence numbers: photon statistics of parametric down-conversion, Physical Review A **80**, 053815 (2009).

[180] K. Oh and U.-C. Paek, *Silica Optical Fiber Technology for Devices and Components: Design, Fabrication, and International Standards* (John Wiley & Sons, 2012).

[181] E. Meyer-Scott, N. Prasannan, C. Eigner, V. Quiring, J. M. Donohue, S. Barkhofen, and C. Silberhorn, High-performance source of spectrally pure, polarization entangled photon pairs based on hybrid integrated-bulk optics, Optics Express **26**, 32475–32490 (2018).

[182] R. Regener and W. Sohler, Loss in low-finesse Ti:LiNbO$_3$ optical waveguide resonators, Applied Physics B **36**, 143–147 (1985).

[183] I. S. Akhmadullin, V. Golenishchev-Kutuzov, S. Migachev, and S. Mironov, Low-temperature electrical conductivity of congruent lithium niobate crystals, Physics of the Solid State **40**, 1190–1192 (1998).

[184] Y. V. Shaldin, V. Gabriélyan, and S. Matyjasik, Pyroelectric properties of real LiNbO3 single crystals grown from a congruent melt, Crystallography Reports **53**, 847–852 (2008).

[185] N. A. Lange, R. Pollmann, M. Rüsing, M. Stefszky, M. Protte, R. Ricken, L. Padberg, C. Eigner, T. J. Bartley, and C. Silberhorn, Photorefraction management in lithium niobate waveguides: high-temperature vs cryogenic solutions, Journal of Applied Physics **139**, 133105 (2026).

[186] M. Kösters, B. Sturman, P. Werheit, D. Haertle, and K. Buse, Optical cleaning of congruent lithium niobate crystals, Nature Photonics **3**, 510–513 (2009).

[187] B. Sturman, M. Kösters, D. Haertle, C. Becher, and K. Buse, Optical cleaning owing to the bulk photovoltaic effect, Physical Review B **80**, 245319 (2009).

[188] L. L. Ding, E. Beyreuther, B. Koppitz, K. Kempf, J. H. Ren, W. J. Chen, M. Rüsing, Y. Zheng, and L. M. Eng, Comparative study of photo-induced electronic transport along ferroelectric domain walls in lithium niobate single crystals, Applied Physics Letters **124**, 252901 (2024).

[189] M. Imlau, H. Badorreck, and C. Merschjann, Optical nonlinearities of small polarons in lithium niobate, Applied Physics Reviews **2**, 040606 (2015).

[190] M. Kirsch, C. Kießler, S. Lengeling, M. Stefszky, C. Eigner, H. Herrmann, and C. Silberhorn, Photorefraction and in-situ optical cleaning in various types of LiNbO$_3$ waveguides, Optics & Laser Technology **193**, 114260 (2026).

[191] H. B. Lin, S. H. Yu, C. X. Shi, X. J. Lv, P. Lv, Z. D. Xie, G. Zhao, and S. N. Zhu, Extended sellmeier equation for the extraordinary refractive index of 5% MgO-doped congruent LiNbO3 at high temperature, AIP Advances **7**, 095201 (2017).

[192] M. Misiaszek, A. Gajewski, and P. Kolenderski, Dispersion measurement method with down conversion process, Journal of Physics Communications **2**, 065014 (2018).

[193] F. Kienle, D. Lin, S.-u. Alam, H. S. S. Hung, C. B. E. Gawith, H. E. Major, D. J. Richardson, and D. P. Shepherd, Green-pumped, picosecond mgo:ppln optical parametric oscillator, Journal of the Optical Society of America B **29**, 144–152 (2012).

[194] M. Protte, “Building blocks for integrated homodyne detection with superconducting nanowire single-photon detectors”, PhD Thesis (Paderborn University, 2023).

[195] M. R. Akanda, A. M. Osman, M. K. Nazal, and M. A. Aziz, Review—Recent Advancements in the Utilization of Indium Tin Oxide (ITO) in Electroanalysis without Surface Modification, Journal of The Electrochemical Society **167**, 037534 (2020).

[196] M. Shen, J. Xie, Y. Xu, S. Wang, R. Cheng, W. Fu, Y. Zhou, and H. X. Tang, Photonic link from single-flux-quantum circuits to room temperature, Nature Photonics **18**, 371–378 (2024).

Appendix A

A.1 Publications

First-author publications

Cryogenic integrated spontaneous parametric down-conversion

Nina Amelie Lange, Jan Philipp Höpker, Raimund Ricken, Viktor Quiring, Christof Eigner, Christine Silberhorn, and Tim J. Bartley
Optica **9**, 108–111 (2022)

Degenerate photons from a cryogenic spontaneous parametric down-conversion source

Nina Amelie Lange, Timon Schapeler, Jan Philipp Höpker, Maximilian Protte, and Tim J. Bartley
Physical Review A **108**, 023701 (2023)

Widely non-degenerate nonlinear frequency conversion in cryogenic titanium in-diffused lithium niobate waveguides

Nina Amelie Lange, Sebastian Lengeling, Philipp Mues, Viktor Quiring, Werner Ridder, Christof Eigner, Harald Herrmann, Christine Silberhorn, and Tim J. Bartley
Optics Express **33**, 50451–50469 (2025)

Photorefraction management in lithium niobate waveguides: High-temperature vs cryogenic solutions

Nina Amelie Lange, René Pollmann, Michael Rüsing, Michael Stefszky, Maximilian Protte, Raimund Ricken, Laura Padberg, Christof Eigner, Tim J. Bartley, and Christine Silberhorn
Journal of Applied Physics **139**, 133105 (2026)

Co-author contributions

Pyroelectric influence on lithium niobate during the thermal transition for cryogenic integrated photonics

Frederik Thiele, Thomas Hummel, **Nina Amelie Lange**, Felix Dreher, Maximilian Protte, Felix vom Bruch, Sebastian Lengeling, Harald Herrmann, Christof Eigner, Christine Silberhorn, and Tim J. Bartley
Materials for Quantum Technology **4**, 015402 (2024)

Cryogenic feedforward of a photonic quantum state

Frederik Thiele, Niklas Lamberty, Thomas Hummel, **Nina Amelie Lange**, Lorenzo M. Procopio, Aishi Barua, Sebastian Lengeling, Viktor Quiring, Christof Eigner, Christine Silberhorn, and Tim J. Bartley
Optica **12**, 720–727 (2025)

Harnessing temporal dispersion for integrated pump filtering in spontaneous heralded single-photon generation processes

Julian Brockmeier, Timon Schapeler, **Nina Amelie Lange**, Jan Philipp Höpker, Harald Herrmann, Christine Silberhorn, and Tim J. Bartley
New Journal of Physics **27**, 074101 (2025)

A.2 Statement on the Use of Artificial Intelligence

The following table outlines the generative AI tools and Large Language Models employed during the preparation of this thesis. These tools were used to assist with the writing process, improve linguistic clarity, and support data visualization, document formatting and literature review tasks. Crucially, all AI-generated suggestions, summaries, and code snippets were manually reviewed, verified against primary literature, and edited by the author to ensure scientific accuracy and personal stylistic consistency. All scientific core contents, data analysis, and interpretations remain the original, independent work of the author.

Table A.1: Overview of AI tools and their specific applications in the preparation of this thesis.

AI Tool	**Scope of Application and Usage**
Gemini 3 Flash	**Linguistic Polishing:** Assisted in refining technical descriptions and academic tone and reorganizing complex sentences to improve logical flow and readability. **LaTeX & Technical Support:** Assisted with typesetting and troubleshooting, specifically debugging compiler errors. **Python Code Optimization:** Optimized data plotting via `matplotlib`, including the implementation of consistent global styling, subplot alignment, and figure scaling.
DeepL Translator	**Proofreading:** Used for automated grammar and spell-checking to ensure linguistic consistency for individual paragraphs.
Perplexity AI	**Literature Screening:** Generated initial summaries of research papers to assess relevance. All selected manuscripts were subsequently read and analyzed by the author.
NotebookLM	**Literature Synthesis:** Assisted with the comparison of various research papers. All findings were subsequently validated through a direct comparison with the primary literature.
OpenAI ChatGPT (GPT-4)	**Idea Generation:** Assisted in developing creative analogies for the thesis introduction, leading to the concept of the “cryogenic traffic jam” metaphor.

A.3 Supplemental material to Chapter 3

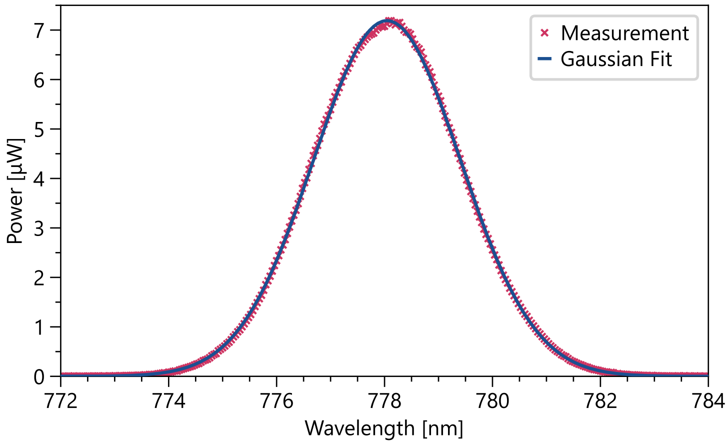

Figure A.1: Spectrum of the SHG beam used to pump the cryogenic proof-of-principle SPDC process, as described in Section 3.1. The Gaussian fit provides the central wavelength of (778.04 ± 0.01) nm and the bandwidth of (3.22 ± 0.01) nm.

A.4 Supplemental material to Chapter 4

A.4.1 Further details for the keen experimental scientist

- When operating the waveguide inside a crystal oven, it is important that the heated waveguide is enclosed as good as possible. Any air flow results in slight temperature changes and thus in fluctuations of the phase-matching spectrum. The default oven cover was too thick to move the out-coupling lens close enough to the waveguide's end facet, but leaving the side wall open resulted in a recognizable air flow. For this reason, I designed a customized side aperture which allows to move the lens close enough and still keeps the required space to slightly move the sample and scan between different waveguides.
- Also included in the optical path of the pulsed laser, but not shown in the experimental setup in Fig. 4.1 for the sake of clarity, are a Faraday isolator, a telescope setup, and a biconvex lens for beam size adjustments. The isolator is crucial because otherwise, back reflections from the end facet of the waveguide can lead to chaotic laser response and potentially damage the laser. I set up a telescope consisting of two plano-convex lenses with a focal length of 15 mm and 30 mm, respectively. The original laser beam is diverging strongly, while the telescope increases the beam diameter by a factor of two which helps to collimate the beam over a longer distance. Additionally, another biconvex lens with a long focal length of 1 m is placed about 1 m in front of the waveguide. This results in a constant beam diameter at the position of the waveguide's in-coupling lens.

The divergence of the pulsed beam over the setup distance was simulated beforehand with a Gaussian beam simulation tool and the lenses were chosen accordingly.

- Moreover, the free-space beam of the NIR laser was modified for waveguide coupling. This laser is a diode laser which fundamentally emits an elliptical-shaped beam. If the application requires a circular beam profile, this may necessitate the use of external correction optics. However, the waveguide mode is asymmetric as well, as the Gaussian profile is skewed in the vertical direction. For this reason, I decided to keep the elliptical laser beam profile, but to ensure it is aligned in the correct orientation. For enhanced overlap with the waveguide mode, the input beam should possess an asymmetric profile that is skewed in the horizontal direction. This requires the initial laser beam to be rotated by 90°. In addition, the optical axis of the emitted laser beam is originally 44 mm lower than the optical axis height of the waveguide coupling stages. Consequently, I installed a periscope immediately after the laser output to rotate the beam and raise the optical axis, in order to meet both considerations. By implementing this periscope and optimizing the focal length of the in-coupling lens, the transmission of the waveguide at 950 nm was increased from approximately 30 % to 51 %.

A.4.2 Additional measurement data

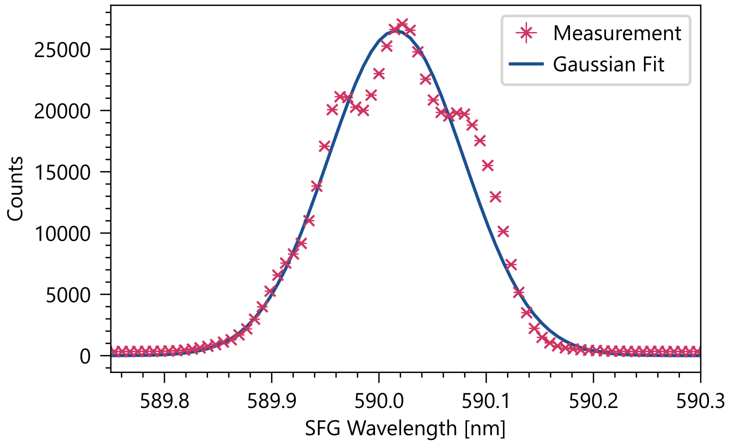

Figure A.2: Spectral shape of the generated pulsed SFG beam which is utilized as the pump light for the cryogenic SPDC source. A Gaussian fit is applied to approximate the central wavelength and the FWHM.

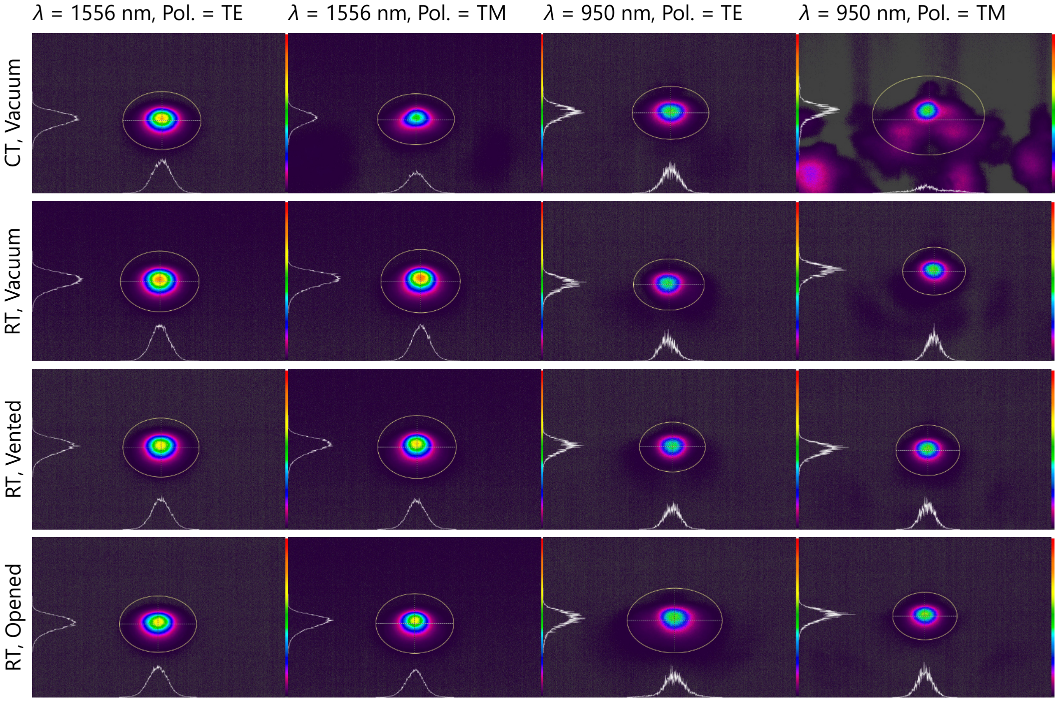
(a) Waveguide 13-1

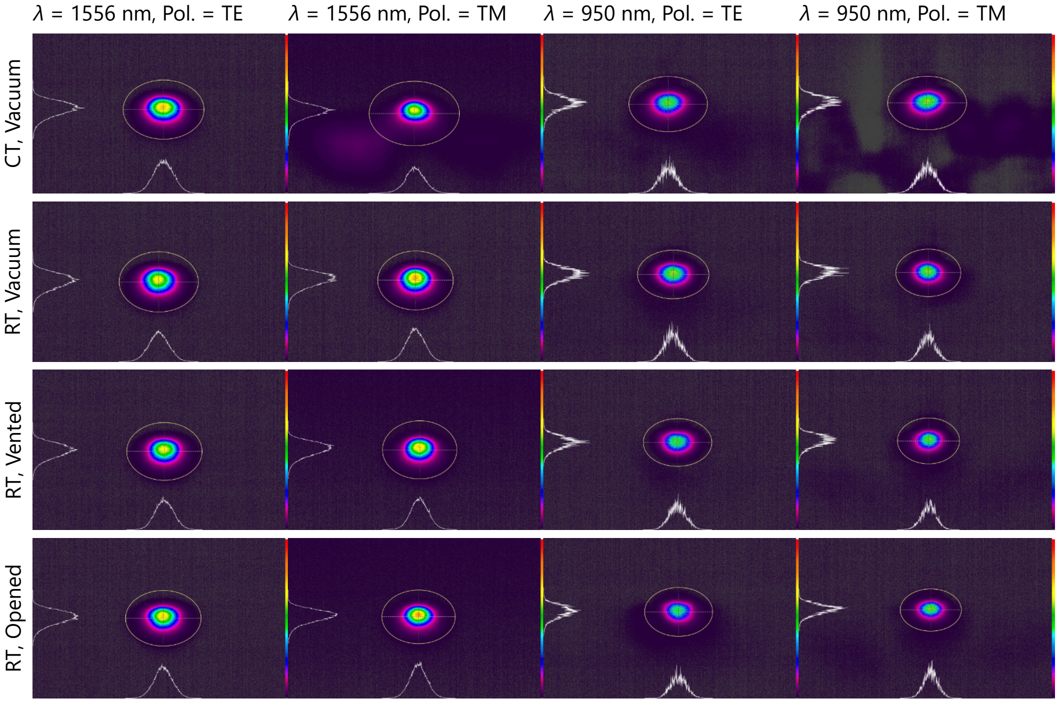
(b) Waveguide 14-2

Figure A.3: Mode images taken within the measurement series described in Section 4.3.1. I recorded an image for all four combinations of wavelength (1556 nm and 950 nm) and polarization (TE and TM) during the following measurement conditions: 1.) cryogenic temperatures, 2.) at room temperature, under low pressure, 3.) after venting the chamber, and 4.) after opening the system.

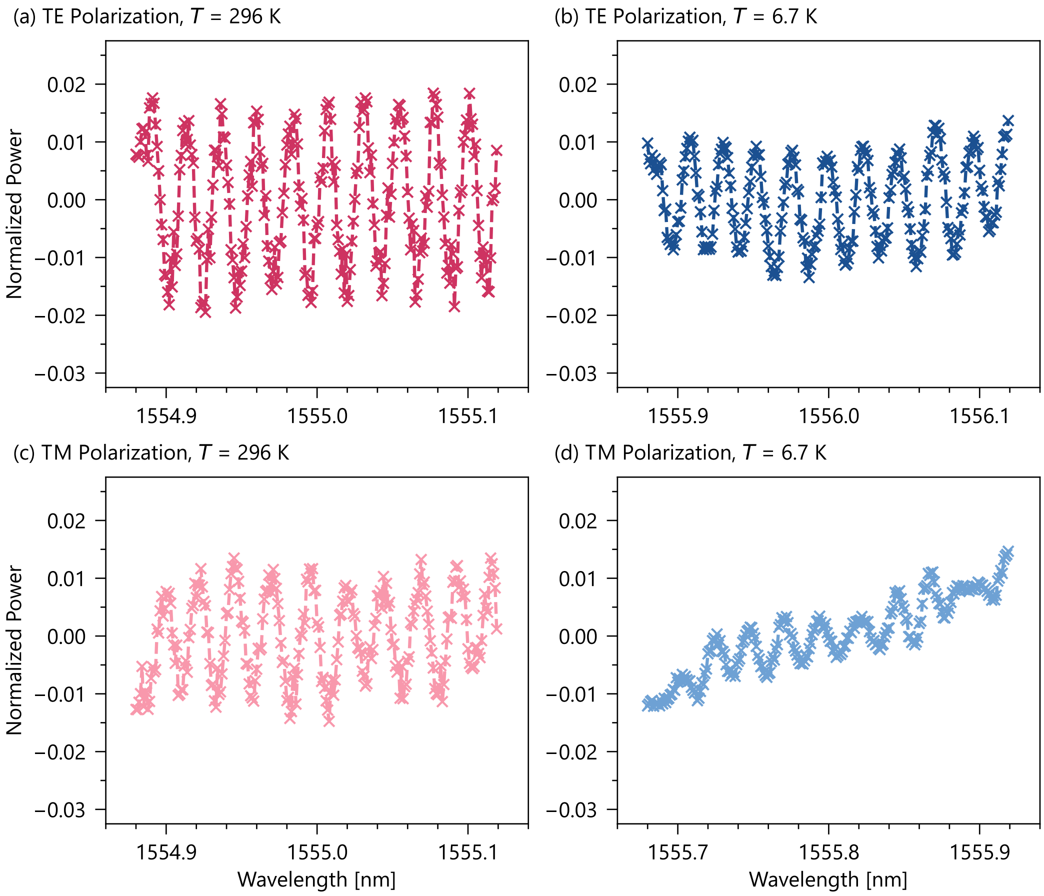

Figure A.4: Normalized transmitted power through waveguide 13-1, measured while scanning the input wavelength. The scan was performed using TE and TM polarization at room temperature of 296 K and cryogenic temperature of 6.7 K. For better comparison, all data is shown on the same y-axis scale.

A.5 Supplemental material to Chapter 5

A.5.1 Measurements on the individual waveguide groups

Group 8: Pulsed SHG with increasing pump power

For each waveguide, the coupling of the pulsed pump beam was optimized for low transmitted pump power of maximum 3 mW. To investigate the acceptable power threshold, in the next step, the transmitted pump power was increased step-by-step while measuring the SHG power. In every measurement, both detected power values dropped significantly when exceeding a certain power threshold. This happened before the maximum available pump power was reached. This threshold varied for the individual waveguides and cooldown cycles.

Fig. A.5 presents the trend of the generated SHG power over the transmitted pump power. As expected, the SHG power scales quadratically (compare Eq. (2.11)). The waveguides enabled SHG in every tested cooldown, albeit with varying conversion efficiencies and different acceptable power thresholds. All waveguides presented the largest resilience to high optical power in CD 6. This can be concluded from the increase of the transmitted pump power to about 15 mW (generating approx. 150 µW SHG power) before the waveguiding collapsed. Notably, the waveguides 8-1 and 8-2 demonstrated a comparably high threshold in the very first cooldown.

CD 1 and CD 5 were conducted following a heat-up of the sample. The highly similar slope of the quadratic increase recorded for all waveguides in these cooldowns indicates that the heat-up had a relaxing effect on the charge carrier distributions. After coupling too high optical power to the waveguides in CD 1, both CD 2 and CD 4 demonstrated lower conversion efficiency. This implies that the induced photorefractive damage is (to some extent) maintained in subsequent cooldowns. However, according to this assumption, the last cooldown would have been expected to demonstrate low conversion efficiency as well. In contrast, all waveguides featured the best performance in the last cycle. This suggests that the waveguiding was more strongly affected by the presence of disturbing pyroelectric fields, rather than long term photorefractive effects.

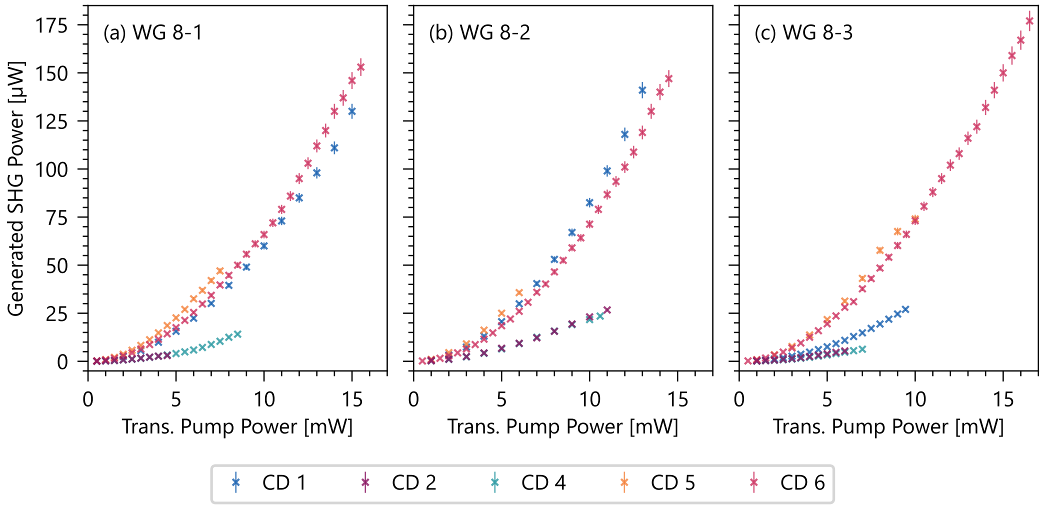

Figure A.5: Generated SHG power for the three waveguides of group 8 over the transmitted pump power for the distinct cooldown cycles. The pump power was increased until both the transmitted pump and the generated SHG power dropped abruptly.

Group 9: Pulsed SHG with low pump power

These measurements were performed with reduced pulsed power to evaluate the waveguide performance if no photorefraction is induced. As the cryogenic waveguides demonstrate high losses, the transmitted pump power was chosen as a reference for the actual optical power guided through the waveguides. While optimizing on the generated SHG power, I ensured that the transmitted power did not exceed 4 mW. After the setup was optimized, the pump power was fine-tuned to meet this predefined target value with a precision of ± 0.025 mW. At this point, the input pump power and the generated SHG power were measured.

This measurement data is visualized in Fig. A.6 (a). Here, a high input power directly corresponds to strong transmission losses. Large generated SHG power values coincide with higher conversion efficiencies for fixed transmitted power. To evaluate the performance, the absolute transmission of the pump beam $T = P_{\mathrm{trans}}/P_{\mathrm{in}}$ is calculated from the ratio of the transmitted pump power P_{trans} to the input power P_{in}. This transmission is presented in Fig. A.6 (b) together with a measure for the conversion of the input beam to the SHG beam, $\eta = P_{\mathrm{SHG}}/P_{\mathrm{in}}$. This figure of merit is calculated from the ratio of generated SHG power P_{SHG} to the detected input pump power.[1] Both the transmission and conversion were initially limited in the very first cooldown. An apparent enhancement was measured

---

[1] Please note that the precise quantification of the external nonlinear conversion efficiency requires knowledge of both the TE- and TM-polarized input power (compare Eq. (4.4)). As the input polarization was not diagonal and the total power in each mode was not recorded for all measurements, a simplified conversion parameter is introduced here in order to compare the performance across all waveguides and cooldowns.

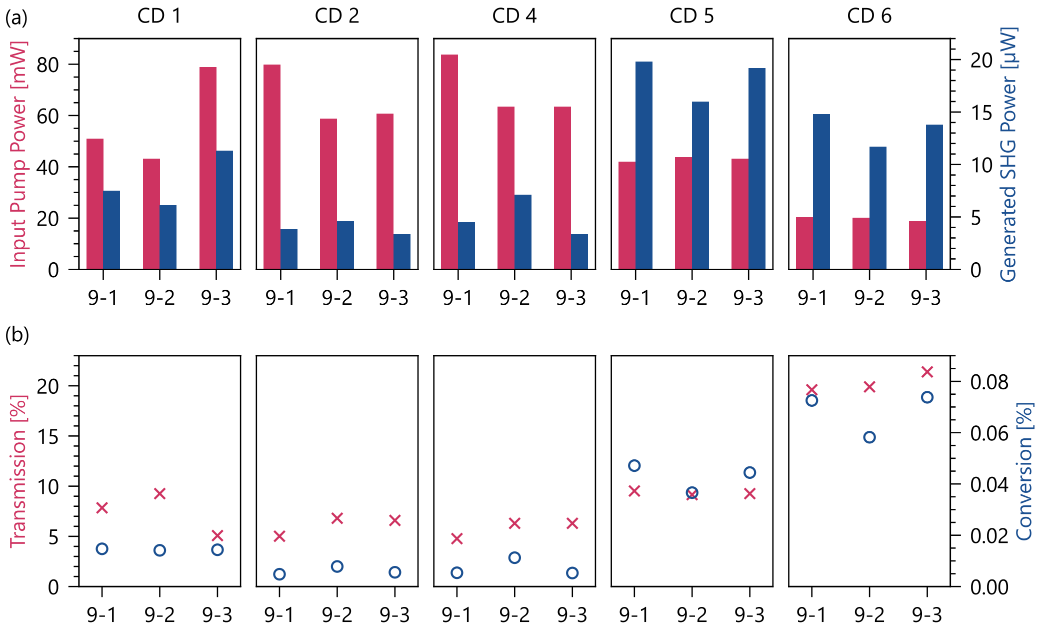

Figure A.6: Overview of the input pump power required to obtain a transmitted pump power of (4.000 ± 0.025) mW and the detected SHG power for WGG 9 within the individual cooldown cycles. (a) Comparison of the raw measurement data and (b) calculated transmission of the pump power and conversion of the input pump power to SHG power.

following the second heat-up (between CD 4 and CD 5), with further improvement in the final cooldown.

The pulsed measurement series for both WGG 8 and WGG 9 revealed that when inspecting the polarization of the pump beam, after optimizing the experimental setup for maximum SHG power, this beam was almost completely TM-polarized. This was verified by inserting a PBS and measuring the optical power in both output arms. I measured 460 µW in the TE-polarized port, which corresponds to only 2 % of the power measured in the TM-polarized port (23.3 mW). The significant contrast between these powers indicates that the TM-polarized mode experiences tremendous transmission losses which must be compensated by excessive optical power levels. However, the TE-mode is guided well so that only low power is required to enable the SHG process. This is consistent with the observation of the transmitted modes on a fluorescent card. TE-polarized light generally featured a collimated mode, while the TM-polarized mode profile was dominated by scattered noise, which often complicated optimization of the coupling. Despite the low waveguide transmission and weak SHG signals, the pulsed experiments for WGG 8 and WGG 9 were successful throughout all cooldowns. This is in contrast to the CW SHG measurements which are discussed next.

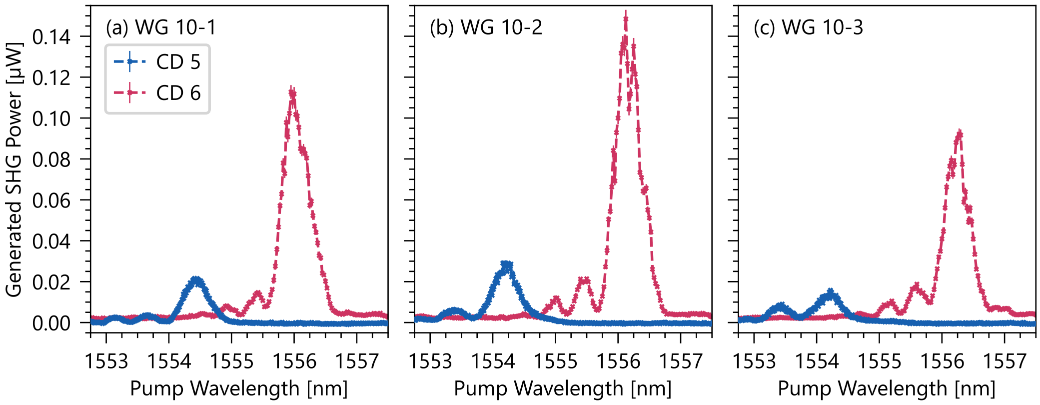

Figure A.7: Cryogenically recorded phase-matching spectra for WGG 10, measured in the cooldowns 5 and 6. In comparison to CD 5, the SHG power increased and the peak shifted to longer wavelengths in the final CD 6.

Group 10: CW SHG with low pump power

This waveguide group was chosen to be operated exclusively with CW pump light, restricted to low optical power, to assess the impact of pyroelectric distortions without additional photorefraction. The pump laser was operated at its lowest power setting, corresponding to an input power of (7.88 ± 0.24) mW. The pulsed excitation of WGG 8 and WGG 9 yielded a detectable SHG signal within the first four thermal cycles, despite poor waveguiding quality for TM-polarized light. However, I was not able to measure a spectrum for the three CW-operated groups, when repeatedly scanning the pump wavelength around the expected phase-matching point of 1556 nm.

Like with the pulsed measurements, the waveguide performance improved in CD 5, following the second heat-up. This time, the TM-polarized beam could be coupled to the waveguide, yielding a collimated mode. This transmitted mode still exhibited some scattered light, which was in contrast to TE polarization. However, in comparison to the prior cooling cycles, the general performance enhanced significantly.

CD 5 and CD 6 resulted in a measurable phase-matching spectrum for each waveguide, shown in Fig. A.7. The scale on the y-axis was chosen to be uniform for all measurements to visualize a strong increase in SHG intensity and signal-to-noise ratio in CD 6. While the input power was kept constant, the average transmitted pump power increased from about (1.63 ± 0.05) mW in CD 5 to (2.6 ± 0.3) mW in CD 6. This observation demonstrates significantly reduced transmission losses. Furthermore, the central wavelength of the spectrum experienced a red shift by approximately 2 nm. This shift is similar for all three waveguides. This indicates that changes in the “frozen-in” charge carrier distributions happened to the complete waveguide group between CD 5 and CD 6.

Group 11: CW SHG with increasing pump power

This group was analyzed with regard to increasing the pump power at cryogenic temperatures to define a threshold of tolerated power. As for WGG 10, these measurements were only successful in the last two cooldowns. The same pump wavelength scan was performed in total twelve times while incrementally increasing the input power from 7.9 mW to the maximally available power of 25.1 mW. Within this range, the spectral shape of the phase-matching spectra did not present significant changes. This is visualized in Fig. A.8. All twelve measurements were normalized to the same peak power (measured for maximum pump power) and subsequently averaged. These average curves are plotted together with the spectra detected at maximum power in Fig. A.8 (a) and (b).

For each waveguide, the averaged curves match the spectra at highest pump power extremely well. This demonstrates that the pump power of up to 25.1 mW did not induce photorefractive damage under cryogenic conditions. This is consistent with the observations from Chapter 3, where the cryogenic SHG process was pumped with 22.0 mW and exhibited a phase-matching spectrum close to the ideal shape (Fig. 3.4). Here, the spectra exhibited an asymmetric shape already at the start of the measurement series. This shape was similar for all three waveguides, which suggests again a pyroelectric charge carrier distribution which spans across the entire group. While these pyroelectric distortions alter the general shape, this shape was not additionally affected by the available pump power.

Fig. A.8 (c) shows that the peak intensities of the generated SHG signal increased substantially from CD 5 to CD 6, consistent with the observations for WGG 10. Here, in both cooling cycles, the generated SHG power scaled quadratically with the input power. The onset of photorefraction would cause a deviation from the quadratic trend, which was not observed in the investigated power range. For these reasons, the presented data implies a common, unpredictable waveguide distortion due to pyroelectricity, while an optical power of up to 25 mW does not induce photorefraction if the general cryogenic waveguiding is sufficient to enable SHG.

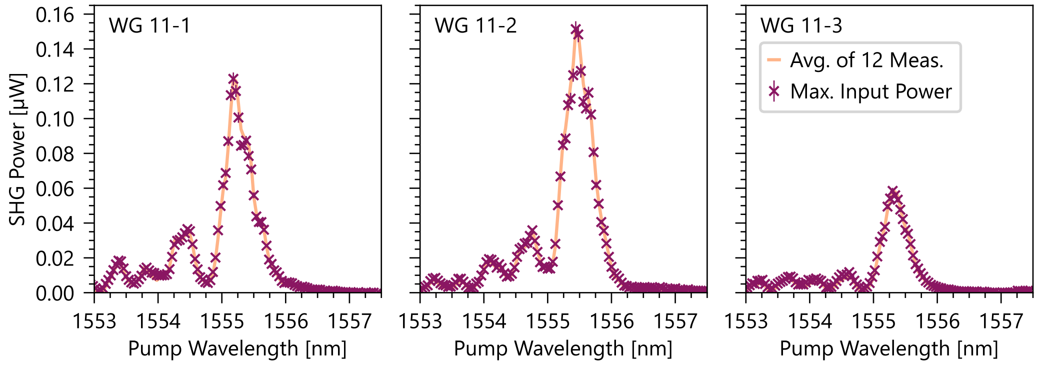
(a) Cooldown 5

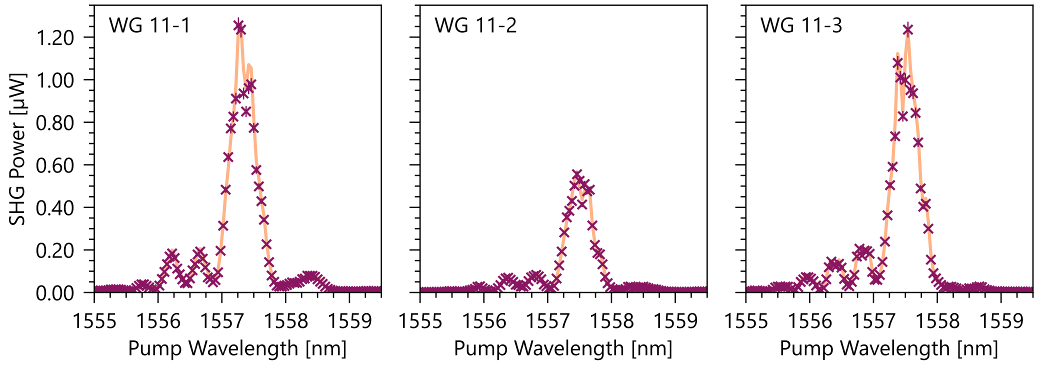
(b) Cooldown 6

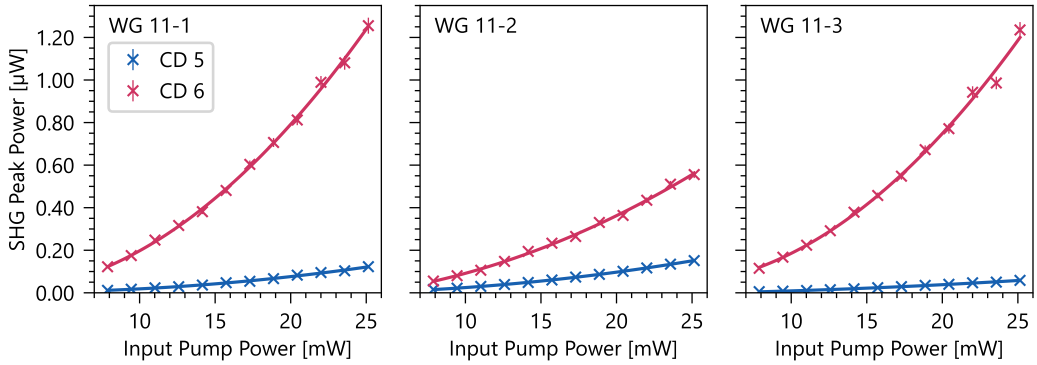
(c) Generated SHG Peak Power

Figure A.8: Cryogenic SHG response of WGG 11 when incrementally increasing the input pump power in twelve steps. For each waveguide, all measured spectra were normalized (to the peak for maximum pump power) and averaged. This average curve is shown in (a) and (b) together with the spectrum measured at maximum power, to visualize that no considerable alterations were recorded when increasing the power. (c) The generated SHG peak power scales quadratically with the input power. The data for CD 5 and CD 6 are plotted together with a quadratic fit on the same y-axis, to demonstrate the large difference in conversion efficiency.

Group 12: CW SHG with high pump power and green laser coupling

The generated SHG power for this waveguide group was directly optimized while operating the waveguides at highest CW pump power (25.1 mW). While the results for WGG 11 demonstrated no onset of photorefraction, here, the effect of the green laser is evaluated on any "frozen-in" charges, that can also originate from pyroelectricity. The phase-matching spectrum was recorded repeatedly while the green laser was coupled to the waveguide in between the measurements. The green light was activated for a duration of 2 min and then turned off again before the next phase-matching spectrum was recorded. This procedure was conducted three times. The data is shown in Fig. A.9.

In comparison to CD 5, the initial phase-matching spectra without green light exposure demonstrate a general shift by approximately 2 nm in CD 6. This shift is accompanied by a significant increase in the generated peak power. Both observations are consistent with the results for the other two groups that were investigated with CW light. When activating the green laser diode, a different response of the waveguides was measured in the two cycles. In CD 5, the central wavelength of the main peak was barely affected. However, in CD 6, the main peak was shifted by about 1 nm to smaller wavelengths directly after the first exposure interval. No further shift was observed in the subsequent two intervals. Consequently, the main changes in the spectra happened directly within only 2 min of green illumination.

The total spectral shape remained mostly unchanged in both cooldowns when coupling the green laser beam. The spectra exhibit an asymmetrical shape with dominant side peaks located only on the shorter wavelengths side. The same general shape was also observed for WGG 10 and WGG 11. This strongly indicates a charge carrier distribution which spreads across several waveguide groups so that the refractive index profiles along these waveguides are altered in a highly similar way. The non-reproducible waveguide response to the green laser beam implies that this method cannot be considered a reliable technique to enhance the cryogenic waveguide performance. While the method clearly induced a homogeneous shift of the complete phase-matching spectra in the final cooldown, both the generated peak power and the spectral shape were not improved. For this reason, this mitigation protocol demands further studies and optimization.

(a) Cooldown 5

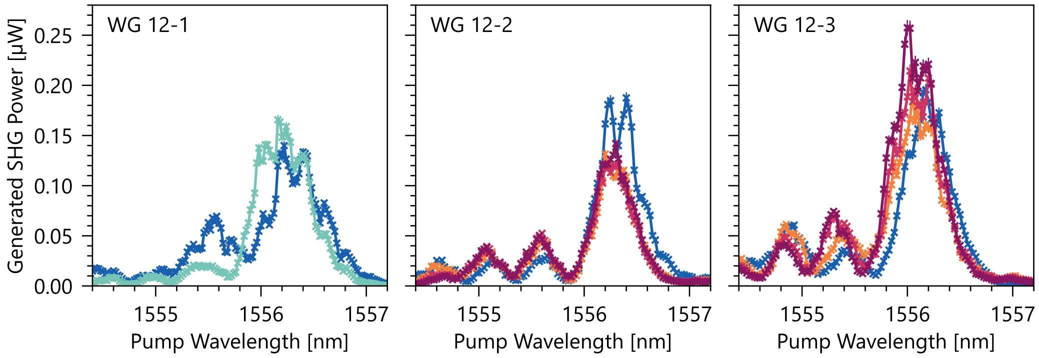

(b) Cooldown 6

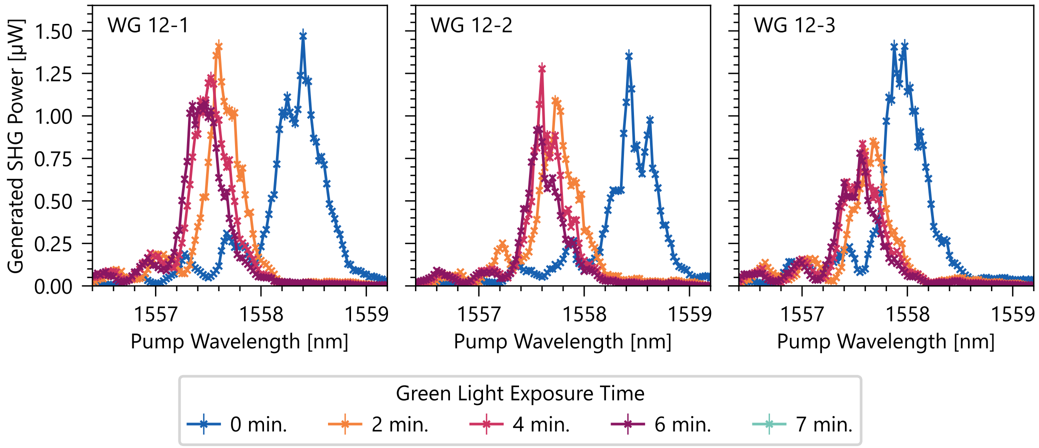

Figure A.9: Cryogenic phase-matching spectra for WGG 12 when pumping the SHG process with a CW input power of 25.1 mW. The green laser diode was activated between the individual measurements for a consistent time interval of 2 min. Note that waveguide 12-1 was operated differently in cooldown 5, as this first measurement was employed to perform additional alignment of the green beam and to define a reasonable time interval to test the green exposure for the other waveguides.

A.6 A narrative about the cryogenic traffic jam

The main results of this thesis on the cryogenic effects of pyroelectricity and photorefraction can be illustrated by revisiting the “cryogenic traffic jam” metaphor. This narrative is meant to express the impact of both effects in a generally understandable way and does not claim physical correctness and completeness.

In this framework, the waveguide is a city street monitored across an extensive temperature range (compare Fig. A.10). On a warm summer day, the photons (represented here by cyclists) propagate freely. Even with cars (charge carriers) on the road, cyclists can navigate the route almost unhindered. However, as the temperature drops significantly in winter and large amounts of snow are falling on the street, the mobility of the system is restricted. The accumulation of pyroelectric charges during the cooldown acts like a buildup of stalled vehicles, which can lead eventually to a state where the system “freezes in”.

This jam is further impaired by the introduction of light, such as a strong optical pump. Within our metaphor, the enhanced accumulation of charges due to the photorefractive effect corresponds to the increased volume of cars during daytime. The obstacles on the road cause a local retardation of the flow. Much like cyclists experience small delays that prevent a steady pace if they must navigate around snow and standing cars, photons encounter localized refractive index modifications. These variations cause unwanted phase shifts, meaning the interacting waves are no longer synchronized, leading to phase-matching distortions. If the road becomes too congested, cyclists may be forced to deviate from their path entirely. This is analogous to spatial mode distortion; when the refractive index changes are sufficiently strong, they act as scattering centers. The photons are then diverted

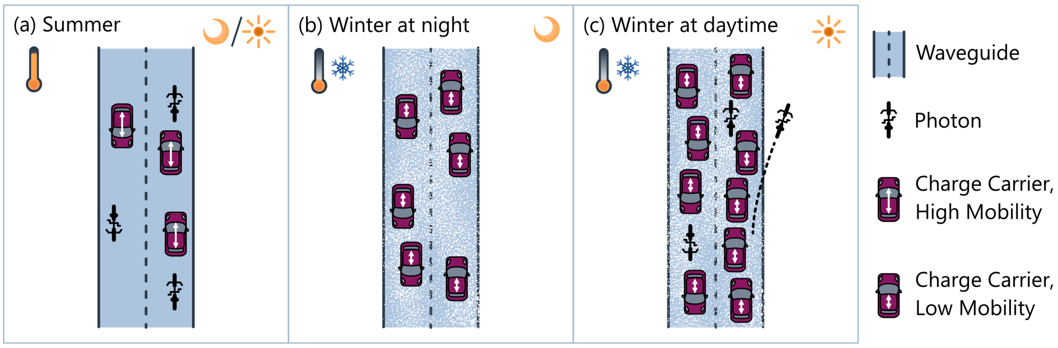

Figure A.10: Illustration of the cryogenic implications on the waveguide performance. The waveguide is occupied by charge carriers of various mobility. (a) Under warm conditions in summer, photons can move freely, regardless of whether it is day or night. (b) The cooldown is analogous to winter conditions at night; pyroelectric charges accumulate and become trapped due to the system’s low mobility. (c) Under daytime illumination, photorefraction generates additional charges, which adversely affect the waveguide transmission by introducing further perturbations. Cyclists must adjust their pace locally or deviate from their route.

into the substrate, resulting in increased transmission losses. Finally, while the photons do not change their group velocity, their movement is increasingly perturbed by the trapped charges, leading to degraded waveguide performance at cryogenic temperatures.

Chapter 4 investigated the implications on the orthogonal polarizations. If these are visualized as two separate streets, the "TE street" appears better shielded from the environment, while the "TM street" remains fully exposed to the elements. The photons (cyclists) can travel along either street. However, the TE street is routed through a protective tunnel (compare Fig. A.11), allowing traffic to flow almost entirely unaffected by the weather. In contrast, on the exposed TM street, the cars (charge carriers) move slowly or stop as the temperature drops. This resulting congestion - symbolizing the "frozen in" charges - disturbs the propagation of TM-polarized modes. Crucially, the severity of this traffic jam is a probabilistic process. Just as every snowy day does not result in the same level of traffic chaos, not every cooldown cycle produces identical charge distributions. This explains why TM-polarized photons experience variable propagation losses across different experimental cycles.

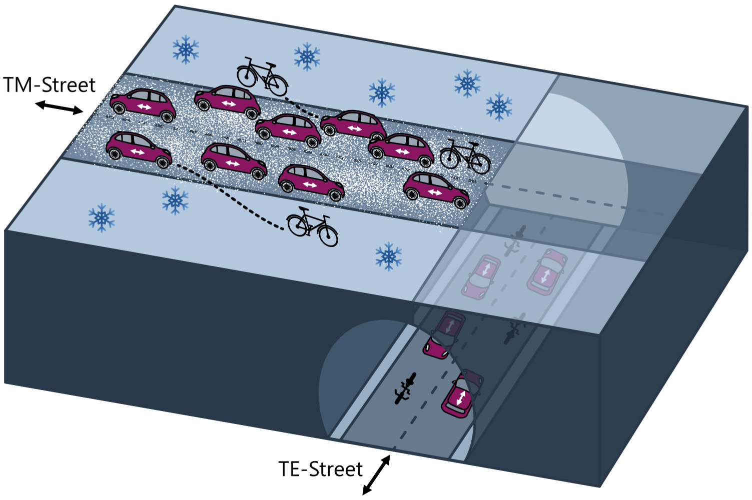

Figure A.11: Illustration of the polarization-dependent impact of cryogenic operation. The orthogonal modes are represented as distinct paths: the "TE street" is effectively shielded from cryogenic disturbances, depicted here as a protective tunnel. In contrast, the "TM street" is highly susceptible to weather conditions.

The experiments presented in Chapter 5 shifted the focus from observing the traffic jam, to actively regulating the flow. The auxiliary green beam can be pictured as activating a set of carefully timed traffic lights. Their purpose is to temporarily mobilize the stalled cars by providing localized energy. It was shown that this illumination does not always produce identical outcomes. Sometimes the lights are perfectly synchronized and the flow improves, at other times they fail and the traffic remains stalled. Likewise, thermal annealing can be seen as sending a road-maintenance crew to clear the snow from the streets and tow away stranded cars. However, when the temperature drops again, new cars eventually get stuck on the same streets and the traffic rearranges into a different pattern.

Together, these mitigation strategies reveal that the cryogenic streets are not immobilized permanently: with the right combination of optical energy and thermal annealing, its internal traffic can still be guided into motion. Ultimately, achieving stable cryogenic operation requires learning the underlying traffic rules - the interplay of pyroelectric and photorefractive effects that dictate how and when mobility can be restored. Once these rules are understood, the cyclists can continue their journey even through the deepest winter.

Acknowledgements

I would like to express my gratitude to everyone who has supported me and my work. First of all, I would like to thank Prof. Dr. Tim J. Bartley. Thank you so much for your tremendous support and great discussions over the last almost eight years. I really appreciate being part of your research group since its early days and watching the whole group develop and grow since my Bachelor project. You have created something impressive, and I am proud to have been a part of it.

I would also like to thank Prof. Dr. Christine Silberhorn, who has been a truly inspiring role model. Thank you for agreeing to evaluate this thesis.

Moreover, I want to thank the funding agencies Bundesministerium für Forschung, Technologie und Raumfahrt and Deutsche Forschungsgemeinschaft, including all members of the SFB/TRR 142.

Special thanks to all my (former) colleagues in the Mesoscopic Quantum Optics group. I had a great time working with you guys. Thanks for many chats, great times in the lab, and for giving me the chance to grow with you. A big thank you to Dr. Jan Philipp Höpker, Dr. Maximilian Protte, Dr. Thomas Hummel, Dr. Frederik Thiele, Dr. Lorenzo Procopio, Johanna Biendl, Aishi Barua, Niklas Lamberty, and Timon Schapeler for all your feedback and support. I want to emphasize that we all did a very good job coordinating our separate projects in a rather small lab. Apart from the fact that you adapted to various ambient light conditions for my sake, I really appreciate your patience with the squeaking noises that occurred whenever I moved any piezo positioners.

Furthermore, I would like to thank everyone who supported my work by fabricating waveguides with various poling periods for the cryogenic processes. Many thanks to Dr. Maximilian Protte (MQO group) and the fabrication teams of the IQO group and PhoQS, specifically Raimund Ricken, Viktor Quiring, Sebastian Lengeling, Philipp Mues, and Dr. Christof Eigner.

I am particularly thankful to Jan Philipp, Aishi, Max, and Johanna for not only being great colleagues, but also becoming my friends. Thank you to the core members of our board game evening crew, including Thomas, Julian Brockmeier, and Timon. Moreover, I would like to thank Silia Babel from the IQO group. Thank you for becoming such an awesome friend whom I could always rely on for emotional support and fresh perspectives in scientific discussions.

Thank you all for assisting me with this project, which yielded so many interesting (although sometimes frustrating) results, driven by the entertaining and non-reproducible behavior of cryogenic lithium niobate. My personal highlights include working with visible light, in particular realizing sum-frequency generation. Whenever the pump wavelengths fulfilled the phase-matching condition, the orange beam on the alignment card reminded me of beautiful tiny sunsets in an otherwise dark lab.

Last but not least, I want to thank my family and friends, who always supported me along the way. Special thanks go to my parents and grandparents. You have always told me that you are proud of me, and you have always been there to listen to how I am doing. Thank you. Finally, I would especially like to thank my soon-to-be husband, Timon Schapeler, who has been with me on this journey from the very beginning. Thank you for your love and unlimited support, without which I would never have come this far.

Erklärung

Ich versichere, dass ich die Arbeit ohne fremde Hilfe und ohne Benutzung anderer als der angegebenen Quellen angefertigt habe und dass die Arbeit in gleicher oder ähnlicher Form noch keiner anderen Prüfungsbehörde vorgelegen hat und von dieser als Teil einer Prüfungsleistung angenommen worden ist. Alle Ausführungen, die wörtlich oder sinngemäß übernommen worden sind, sind als solche gekennzeichnet.

Ort, Datum	Unterschrift